Dissertation

submitted to the

Combined Faculties of the Natural Sciences and Mathematics of
the Ruperto-Carola-University of Heidelberg, Germany

for the degree of

Doctor of Natural Sciences

Put forward by

Philipp Cörlin

born in Böblingen

Oral examination: October 14th, 2015

Tracing ultra-fast molecular dynamics in O_2^+ and N_2^+ with XUV–IR pump–probe experiments

Referees:

Priv.-Doz. Dr. Robert Moshammer
Prof. Dr. Andreas Wolf

Abstract Within this thesis, molecular dynamics of diatomic molecules is studied using the XUV–IR pump–probe technique. Here, a single extreme ultraviolet (XUV) photon created by high-harmonic generation ionizes the diatomic target molecule. The initiated dynamics is probed after a variable time delay by an ultrashort (12 fs) infrared (IR) laser pulse. The 3-dimensional momenta of all charged fragments are measured using a reaction microscope.
In an experiment on O_2, a nuclear wave-packet oscillation is observed on the binding potential-energy curve (PEC) of the $O_2^+(a\,^4\Pi_u)$ electronic state. By comparing simulated results with experimental data, theoretically predicted PECs are tested. The experimental results are best reproduced if the wave packet is propagated on a Morse potential adjusted to the experimental data. This demonstrates the sensitivity of our method and its ability to predict accurate PECs from the measured wave-packet evolution.
In an N_2 experiment, the pump–probe delay dependent yield of stable N_2^{++} is observed. It is interpreted as a sequential double ionization via a highly excited antibonding cationic state. The dissociation of the intermediate state is temporally resolved and can be interrupted by multi-photon ionization with the IR pulse within ≈ 15 fs after XUV ionization.

Abstract Für diese Arbeit wurden Moleküldynamiken mit Hilfe der Pump-Probe Technik untersucht. Dabei ionisiert ein einzelnes durch hohe harmonische Erzeugung hervorgebrachtes, extrem ultraviolettes (XUV) Photon das zu untersuchende zweiatomige Molekül. Die so in Gang gesetzte Dynamik wird nach einer variablen Verzögerungszeit von einem ultrakurzen (12 fs) infraroten (IR) Laserpuls abgefragt. Die dreidimensionalen Impulse aller Fragmente werden mit einem Reaktionsmikroskop gemessen.
In der Untersuchung von O_2 wird ein Kernwellenpaket auf der bindenden Potentialkurve (PEC) des elektronischen $O_2^+(a\,^4\Pi_u)$ Zustandes beobachtet. Durch den Vergleich von simulierten Ergebnissen mit den experimentellen Daten werden theoretisch vorhergesagte PECs überprüft. Die experimentellen Ergebnisse werden am Besten wiedergegeben, wenn das Wellenpaket in einem Morsepotential entwickelt wird, welches an die experimentellen Daten angepasst wurde. Dies demonstriert die Empfindlichkeit unserer Methode und ihre Fähigkeit genaue PECs aus der gemessenen Wellenpaketdynamik vorherzusagen.
In einem Experiment zu N_2 wird die von der Verzögerungszeit abhängige Erzeugung von stabilem N_2^{++} beobachtet. Dies wird durch eine sequentielle Doppelionisation mit einem instabilem Zwischenzustand erklärt. Die Dissoziation des Zwischenzustandes wird zeitlich aufgelöst und kann innerhalb von etwa 15 fs durch eine Mehrphotonenionisation mit dem IR Puls unterbrochen werden.

List of Publications

Probing calculated O_2^+ potential-energy curves with an XUV-IR pump-probe experiment
P. Cörlin, A. Fischer, M. Schönwald, A. Sperl, T. Mizuno, U. Thumm, T. Pfeifer, and R. Moshammer
Phys. Rev. A **91**, 043415 (2015)

Molecular wave-packet dynamics on laser-controlled transition states
A. Fischer, M. Gärttner, P. Cörlin, A. Sperl, M. Schönwald, T. Mizuno, G. Sansone, A. Senftleben, J. Ullrich, B. Feuerstein, T. Pfeifer, and R. Moshammer
Submitted
arXiv:1410.8032 [physics] (2014)

Measurement of the autoionization lifetime of the energetically lowest doubly excited $Q_1\,{}^1\Sigma_u^+$ state in H_2 using electron ejection asymmetry
A. Fischer, A. Sperl, P. Cörlin, M. Schönwald, S. Meuren, J. Ullrich, T. Pfeifer, R. Moshammer and A. Senftleben
J. Phys. B: At. Mol. Opt. Phys. **47**, 021001 (2014)

Electron Localization Involving Doubly Excited States in Broadband Extreme Ultraviolet Ionization of H_2
A. Fischer, A. Sperl, P. Cörlin, M. Schönwald, H. Rietz, A. Palacios, A. González-Castrillo, F. Martín, T. Pfeifer, J. Ullrich, A. Senftleben, and R. Moshammer
Phys. Rev. Lett. **110**, 213002 (2013)

Contents

1. Introduction **3**

2. Diatomic molecules (in light fields) **9**

2.1. Born-Oppenheimer approximation . . . 10
2.1.1. Molecular orbitals . . . 11
2.1.2. Spectroscopic notation and symmetries . . . 14
2.1.3. Potential-energy curves . . . 15
2.1.4. Vibrational states . . . 17
2.2. Resonant transitions between electronic states . . . 18
2.3. Ionization and related phenomena . . . 20
2.3.1. Franck-Condon principle . . . 21
2.3.2. Strong-field ionization . . . 21
2.3.3. High-harmonic generation . . . 28
2.4. Wave-packet dynamics . . . 32
2.4.1. Quantum-beat period T_{QB} and revival time T_{rev} . . . 32
2.4.2. Adjusting a Morse potential to measured times T_{QB} and T_{rev} . . . 34
2.5. Simulation of molecular dynamics . . . 36
2.5.1. Propagation of a wave packet on PECs . . . 36
2.5.2. Coupled-channel simulation . . . 37
2.5.3. Split-step algorithm . . . 39

3. Ultrashort laser pulses and optical setup **43**

3.1. Theoretical description . . . 43
3.1.1. Modelocking . . . 44
3.1.2. Dispersion . . . 46
3.1.3. Nonlinear optics and self-phase modulation . . . 47
3.2. Generation of XUV pump and IR probe pulses . . . 48
3.2.1. Ti:sapphire oscillator . . . 50
3.2.2. Ti:sapphire multi-pass amplifier . . . 51
3.2.3. Hollow-core fiber and chirped-mirror compressor . . . 52
3.2.4. High-harmonic generation and pump–probe interferometer . . . 54
3.2.5. Pulse overlap and determination of the pulse duration . . . 59

4. Reaction microscope **61**
4.1. Working principle and technical specifications . . . 61
4.1.1. Gas jet and vacuum . . . 63
4.1.2. Electric and magnetic field . . . 66
4.1.3. Micro-channel-plate detector and delay-line anodes . . . 66
4.2. Momentum reconstruction . . . 68
4.2.1. Ions . . . 69
4.2.2. Electrons . . . 70
4.2.3. 4π acceptance and momentum resolution . . . 72
4.3. Experimental techniques . . . 75
4.3.1. Optimizing the pulse overlap . . . 75
4.3.2. Post analysis and particle coincidences . . . 76

5. Probing O_2^+ potential-energy curves with an XUV–IR pump–probe experiment **79**
5.1. Historical overview of wave-packet dynamics in diatomic molecules . . 80
5.2. Experimental spectra and vibrational wave-packet dynamics . . . 82
5.2.1. Experimental parameters . . . 83
5.2.2. Pump–probe delay independent spectra and identification of reaction channels . . . 83
5.2.3. Wave-packet dynamics and pump–probe scheme . . . 86
5.2.4. Adjusting a Morse potential to the experimental data . . . 90
5.2.5. Fourier transform and QB energies . . . 90
5.2.6. Angular dependence of the time-dependent O^+ yield . . . 95
5.2.7. Photoelectron spectra . . . 96
5.3. Comparison between experimental data and simulated spectra . . . 99
5.3.1. Using the repulsive PEC from Marian et al. [MMP+82] . . . 102
5.3.2. Using the repulsive PEC from Magrakvelidze et al. [MAT12] 106
5.4. Limitations of the quantum simulation . . . 109
5.4.1. Influence of pump step on the simulated spectra . . . 110
5.4.2. Influence of probe pulse parameters on the simulated spectra . . 111
5.5. Summary of the O_2 experiments . . . 113

6. Sequential XUV–IR double ionization of N_2 via an anti-bonding cationic state **115**
6.1. Experimental parameters . . . 116
6.2. Pump–probe delay independent spectra and identification of N_2^{++} events 117
6.3. Pump–probe delay dependent yield of N_2^{++} . . . 118
6.3.1. Pump–probe scheme . . . 120
6.3.2. Ion spectra . . . 121
6.3.3. Photoelectron spectra . . . 124
6.4. Comparison between simulation and experiment . . . 126
6.5. Pump–probe delay dependent yield of N^+ fragments . . . 131
6.6. Summary of the N_2 experiments . . . 133

7. Summary and outlook **135**
7.1. Summary of the O_2 experiments 135
7.2. Summary of the N_2 experiments 137
7.3. Outlook 138

Appendices **142**

A. Atomic unit system and other non-SI units **142**

B. Hamilton operator of diatomic molecule **143**

C. Results of coupled-channel simulations for varying IR pulse parameters **144**

Bibliography **149**

1. Introduction

A detailed understanding of reaction pathways and their intermediate states is of great interest to many fields of chemistry and even life sciences. Due to the typical bond strength in the range of a few electronvolt [BE03] and the small bond length on the order of an Angstrom (1×10^{-10} m) [HL07], the formation and the breakup of molecular bonds (and thus a chemical reaction) occurs within tens of femtoseconds[1]. Such processes cannot be captured on camera with classical photography, as no mechanical shutter or electronic circuit operates at these timescales.

Due to this, the temporal resolution necessary for the study of transition states was not reached for several decades. At the molecular level, chemistry was therefore restricted to the investigation of the 'before' and 'after' of chemical reactions [Smi87]. The situation changed drastically in the late 1980s, when so-called pump–probe experiments employing ultrashort laser pulses reached a temporal resolution on the femtosecond timescale enabling the observation of transition states of chemical reactions [Zew88]. These groundbreaking experiments ultimately led to the birth of a new scientific field, the *femtochemistry* [Zew00].

At about the same time, improvement of recoil-ion momentum spectrometers was stimulated by ion-collision experiments [USB87]. By charge-state-resolved detection of the recoil ions, this type of experiment allowed to measure charge-differential ionization cross sections at very small scattering angles (corresponding to large impact parameters) [USBK88]. Additional cooling of the target atoms in a supersonic expansion enhanced the momentum resolution in these apparatuses significantly. In reaction microscopes [MUU+94], the latest generation of momentum spectrometers, coincident detection of ions and electrons over the full solid angle and with high momentum resolution is made possible by an additional magnetic field. This allows to conduct kinematically complete experiments on the ionization of atoms and small molecules.

Combining these momentum spectrometers developed for collision experiments with the ultrashort laser pulses allows to conduct experiments on ultra-fast quantum dynamical processes in single atoms and molecules. The pump–probe technique applied in these measurements is illustrated in Fig. 1.1 for the special case of an XUV–IR[2] pump–probe experiment on diatomic molecules. The underlying principle, however, is independent of the utilized laser pulses: First a so-called pump pulse

[1] This estimation from $T = \frac{s}{v} = \frac{s}{\sqrt{2E/m}} \approx 30\,\text{fs}$ with $s = 1 \times 10^{-10}\,\text{m}$, $E = 1\,\text{eV}$, and $m = 16\,\text{amu}$ turns out to be in surprisingly good agreement with the timescales of the quantum-dynamical processes measured within this thesis.

[2] In this thesis, the abbreviations for extreme ultraviolet (XUV) and infrared (IR) are used.

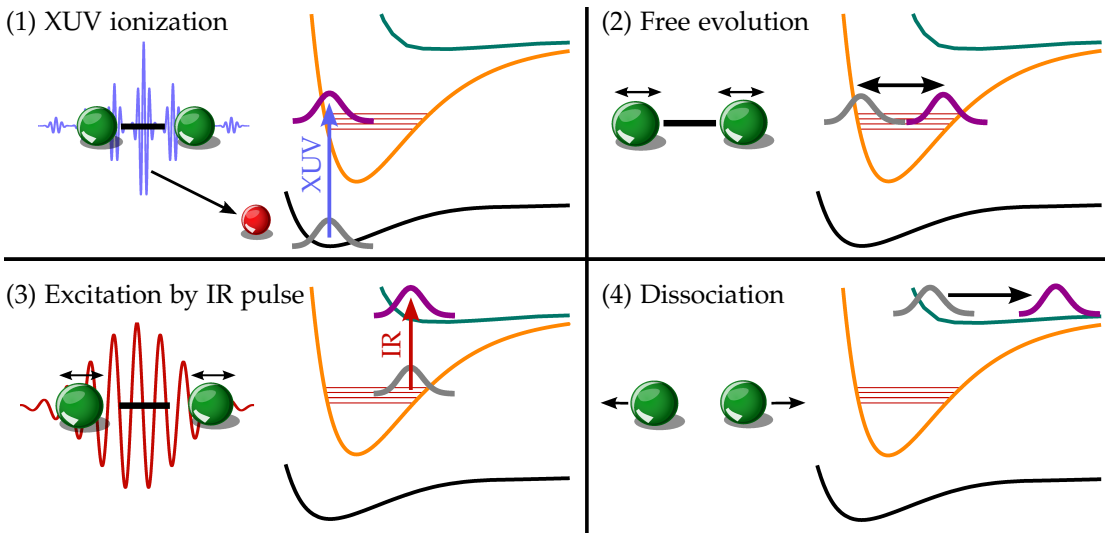

Fig. 1.1. Illustration of a typical XUV–IR pump–probe scheme used to investigate the nuclear dynamics in diatomic molecules with a reaction microscope. **Panel (1):** Ionization by the XUV pump pulse creates a nuclear wave packet on an ionic potential-energy curve (orange curve). The emitted photoelectron (red ball) is detected with the reaction microscope. **Panel (2):** The wave packet evolves for a variable time delay. **Panel (3):** The IR probe pulse promotes the nuclear wave packet to an anti-bonding potential-energy curve (green curve). **Panel (4):** The molecular ion dissociates and the charged fragments are detected using a reaction microscope. Repeating the experiment for various pump–probe delays allows to reconstruct the temporal evolution of the nuclear wave packet.

initiates a dynamical process, typically by electronic excitation or ionization of the target. Afterwards, the system evolves freely, until its current state is probed by a second laser pulse. Repeating the experiment for varying pump–probe delays allows to image the field-free evolution of the system.

Employing an IR–IR pump–probe scheme, the dissociation of H_2^+ and D_2^+ – and thus the break of the arguably simplest chemical bond – on timescales of a few tens of femtoseconds was traced in real time [AUT+05, ERF+05, ALO+06]. In the following years, vibrational wave packets in the cations of various diatomic molecules were observed in a series of experiments [REF+06, ERF+06, NVC06, KLS+09, DBM+10, DMB+11]. Measuring the time evolution of these wave packets over a large range of pump–probe delays allows to deduce detailed information about the vibrational level spacing and the shape of involved binding potentials. Interpretation of pump–probe experiments on poly-atomic molecules is more challenging due to the additional degrees of freedom in the nuclear motion. The time-resolved observation of a hydrogen migration in acetylene (C_2H_2), however, proves that isomerization and the formation of chemical bonds can be imaged in real time [HMFT07, JRH+10, MFTH11].

The ability to trace molecular dynamics in the time domain is considered an im-

portant step towards the steering of chemical reactions with laser pulses. While the laser-control of complex chemical reactions is still fiction, many proof-of-principle experiments have already been performed. The fragmentation dynamics of H_2 [KFF+09] but also that of larger molecules such as acetylene [AKS+14] has been influenced substantially by the carrier-envelope phase of few-cycle laser pulses. Generation of tailored laser pulses using evolutionary algorithms allows to modify the branching ratios in the fragmentation of poly-atomic molecules [LMR01] or influence energy transfer mechanisms in light-harvesting complexes [HWC+02].

The temporal resolution achieved in pump–probe experiments is usually limited by the pulse duration. Common femtosecond laser systems emit light at a center wavelength of about 800 nm. At this wavelength, state-of-the-art few-cycle pulses [BK00] approach the fundamental single-cycle limit of 2.5 fs. This is short enough to resolve most nuclear dynamics. The beating between electronic states separated by a few electronvolts, however, occurs at timescales of $T \lesssim h/(1\,\mathrm{eV}) \approx 4\,\mathrm{fs}$. Thus, the dynamics of deeply bound electrons can only be resolved with laser pulses in the ultraviolet or even extreme ultraviolet (XUV) regime where the single-cycle limit is pushed into the attosecond timescales.

This became feasible with the discovery of the high-harmonic generation (HHG) process [MGJ+87, FLL+88] which allows to generate attosecond pulses in the XUV energy regime with pulse durations below 100 as [GSH+08, ZZC+12]. This is short enough to track down electron dynamics. Although single-attosecond pulse sources are still not intense enough to perform XUV–XUV pump–probe experiments on a daily basis, first prototype experiments already exist [TSN+11] and it is only a matter of time until further experiments will be performed [LIV14].

Today, an increasing number of laboratories routinely conduct XUV–IR pump–probe experiments using the fundamental IR pulse as a probe for dynamics initiated by the XUV pulse. Due to the HHG process, the phase relation between the two pulses is intrinsically fixed. This allows to perform new types of measurements. In attosecond streaking, for example, photoelectrons created by XUV ionization are accelerated by the IR laser field. By measuring the photoelectron momentum as a function of the pulse delay, the electric field of the driving IR laser pulse and the duration of the attosecond pulse can be precisely reconstructed [KGU+04]. Using streaking techniques, experiments on ionization delays can be conducted with temporal resolutions down to a few attoseconds [SFK+10, MGA+14]. In XUV–IR transient absorption experiments, the optical density of a target is investigated in the presence of an additional strong IR field. This is, for example, used to study Fano resonances [OKR+13, KOB+14] or electron correlations [OKA+14].

For this thesis, time resolved experiments have been performed on diatomic molecules using different XUV–IR pump–probe schemes. This has several advantages compared to an IR–IR pump–probe experiment: First of all, only a single XUV photon is absorbed in the pump step. Thus, if the XUV spectrum is known, detection of photoelectrons and

ions in a kinematically complete experiment allows to determine the electronic states participating in the observed reaction [GRT+07, CDS+10]. Due to the large number of electronic states in molecules, this simplifies the interpretation of experimental spectra tremendously. Furthermore, the single-photon ionization cross sections are usually well known from synchrotron experiments or calculations. Finally, field-dressing by the XUV pulse in the pump step is negligible and the excitation of vibrational states is well described by the Franck-Condon principle.

In this work, O_2 and N_2 have been investigated. Due to their large number of binding electronic states, identification of experimentally observed reaction channels is often challenging. As a result, they have been investigated less frequently in pump–probe experiments than e.g. H_2 or D_2, although being very interesting and important due to their abundance in the earth's atmosphere. In spite of featuring many states, O_2 and N_2 are well understood by theory and their single nuclear degree of freedom allows to explain the nuclear dynamics on one dimensional Born-Oppenheimer potential-energy curves (PECs). Thus, the experimental data can be interpreted using comparably simple quantum calculations. This is in contrast to pump–probe experiments on polyatomic molecules which often require sophisticated time-dependent quantum-chemistry calculations in order to be interpreted [CAT+14].

The first experiment presented in this thesis investigates the vibrational wave-packet dynamics in the binding $a\,^4\Pi_u$ electronic state of the O_2^+ molecular ion. The measured time-evolution of this wave packet is used to adjust a Morse potential. With this, we able to predict the shape of the $a\,^4\Pi_u$ PEC and therefore the molecular bond strength as a function of the internuclear distance. Using a large range of pump–probe delays, the vibrational level spacing in the binding PEC is determined with a high accuracy. In contrast to the results of a previous IR–IR pump–probe experimentDe2011, our data is in good agreement with the computed vibrational levels of the $a\,^4\Pi_u$ PEC predicted by Ref. [MAT12].

Furthermore, the experimental data is compared to results of coupled-channel simulations. Our simulations show that the shape of some PECs predicted in Refs. [MMP+82, MAT12] contradicts our experiment. Moreover, certain features in the experimental spectra cannot be reproduced with any of the theoretical PECs. On the other hand, we find an excellent agreement with the experimental data, if the wave-packet dynamics is simulated with the Morse potential. This demonstrates that highly accurate PECs can be predicted by measuring the time-evolution of a nuclear wave packet. In addition, our method is sensitive to small variations in the shape of the binding potential and can be used test PECs calculated by theory.

In a second measurement, the delay-dependent sequential double ionization of N_2 has been investigated with an XUV–IR pump–probe experiment. In an earlier experiment, an increase of the N_2^{++} yield was observed in the temporal overlap of the

laser pulses. However, due to the rather long IR pulse durations (28 fs), the authors were not able to investigate details of the involved reaction [GRT+07, Supplementary Material].

That measurement has been repeated with shorter (12 ± 3) fs IR pulses, in this work. Due to the resulting superior temporal resolution, we were able to measure the nature of this two-step process in more detail. The new features observed in our data can be explained by a sequential double ionization via a highly excited cationic intermediate state. Since this state is anti-bonding, its population by ionization with the XUV pulse causes the molecule to dissociate immediately. This bond breaking is temporally resolved in our experiment. For pump–probe delays smaller than about 15 fs, further ionization with the IR laser pulse interrupts the molecular fragmentation and leads to the formation of stable N_2^{++}. By comparing the experimental results with a simple quantum simulation, we obtain additional information on the PEC of the highly excited intermediate state. The agreement between our experimental data and the simulation is best, if we include an intermediate state in our calculations that was not considered to be significantly populated by XUV ionization in Ref. [GRT+07].

Structure of this thesis An introduction to the physics of diatomic molecules with a focus on the Born-Oppenheimer approximation is given in Chap. 2. Within this approximation, nuclear dynamics occurs on PECs. This is used throughout this thesis for an intuitive interpretation of the measured molecular dynamics. Subsequently, a brief introduction to resonant transitions and (strong-field) ionization of molecules is given. Methods for the simulation of molecular dynamics are described afterwards.

Chap. 3 introduces the theoretical description of ultrashort laser pulses and presents the optical setup including the laser system and the high-harmonic generation vacuum chamber. The working principle of the reaction microscope is explained in Chap. 4.

Afterwards, the experimental data on the vibrational wave-packet dynamics in O_2^+ is presented and compared to simulations in Chap. 5. Results of an XUV–IR pump–probe experiment on the sequential double ionization of N_2 via an anti-bonding cationic intermediate state are discussed in Chap. 6.

Finally the results of this work are summarized in Chap. 7. In addition, an outlook on planned improvements of our experimental setup and on future experiments is given.

2. Diatomic molecules (in light fields)

Contents

2.1. Born-Oppenheimer approximation 10
2.2. Resonant transitions between electronic states 18
2.3. Ionization and related phenomena 20
2.4. Wave-packet dynamics 32
2.5. Simulation of molecular dynamics 36

The observation of the Balmer series in the hydrogen spectrum [Bal85] – among other experimental discoveries such as the photo-electric effect [Her87] and the black-body radiation [Kir60] – triggered the invention of quantum physics in the beginning of the 20th century. Since then, the urge to understand the increasingly detailed experimental spectra of atoms has substantially contributed to the development of quantum theories. The pinnacle of this evolution was the theory of quantum electrodynamics which could explain the so-called Lamb shift [LR47], not described by Dirac's theory, for the first time.

Today, quantum electrodynamics is the most precise fundamental theory in physics. Unfortunately, describing molecules with this theory is too complicated. Worse, without approximations, even the (comparably simple) non-relativistic Schrödinger equation cannot be solved analytically for any molecule. As a result, theoretical predictions can only be made by solving the equations numerically and/or by applying certain approximations. Thus, modern experiments performed on atoms or molecules with many active electrons – possibly involving strong external (laser) fields – are often used to test existing and trigger the development of new numerical methods and approximations. Performing time-resolved pump–probe experiments on molecular dynamics using ultrashort laser pulses, we are able to trace the time evolution of nuclear wave packets on femtosecond timescales. The experimental results allow to extract information about the shape of the involved potential-energy curves which can be compared to potential curves predicted by theory.

This chapter begins in Sec. 2.1 with an introduction to the Born-Oppenheimer approximation which is commonly used to calculate molecular orbitals and potential-energy curves. Afterwards, in Sec. 2.2, resonant electronic transitions in dipole approximation are explained. In Sec. 2.3, the chapter continues with a description of ionization with a focus on the Franck-Condon principle and strong field ionization (including

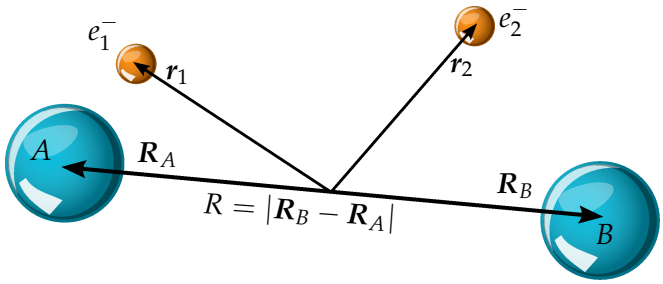

Fig. 2.1. Coordinates in the center-of-mass system for a diatomic molecule with two electrons (orange balls).

high-harmonic generation). Properties of the dynamics of nuclear wave packets within molecular potential-energy curves are explained in Sec. 2.4. The chapter ends in Sec. 2.5 with a description of the numerical simulations used to compare theoretical predictions with experimental data in Chaps. 5 and 6.

2.1. Born-Oppenheimer approximation

Even for the simplest neutral molecule, H_2 (illustrated in Fig. 2.1), consisting of two electrons and two protons only, the Schrödinger equation[1]

$$\hat{H}(\boldsymbol{r}, R)\Psi(\boldsymbol{r}, R) = E\Psi(\boldsymbol{r}, R) \tag{2.1}$$

(the Hamilton operator $\hat{H}(\boldsymbol{r}, R)$ describing a diatomic molecule is introduced in Appendix B) cannot be solved analytically [Dem10, p. 15-17]. Thus, molecular eigenstates and spectra must be calculated numerically. In order to simplify the numerical problem, the Born-Oppenheimer approximation [BO27] is often applied.

In this approximation the nuclear frame is considered to be stationary on the timescales of the electronic motion. In other words, the electrons adapt instantaneously to the Coulomb potential created by the nuclei. In most situations, this approximation is well justified due to the small mass of the electrons compared to the nuclear masses. In the Born-Oppenheimer approximation, the total wave function $\Psi(\boldsymbol{r}, R)$ is split into a purely electronic wave function $\phi(\boldsymbol{r}; R)$ and a nuclear wave function $\psi(R)$:

$$\Psi(\boldsymbol{r}_1, \ldots, \boldsymbol{r}_N, R) = \phi(\boldsymbol{r}_1, \ldots, \boldsymbol{r}_N)\psi(R) = \phi(\boldsymbol{r}; R)\psi(R). \tag{2.2}$$

The molecular orbitals (see Sec. 2.1.1) obtained and the spectroscopic notation (see Sec. 2.1.2) used in the Born-Oppenheimer approximation are introduced in the following. This product ansatz will lead to so-called potential-energy curves (PECs) introduced in Sec. 2.1.3 within which the nuclear vibrational states (see Sec. 2.1.4) are

[1] Unless otherwise noted, the atomic unit system is used throughout this chapter. See Appendix A for conversion to SI units.

embedded. All interpretations of our experimental data will involve these PECs, as the Born-Oppenheimer approximation often provides an intuitive picture of nuclear dynamics.

2.1.1. Molecular orbitals

By considering the nuclear frame as frozen, the electronic part of the Hamilton operator for a fixed internuclear distance R is given by

$$\hat{H}^{\mathrm{el}} = \hat{T}_e + V(\boldsymbol{r}, R) \tag{2.3}$$

[see Appendix B for introduction of the electron kinetic energy operator $\hat{T}_e$ and the Coulomb potential $V(\boldsymbol{r}, R)$] and the Schrödinger equation is written as

$$\hat{H}^{\mathrm{el}}\phi_\gamma(\boldsymbol{r}; R) = U_\gamma(R)\phi_\gamma(\boldsymbol{r}; R). \tag{2.4}$$

Here, the electronic wave functions $\phi_\gamma(\boldsymbol{r}; R)$ and the eigenenergies $U_\gamma(R)$ depend on a set of quantum numbers (indicated by γ) and the internuclear distance R which is a parameter. Thus the internuclear distance is taken into account by solving the electronic problem for different values of R which will (with an additional term describing the Coulomb repulsion between the nuclei) lead to the PECs (see Fig. 2.3 and Sec. 2.1.3). For now, we focus on methods to solve Eq. (2.4) and properties of the electronic wave functions ϕ_γ.

A standard approach for finding approximations for the eigenenergies $U_\gamma(R)$ and for the wave functions ϕ_γ is a variational method. In this, a suitable parametrized "trial function" $\Phi(\boldsymbol{r}; R)$ is chosen and the Schrödinger equation [Eq. (2.4)] is rewritten as $\hat{H}\Phi = W\Phi$ with

$$W = \min \frac{\int \Phi^* \hat{H} \Phi \mathrm{d}^3\boldsymbol{r}}{\int \Phi^* \Phi \mathrm{d}^3\boldsymbol{r}}. \tag{2.5}$$

By variation of the parameters defining Φ, the eigenenergy $W(\Phi)$ is minimized in order to obtain the best eigenenergy W and orbital Φ [HS15, p. 179]. Two different approaches to find suitable "trial functions" $\Phi(\boldsymbol{r}; R)$ are introduced in the following for the special case of H_2. As we will see, the choice of $\Phi(\boldsymbol{r}; R)$ can strongly influence the magnitude of the calculated dissociation energy D_e of the H_2 ground state.

Heitler-London approximation [HL27] In the Heitler-London approximation, the two-electron wave function of the H_2 ground state is constructed from a linear combination of two functions $\Phi^{HL}_{1/2}$. These are product wave functions of two hydrogen atom $1s$ orbitals:

$$\Phi^{\mathrm{HL}}_1 = \Phi_A(\boldsymbol{r}_1) \cdot \Phi_B(\boldsymbol{r}_2) \tag{2.6}$$

$$\Phi^{\mathrm{HL}}_2 = \Phi_A(\boldsymbol{r}_2) \cdot \Phi_B(\boldsymbol{r}_1). \tag{2.7}$$

Experimental value	Heitler-London	Simple MO	Improved MO	Ref. [KR60]
(4.7470 ± 0.0003) eV	3.14 eV	2.7 eV	4.02 eV	4.7467 eV

Tab. 2.1. Measured and calculated dissociation energy of the H_2 electronic ground state. Experimental value from Ref. [Dem10, p. 339].

Here $\Phi_A(\boldsymbol{r}_1)$ describes the $1s$ orbital of electron 1 centered at nucleus A and $\Phi_B(\boldsymbol{r}_2)$ describes electron 2 centered around nucleus B. Since the electrons are indistinguishable, Eq. (2.7) where electron 1 and electron 2 are exchanged, must be taken into account as well. The total wave function of the H_2 molecule is described by

$$\Phi^{\mathrm{HL}}_{\mathrm{H}_2}(\boldsymbol{r};\, R) = c_1\Phi^{HL}_1 + c_2\Phi^{HL}_2 = c_1\Phi_{A,B}(\boldsymbol{r}_1,\boldsymbol{r}_2) + c_2\Phi_{A,B}(\boldsymbol{r}_2,\boldsymbol{r}_1). \tag{2.8}$$

Here we use the abbreviations $\Phi_{A,B}(\boldsymbol{r}_1,\boldsymbol{r}_2) = \Phi_A(\boldsymbol{r}_1)\cdot\Phi_B(\boldsymbol{r}_2)$ for the product wave functions. Due to the Pauli principle, the spatial wave function must be either symmetric or antisymmetric under particle exchange[2]. This implies $c_1 = c = \pm c_2$ and two molecular wave functions are obtained

$$\Phi^{\mathrm{HL}}_{\mathrm{H}_2}(\boldsymbol{r};\, R) = c[\Phi_{A,B}(\boldsymbol{r}_1,\boldsymbol{r}_2) \pm \Phi_{A,B}(\boldsymbol{r}_2,\boldsymbol{r}_1)], \tag{2.9}$$

where c is a normalization constant[3]. Depending on the sign, either a 'gerade' or 'ungerade' molecular wave function is obtained (see Sec. 2.1.2 and Fig. 2.2). Energetically the symmetric wave function (with plus sign) is more favorable and features a dissociation energy D_e of 3.14 eV [Dem10, p. 339]. This value is compared to the experimentally measured dissociation energy of (4.7470 ± 0.0003) eV [Dem10, p. 339] in Tab. 2.1.

Molecular orbital approximation: In the molecular orbital (MO) approximation, first the single electron wave function of the H_2^+ molecular ion is constructed from a linear combination of atomic orbitals (LCAO). In a second step the two-electron wave function of H_2 is constructed from the orbitals of two H_2^+. This is conceptually different from the Heitler-London approximation where the two-electron wave function of H_2 was directly written as a product of two atomic orbitals [Dem10, p. 338].

The total H_2^+ wave function constructed by the LCAO describing a single electron orbiting either nucleus A or B is written as [Dem10, p. 331]

$$\Phi^{\mathrm{LCAO}}_{\mathrm{H}_2^+}(\boldsymbol{r}_1;\, R) = c_1\Phi_A(\boldsymbol{r}_1) + c_2\Phi_B(\boldsymbol{r}_1) = c_{\mathrm{H}_2^+}[\Phi_A(\boldsymbol{r}_1) \pm \Phi_B(\boldsymbol{r}_1)] \tag{2.10}$$

[2] The total wave function including the electron spin must be antisymmetric. The electron spin is not considered in the following simple examples.

[3] The coefficient c depends on the spatial overlap of the two atomic orbitals and therefore on the internuclear distance R.

where the expression $c_1 = c_{H_2^+} = \pm c_2$ was used. This is required due to symmetry arguments. Again, a symmetric (plus sign) and an antisymmetric (minus sign) spatial wave function was constructed. The bonding symmetric orbital is energetically favorable whereas the antisymmetric orbital is anti-bonding [Dem10, p. 333]. Since we are interested in the electronic ground state of H_2, the two-electron wave function is constructed from a product of symmetric H_2^+ molecular orbitals [plus sign in Eq. (2.10)]

$$\Phi_{H_2}^{MO}(\boldsymbol{r};\, R) = \Phi_{H_2^+}^{LCAO}(\boldsymbol{r_1};\, R) \cdot \Phi_{H_2^+}^{LCAO}(\boldsymbol{r_2};\, R) \tag{2.11}$$

$$= c_{H_2^+}^2 \left[\Phi_{A,B}(\boldsymbol{r}_1, \boldsymbol{r}_2) + \Phi_{A,B}(\boldsymbol{r}_2, \boldsymbol{r}_1) + \Phi_{A,A}(\boldsymbol{r}_1, \boldsymbol{r}_2) + \Phi_{B,B}(\boldsymbol{r}_1, \boldsymbol{r}_2)\right]. \tag{2.12}$$

Compared to the Heitler-London approximation [Eq. (2.9)], two additional terms $\Phi_{A,A}(\boldsymbol{r}_1, \boldsymbol{r}_2)$ and $\Phi_{B,B}(\boldsymbol{r}_1, \boldsymbol{r}_2)$ appear. These describe a molecule where both electrons are localized at the same nucleus. The dissociation energy of H_2 calculated in this simple MO approximation is 2.7 eV only and in less agreement with the experiment than the Heitler-London approximation (see Tab. 2.1). This is because all terms in Eq. (2.12) are weighted equally, although the latter two terms should be suppressed. Ignoring these terms the Heitler-London approximation gives the better results. The MO approximation is easily improved by adding a parameter $0 < \lambda < 1$ in Eq. (2.12). In the resulting improved MO approximation

$$\Phi_{H_2}^{MO}(\boldsymbol{r};\, R) \tag{2.13}$$

$$= c_1 \left(\Phi_{A,B}(\boldsymbol{r}_1, \boldsymbol{r}_2) + \Phi_{A,B}(\boldsymbol{r}_2, \boldsymbol{r}_1) + \lambda \left[\Phi_{A,A}(\boldsymbol{r}_1, \boldsymbol{r}_2) + \Phi_{B,B}(\boldsymbol{r}_1, \boldsymbol{r}_2)\right]\right). \tag{2.14}$$

the parameter $\lambda = \lambda(R)$ is optimized [using Eq. (2.5)] such that the eigenenergy is minimized for each internuclear distance R. This reduces the weight of the latter terms and a dissociation energy of 4.02 eV is obtained (see Tab. 2.1)[4].

At this state, the agreement with the experimental data is not very convincing. One reason is that only spherical 1s orbitals were used to construct the MOs. The deformation of the electron orbitals due to electron-electron interaction and the interaction between one electron and the other nucleus is not described by a 1s orbital centered around a nucleus. This can be taken into account by using non-spherical basis wave functions. Using 50 basis functions, the binding energy of the H_2 ground state was calculated to -4.7467 eV in Ref. [KR60] in excellent agreement with the experiment (see Tab. 2.1).

With modern computers and quantum chemistry programs, molecular potentials and wave functions can be calculated very accurately – at least for small molecules and not too high electronic excitations. Large basis sets of atomic and molecular orbitals in

[4] By adding the ionic H^-H^+ terms in the Heitler-London approximation and introducing the parameter λ as well, Heitler-London and the MO approximation yield identical results at this state of improvement [Dem10, p. 339].

$\Lambda =$	0	1	2	3
Name of state:	Σ	Π	Δ	Φ

Tab. 2.2. Designation of states with different quantum numbers Λ. Adapted from [HS15, p. 191].

combination with elaborated Hartree-Fock methods (HF-SCF) including configuration interaction (CI) are employed by these programs [HS15, p. 211]. However, larger molecules, molecular ions, excited states and open shells are still difficult to calculate and experiments are necessary in order to test theoretically predicted potential-energy curves (see Chap. 5).

2.1.2. Spectroscopic notation and symmetries

Diatomic molecules exhibit a rotational symmetry around the nuclear axis (in contrast to atoms which feature a spherical symmetry). In this case the operator for the orbital angular momentum $\hat{L}$ does not commute with the Hamilton operator and the corresponding quantum number l is not a good quantum number [HS15, p. 190]. The projection of $\hat{L}$ on the molecular axis $\hat{L}_z$ with eigenenergies $\hbar m_l$, however, is conserved and $\lambda = |m_l|$ is a good quantum number[5].

For many-electron wave functions, the quantum number for projection of the total orbital angular momentum on the molecular axis is called Λ and $\Lambda \leq \sum \lambda_i$ due to the vectorial addition of the angular momenta [HS15]. Λ is important for the designation of molecular states [see Eq. (2.17) and Tab. 2.2].

The wave functions of homonuclear diatomic molecules are either symmetric or antisymmetric under inversion at the center of mass $\boldsymbol{r} \rightarrow -\boldsymbol{r}$ and thus can be categorized in two groups, *gerade* and *ungerade* wave functions:

$$\text{gerade:} \quad \Phi_g(\boldsymbol{r}) = \Phi_g(-\boldsymbol{r}) \tag{2.15}$$

$$\text{ungerade:} \quad \Phi_u(\boldsymbol{r}) = -\Phi_u(-\boldsymbol{r}) \tag{2.16}$$

The dipole selection rules for resonant excitation will be introduced in Sec. 2.2. It will be shown that the angular momentum Λ, the parity and the electron spin of the initial and final molecular state pose strict selection rules onto dipole allowed electronic transitions. Molecular states are therefore denoted by these quantities:

$$X\,^{2S+1}\Lambda_{g,u} \tag{2.17}$$

Here the quantum number S of the total electron spin has been introduced. This causes a multiplicity of $2S+1$ of all electronic states similar to the atomic case. States are

[5] The sign of the quantum number m_l does not influence the energy.

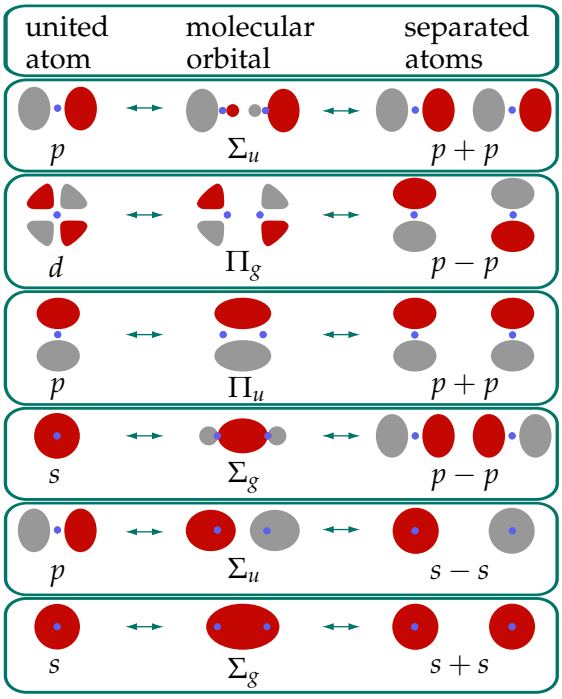

Fig. 2.2. The superposition of atomic orbitals with equal quantum number λ (right column) forms the molecular orbitals if the internuclear distance is reduced (center column). In the limit of vanishing internuclear distance, the "molecule" is described by atomic quantum numbers. Without an external field, the molecular orbitals of diatomic molecules feature a rotational symmetry around the nuclear axis. Figure adapted from Ref. [HS15, p. 193].

additionally classified by roman letters $(X,\ A,\ B,\ \dots)$ where X is the ground state, A labels the first excited state etc. Due to a different total electron spin, certain stated cannot be accessed from the X state by a resonant dipole transition. These states are labeled $(a,\ b,\ c,\ \dots)$. Some states have been discovered after the assignment of known a state and are labeled $(A',\ B'\ \dots)$ accordingly [Dem10, p. 338f].

Exemplary molecular orbitals with different quantum number Λ and parity are illustrated in Fig. 2.2. This figure also indicates, how the superposition of atomic orbitals of separated atoms combine to a molecular orbital when the internuclear distance is decreased. In the limit of $R = 0$, the nuclei are united into a single atom. The parity of the wave function does not change in this process.

2.1.3. Potential-energy curves

So far, we mainly discussed the molecular orbitals obtained when solving the electronic Schrödinger equation in Born-Oppenheimer approximation [see Eq. (2.4)]

$$\hat{H}^{\mathrm{el}}\phi_\gamma(\boldsymbol{r};\, R) = U_\gamma(R)\phi_\gamma(\boldsymbol{r};\, R).$$

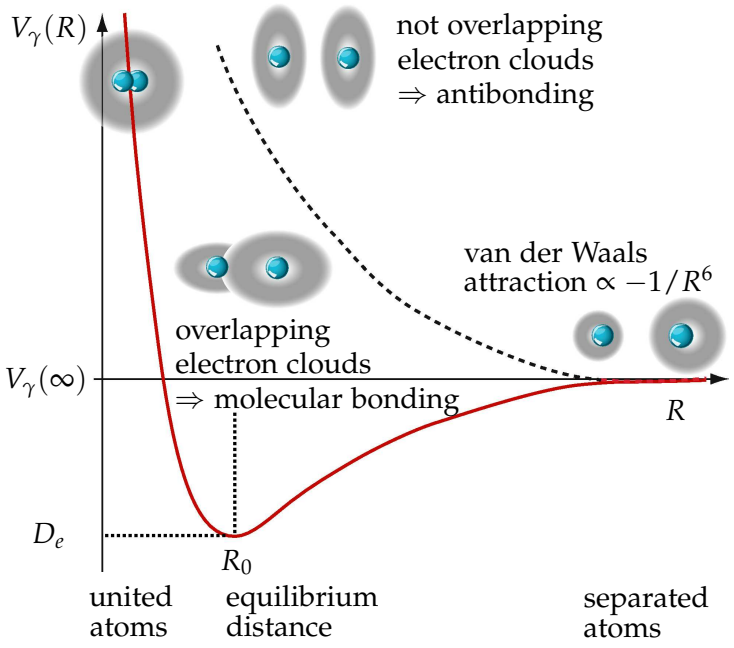

Fig. 2.3. Schematic potential-energy curves (PECs) of a diatomic molecule. Bonding electronic states form binding potentials with a depth D_e and an equilibrium distance R_0. Antibonding electronic states form repulsive PECs. Stable molecules do not exist in such electronic configurations. Figure adapted from Ref. [HS15, p. 141].

For the interpretation of our experimental results, however, the electronic energy eigenvalues $U_\gamma(R)$ are of higher importance. Calculating (and plotting)

$$V_\gamma(R) = U_\gamma(R) + \frac{Z_A Z_B}{R} \tag{2.18}$$

as function of the internuclear distance results in so-called potential-energy curves (PECs) shown in Fig. 2.3. Each PEC corresponds to an electronic state. The PECs are usually labeled according to the notation introduced in Eq. (2.17)[6]. For large internuclear distances, the PECs asymptotically reach the total energy of two separated atoms which is called the dissociation limit. Depending on the electronic excitation of the atoms, a great variety of dissociation limits (and PECs) exists. For small internuclear distances, the energy of all PECs diverges due to the Coulomb repulsion between the two nuclei [HS15, p. 141].

Depending on whether or not the PECs feature a potential minimum, they are either called binding or repulsive PECs. The former ones lead to stable molecules while an excitation to the latter ones causes the molecule to break apart. These two types of PECs are sketched in Fig. 2.3. D_e denotes the depth of the binding PEC relative to the limit of two separated atoms. In the case of a binding PEC, the potential minimum at $R = R_0$ is in the following called the equilibrium distance. For molecules in the vibrational ground state, this distance is usually in good agreement with the expectation value of the internuclear distance. There are, however, exceptions from this rule, such as the He dimer ($^4He_2$). The ground-state PEC of this molecule features an equilibrium distance of $R_0 = 5.6$ a.u. [TTY95], whereas the expectation value of the internuclear distance R was measured as 98 a.u. [GST+00].

2.1.4. Vibrational states

Up to now, only the solution of the electronic Schrödinger equation has been discussed. In the following, we consider the nuclear problem. The Hamilton operator describing the nuclei in the Born-Oppenheimer approximation is given by (see Ref. [HS15, p. 142f] for a derivation)

$$\hat{H}_n = \hat{T}_n + V_\gamma(R) = -\frac{1}{2\mu}\nabla_R^2 + V_\gamma(R) \tag{2.19}$$

and the corresponding Schrödinger equation is

$$\hat{H}_n \psi(R) = \left[-\frac{1}{2\mu}\nabla_R^2 + V_\gamma(R)\right] \Psi(R) = E_n \psi(R). \tag{2.20}$$

Solutions of this equation are illustrated in Fig. 2.4. The nuclear wave functions $\psi(R)$ are confined by the PEC in analogy to the wave functions in a harmonic oscillator. The

[6] For convenience we informally use the label of the corresponding electronic state to refer to certain PECs throughout this work.

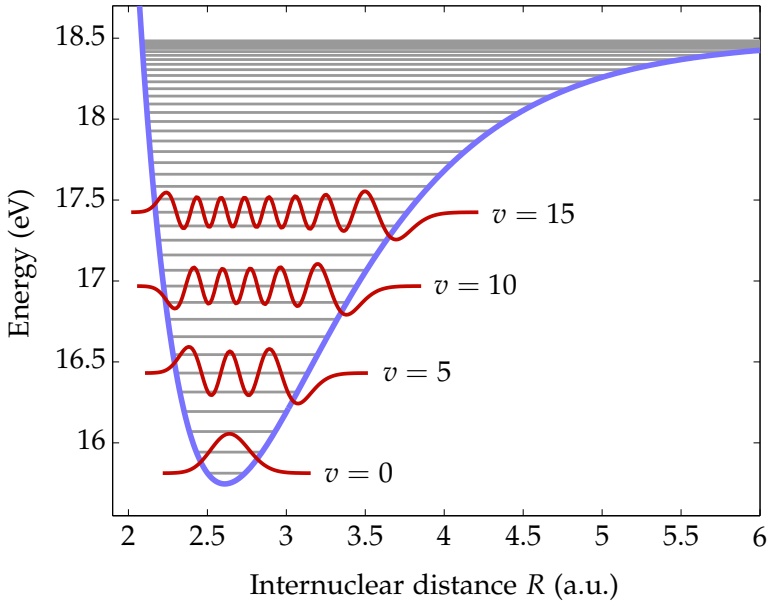

Fig. 2.4. Calculated vibrational energies of O_2^+ in a Morse potential. The level spacing is not constant due to the anharmonicity. Still, in contrast to e.g. the Coulomb potential, only a finite number of bound states exists. Calculated eigenfunctions (red curves) are plotted for some quantum numbers.

states can be described by a single quantum number which is usually designated v and the eigenenergy E_v of the vibrational states increases monotonically with v. In contrast to the harmonic oscillator, the vibrational levels within molecular PECs are not equidistant and the level spacing decreases towards the dissociation limit due to the potential's anharmonicity (see Fig. 2.4).

The absolute square of the vibrational wave functions $|\psi(R)|^2$ gives the probability density for finding a molecule at a certain internuclear distance R. In most cases, the potential minimum of binding PECs can be approximated by a harmonic potential. In this case the vibrational ground-state wave function is well described by a Gaussian function that is symmetric around R_0.

2.2. Resonant transitions between electronic states

This section introduces resonant transitions between electronic states in the dipole approximation. Such transitions (and their selection rules) are relevant for the understanding of the pump–probe scheme applied for the observation of the molecular wave-packet dynamics in O_2 (see Chap. 5).

The quantum mechanical transition from an initial state Ψ_i to a final state Ψ_f is

described by a transition amplitude

$$A_{fi} = \langle \Psi_f | \hat{H} | \Psi_i \rangle = \langle \phi_f, \psi_f, \chi_f | \hat{H} | \phi_i, \psi_i, \chi_i \rangle \tag{2.21}$$

where $\hat{H}$ is the interaction Hamilton operator. Here the Born-Oppenheimer approximation was used to express the total wave function as a product of an electronic wave function ϕ, a nuclear wave function ψ and a spin wave function χ.

In the following we consider the special case of a dipole transition induced by a laser field linearly polarized in z-direction. It features an amplitude $\mathcal{E}$ and a carrier frequency ω_0. The interaction Hamilton in dipole approximation is given by[7]

$$\hat{H}_{\mathrm{D}} = -z\mathcal{E}\cos(\omega_0 t) \tag{2.22}$$

and Eq. (2.21) is written as

$$\begin{aligned} A_{fi} &= \langle \phi_f, \psi_f, \chi_f | \hat{H}_{\mathrm{D}} | \phi_i, \psi_i, \chi_i \rangle && (2.23)\\ &= \langle \chi_f | \chi_i \rangle \langle \psi_f | \langle \phi_f | \hat{H}_{\mathrm{D}} | \phi_i \rangle | \psi_i \rangle && (2.24)\\ &= \langle \chi_f | \chi_i \rangle \langle \psi_f | M_{fi} | \psi_i \rangle . && (2.25) \end{aligned}$$

where the electric dipole operator does not act on the nuclear wave functions and the spin wave functions χ.

From the first term we obtain the dipole selection rule

$$\langle \chi_f | \chi_i \rangle \neq 0 \Leftrightarrow \triangle S = 0.$$

Thus, the total electron spin must be conserved in order to obtain a non-vanishing dipole transition amplitude.

The second term imposes restrictions on the electronic wave functions ϕ_f and ϕ_i. Arguments from group theory can be used to evaluate very efficiently for which combinations of ϕ_f and ϕ_i the integral

$$M_{fi} = \langle \phi_f | \hat{H}_{\mathrm{D}} | \phi_i \rangle \tag{2.26}$$

does vanish and the transition is dipole forbidden. Without going into detail, one can show that for diatomic, homonuclear molecules a dipole transition is allowed if the relation [HS15, p. 310]

$$\Gamma_f \otimes \Gamma_{\hat{H}_{\mathrm{D}}} \otimes \Gamma_i \supset \Sigma_g^+ \tag{2.27}$$

is fulfilled. Here Γ denotes the so-called irreducible representation (irrep) of the initial and final electronic state as well as that of the dipole operator. The whole argument boils down to a very simple idea: If the direct product of all irreps in Eq. (2.27) does not include the fully symmetric irrep Σ_g^+, the transition is dipole forbidden since the integral over all electron coordinates $\boldsymbol{r}$ in Eq. (2.26) vanishes.

[7] Here we do not consider rotational states and their excitation.

$\phi_i \diagdown \phi_f$	Σ_g^+	Σ_g^-	Σ_u^+	Σ_u^-	Π_g	Π_u
Σ_g^+			$P_\parallel$			$P_\perp$
Σ_g^-				$P_\parallel$		$P_\perp$
Σ_u^+	$P_\parallel$				$P_\perp$	
Σ_u^-		$P_\parallel$			$P_\perp$	
Π_g			$P_\perp$	$P_\perp$		$P_\parallel$
Π_u	$P_\perp$	$P_\perp$			$P_\parallel$	

Tab. 2.3. Dipole transitions from initial state ϕ_i to final state ϕ_f allowed for parallel ($P_\parallel$) and perpendicular ($P_\perp$) alignment of laser polarization and molecular axis. Table adapted from [Dun62, Gop10].

The irrep of the dipole operator $\Gamma_{\hat{H}_D}$ depends on the orientation of laser polarization and molecular axis. The electric field $\mathcal{E}$ can be expressed as a superposition of a field parallel to the molecular axis $\mathcal{E}_{||}$ and a field perpendicular to the molecular axis $\mathcal{E}_\perp$,

$$\mathcal{E} = \mathcal{E}_{||} \cos(\theta) + \mathcal{E}_\perp \sin(\theta), \tag{2.28}$$

where the angle θ between the molecular axis and the polarization of the laser field was introduced. Thus it is useful to consider two special cases for the evaluation of this term: The so-called parallel transitions, where the molecular axis and the laser polarization are aligned and perpendicular transitions where the molecular axis is perpendicular to the laser polarization direction.

For the parallel transition, the irrep of the dipole operator is Σ_u^+ and only transitions labeled $P_\parallel$ in Tab. 2.3 are dipole allowed. For perpendicular transitions, the irrep of the dipole operator reads Π_u and only dipole transitions labeled $P_\perp$ in Tab. 2.3 are possible.

If the molecular axis is neither perpendicular nor parallel to the laser polarization, the transition amplitudes will depend on the angle θ, because A_{fi} depends on the electric field strength [see Eq. (2.22)].

2.3. Ionization and related phenomena

In the XUV–IR pump–probe experiments conducted in the framework of this thesis, a single photon from the XUV pump pulse ionizes a target molecule. This leads to a population of vibrational states according to the Franck-Condon principle which is introduced in the following in Sec. 2.3.1. Afterwards, in Sec. 2.3.2 strong-field ionization in the multi-photon and tunnel regime is discussed. The former is relevant for the pump–probe scheme used in the experiments on nuclear fragmentation dynamics of N_2. The latter is closely related to the process of high-harmonic generation (HHG), which is discussed in the end of this section in Sec. 2.3.3 with a focus on the semi-classical three-step model.

2.3.1. Franck-Condon principle

In single photon ionization of molecules, vibrational states in the ionic PEC are excited according to the Franck-Condon principle. This is described in the following. Ignoring the electron spin, the total transition amplitude $A_{fi} = \langle \Psi_f | \hat{H} | \Psi_i \rangle$ for an ionization from an initial state $|\Psi_i\rangle$ to a final state $|\Psi_f\rangle$ can be written as

$$A_{fi} = \langle \phi_f, \psi_f | \hat{H}_\mathrm{D} | \phi_i, \psi_i \rangle \tag{2.29}$$

$$= \int \psi^*_{\gamma_f, v_f}(R) \left[\int \phi^*_f(\boldsymbol{r}; R) \hat{H}_\mathrm{D}(\boldsymbol{r}) \phi_i(\boldsymbol{r}; R) \, \mathrm{d}\boldsymbol{r} \right] \psi_{\gamma_i, v_i}(R) \, \mathrm{d}R \tag{2.30}$$

$$= \int \psi^*_{\gamma_f, v_f}(R) M_{fi}(R) \psi_{\gamma_i, v_i}(R) \, \mathrm{d}R \tag{2.31}$$

where the dipole transition matrix element $M_{fi} = \int \phi^*_f(\boldsymbol{r}; R) \hat{H}_\mathrm{D}(\boldsymbol{r}) \phi_i(\boldsymbol{r}; R) \, \mathrm{d}\boldsymbol{r}$ explicitly depends on R. The separation of these two integrals will be possible, if M_{fi} varies only slowly with R and at least one of the vibrational wave functions is localized to a small range of R [HS15, p. 305]. These conditions are usually fulfilled (especially for ionization from the vibrational ground state) and thus Eq. (2.31) is approximated by

$$A_{fi} = M_{fi} \int \psi^*_{\gamma_f, v_f}(R) \psi_{\gamma_i, v_i}(R) \, \mathrm{d}R.$$

The integral over the vibrational wave functions is incorporated in the Franck-Condon factor

$$\mathrm{FC}(\gamma_f, v_f \leftarrow \gamma_i, v_i) = | \langle \psi_f | \psi_i \rangle |^2 = | \int \psi^*_{\gamma_f, v_f}(R) \psi_{\gamma_i, v_i}(R) \, \mathrm{d}R |^2. \tag{2.32}$$

This factor describes the overlap integral of two nuclear wave functions with quantum numbers v_i and v_f within the electronic states with quantum numbers γ_i and γ_f. This is equivalent to the relative population amplitude of the vibrational states in the final electronic state after ionization.

The Franck-Condon principle can be understood in a simple semi-classical picture: The photo ionization occurs very fast compared to the timescales of nuclear dynamics. As a result, electronic transitions are vertical as illustrated in Fig. 2.5. The transition amplitude is usually largest close to the classical turning points of the vibrational motion. In the semi-classical picture, this is explained by a conservation of nuclear kinetic energy during the transition. Quantum mechanically this is due to the large wave-function overlap at the classical turning points.

2.3.2. Strong-field ionization

The theoretical description of strong-field ionization by intense laser fields is challenging. Thus, a variety of interesting physical processes is observed in experiments on ionization by ultrashort and intense laser pulse [Zro05, Erg06, Kre09, EPC+08, PCS+11]. In the experiments on N_2 , discussed in Chap. 6, multi-photon ionization occurs in the

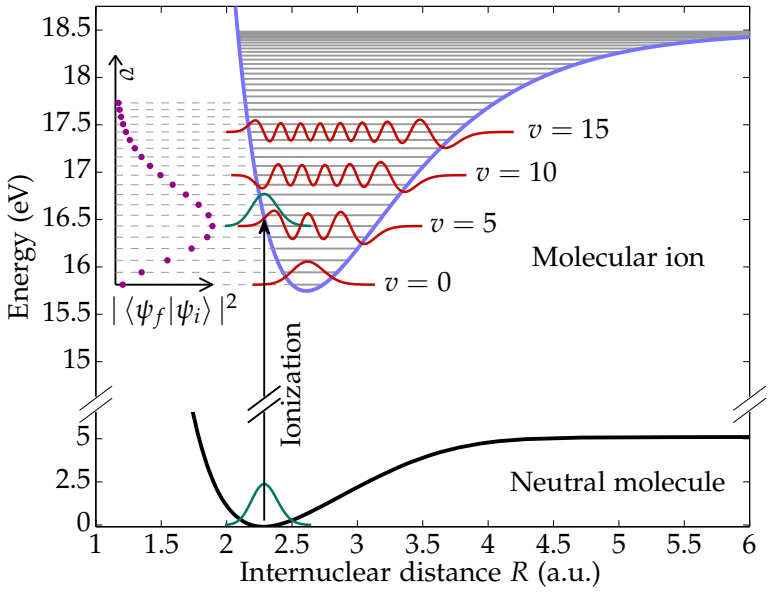

Fig. 2.5. Upon ionization, the vibrational wave function of the neutral molecule (green curve) is vertically promoted to the ionic PEC (blue). The eigenenergies in this PEC are drawn as (grey) horizontal lines. For some of these states, the vibrational wave functions are drawn (red curves). The initial wave function (green curve) must be expanded in the new basis, since it is no eigenfunction to the ionic PEC. The expansion coefficients given by the Franck-Condon factors $|\langle\psi_f|\psi_i\rangle|^2$ are plotted as a function of the excited states' quantum number v with purple dots.

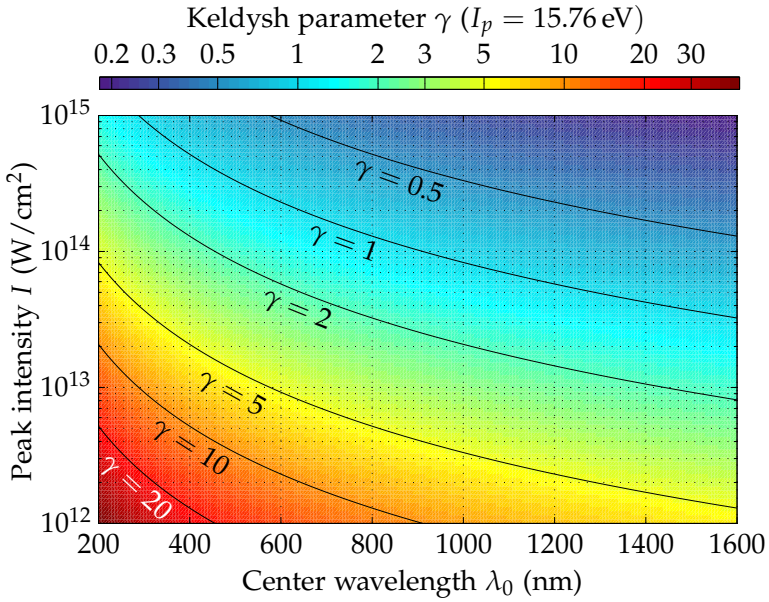

Fig. 2.6. Keldysh parameter (logarithmic color scale) as a function of center wavelength λ_0 and peak intensity I of laser pulse (logarithmic y-axis). The ionization potential $I_p = 15.76\,\mathrm{eV}$ of argon was used to calculate the Keldysh parameter. Figure adapted from [Fec14, p. 34].

probe step. The high-harmonic generation process important for the creation of the XUV pump pulses, is closely related to another regime of strong field ionization, the so-called tunnel ionization. Therefore basic principles of multi-photon ionization and tunnel ionization are introduced in the following.

Strong field ionization can be described by two different pictures, the tunnel ionization and the multi-photon ionization, depending on the laser parameters and the ionization potential. These regimes can be classified by the Keldysh parameter [Kel65] (in SI units)

$$\gamma = \omega_0 \hbar \sqrt{\frac{2I_p}{I}} = E_{\hbar\omega} \sqrt{\frac{2I_p}{I}} = \frac{hc}{\lambda_0} \sqrt{\frac{2I_p}{I}} \tag{2.33}$$

where I denotes the peak intensity of the laser pulse. ω_0, λ_0, and $E_{\hbar\omega}$ denote center frequency, center wavelength and photon energy, respectively. The ionization potential of the target atom is given by I_p.

The Keldysh parameter γ for ionization of argon is plotted in Fig. 2.6 as a function of the center wavelength λ_0 and peak intensity I. Additionaly, γ as a function of the laser peak intensity I and the ionization potential I_p is plotted in Fig. 2.7 for a fixed center wavelength $\lambda_0 = 760\,\mathrm{nm}$. For Keldysh parameters $\gamma \gg 1$, the ionization is well described by the multi-photon picture, whereas $\gamma \ll 1$ indicates the regime of tunnel ionization. As shown in the following, the theoretical treatment of those two

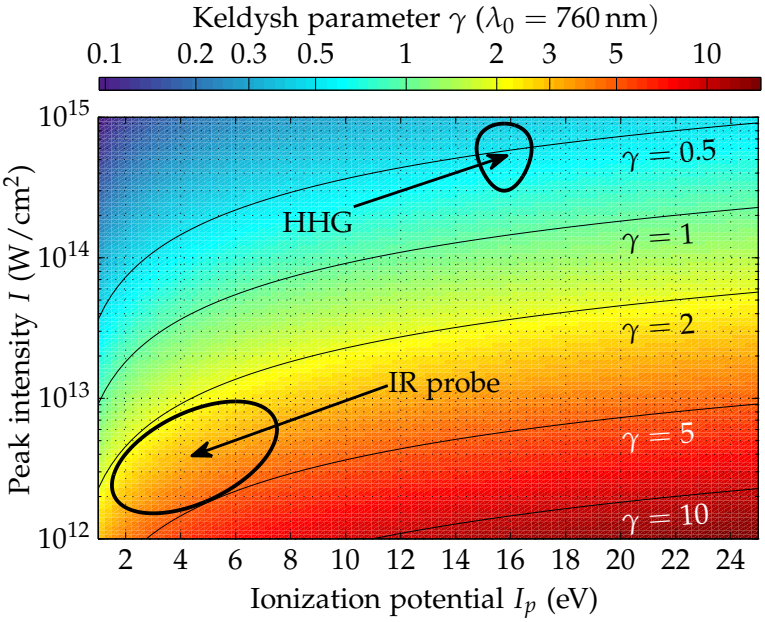

Fig. 2.7. Keldysh parameter (logarithmic color scale) as a function of ionization potential I_p and peak intensity I of laser pulse (logarithmic y-axis). The center wave length λ_0 is fixed to 760 nm, a typical value in our experiments. Keldysh parameters for the HHG process (see Sec. 2.3.3) and the ionization of highly excited molecules by the IR probe pulse in the Remi (see Chap. 6) are marked. The former process is clearly in the tunneling regime while the latter process is described by multi-photon ionization.

regimes is fundamentally different. The multi-photon regime is well described by the time-dependent perturbation theory, if the electric field of the laser is small compared to the atomic or molecular field strength [DK00, p. 85ff.]. In contrast, for strong field ionization, the electric field of the laser pulse is in the same order of magnitude as the electric field of the Coulomb potential. In the intermediate regime at $\gamma \approx 1$, effects from both regimes must be taken into account [ISS05, Rei08] and a theoretical description proves to be difficult [BK00, p. 565].

Multi-photon ionization

For a given ionization potential I_p, the ionization process is well described by the multi-photon picture if the field intensity is small (compared to the tunneling regime) or if the photon energy is high[8] [see Fig. 2.6 and Eq. (2.33)]. The process is illustrated in Fig. 2.8: By simultaneous absorption of multiple low energetic photons, the target molecule is ionized [BK00, p. 570]. The process can be understood as a sequential excitation to intermediate virtual states by single photons [GM31]. In principle all possible intermediate states (including continuum states) must be taken into account. For practical reasons, however, states which are very far of resonance can usually be neglected [GM31].

At very high laser intensities, more photons than necessary for the ionization may be absorbed. This process is called above-threshold ionization [AFM+79, SYDK93] and manifests in distinct peaks in the photoelectron energy spectrum (illustrated in Fig. 2.8).

Tunnel ionization

The tunnel ionization regime is reached for laser pulses with small photon energies (and thereby large center wavelengths λ_0) and large field intensities. For low frequencies of the laser field, the electron wave function reaches a quasi-static state before the laser field changes significantly [BK00, SPDC90]. In this case the electron can tunnel through the potential barrier formed by the superposition of the Coulomb field and laser field. This process is illustrated in Fig. 2.9. Right after tunneling the electron is assumed to be at rest in most theoretical models. The observed (non-zero) kinetic energy of the photoelectrons is due to an acceleration within the laser field *after* it has been removed from its parent atom. For certain combinations of ionization time and phase of the (linearly polarized) laser field, the electron trajectories may be closed. In this case the electron can recollide with its parent ion. Among other processes, this can lead to an emission of a highly-energetic photon by the process of high-harmonic generation (see Sec. 2.3.3).

The ionization rate in the tunneling regime is described by the ADK[9] theory [ADK86]. This model, however, does not take the laser frequency into account and depends only

[8] If the photon energy is larger than I_p, single photon ionization occurs.
[9] Ammosov, Delone, and Krainov.

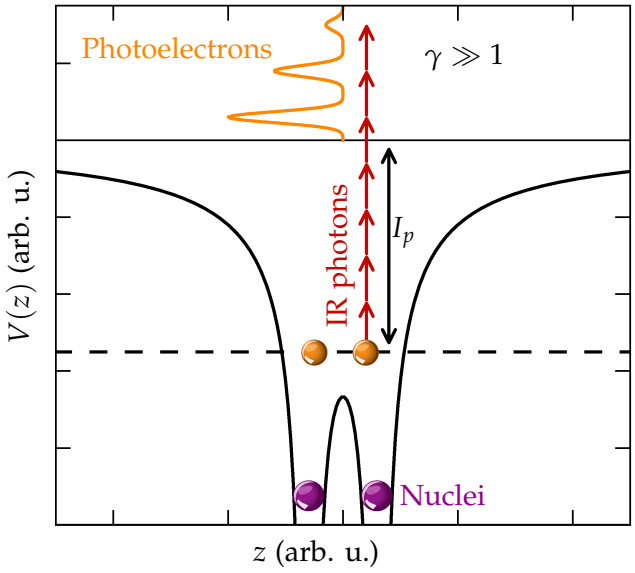

Fig. 2.8. Illustration of multi-photon ionization of a diatomic molecule for Keldysh paramters $\gamma \gg 1$. An electron (orange balls) is excited "vertically" by absorption of several IR photons (red arrows) and overcomes the ionization potential I_p. If additional photons are absorbed, so-called above-threshold ionization (ATI) peaks are formed in the photoelectron spectrum (orange curve). Figure adapted from [Fis15, p. 11].

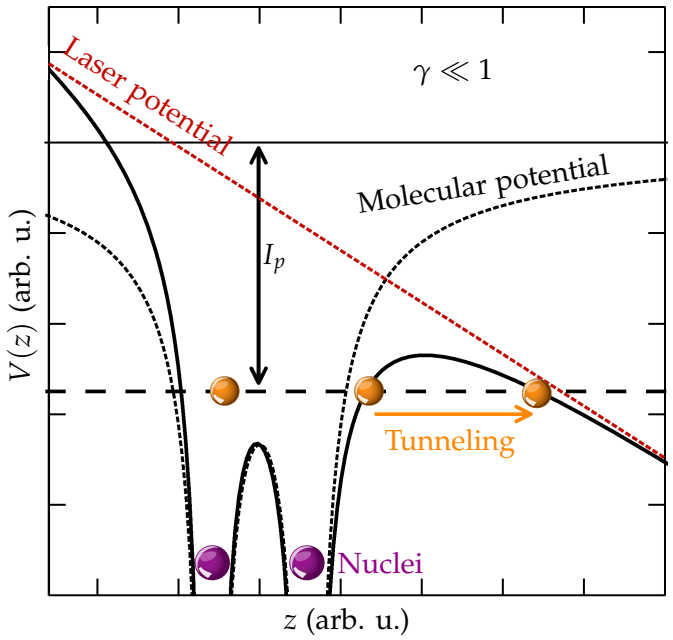

Fig. 2.9. Illustration of tunnel ionization of a diatomic molecule for Keldysh paramters $\gamma \ll 1$. The laser field is polarized parallel to the molecular axis (z-axis). The superposition of the laser potential (dashed red line) and the molecular potential (dashed black curve) leads to a potential barrier (solid black curve). An electron (orange balls) can tunnel "horizontally" through this barrier (indicated by the orange arrow). Figure adapted from [Fis15, p. 7].

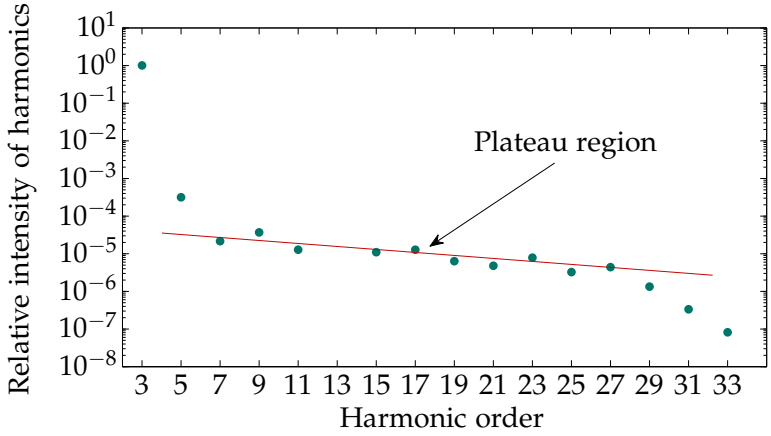

Fig. 2.10. Typical XUV spectrum created by HHG in argon. The green data is taken from Ref. [FLL+88]. The red line indicates the plateau region.

on the laser field intensity and (effective) quantum numbers of the target atom's state. The theory therefore breaks down for fast oscillating laser field where the electron wave function cannot follow the rapid change of the electric field adiabatically. For very strong laser fields, the electron may escape the atom over the barrier instead of by tunneling. In the ADK model saturation is reached at such fields [HS15, p. 437].

The ionization of diatomic molecules cannot be described by the original ADK theory, due to the rotational symmetry of the molecular orbitals. The MO-ADK theory [TZL02] describing tunnel ionization rates in diatomic molecules must therefore take the angle between molecular axis and laser polarization into account.

2.3.3. High-harmonic generation

If intense infrared or visible laser pulses are focused into a dense gas target, a beam of highly-energetic photons in the XUV or even soft X-ray regime [SSV+05, PCA+10, PCP+12, SSL+14] is emitted in the forward direction. This phenomenon is called high-harmonic generation (HHG) and was observed for the first time in the late 1980s [MGJ+87, FLL+88, LSK91]. A typical photon energy spectrum is shown in Fig. 2.10. It features distinct peaks at the odd harmonics of the fundamental laser pulse's center frequency ω_0. The intensity of these harmonics is almost constant over a large range of frequencies in the so-called plateau region. At a certain cutoff energy, the intensity drops rapidly.

These findings triggered numerical quantum simulations [KS89] which correctly predicted the $2\hbar\omega_0$ spacing of the harmonics and revealed a dependence of the cutoff energy on the laser pulse intensity. By further numerical calculations, the cut-off energy E_{cutoff} was predicted (in good agreement with experiment) as [KSK92]

$$E_{\text{cutoff}} = I_p + \beta U_p. \tag{2.34}$$

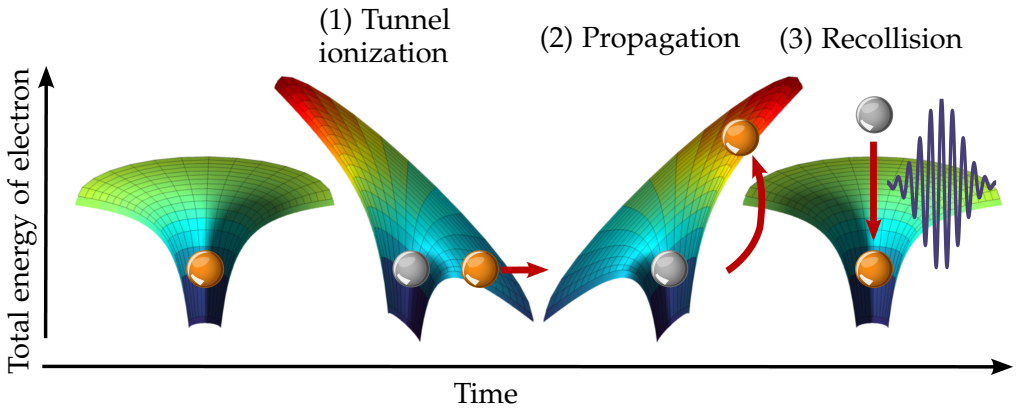

Fig. 2.11. Illustration of the three-step model. **(1)** The Coulomb potential of a target atom is deformed by the strong laser field and the atom is tunnel-ionized. **(2)** The quasi-free photoelectron (orange ball) is accelerated by the oscillating laser field on a closed trajectory. **(3)** The photoelectron recollides with its parent ion (and is possibly recaptured by emission of a high energetic photon).

The parameter $\beta \approx 3$ was determined empirically. Here I_p denotes the ionization potential of the target atom. The ponderomotive energy U_p is defined as

$$U_p = \frac{I}{4\omega_0}. \tag{2.35}$$

This is the cycle-averaged kinetic energy a free electron gains in a laser field [BK00, p. 565]. It depends on the pulse intensity I and the center frequency ω_0.

Three-step model The semi-classical three-step model [Cor93] gives an intuitive explanation for the origin of the high-harmonic radiation and can predict the parameter $\beta = 3.17$ correctly. It is therefore instructive to discuss this model (illustrated in Fig. 2.11) in more detail.

In the first step, the the target gas is ionized by the fundamental laser pulse. This process is described by tunnel ionization. As illustrated in Fig. 2.12 (a), the ionization probability is largest at the maximums of the fundamental laser field. The photoelectron is assumed to be at rest directly after the ionization.

In the second step, the electron is accelerated by the alternating electric field of the laser pulse. In the three-step model, the electron trajectories within the external field are calculated classically and the Coulomb potential is neglected. Only closed trajectories, in which the electrons returns to the vicinity of the parent ion, are relevant for the HHG process. As shown in Fig. 2.12 (b), these trajectories occur, if the electron tunnels after the external field has reached its maximum. If the electron tunnels at time t_0, the recollision time t_0' can be determined geometrically by drawing a tangent (orange solid line) to the electric field [Cha11, p. 168f]. Analytically, the return time

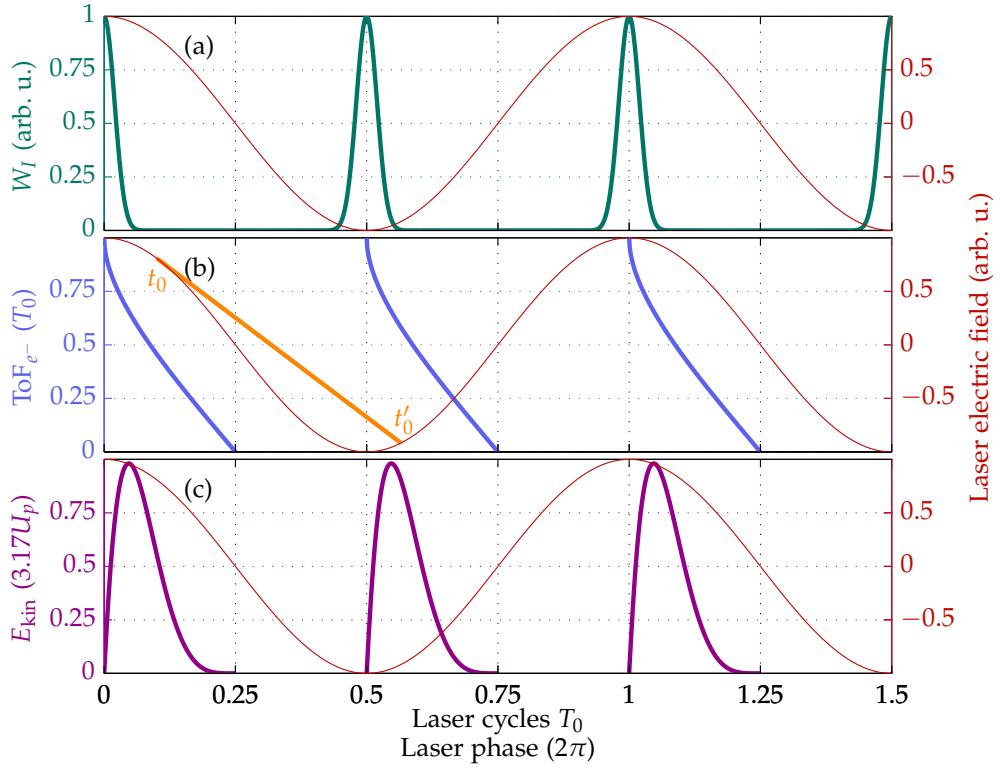

Fig. 2.12. Important quantities of the three step model as function of the laser phase. In all panels, the laser electric field is plotted as a red curve. **Panel (a):** The tunnel-ionization rate W_I [Cha11, p. 185] as a function of the laser phase is given by the green curve. **Panel (b):** Flight time ToF_{e^-} (blue curve) of the quasi-free electron in units of laser cycles as a function of the tunneling time t. The return time t' can be determined geometrically, as illustrated by the orange tangent. For certain t, closed trajectories do not exist. **Panel (c):** The kinetic energy E_{kin} (purple curve) of the electron upon recollision with the nuclei as a function of the tunneling time.

cannot be calculated. The electron's flight time $\mathrm{ToF}_{e^-} = t' - t$ is plotted as a function of the tunneling time t in Fig. 2.12 (b) (blue solid curve). The kinetic energy E_{kin} of the electron at the moment of recollision, plotted in Fig. 2.12 (c) (purple curve), only depends on the tunneling time t and the ponderomotive potential of the laser field. The electron will gain the maximum kinetic energy $E_{\mathrm{kin}}^{\mathrm{max}} = 3.17U_p$, if it tunnels at a phase of $0.05 \times 2\pi$rad [Cha11, p. 171].

In the third and final step of the three step model, the electron is recaptured by its parent ion into its original orbital. In this case the total energy of

$$\hbar\omega_{\mathrm{XUV}} = I_p + E_{\mathrm{kin}} \leq I_p + 3.17U_p \tag{2.36}$$

is converted into a single highly-energetic photon [Cor93].

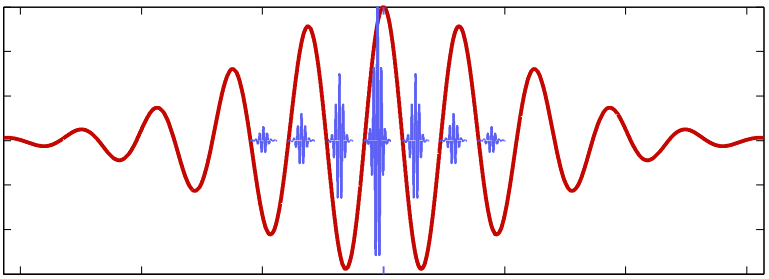

Fig. 2.13. Illustration of an attosecond pulse train. It is created by emission of attosecond pulses (blue pulses) at every half-cycle of the driving IR laser pulse (red pulse).

To improve the three-step model, a fully quantum mechanical description of the HHG was developed in the beginning of the 1990s [LBI+94]. In this model the strong-field approximation is applied and the electron wave function is propagated in the oscillating laser field neglecting the influence of the atomic Coulomb potential (compare [BLHE12, p. 1018f] and Refs. therein). Except for a minor correction in the first term, the cutoff energy predicted by the three-step model is confirmed by the quantum mechanical calculations.

Experimentally, high-harmonic generation is done in a gas target and the process described above takes place in many target atoms simultaneously. This has two important consequences not discussed so far: First, the XUV radiation emitted from individual target atoms will interfere. This interference has a strong impact on the emitted intensity. The optimization process towards constructive interference is called phasematching [Cha11, p. 281]. Furthermore, the process described by the three-step model takes place at every half cycle of the laser pulse. As a result, usually a train of attosecond pulses is emitted (as illustrated in Fig. 2.13). The temporal duration of each of these pulses is on the order of only 250 as [PTB+01] due to the very narrow time window within which tunnel ionization is possible and closed electron trajectories occur [Cha11, p. 186]. Due to its temporal structure, the attosecond pulse train features a spectrum of distinct frequencies separated by $2\omega_0$ in the Fourier domain.

With fundamental laser pulses featuring only a single pronounced field maximum or by applying one of various gating techniques (see Ref. [CZC14] and Refs. therein), it is possible to create an isolated attosecond pulse with a duration of less than 100 as [SBC+06, GSH+08, ZZC+12]. The experimental control over the XUV light fields increases steadily and nowadays for instance elliptically polarized high-harmonics can be generated [FKD+14, KGT+15]. The interested reader is referred to the Reviews [Ede04, AD04] for further information about HHG.

2.4. Wave-packet dynamics

Upon ionization of a molecule, a multitude of vibrational states are excited in the molecular ion according to the Franck-Condon principle (see Sec. 2.3.1). Thus, the resulting time-dependent nuclear wave function $\psi(R,t)$ in the ionic PEC is described by a superposition of eigenstates $\psi_v(R)$:

$$\psi(R,t) = \sum_v a_v \psi_v(R) e^{-i\varphi_v(t)} = \sum_v a_v \psi_v(R) e^{-iE_v t}. \tag{2.37}$$

Here, the eigenenergies are given by E_v and the expansion coefficients a_v are determined by the overlap integral $a_v = \int \psi_i^*(R)\psi_v(R)\,\mathrm{d}R$ with the nuclear wave function $\psi_i(R)$ of the initial (neutral) molecule. The temporal evolution of $\psi(R,t)$ depends on the vibrational energies E_v and therefore on the shape of the PEC. Due to this, time resolved experiments can be used to test theoretically predicted PECs as demonstrated in Chap. 5.

This section begins in Sec. 2.4.1 with the definition of the characteristic times T_{QB} and T_{rev} of the wave-packet dynamics. Afterwards, Sec. 2.4.2, a method to adjust a Morse potential to the experimentally observed times T_{QB} and T_{rev} is introduced.

2.4.1. Quantum-beat period T_{QB} and revival time T_{rev}

Assuming a dense number of vibrational states, the vibrational eigenenergies E_v can be approximated as a continuous function $E(v)$ of the quantum number v. If the vibrational wave packet is composed of a number of eigenstates around a central quantum number v_0, the eigenenergies $E(v)$ can be expanded as

$$E(v) \approx E(v_0) + E'(v_0)(v-v_0) + \frac{E''(v_0)}{2}(v-v_0)^2 + \frac{E'''(v_0)}{6}(v-v_0)^3 + \dots \tag{2.38}$$

where $E'(v_0) = (\mathrm{d}E_v/\mathrm{d}v)_{v=v_0}$ and so forth [Rob04, p. 7].

The phase evolution $\varphi_v(t) = E_v t$ in Eq. (2.37) is then given by

$$\varphi_v(t) = -it\left[E(v_0) + E'(v_0)(v-v_0) + \frac{E''(v_0)}{2}(v-v_0)^2 + \dots\right] \tag{2.39}$$

$$= -i\left[E_0 t + 2\pi(v-v_0)t/T_{\mathrm{QB}} + 2\pi(v-v_0)^2 t/T_{\mathrm{rev}} + \dots\right], \tag{2.40}$$

where the substitution

$$T_{\mathrm{QB}} \equiv 2\pi\frac{1}{|E'(v_0)|}; \quad T_{\mathrm{rev}} \equiv 2\pi\frac{2}{|E''(v_0)|} \tag{2.41}$$

has been made. The term $E_0 t$ in Eq. (2.40) is independent of v and cannot be accessed in our experiments. It is therefore ignored in the following discussion. The other terms, however, depend on v and describe the dynamics of the wave packet. As explained

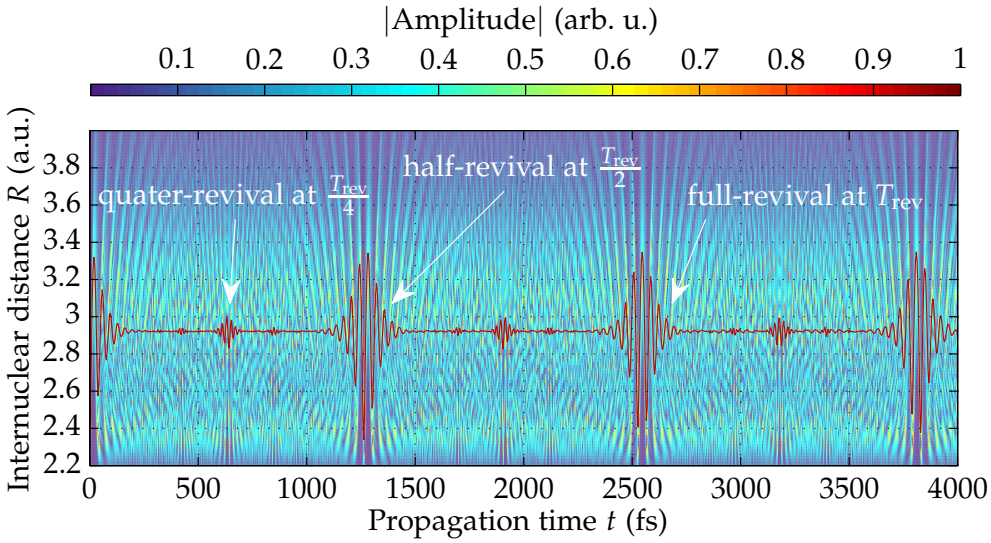

Fig. 2.14. Simulated wave-packet dynamics on a Morse potential. The amplitude of the wave function (color scale) is plotted as function of the internuclear distance R and the propagation time t. The expectation value $\langle R \rangle$ is plotted as a red curve.

in the following, the period T_{QB} and the so-called revival time T_{rev}, are important characteristic times for the wave-packet evolution.

The results of a simulated wave-packet oscillation on a Morse potential is shown in Fig. 2.14. The amplitude of the nuclear wave function (color scale) is given as a function of the internuclear distance R and the propagation time t. The expectation value $\langle R(t) \rangle$ of the internuclear distance is plotted as a red curve. The fast oscillation of $\langle R(t) \rangle$ occurs with a period of T_{QB}. The timescales of the revival time T_{rev} are usually much longer [Rob04, p. 9].

For $t \ll T_{\mathrm{rev}}$ the phase evolution of all vibrational state is described by

$$\varphi_v(t) = E_v t \approx 2\pi(v - v_0)t/T_{\mathrm{QB}}$$

according to Eq. (2.40). Since the quantum numbers v are integers, $\varphi_v(t = nT_{\mathrm{QB}}) = \varphi_v(t = 0)$ for all v and for all $n \in \mathbb{N}$. Thus the wave packet is localized at its original position after multiples of the time $t = T_{\mathrm{QB}}$.

If only two vibrational states are excited, they will beat with a period of T_{QB}. Thus, T_{QB} is referred to as the quantum-beat (QB) period throughout this work. The quantum-beat energy E_{QB} which is equivalent to the level spacing $\triangle E$ is then given by

$$E_{\mathrm{QB}} := \omega_{\mathrm{QB}} = 2\pi \frac{1}{T_{\mathrm{QB}}} = \triangle E \tag{2.42}$$

As a result, time resolved spectroscopy of nuclear wave packets allows to determine the eigenenergies of vibrational states.

The third term in Eq. (2.40) describes a dephasing and a delocalization of the wave packet which causes the oscillatory behavior in Fig. 2.14 to vanishes after a few QB periods. After the revival time T_{rev} all vibrational modes are in phase again and the wave packet *revives* into its original[10] shape at $t = 0$. The revival time is inversely proportional to $E''(v)$ and therefore to the change in the level spacing. Thus it only plays a role in anharmonic potentials and there is no dephasing of the wave packet in the Harmonic oscillator.

At so-called fractional revivals at times

$$t = \frac{p}{q} T_{\text{rev}}, \quad p, q \in \mathbb{N},$$

parts of the vibrational modes are in phase. A special case is the so-called half-revival at $p/q = 1/2$ which compared to a full revival only incorporates an additional phase factor [Rob04, p. 14]. The experimentally observed oscillation amplitude, however, is similar to that of a full revival (see Fig. 2.14). The revival structure observed in the experimental data is actually a half-revival (see Sec. 5.2.3). The experimentally observed characteristic times T_{QB} and T_{rev} can be used to adjust a Morse potential with a method described in the following.

2.4.2. Adjusting a Morse potential to measured times T_{QB} and T_{rev}

So far no restrictions have been made to the binding potential. In the following the special case of a Morse potential [Mor29]

$$V(R) = D_e \left(e^{-2a(R-R_0)} - 2e^{-a(R-R_0)} \right) \tag{2.43}$$

is discussed. Morse potentials with various depths D_e and widths a are plotted in Fig. 2.15. The potential minimum R_0 is set to $R_0 = 2.6$.

The eigenenergies of the Morse potential can be calculated analytically and are given by

$$E_{\text{Morse}}(v) = a\sqrt{\frac{2D_e}{\mu}} \cdot \left[\left(v + \frac{1}{2} \right) - a\sqrt{\frac{2}{\mu D_e}} \left(v + \frac{1}{2} \right)^2 \right], \tag{2.44}$$

where μ denotes the reduced mass. Using Eq. (2.41), the characteristic times for the Morse potential are computed to

$$\frac{2\pi}{T_{\text{QB}}} = \left| a\sqrt{\frac{2D_e}{\mu}} - \frac{a^2}{\mu} \left(v_0 + \frac{1}{2} \right) \right| \tag{2.45}$$

$$\frac{2\pi}{T_{\text{Rev}}} = \left| -\frac{a^2}{\mu} \right|. \tag{2.46}$$

[10] This is only true if higher order terms in Eq. (2.40) can be neglected. They are not discussed here since they are not observed in our experiment.

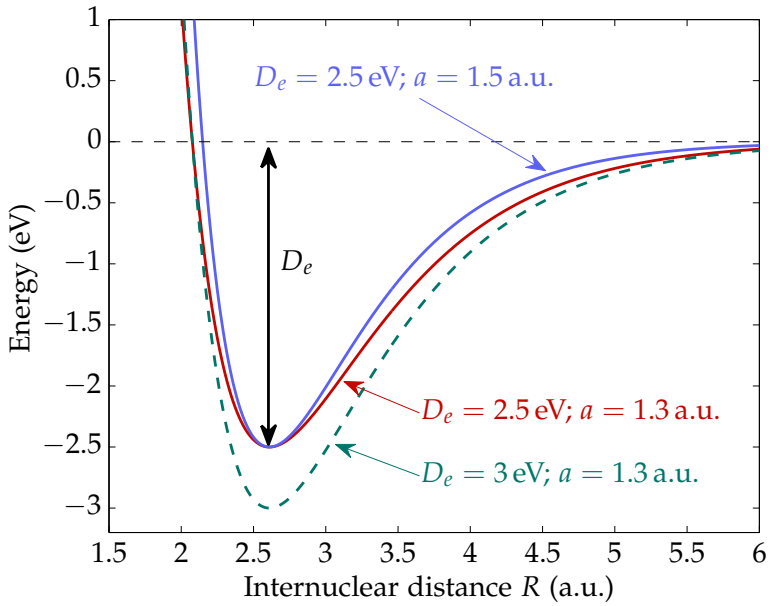

Fig. 2.15. Morse potentials $V(R) = D_e\left(e^{-2a(R-R_0)} - 2e^{-a(R-R_0)}\right)$ plotted as a function of the internuclear distance R. Different parameters D_e for the depth and a for the width are used according to the labels. The equilibrium distance $R_0 = 2.6$ is equal for all potentials drawn.

Using Eq. (2.46), the parameter a can be determined directly from measurement the of the revival time T_{rev}. The QB period T_{QB}, however, depends on the depth D_e as well as the central quantum number v_0 of the excited states. But without input from theory, it is not possible to measure v_0 in our experiment. In Sec. 5.2.4, this is overcome by comparing the adjusted Morse potential for varying v_0 to theoretically predicted PECs.

2.5. Simulation of molecular dynamics

By comparing the experimental data presented in Chaps. 5 and 6 with simulated results, deeper insight into the involved processes is gained. In addition, this allows to test PECs predicted by theory. The methods used to compute the nuclear dynamics in the N_2 and O_2 experiment are introduced in Sec. 2.5.1 and Sec. 2.5.2, respectively. In both cases, the occurring time-dependent Schrödinger equations are solved numerically using a split-step algorithm introduced in Sec. 2.5.3.

2.5.1. Propagation of a wave packet on PECs

In Chap. 6, experimental results on molecular dynamics in highly-excited electronic states of N_2^+ are presented. In the applied pump–probe scheme (which will be described in detail in Sec. 6.3.1), the nuclear wave function of the N_2 ground-state is promoted to the ionic PEC. The wave packet evolves on this PEC, until it is further promoted to the dicationic ground state by multi-photon ionization with the IR pulse. For small pump–probe delays, this creates stable N_2^{++} ions which are detected experimentally. This sequential double ionization is described by a simple quantum mechanical model introduced in the following.

In this model, all nuclear dynamics is described by the Schrödinger equation in the Born-Oppenheimer approximation (introduced in Sec. 2.1.4)

$$\hat{H}_n\psi(R,t) = \left[-\frac{1}{2\mu}\nabla_R^2 + V(R)\right]\Psi(R,t) = E_n\psi(R,t). \tag{2.47}$$

Here V denotes the PEC and μ denotes the reduces mass of N^+. The experiment is modeled in four steps. The first three steps are illustrated in Fig. 2.16.

1. **XUV ionization:** The ionization by the XUV pulse is described by the Franck-Condon principle. Thus after ionization at $t = 0$, the wave function in Eq. (2.47) is given by $\psi(R, t = 0) = \psi_0$, where ψ_0 denotes the vibrational ground-state wave function of N_2.

2. **Propagation on the N_2^+ PEC:** The propagation of the initial wave function $\psi(R, t = 0)$ up to the time $t = \tau$ is described by Eq. (2.47) with $V = V_{N_2^+}$. Equation (2.47) is solved numerically with a split-step algorithm that will be introduced in Sec. 2.5.3.

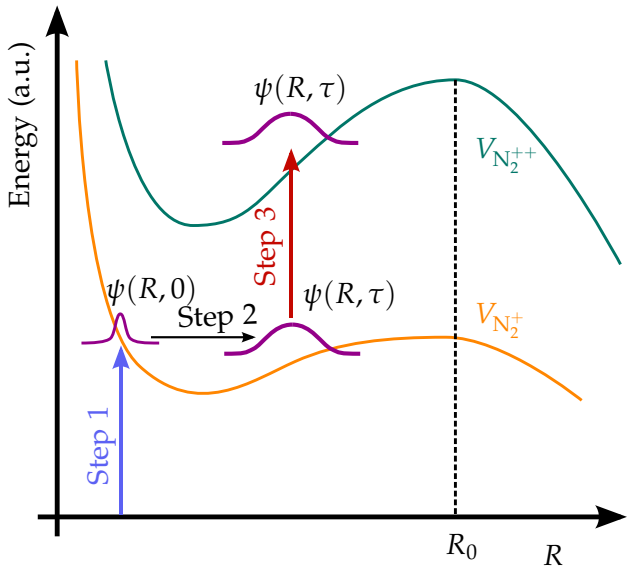

Fig. 2.16. Illustration of the model used to simulate the pump–probe dependent yield of N_2^{++} observed in Chap. 6.

3. **Multi-photon ionization:** At time τ, the wave packet is probed by multi-photon ionization with the IR pulse. In the simulation, this process is taken into account with a very simple model: The wave function $\psi(R, t = \tau)$ is promoted instantaneously to the dicationic PEC with unit probability.

4. **Propagation on cationic PEC:** After the probe step, the propagation of the wave packet $\psi(R, t = \tau)$ is again described by Eq. (2.47) but using the dicationic PEC $V = V_{N_2^{++}}$. The wave function is propagated from $t = \tau$ to $t = t_{\text{end}}$ with the split-step algorithm until the bound parts are clearly separated from the dissociating parts of the wave packet. The simulated yield of stable N_2^{++} is then given by the integral

$$\int_0^{R_0} |\psi(R, t = t_{\text{end}})|^2 \, \mathrm{d}R \tag{2.48}$$

where R_0 denotes the position of the potential barrier of the dicationic PEC (compare Fig. 2.16).

The four steps listed above are repeated for varying τ, in order to compute the N_2^{++} yield as function of the pump–probe delay. The simulated results are compared to the experimental data in Sec. 6.4.

2.5.2. Coupled-channel simulation

In the pump–probe experiments on O_2 presented in Chap. 5, a time-dependent nuclear wave packet is observed. Properties of such wave packets and their evolution on a

single binding PEC have been introduced in the previous section (Sec. 2.4). In our experiments the wave-packet dynamics can only be observed by transferring population to a repulsive PEC with the IR pulse and detection of the resulting molecular fragments. Thus, in order to simulate the experimental pump–probe scheme, the coupling between the two electronic states must be taken into account. By comparing simulated results with the experimental spectra, the shapes of predicted PECs will be tested. For these simulations, a software framework developed by A. Fischer has been used. An introduction to the basic principles of this so-called coupled-channel simulation is given in the following. The interested reader is referred to the PhD thesis of A. Fischer [Fis15, p. 88-100] for a more detailed description of the method.

The coupled-channel simulation is based on the Born-Oppenheimer approximation. As discussed in Sec. 2.1, this allows to express a molecular state $\Psi_\gamma(\boldsymbol{r}, R)$ as a product state of an electronic wave function $\phi_\gamma(\boldsymbol{r}; R)$ and a nuclear wave function $\psi_\gamma(R)$. A superposition of two molecular states is then written as

$$\Psi_{\text{tot}}(\boldsymbol{r}, R, t) = a_{\gamma_1}\Psi_{\gamma_1}(\boldsymbol{r}, R, t) + a_{\gamma_2}\Psi_{\gamma_2}(\boldsymbol{r}, R, t) \tag{2.49}$$

$$= a_{\gamma_1}\phi_{\gamma_1}(\boldsymbol{r}, t; R)\psi_{\gamma_1}(R, t) + a_{\gamma_2}\phi_{\gamma_2}(\boldsymbol{r}, t; R)\psi_{\gamma_2}(R, t) \tag{2.50}$$

where population of the states is described by the coefficients a_γ.

Without an external field, the electronic states are eigenstates of the Hamilton operator. As a result, the two terms above are decoupled and the time evolution of the nuclear wave functions $\psi_\gamma(R, t)$ is described by two separate Schödinger equations. These can be expressed as a matrix

$$i\frac{d}{dt}\begin{pmatrix}\psi_{\gamma_1}(R,t)\\ \psi_{\gamma_2}(R,t)\end{pmatrix} = \begin{pmatrix}-p^2/(2\mu) + V_{\gamma_1} & 0\\ 0 & -p^2/(2\mu) + V_{\gamma_2}\end{pmatrix}\begin{pmatrix}\psi_{\gamma_1}(R,t)\\ \psi_{\gamma_2}(R,t)\end{pmatrix} \tag{2.51}$$

in which V_γ denote the PECs. In the simulation, this system of (decoupled) differential equations is used to describe the field free propagation of the nuclear wave packet prior to and after the interaction with the probe pulse.

The probe process itself couples the two Schrödinger equations because the additional laser field can induce transitions between the electronic states. As a result, these electronic states are not longer eigenstates. In dipole approximation and for a linear laser polarization in z-direction, this is described by

$$i\frac{d}{dt}\begin{pmatrix}\psi_{\gamma_1}(R,t)\\ \psi_{\gamma_2}(R,t)\end{pmatrix} = \begin{pmatrix}-p^2/(2\mu) + V_{\gamma_1} & -\langle\phi_{\gamma_1}|\, z\,|\phi_{\gamma_2}\rangle\, \mathcal{E}(t)\\ -\langle\phi_{\gamma_2}|\, z\,|\phi_{\gamma_1}\rangle\, \mathcal{E}(t) & -p^2/(2\mu) + V_{\gamma_2}\end{pmatrix}\begin{pmatrix}\psi_{\gamma_1}(R,t)\\ \psi_{\gamma_2}(R,t)\end{pmatrix} \tag{2.52}$$

with the time-dependent laser field $\mathcal{E}(t) = \mathcal{E}\cos(-\omega t)$. For non-zero off-diagonal terms, the coupling matrix mixes the nuclear wave functions on the two different PECs and describes population transfer between the electronic states. The off-diagonal terms are given by the dipole matrix elements $M_{fi} = \langle\phi_f|\,\hat{H}_D\,|\phi_i\rangle$ introduced in Eq. (2.25). The magnitude $\langle\phi_{\gamma_1}|\, z\,|\phi_{\gamma_2}\rangle$ depends in the internuclear distance R. For the simulations

performed in the framework of this theses, this quantity is taken from Ref. [MAT12] (plotted in Fig. 5.15).

The coupling matrix in Eq. (2.52) can be split into a sum of matrices

$$\hat{H}(t) = \begin{pmatrix} \frac{-p^2}{2\mu} & 0 \\ 0 & \frac{-p^2}{2\mu} \end{pmatrix} + \begin{pmatrix} V_{\gamma_1} & 0 \\ 0 & V_{\gamma_2} \end{pmatrix} + \begin{pmatrix} 0 & -\langle \phi_{\gamma_1} | z | \phi_{\gamma_2} \rangle \mathcal{E}(t) \\ -\langle \phi_{\gamma_2} | z | \phi_{\gamma_1} \rangle \mathcal{E}(t) & 0 \end{pmatrix} \tag{2.53}$$

$$= T + V_0 + V_{\text{int}}(t) = T + V(t). \tag{2.54}$$

The matrix T contains the kinetic energy operators, V_0 contains the (time-independent) PECs and $V_{\text{int}}(t)$ describes the time-dependent coupling terms. The sum of latter two is given by $V(t)$.

In principle, the coupled-channel model is valid in the presence of a strong laser field as long as all PECs with a significant mutual coupling are taken into account in Eq. (2.52). If the density of states is high, the probability for finding more than two PECs that can be coupled resonantly increases. Especially if multi-photon transitions become relevant in very strong laser fields (such as the ones simulated in Sec. 5.4.2), a coupling matrix involving only two states might not describe the probe process correctly.

2.5.3. Split-step algorithm

The split-step algorithm described in the following is used to solve the time-dependent Schrödinger equations Eq. (2.47), and Eq. (2.52) encountered in the simulations of the N_2 and O_2 pump-probe experiments, respectively. This section gives only a brief introduction to the topic, for details see for example Refs. [Fis15, p. 88-100] and [Nie07, p. 7-25].

The time evolution from t_0 to t of a known state $|\psi, t_0\rangle$ is described by

$$|\psi, t\rangle = U(t, t_0) |\psi, t_0\rangle \tag{2.55}$$

where $U(t, t_0)$ is the so-called time-evolution operator. For an infinitesimal time step $\mathrm{d}t$, the operator is written as [Sak09, p. 83]

$$U(t + \mathrm{d}t, t) = 1 - i\hat{H}(t)\mathrm{d}t. \tag{2.56}$$

The time evolution operator for a small finite time $\triangle t$, is given by a product of

infinitesimal time steps

$$U(t_0+\triangle t,t_0) = \lim_{N\to\infty} U(t_0+\triangle t, t_0+\frac{N-1}{N}\triangle t)\cdots U(t_0+\frac{1}{N}\triangle t,t_0) \tag{2.57}$$

$$= \lim_{N\to\infty}\left(1-i\hat{H}\left(t_0+\frac{N-1}{N}\triangle t\right)\frac{\triangle t}{N}\right)\cdots\left(1-i\hat{H}(t_0)\frac{\triangle t}{N}\right) \tag{2.58}$$

$$\approx \lim_{N\to\infty} U\left(t_0+\frac{\triangle t}{N},t_0\right)^N = \lim_{N\to\infty}\left(1-i\hat{H}(t_0)\frac{\triangle t}{N}\right)^N \tag{2.59}$$

$$= e^{-i\hat{H}(t_0)\triangle t} \tag{2.60}$$

where the time-dependent Hamilton operator $\hat{H}(t)$ was approximated as $\hat{H}(t)\approx\hat{H}(t_0)$ for $t\in(t_0,t_0+\triangle t)$. By choosing a suitable step size $\triangle t$ and reevaluating $H(t)$ after each time step, the propagation over a macroscopic time $t_0\to t$ is approximated arbitrarily well by

$$|\psi,t\rangle = e^{-i\hat{H}(t-\triangle t)\triangle t}\cdot e^{-i\hat{H}(t-2\triangle t)\triangle t}\cdots e^{-i\hat{H}(t_0)\triangle t}|\psi,t_0\rangle\,. \tag{2.61}$$

This is the basis the numerical solution of the time-dependent Schrödinger equation with the split-step method, as described in the following for the special case of the coupled-channel simulation.

Using the time-dependent Hamilton operator $\hat{H}(t)$ from Eq. (2.54), the time evolution by a step $\triangle t$ is approximated by

$$U(t+\triangle,t)\approx e^{-i\hat{H}(t)\triangle t} = e^{-i[T(p)+V(x,t)]\triangle t}. \tag{2.62}$$

The kinetic energy operator $T(p)$ is diagonal in momentum space. In the field-free situation, the potential $V(x,t)$ is diagonal in coordinate space [see Eq. (2.51)]. In the general case, with an external laser field, the matrix $V(x,t)$ can be diagonalized using transformation matrices[11] $\ddot{\mathrm{U}}^\dagger$ and $\ddot{\mathrm{U}}$

$$V_D(x,t) = \ddot{\mathrm{U}}V(x,t)\ddot{\mathrm{U}}^\dagger. \tag{2.63}$$

The diagonal operators $V_D(x,t)$ and $T(p)$ are used in the split-step algorithm in which the time evolution operator is further approximated by

$$U(t+\triangle,t)\approx e^{-iT(p)\triangle t/2}\cdot e^{-iV_D(x,t)\triangle t}\cdot e^{-iT(p)\triangle t/2}. \tag{2.64}$$

In this, the operators $T(p)$ and $V_D(x,t)$ are evaluated in momentum space and real space, respectively. The flowchart of the propagation of a wave function $\psi(p,t_0)$ for a single time step $\triangle t$ by the split-step algorithm is given in Fig. 2.17.

[11] The letter $\ddot{\mathrm{U}}$ is not to be confused with the second derivative $\ddot{U}=\partial^2U/\partial t^2$.

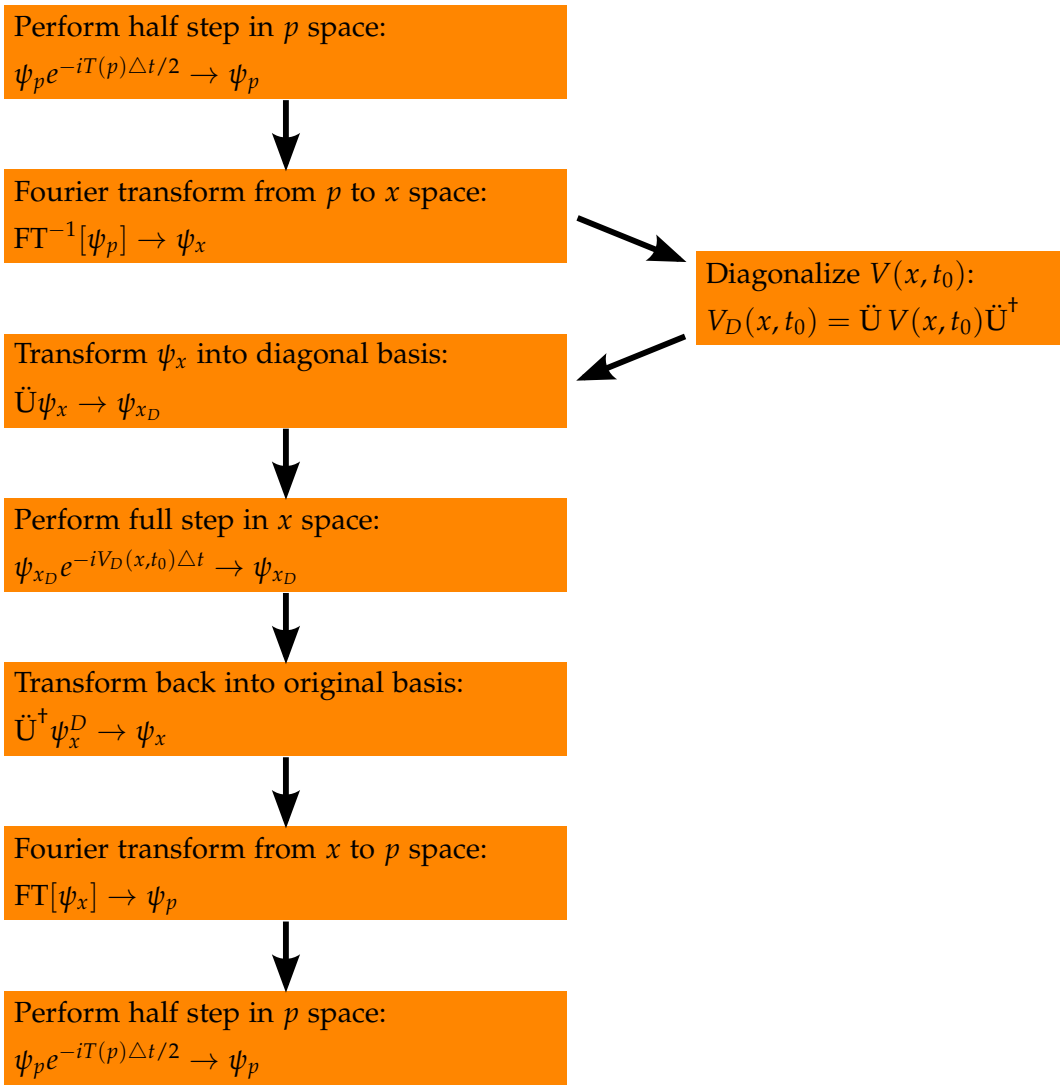

Fig. 2.17. Flow chart of a single time step $\triangle t$ in the coupled-channel simulation. The wave packet is propagated in momentum space as well as in real space.

3. Ultrashort laser pulses and optical setup

Contents

3.1. Theoretical description 43
3.2. Generation of XUV pump and IR probe pulses 48

Only few inventions influenced experimental techniques in atomic or molecular physics as much as that of the laser in 1960 [Mai60]. Since then, the rapid development of lasers led to a great number of applications. Today lasers exist in all sizes, reaching from diode lasers on chips [SIKS79] to gigantic machines filling entire experimental halls. Some fields in laser physics strive for the highest possible optical peak intensities, reaching up to hundreds of terawatts in pulsed systems [YCK+08]. Other research groups construct lasers with extremely low lasing thresholds which can be operated at a few hundred nano watts input power [MA13]. Narrow bandwidth continuous wave laser reach linewidths below a Hertz [KHG+12] whereas spectra of pulsed lasers can span more than an octave. The latter ones are used for example in the creation of frequency combs [ZGH+04, FKZ+04] or for the generation of ultrashort laser pulses.

For the time-resolved pump–probe experiments performed in the framework of this thesis, a titanium-doped sapphire (Ti:sapphire) femtosecond laser was used. In our system, pulse durations of about 12 fs are reached. We will see in Sec. 3.1 that the minimal duration of a laser pulse is limited by its spectral width which in our experiment is in the order of 100 nm. This chapter intends to give a brief overview over the theoretical description and the experimental generation of such ultrashort laser pulses. For further information, the interested reader is referred to the Review [SCBK94].

We begin in Sec. 3.1 with an introduction to theoretical concepts important for the generation of femtosecond pulses and for their propagation through optical media. Afterwards, in Sec. 3.2, the laser system as well as the Mach-Zehnder interferometer used to create the pump and the probe pulses are presented.

3.1. Theoretical description

This section gives a brief introduction to the theoretical description of ultrashort laser pulses and their interaction with optical media. At the pulse intensities used in our experiments, only the electric part of the electro-magnetic field is relevant for the

description of transitions in atoms or molecules. Thus the magnetic field is neglected in the following. The oscillating electric field of a monochromatic light wave at a fixed point in space is given by

$$E(t) = \widetilde{A}\cos(\omega t + \phi) = \mathrm{Re}\left\{\widetilde{A}e^{i(\omega t+\phi)}\right\} \tag{3.1}$$

with the field amplitude $\widetilde{A}$, the angular frequency ω and a phase ϕ. To describe a laser pulse we superimpose an infinite number of monochromatic waves with frequencies ω, (spectral) amplitudes $\widetilde{A}(\omega)$, and phases $\phi(\omega)$

$$E(t) = \mathrm{Re}\left\{\int_{-\infty}^{\infty}\widetilde{A}(\omega)e^{i[\phi(\omega)+\omega t]}\mathrm{d}\omega\right\} = \mathrm{Re}\left\{\int_{-\infty}^{\infty}\widetilde{E}(\omega)e^{i\omega t}\mathrm{d}\omega\right\}. \tag{3.2}$$

Here the complex amplitude $\widetilde{E}(\omega) = \widetilde{A}(\omega)e^{i\phi(\omega)}$ was introduced. The quantity $\widetilde{A}(\omega)$ is called the spectral amplitude and the quantity $\phi(\omega)$ is called the spectral phase. The complex amplitude $\widetilde{E}(\omega)$ and the electric field in the time domain $E(t)$ are related by a Fourier transform

$$E(t) = \mathrm{Re}\left[\mathrm{FT}\left\{\widetilde{E}(\omega)\right\}\right]. \tag{3.3}$$

Due to this Fourier relation, the duration of a laser pulse is limited by its the spectral width. Therefore broadband gain media are used in femtosecond oscillators which emit light on a large number of longitudinal cavity modes. In order to create the shortest possible laser pulses, all these modes must oscillate in phase. This is explained in the following (Sec. 3.1.1) where a brief introduction to modelocking is given. This technique is the foundation for the creation of ultrashort laser pulses with Ti:sapphire laser oscillators. Due to their large spectral bandwidth, the temporal shape of such pulses is modified when they propagate through dispersive media (including air) as described in Sec. 3.1.2. Experimentally this usually increases the pulse length, thus an understanding of dispersion is important. This section ends (Sec. 3.1.3) with a brief discussion of self-phase modulation which can be used to spectrally broaden the laser pulses generated by a commercial laser system in order to further reduce the pulse duration.

3.1.1. Modelocking

The frequency separation of adjacent longitudinal modes[1] in a confocal resonator is given by [Dem14, p. 283]

$$\triangle\omega = \frac{2\pi c}{2d} \tag{3.4}$$

where c denotes the speed of light and d is the cavity length.

[1] Here we assume that only the fundamental axial TEM_{00} mode (see [Dem14, p. 270ff, 283] for further information) is excited.

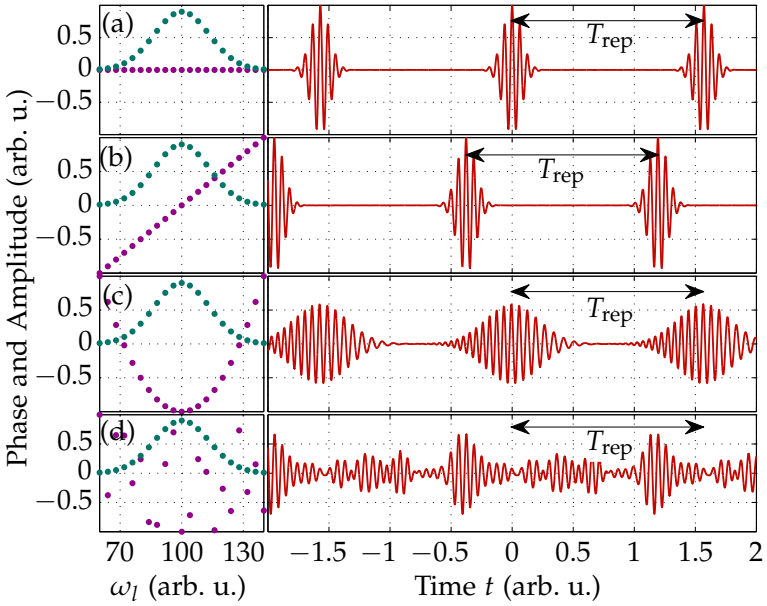

Fig. 3.1. Calculated laser pulses (red curves) obtained by superposition of cavity modes with frequencies ω_l. The spectral amplitude $\widetilde{A}(\omega_l)$ of the cavity modes (green dots) is equal for all panels. The phase ϕ_l (purple dots) of the cavity modes is varied from panel (a) to (d). **Panel (a):** $\phi_l(\omega_l) = 0$ results in a Fourier limited pulse. **Panel (b):** $\phi_l(\omega_l) \propto \omega_l$ results in a Fourier limited pulse delayed in time. **Panel (c):** $\phi_l(\omega_l) \propto \omega_l^2$ results in a chirped pulse. **Panel (d):** $\phi_l(\omega_l)$ is random which results in a stochastic field.

The electric field created by the superposition of $2n+1$ longitudinal modes with spectral amplitudes $\widetilde{A}(\omega_l)$, equidistant frequency $\omega_l = \omega_0 + l\triangle\omega$ and phase $\phi_l(\omega_l)$ reads [in analogy to Eq. (3.2)]

$$E(t) = \mathrm{Re}\left\{\sum_{l=-n}^{n} \widetilde{A}(\omega_l) e^{i[\phi_l(\omega_l)]+\omega_l t}\right\} = \mathrm{Re}\left\{\sum_{l=-n}^{n} \widetilde{E}(\omega_l) e^{i\omega_0 t}\right\} \tag{3.5}$$

where the substitution

$$\widetilde{E}(\omega_l) = \widetilde{A}(\omega_l) e^{i(l\triangle\omega_l t+\phi_l)} \tag{3.6}$$

has been made.

So far no restriction has been made to the phases ϕ_l of the cavity modes. The phases ϕ_l, however, influence the temporal structure of the oscillator pulses drastically, as illustrated in Fig. 3.1 and discussed in the following. As long as $\triangle\phi = \phi_{l+1} - \phi_l$ is constant for all l or zero for all l [Fig. 3.1 (a) and (b)], the modelocking generates Fourier-limited pulses [Sve10, p. 343]. Their instantaneous electric field $E(t)$

$$E(t) = \mathrm{Re}\left\{A(t) e^{i\omega_0 t}\right\} \tag{3.7}$$

is described by a slowly varying time-dependent pulse envelope $A(t)$ and a single center frequency ω_0. Due to the Fourier-relation between temporal domain and frequency space, the pulse duration $\triangle\tau$ of a Fourier-limited pulse is limited by the spectral width $\triangle\widetilde{A}(\omega_l)$ [Sve10, p. 341]:

$$\triangle\tau \propto \frac{1}{\triangle\widetilde{A}(\omega_l)}. \tag{3.8}$$

If the phases ϕ_l of the cavity modes are neither constant nor linear in ω_l, the resulting pulse durations are always longer than the Fourier limit. This is illustrated in Fig. 3.1 (c), where the quadratic dependence $\phi_l \propto \omega_l^2$ causes the pulses to be chirped. In this case, the instantaneous laser frequency $\omega(t)$ is time dependent. For random phases ϕ_l, no pulses are created at all. Note, however, that the periodicity $T_{\text{rep}} \propto 1/(\triangle\omega)$ of the electric field still exists and is independent of ϕ_l. In pulsed operation, the time T_{rep} corresponds to the round-trip time of the pulse inside the cavity.

There are various techniques to achieve the modelocking condition (see e.g. [Sve10, Sec. 8.6]). Inside a Ti:sapphire osciallator, the modelocking is usually achieved by the so-called Kerr-lens effect which will be briefly explained in Sec. 3.1.3. For further information on Kerr-lens modelocking and femtosecond oscillator design principles, the interested reader is referred to the Reviews [Kel10] and [SCBK94], respectively.

3.1.2. Dispersion

As discussed before, femtosecond laser pulses feature a large spectral bandwidth. The index of refraction $n_0(\omega)$ of most optical media is frequency dependent. Thus the spectral phase [DR06, p. 22]

$$\phi(L,\omega) = \phi(0,\omega) + \frac{\omega n_0(\omega)}{c} L \tag{3.9}$$

accumulated by a pulse propagating through a medium with length L will depend in the frequency as well. This effect is called dispersion.

If the index of refraction is constant (which over a large spectral range is only given in vacuum), the accumulated phase $\phi(L, \omega)$ will be linear in ω. In this case the pulse envelope $A(t)$ of a Fourier-limited pulse is not altered. In all other situations, the pulse envelope of a the Fourier-limited pulse will have spread in time according to Eq. (3.2).

As dispersion will always increase the temporal duration of a Fourier-limited pulse, it is kept as low as possible in the experiment. Sometimes, however, the use of dispersive media e.g. in glass windows cannot be circumvented and even the propagation through air will modify the spectral phase according to Eq. (3.9). Thus methods must be employed to (pre-)compensate dispersion in order to get the shortest possible laser pulses within the reaction microscope. Such methods will be introduced in Sec. 3.2.3.

3.1.3. Nonlinear optics and self-phase modulation

In the previous discussion of the dispersion, a frequency dependent index of refraction $n_0(\omega)$ was assumed. If, however, the laser intensities are large, an intensity dependent contribution to the refractive index [DR06, p. 193]

$$n = n_0 + n_2\, I(t) \tag{3.10}$$

must be taken into account. In this, n_0 is the "normal" index of refraction encountered in linear optics. The second term $n_2\, I(t)$ becomes relevant for the high laser intensities $I(t)$ in the focus of a femtosecond pulse.

Let us consider a Fourier-limited femtosecond pulse with center frequency ω_0 that propagates tightly focused through a medium of length L. Neglecting the "normal" dispersion, we only consider the instantaneous phase[2] $\phi_{\mathrm{NL}}(t)$ accumulated due to the second term in Eq. (3.10). $\phi_{\mathrm{NL}}(t)$ is given by [Boy08, p. 375]

$$\phi_{\mathrm{NL}}(t) = -n_2\, I(t) \frac{\omega_0}{c} L, \tag{3.11}$$

where ω_0 denotes the center frequency. We further introduce the instantaneous frequency [Boy08, p. 376]

$$\omega(t) = \omega_0 + \delta\omega(t) = \omega_0 + \frac{\mathrm{d}}{\mathrm{d}t}\phi_{\mathrm{NL}}(t) \tag{3.12}$$

which describes a time-dependent frequency of the laser pulse. The frequency shift $\delta\omega(t)$ is then given by

$$\delta\omega(t) = \frac{\mathrm{d}}{\mathrm{d}t}\phi_{\mathrm{NL}}(t) = -n_2 \frac{\omega_0}{c} L \frac{\mathrm{d}}{\mathrm{d}t} I(t). \tag{3.13}$$

$\delta\omega(t)$ depends on the time-derivative of the intensity envelope $I(t)$. Therefore inside the medium, frequency components $\omega(t) < \omega_0$ are created at the rising edge of the pulse. At the falling edge, frequency components $\omega(t) > \omega_0$ are generated. This process is called self-phase modulation and does not alter the intensity envelope as illustrated in Fig. 3.2. In that figure, panel (a) shows a Fourier limited pulse. After self-phase modulation, the instantaneous frequency $\omega(t)$ is time dependent as shown in panel (b). The intensity envelope (green Gauss function) remains unchanged. The change in frequency $\delta\omega(t)$ is proportional to the derivative of the Gaussian intensity envelope $-\frac{\mathrm{d}}{\mathrm{d}t} I(t)$ (blue curve). The pulse shown in panel (b) is not Fourier limited and thus can be further compressed in time.

The above considerations are simplified. In fact, besides the neglected "normal" dispersion, nonlinear effects like self-steepening (see [Boy08, p. 568] for further information) and finite nonlinear response times (see [Boy08, p. 211] for further information)

[2] In contrast to the spectral phase $\phi(\omega)$ the instantaneous phase describes the laser pulse in the time domain.

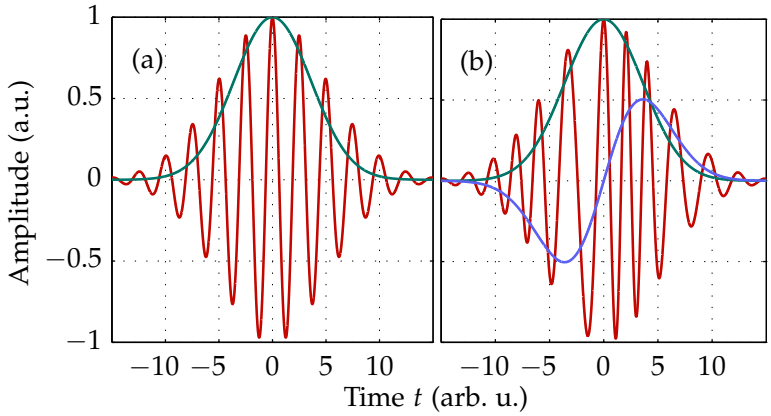

Fig. 3.2. Illustration of the self-phase modulation. Electric fields are plotted as a red curve. The intensity envelopes are given by the green Gauss function. **Note:** Normal dispersion and nonlinear effects other than self-phase modulation are not considered. **Panel (a):** A Fourier limited pulse. **Panel (b):** Pulse after self-phase modulation. The modification of the center frequency is proportional to $-\frac{\mathrm{d}}{\mathrm{d}t}I(t)$ (plotted as a blue curve).

must be considered. In reality, the pulse will be chirped and will not resemble the ideal pulse shown in Fig. 3.2 (b).

In our setup, the self-phase modulation takes place inside an neon-filled hollow-core fiber and the recompression of the chirped pulse is done with a chirped-mirror compressor. Both setups will be introduced in Sec. 3.2.3.

3.2. Generation of XUV pump and IR probe pulses

In this section, the experimental setup used for the generation of ultrashort XUV and IR laser pulses is introduced. It is illustrated in Fig. 3.3 and can be divided in four segments. These define the outline of this section, beginning in Sec. 3.2.1 with a description of the Ti:Sapphire laser oscillator (green box in Fig. 3.3). Afterwards (in Sec. 3.2.2) the working principle of the *chirped-pulse amplification system* (blue box in Fig. 3.3) is explained. The section continues (Sec. 3.2.3) with introducing the *hollow-core fiber* setup and the *chirped-mirror compressor* (orange box in Fig. 3.3). We continue (Sec. 3.2.4) with a description of the *HHG vacuum chamber* (purple box in Fig. 3.3). In this chamber, the fundamental laser pulses are split into two parts. One part is used to generate an XUV pulse by the HHG process and the other part is delayed in time. Both pulses are focused into the reaction microscope where they are used to perform pump and probe experiments. Finally, in Sec. 3.2.5, experimental data of IR assisted XUV ionization of argon is presented. The pulse duration and the spatial overlap between the laser pulses can be estimated from the occurring sidebands.

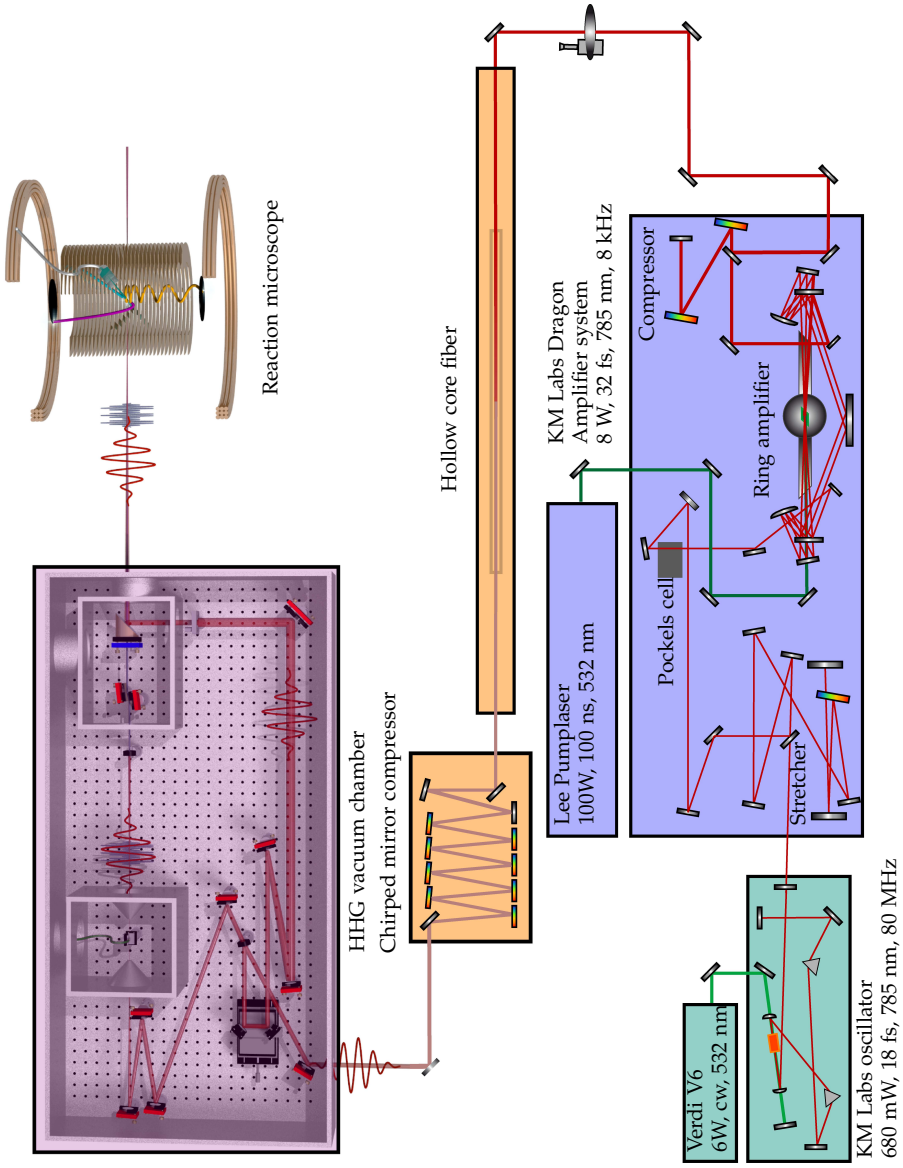

Fig. 3.3. Schematics of the experimental setup including the Ti:sapphire oscillator system (green), the chirped-pulse amplifier (blue), the hollow-core fiber and chirped-mirror compressor (orange), the HHG vacuum chamber (purple), and the reaction microscope. Figure adapted from [Spe13, p. 42].

Oscillator pulses	
Pulse duration	18 fs
Center wavelength	785 nm
Repetition rate	80 MHz
Average power	680 mW
Pulse energy	9 nJ

Tab. 3.1. Oscillator pulse properties.

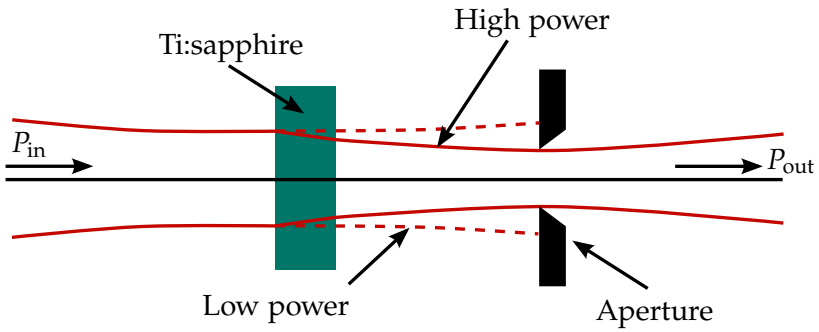

Fig. 3.4. Illustration of the Kerr lens effect. This can be used to suppress low power modes in a Ti:sapphire oscillator. Figure adapted from [Sve10, p. 354].

3.2.1. Ti:sapphire oscillator

The commercially available Ti:sapphire laser oscillator manufactured by *Kapteyn-Murnane Laboratories* used in our experimental setup is illustrated in Fig. 3.3 (blue box). The properties of the oscillator pulses created with this system are listed in Tab. 3.1. For general design principles of femtosecond oscillators, the interested reader is referred to Ref. [SCBK94]. The band structure of titanium-doped sapphire (Ti:Al_2O_3) which leads to a broadband gain in mode-locked operation of the oscillator is explained in Ref. [Sve10, p. 394].

In our setup, the Ti:sapphire crystal inside the oscillator is pumped by a continuous-wave, frequency-doubled Nd:YVO solid-state laser (*Verdi V6* manufactured by *Coherent*) with an optical power of about 6 W. In mode-locked operation, the oscillator pulse duration is about 18 fs at a repetition rate of 80 MHz. The center wavelength is 785 nm and the average output power is 680 mW. Due to the high repetition rate, this corresponds to a very low pulse energy of only 9 nJ. The modelocking is achieved by the *Kerr-lens* effect which is briefly explained in the following.

Kerr-lens modelocking The refractive index of Ti:sapphire is intensity dependent which leads to nonlinear optical effects [see Sec. 3.1.3 and Eq. (3.11)]. In combination with the Gaussian intensity distribution of the laser beam, this results in an increased

index of refraction in the center of the beam. Thus, the Ti:sapphire crystal itself focuses the intense parts of the laser beam. This phenomenon is called optical Kerr lens [Sve10, p. 354]. This effect can be used to design the cavity such that low power parts of the beam are attenuated, for example with an iris aperture (as illustrated in Fig. 3.4) or by using a tightly focused pump laser. With such a setup, high intensity spikes in a noisy pulse [as the ones illustrated in Fig. 3.1 (d)] are amplified whereas other modes are attenuated. Within a very short time the mode competition leads to the formation of a single pulse oscillating inside the cavity and a mode-locked operation. For further information about Kerr-lens modelocking, the interested reader is referred to the Refs. [Dem15, Kel10].

3.2.2. Ti:sapphire multi-pass amplifier

The pulse energy of femtosecond oscillators is very low due to their high repetition rate (which is given by the cavity length). While it is possible to create XUV radiation by HHG with such pulses [JMTY05, GUH+05], the obtained XUV intensities to low to be used in our experiment. Thus amplification of the oscillator pulses is necessary. This is done with the *Chirped-pulse amplifier* illustrated in Fig. 3.3 (blue box). This type of amplifier was realized for the first time in the 1980s (see for instance Refs. [SM85,PMM87]) and its functional principle is explained in the following. The interested reader is referred to the Review [BDMK98] for additional information about the design principles of chirped-pulse amplifiers.

Chiped pulse amplification Amplification of the oscillator pulses is achieved by focusing them (multiple times) into a Ti:sapphire crystal that is pumped simultaneously by a high-power pump laser. Without precautions the direct amplification process of the femtosecond pulses leads to very high peak intensities inside the gain medium exceeding its damage threshold. Thus a technique to reduce the peak intensities during the amplification process is required.

In the chirped-pulse amplification scheme, this is achieved by stretching the femtosecond pulses in the time domain to a duration of typically 100 ps [BDMK98, p. 1208]. In our setup, the *stretcher* (illustrated in Fig. 3.3 blue box) consists of a set of gratings which introduce a wavelength dependent optical path length and thereby introduce a chirp. The chirped pulses are then focused into the optically pumped gain medium for 13 times[3] in a *ring amplifier* (illustrated in Fig. 3.3 blue box). After amplification, the pulses are sent through a grating compressor (illustrated in Fig. 3.3 blue box) which recompresses the pulses in the time domain. Besides the chirp introduced inside the stretcher, the dispersion introduced by the gain medium, is compensated.

[3] Depending on the design parameters, 4 to 50 passes through the gain medium are typically needed [BDMK98, p. 1208].

Amplifier pulses	
Pulse duration	32 fs
Center wavelength	785 nm
Repetition rate	8 kHz
Average power	8 W
Pulse energy	1 mJ

Tab. 3.2. Properties of the amplified laser pulses.

Compared to the original oscillator pulses, the spectral width of the amplified pulses is usually reduced due to gain narrowing. Thus Fourier limited amplifier pulses feature increased durations of typically above 20 fs [BDMK98, p. 1215 & 1218]. Nowadays, the average power of high repetition rate chirped-pulse amplification systems is limited to a few tens of watts by the power of available pump-lasers. Thus, in order to generate amplifier pulses in the millijoule energy range, it is necessary to reduce the MHz repetition rate of the oscillator to a few kilohertz prior to amplification. In our setup, this is achieved with a Pockels cell (illustrated in Fig. 3.3 blue box) followed by a polarizer.

The *Dragon* multi-pass chirped-pulse amplifier used in our laboratory was manufactured by *Kapteyn-Murnane Laboratories*. The Ti:sapphire gain medium is pumped by a frequency doubled, Q-switched Nd:YAG laser manufactured by *Lee Laser, Inc.* Parameters of the amplified pulses generated by the lasersystem are listed in Tab. 3.2.

3.2.3. Hollow-core fiber and chirped-mirror compressor

The temporal resolution of a pump-probe experiment is (in many cases) determined by the pulse duration of pump and probe pulse. To be able to observe the molecular dynamics investigated in this work (see Chap. 6) which features typical timescales of 10 to 20 fs, it is necessary to further reduce the duration of 30 fs amplifier pulses. Due to the Fourier relation between spectral width and pulse length [see Eq. (3.8)], this requires a spectral broadening. In our setup, this is achieved by focusing the pulses into a 1 m long neon-filled hollow-core fiber with an inner diameter of 250 µm. Inside the fiber, the beam is collimated over a long distance and due to the high intensities additional frequencies are generated by the nonlinear optical process of self-phase modulation (compare Sec. 3.1.3).

The hollow-core fiber used in our experiment (illustrated in Fig. 3.3 orange box) was set up and characterized by A. Sperl. The interested reader is referred to his PhD thesis [Spe13] and the references therein for further information. A typical spectrum after spectral broadening inside the fiber is shown in Fig. 3.5 (a). Assuming a flat spectral phase, the electric field of the corresponding Fourier-limited pulse can be calculated using Eq. (3.3). The result is shown in Fig. 3.5 (b), where the electric field

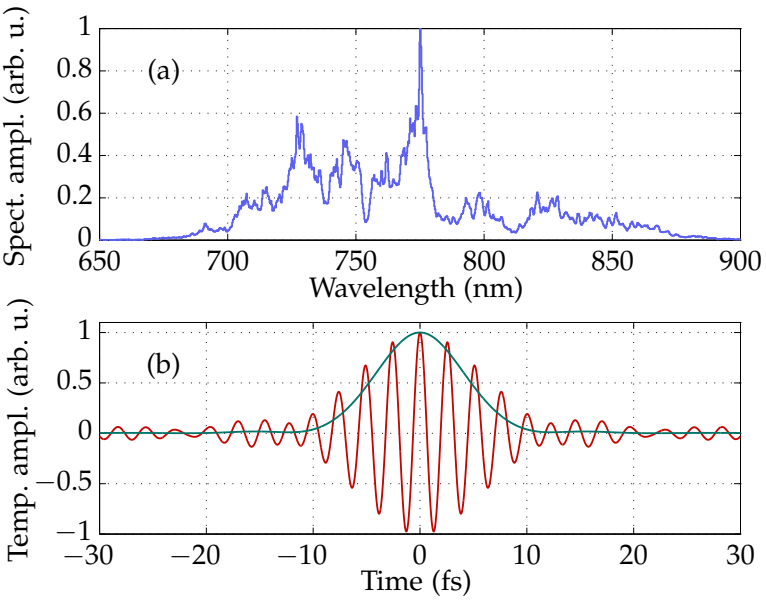

Fig. 3.5. Panel (a): Spectrum of the femtosecond laser pulses measured behind the hollow-core fiber. **Panel (b):** Electric field (red curve) and corresponding intensity envelope (green curve) obtained by Fourier transform of the experimental spectrum plotted in panel (a) assuming a flat spectral phase. The reconstructed Fourier-limited pulse features a temporal duration of 9.6 fs (FWHM of intensity) and a central wave-length of $\lambda_0 = 760\,\text{nm}$.

is given by the red curve and the intensity envelope is given by the green curve. The calculated Fourier-limited pulse duration is 9.6 fs (FWHM of intensity) and the center wavelength is $\lambda_0 = 760\,\text{nm}$.

After propagation through the hollow-core fiber, the pulses are no longer Fourier limited due to the self-phase modulation and additional normal dispersion. In order to obtain a (close to) Fourier-limited pulse, this dispersion is compensated[4] with a chirped-mirror compressor. Chirped mirrors are multi-layer mirrors coated in such a way that the penetration depth into the substrate is wavelength dependent [SSKF94]. If the design of the mirrors is matched to the experimental conditions, even high orders of dispersion can be efficiently compensated at low losses [PTS+08].

Usually chirped mirrors are employed in pairs of two complementary coated mirrors. The chirped mirrors[5] used in our setup, however, all feature the same multi-layer coating. Instead of using different coatings, the mirrors must be hit in pairwise different incident angles. This design principle simplifies the coating process and reduced the variance in performance between different charges [PAT+09].

[4] In addition, dispersion created by later propagation through air and glass windows must be precompensated.

[5] Manufactured by *UltraFast Innovations GmbH*.

3.2.4. High-harmonic generation and pump–probe interferometer

After spectral broadening inside the hollow-core and recompression by the chirped mirrors, the pulses are send into the high-harmonic generation vacuum chamber (illustrated in Fig. 3.6). The Mach-Zehnder interferometer located inside this chamber creates mutually delayed XUV-pump and IR-probe pulses with which experiments are performed inside the reaction microscope. The two interferometer arms are described in the following.

In one interferometer arm, the XUV pump pulses are created by the process of high-harmonic generation (HHG). For this, the fundamental pulses are focused by a spherical mirror with 50 cm focal length into an aluminum tube filled with argon gas [Fig. 3.6 panel (a)]. A train of XUV attosecond pulses is created by HHG in the noble gas (for further information about and characterization of the XUV source, see H. Rietz [Rie07, Rie12]). The created XUV radiation co-propagates with the remainder of the fundamental IR light. The latter is blocked by an aluminum filter [Fig. 3.6 panel (b)] which is opaque for photon energies below 17 eV. Afterwards, the XUV beam is focused into the reaction microscope by a pair of gracing incident mirrors [Fig. 3.6 panel (e)]. The energy spectrum the XUV pulses generated in our beamline is shown in Fig. 3.7.

Within the second interferometer arm, the IR probe pulse is delayed by a movable retro-reflector [Fig. 3.6 panel (d)] with respect to the XUV pulse. With this setup, pump–probe delays of up to 10 ps can be realized. For the observation of molecular dynamics on timescales of tens of femtoseconds, this setup is superior to (grazing incidence) split-mirror setups which can cause significant beam walk-offs for delay ranges larger than 50 fs [Ott12, p. 54]. The intensity of the IR probe pulse can be tuned by a motorized iris [Fig. 3.6 panel (f)].

Finally, the beams from both interferometer arms are spatially overlapped behind a holey parabolic mirror [Fig. 3.6 panel (c)] which focuses the IR beam into the reaction microscope.

In the framework of this thesis, the interferometer was redesigned in order to reduce interferometric drifts (see Ref. [Rie12, p. 61] for old setup). This was achieved by decreasing the interferometer arm length from about 4 m to 2 m and reducing the total number of reflections inside the interferometer arms from 23 to 13. With the new setup, the interferometric drift is estimated to be less than 2.5 fs over the period of 24 hours (see Fig. 3.8). When the femtosecond laser is switched on, the interferometer drifts rapidly within the first two hours due to a heating of optical elements. Therefore the laser should be aligned into the chamber as early as possible such that the drifts have slowed down when the data acquisition is started.

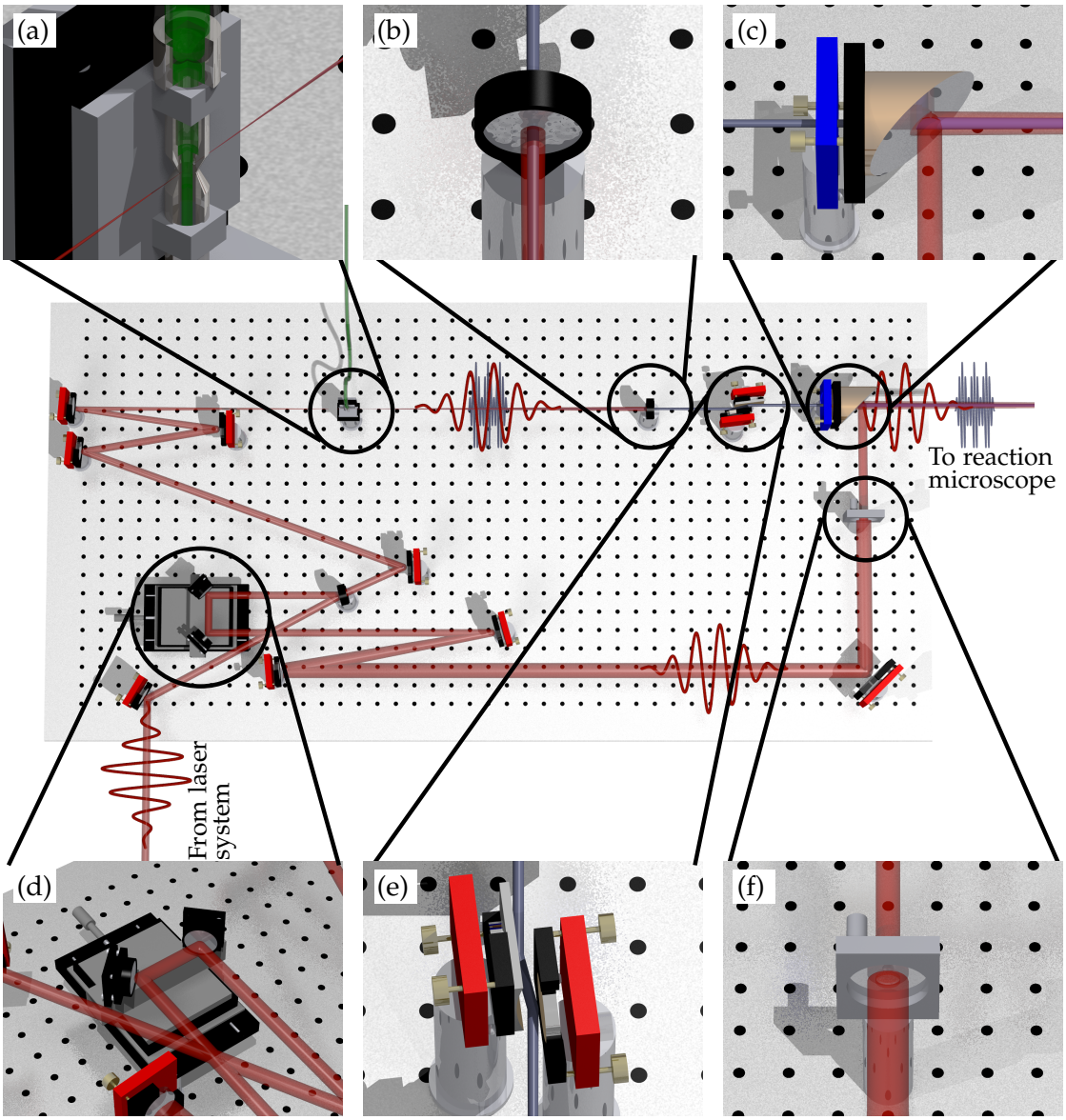

Fig. 3.6. Illustration of the Mach-Zehnder interferometer used to create the XUV-pump and IR-probe laser pulses. The whole breadboard is located inside a vacuum chamber. Components described in the text are pictured in panels (a) to (f): **Panel (a):** High-harmonic generation target. **Panel (b):** Aluminum filter. **Panel (c):** Holey parabolic mirror. **Panel (d):** Delay stage. **Panel (e):** XUV focusing mirrors. **Panel (f):** Motorized iris.

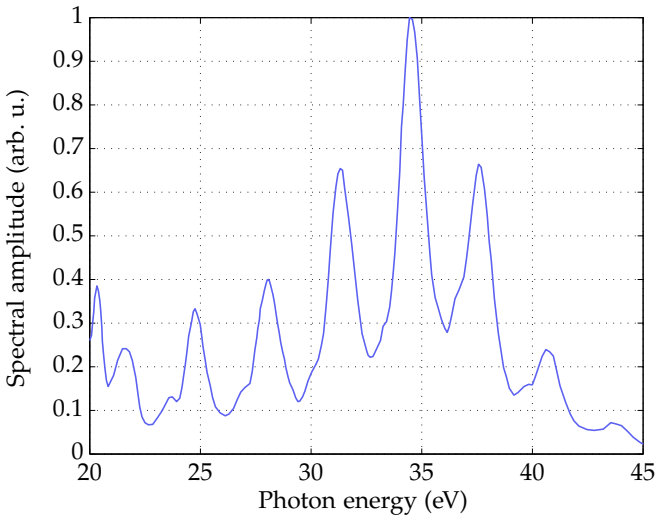

Fig. 3.7. Typical spectrum of the XUV pulses generated in our experiment. Data from Ref. [Sch15, p. 95].

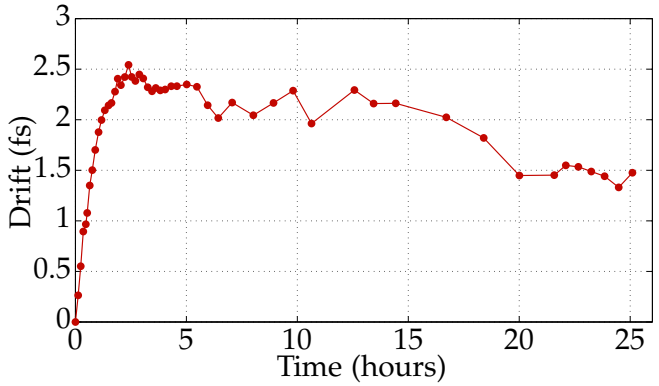

Fig. 3.8. Drift of the pump-probe interferometer over the period of 25 hours measured within the reaction microscope. At time zero, the femtosecond laser is switched on. The rapid drift at the beginning is due to a heating of optical elements by the laser beam.

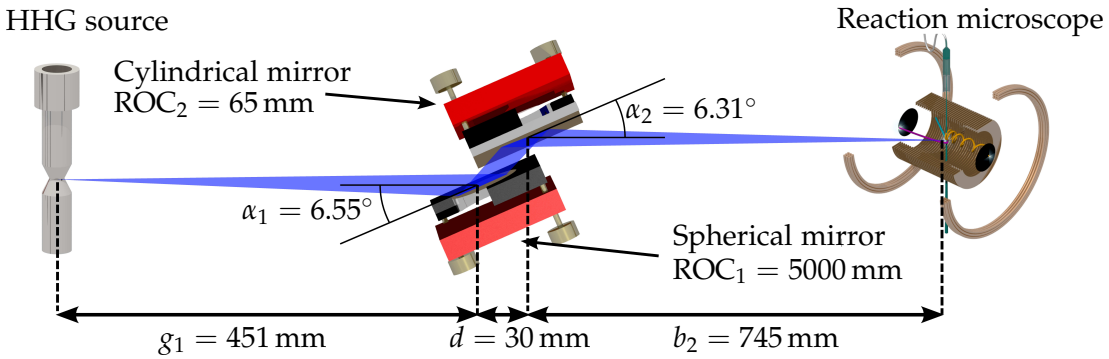

Fig. 3.9. Focusing of the XUV beam by a combination of a spherical and cylindrical mirror. If both mirrors are hit under the correct angle of incidence, an astigmatism free focus is obtained inside the reaction microscope.

Focusing of XUV pulses

The success of all pump–probe experiments depends on the spatial overlap of the XUV focus with the IR focus. The existing XUV focusing system (see [Rie12, p. 64]), however, had turned out to create an XUV focal spot much larger than the IR focal size. This is undesired, since it will prevent target molecules pumped by the XUV pulse from being probed by the IR pulse. In the framework of this thesis, the focusing system was redesigned in order to optimize the focusing of the XUV beam. The new setup with measured distances is illustrated in Fig. 3.9. The incidence angles α_1 and α_2 on the mirrors are calculated such that an astigmatism free focus is obtained in the center of the reaction microscope. Both mirrors used in the new setup are coated with a 30 nm B_4C (boron carbide) layer which features an improved reflectivity compared the to Au (gold) coating which was used before [see Fig. 3.10 (b)].

The two-mirror focusing system illustrated in Fig. 3.9 includes a spherical and a cylindrical mirror. Such a setup is required because broadband XUV radiation in the energy range of 20 to 40 eV is not efficiently reflected under normal incidence, as illustrated in Fig. 3.10 (a). Thus all XUV mirrors must be hit under grazing incidence and the beam cannot be focused by a single spherical mirror as explained in the following.

If a spherical mirror with focal length f is hit under an angle[6] $\alpha \neq 90°$, the rays in the tangential (sometimes also called meridional) plane are focused closer to the mirror than rays within the sagittal plane. The effective focal lengths for tangential and sagittal

[6]Here and in the following the angle of incidence is defined with respect to the mirror surface and not with respect to the surface normal. See Fig. 3.9 for illustration.

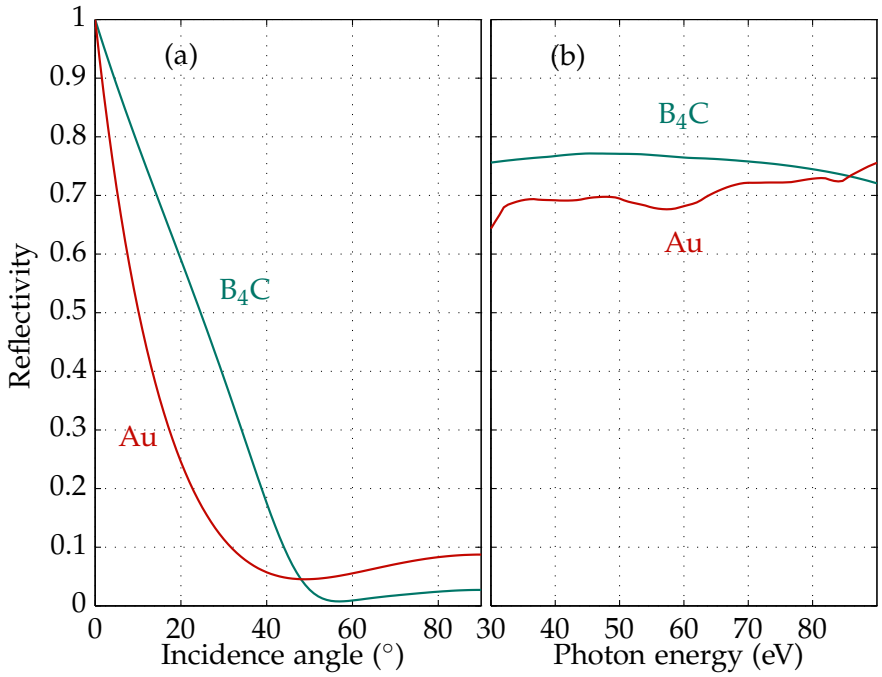

Fig. 3.10. Calculated reflectivity of mirrors coated with a 30 nm layer of Au (gold) and B_4C (boron carbide) for p-polarized light. **Panel (a):** As function of angle of incidence for a fixed photon energy of 30 eV. **Panel (b):** As function of photon energy for a fixed angle of incidence $\alpha = 6.5°$. Data from Ref. [fXRO].

rays are given by

$$f_{\text{eff}}^{\text{tan}} = f\cos(\alpha) \leq f = \frac{\text{ROC}}{2} \tag{3.14}$$

$$f_{\text{eff}}^{\text{sag}} = f\frac{1}{\cos(\alpha)} \geq f = \frac{\text{ROC}}{2}, \tag{3.15}$$

where ROC denotes the radius of curvature. Therefore, in order to create an astigmatism free focal spot within the reaction microscope, either a single non-spherical mirror (such as a toroidal or a elliptical mirror) or multiple mirrors must be utilized. In our setup, a combination of a spherical mirror and a cylindrical mirror is employed. The alignment of the incidence angles is crucial for focusing the saggital rays and tangential rays at the same spot.

Figure 3.11 shows a photograph of the XUV focal spot on a phosphor screen inside the reaction microscope obtained with the new focusing system. The focal diameter is estimated to 60 µm (FWHM) which is still about a factor of two larger than the calculated focal size of the IR probe pulse. Experiments in argon discussed in the next section, however, show that the spatial overlap between pump and probe pulse was improved significantly by the redesign of the focusing system.

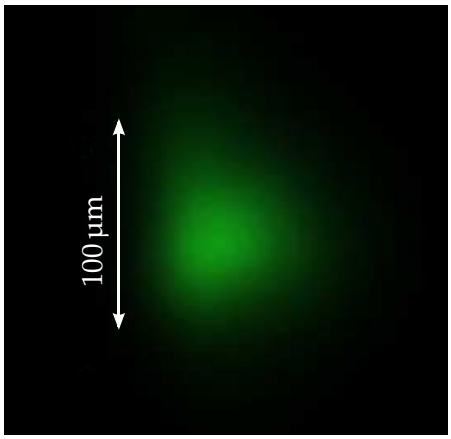

Fig. 3.11. Photograph of the XUV beam focused onto a phosphor screen inside the reaction microscope.

3.2.5. Pulse overlap and determination of the pulse duration

Spectra of so-called photoelectron sidebands obtained by ionization of argon inside the reaction microscope are presented in this section. A very brief introduction to the topic is given in the following. The focus of this section, however, lies on the estimation of the pulse duration with the help of these sidebands. In addition, the spatial overlap between the pulses (and thereby the focusing of the XUV pulse) can be tested in these experiments. For additional information, the interested reader is referred to Ref. [Rie12, p. 33].

The attosecond pulse train created by the process of HHG features a spectrum of distinct energies separated by $2\hbar\omega_{\mathrm{IR}} \approx 3.2\,\mathrm{eV}$. In the ionization of argon, this photon spectrum is imprinted onto the kinetic energies of the photoelectrons. Therefore the electron spectrum will as well feature peaks separated by 3.2 eV. This changes if an additional IR pulse is temporally and spatially overlapped with the XUV pulse. In this situation, an IR photon with energy $\hbar\omega_{\mathrm{IR}} \approx 1.6\,\mathrm{eV}$ may be absorbed or emitted during the ionization. Thus sidebands in the electron spectrum appear in between the main peaks.

The photoelectron yield as a function of the pump–probe delay and the kinetic energy E_e is plotted in Fig. 3.12. In this figure, the pulses are temporally overlapped at zero pump–probe delay. Outside the temporal overlap, the harmonic spectrum is clearly imprinted onto E_e for both datasets. Within the temporal overlap, the harmonic structure is washed out [best visible in panel (a)] due to the formation of sidebands. The increased intensity of the sidebands in panel (a) compared to panel (b) demonstrates the improved spatial overlap between the XUV and IR pulse after the optimization of the XUV focusing mirrors.

The temporal envelope of the sidebands is a cross correlation between the temporal

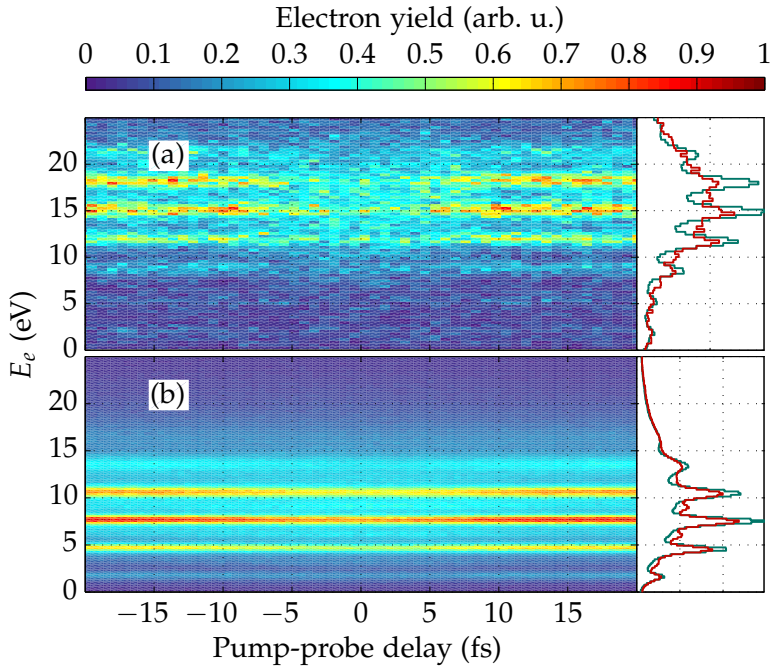

Fig. 3.12. Sidebands measured in argon after [**panel (a):** April 2014] and before [**panel (b):** April 2013] the redesign of the XUV focusing system. Plotted is the photoelectron yield as a function of the pump–probe delay and the electron's kinetic energy. The intensity of the sidebands created in the temporal pulse overlap is a measure for the quality of the spatial pulse overlap. Projections of the kinetic energy spectrum within the temporal overlap (red curve) and outside the overlap (green curve) are shown.

profiles of the XUV and IR pulse [GSCS96]. Assuming Gaussian temporal profiles, the width τ_{cross} of the sidebands is related to the XUV pulse duration τ_{XUV} and the IR pulse duration τ_{IR} by [LMMJ+04]

$$\tau_{\text{cross}}^2 = \tau_{\text{XUV}}^2 + \tau_{\text{IR}}^2. \tag{3.16}$$

The sidebands in Fig. 3.12 (a) – obtained immediately before beginning the N_2 pump–probe experiment presented in Chap. 6 – feature a width $\tau_{\text{cross}} = 14\,\text{fs}$ (FWHM). Assuming an XUV pulse duration of $\tau_{\text{XUV}} \approx 0.65\tau_{\text{IR}}$ [Rie12, p. 89], the pulse durations (intensity FWHM) can be estimated to

$$\tau_{\text{XUV}} \approx 8\,\text{fs} \text{ and } \tau_{\text{IR}} \approx 12\,\text{fs}, \tag{3.17}$$

respectively.

4. Reaction microscope

Contents

4.1. Working principle and technical specifications 61
4.2. Momentum reconstruction 68
4.3. Experimental techniques 75

The experiments performed in the framework of this thesis are dedicated to the study of molecular (fragmentation) dynamics using the pump–probe technique. In our setup, the 3-dimensional momenta of charged molecular fragments are measured as a function of the delay time with a reaction microscope (REMI) [MUU+94]. This apparatus allows the detection of electrons and ionic fragments over the full 4π solid angle over a large range of kinetic energies. With this, molecular dynamics can be studied on a single-molecule level.

The working principle and technical specifications of the REMI used in this work are explained in the following section (Sec. 4.1). Afterwards, in Sec. 4.2, the reconstruction of the initial momenta from measured flight times and hit positions is explained. The chapter ends (Sec. 4.3) with a technical discussion of the pulse alignment and the use of particle coincidences in the data evaluation.

4.1. Working principle and technical specifications

Reaction microscopes are multi-purpose detectors used in atomic and molecular physics. While they are utilized in a wide range of experiments, the underlying principle is always the same: projectiles (e.g. electrons, ions or photons) ionize (and possibly dissociate) target atoms or molecules. The initial momenta of all charged fragments is reconstructed from their flight times and hit positions on particle detectors.

The REMI used for all experiments presented throughout this work is illustrated in Fig. 4.1. It was constructed in the framework of R. Gopal's PhD thesis and is described in detail in Ref. [Gop10, p. 53-61]. For the purpose of this work, the coordinate system shown in Fig. 4.1 is used. The z-direction parallel to the electric and magnetic field (and the laser polarization) is referred to as the *longitudinal* (momentum) direction. *Transversal* (momentum) direction denotes directions perpendicular to the spectrometer axis.

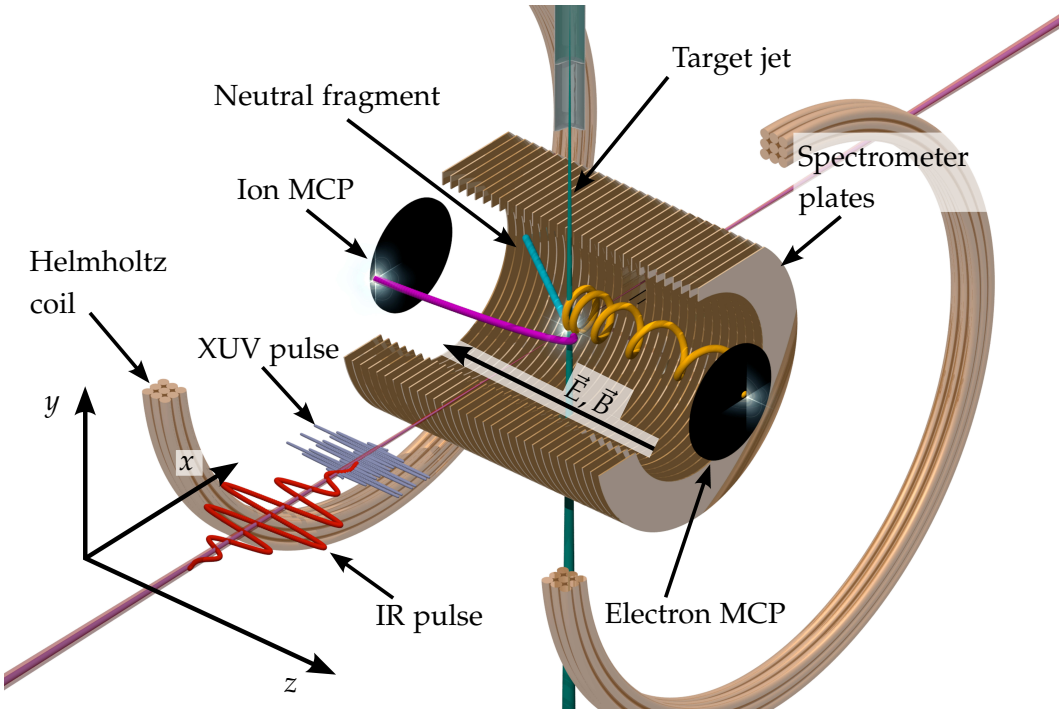

Fig. 4.1. Illustration of a REMI used in XUV–IR pump–probe experiments. Target molecules in a supersonic gas jet (green) are ionized (and possibly dissociated) by XUV (blue) and IR (red) laser pulses. Created photoelectrons (orange) and ions (purple) are guided towards position sensitive MCP detectors by electric and magnetic fields. Neutral fragments (turquoise) cannot be detected. Helmholtz coils not to scale.

Jet stagnation pressure (typ.)	2 bar
Background pressure in the main chamber (typ.)	1×10^{-10} mbar
Nozzle diameter [Gop10, p. 54]	30 µm
Skimmer 1 diameter [Gop10, p. 54]	200 µm
Skimmer 2 diameter [Gop10, p. 54]	400 µm
Jet stage length [Gop10, p. 55]	112 mm
Jet temperature (expansion direction)	$\mathcal{O}(10\,\mathrm{K})$
Jet momentum spread (expansion direction)	≈ 1.3 a.u.
Jet temperature (transversal) [Gop10, p. 55]	$\mathcal{O}(0.1\,\mathrm{K})$
Jet momentum spread (transversal)	≈ 0.2 a.u.

Tab. 4.1. Jet and vacuum parameters.

In our experiments, XUV and IR laser pulses are focused into a supersonic gas jet of target atoms or molecules[1]. The setup for the creation of this target jet and its properties are described in Sec. 4.1.1. Ionization by the laser pulses creates electrons and ions which are guided by homogeneous electric and magnetic fields towards position sensitive particle detectors (labeled 'MCP' in Fig. 4.1). The fields are created by spectrometer anodes (labeled 'Spectrometer plates' in Fig. 4.1) and a pair of Helmholtz coils (not to scale in Fig. 4.1). Properties of the electric and the magnetic fields are briefly described in Sec. 4.1.2. The particle detectors consist of micro-channel-plate (MCP) detectors with a delay-line anode as described in Sec. 4.1.3. With these, the time-of-flight (ToF) and hit position of all charged particles is measured. This allows to reconstruct the 3-dimensional momenta of the particles with methods described in Sec. 4.2.

4.1.1. Gas jet and vacuum

Cold target molecules are crucial for recoil ion momentum spectroscopy experiments since typical recoil momentum transfers from photoelectrons to the ions are on the order of 1 a.u. whereas the mean quadratic momentum from the Maxwell–Boltzmann distribution at room temperature is in the order of 10 a.u. for N_2 and O_2. This problem is solved by cooling the target gas in a supersonic expansion[2]. Important parameters of the jet and properties of the vacuum are summarized in Tab. 4.1. For a detailed description of the jet stage used in our REMI, the reader is referred to Ref. [Gop10, p. 53-55].

[1] From hereon the target is assumed to be molecular (N_2 or O_2) unless mentioned otherwise.

[2] In a so-called MOTRemi (see for example [SZS+11, FGG+12, SBGG+13]), the target atoms are stored in a magneto optical trap.

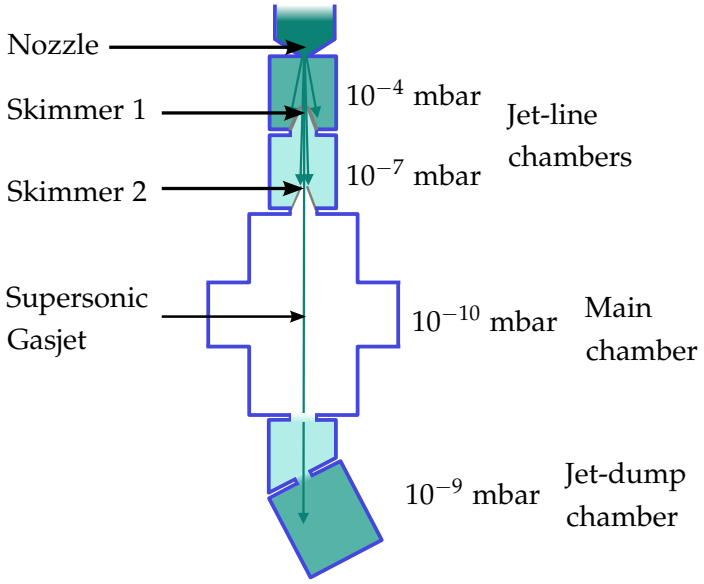

Fig. 4.2. Illustration of the jet stage. Figure adapted from Ref. [Spe13].

Jet stage and vacuum

The jet stage is illustrated in Fig. 4.2. The stagnation pressure of the target gas at room temperature is typically 1 to 5 bar. The gas escapes through a nozzle ($\varnothing = 30\,\mu m$) into the vacuum of the first jet stage (typical pressure of 1×10^{-4} mbar). This leads to a supersonic expansion [Cam84]. A skimmer ($\varnothing = 200\,\mu m$), placed in to zone of silence separates the supersonic beam from the warm background gas [Gop10, p. 53]. In addition the skimmer acts as a differential pump stage separating the first and the second jet stage. The latter is at a typical pressure of 1×10^{-7} mbar. Finally the gas jet escapes into the main chamber through a second skimmer ($\varnothing = 400\,\mu m$). In order to maintain the very low background pressure within the main chamber (typically 1×10^{-10} mbar), the jet is dumped in a dedicated chamber, separated from the main reaction chamber by a differential pump stage.

Momentum spread in the target jet

In the following, the momentum spread in the target jet is estimated from the jet temperature. These values are needed to estimate the momentum uncertainty in the experiments. It is important to note that the temperature in the jet propagation direction T_y depends on the expansion process while the temperatures perpendicular to the expansion direction $T_{z,x}$ are mostly governed by the geometrical setup of the jet stage. For a comprehensive introduction of this topic, the reader is referred to Ref. [Mil88]. The most important concepts and formulas are summarized in Ref. [Sch14, p. 50-51].

Target species	A	B	C_6/k_B (10^{-43} cm^6 K)	T_0 (K)	p_0 (bar)	S_∞	T_y (K)
N_2	0.78	0.35	6.2 (9.2)^b	300	2	8.9 (9.3)^b	13 (12)^b
O_2	0.78	0.35	8.3	300	2	9.2	12

Tab. 4.2. Numbers from Ref. [Mil88, p. 30 & p. 46]. ^{b} Alternative set of values.

The jet temperature in propagation direction T_y can be estimated by

$$T_y = T_0 \frac{\gamma}{\gamma - 1} \frac{1}{S_\infty^2} \tag{4.1}$$

where $\gamma = 1 + 2/f$. Here, f denotes the number of motional degrees of freedom. For diatomic molecules at room temperature with 3 translational and 2 rotational degrees of freedom[3] $f = 5 \rightarrow \gamma = 1.4$. The speed ratio S_∞, given by the ratio between the longitudinal jet velocity v_y and the thermal velocity v_{therm} is empirically described with (compare [Mil88] and [Sch14, p. 51])

$$S_\infty = \frac{v_y}{v_{\text{therm}}} = A \left[\sqrt{2} \frac{P_0 d}{k_B T_0} \left(\frac{53 C_6}{k_B T_0} \right)^{1/3} \right]^B . \tag{4.2}$$

Here the nozzle diameter d, the stagnation pressure P_0 and the initial temperature T_0 are experimental parameters. k_B is the fundamental Boltzmann-constant. A, C_6 and B are empirical constants which depend on the target species. All constants as well as the speed ratio S_∞ and the jet temperature T_y for the target species presented in this work are listed in Tab. 4.2.

For the species N_2 and O_2, the momentum spread in propagation direction is given by

$$\triangle p^y_{\text{therm}} = \sqrt{k_B T_y m_i} \approx 1.3\,\text{a.u.}, \tag{4.3}$$

using $T_y = 10\,\text{K}$ and $m_i = 30\,\text{amu}$.

Typically, the momentum spread perpendicular to the expansion direction $\triangle p^{x,z}_{\text{therm}}$ is lower than $\triangle p^y_{\text{therm}}$ since it is determined geometrically by the skimmers. In our setup, the gas beam divergence is $\theta = 2 \cdot 0.4^\circ$ (calculated for a $\varnothing = 400\,\mu\text{m}$ second skimmer at a distance of 3 cm from the nozzle). For an N_2 or O_2 gas jet with an initial temperature $T_0 \approx 300\,\text{K}$, the momentum in jet direction can be estimated to [Fis03, p. 41]

$$p_y \approx \sqrt{5 k_B T_0 m_i} \approx 16\,\text{a.u.} \tag{4.4}$$

The transversal momentum spread is therefore estimated by

$$\triangle p^{x,z}_{\text{therm}} = \tan(\theta) p_y \approx 0.2\,\text{a.u.}. \tag{4.5}$$

According to Eq. (4.3), this corresponds to a temperature of $T_{x,z} \approx 0.2\,\text{K}$.

[3] Vibrational degrees of freedom are not excited at ambient temperature.

4.1.2. Electric and magnetic field

In order to provide a near 4π solid angle acceptance for ions and electrons, electric and magnetic fields are used in the REMI to project charged particles onto MCP detectors. For a successful reconstruction of the initial momenta from the particles' measured ToFs and hit positions, homogeneous extraction fields are of utter importance. A detailed description of the spectrometer and the Helmholtz coils is given in Ref. [Gop10, p. 55-58].

The electric field created by 32 spectrometer plates (illustrated in Fig. 4.1) guarantees a full solid angle acceptance for recoil ions and charged fragments of low energetic molecular dissociations. Typical photoelectron energies in our experiments, however, are in the range of 10 to 25 eV (compare Fig. 3.12). Due to their high energy, an additional homogeneous magnetic field is needed to maintain a full solid angle acceptance for these electrons[4]. This results in helical electron trajectories within the REMI (as illustrated in Fig. 4.1). The magnetic field of typically 7.9 G is provided by a pair of Helmholtz coils with a diameter of 710 mm separated by 400 mm [Gop10, p. 57].

4.1.3. Micro-channel-plate detector and delay-line anodes

The micro-channel-plate detectors (MCP) are an array of microscopic channels, each acting as a photomultiplier: The primary particle is accelerated by a potential towards the front side of the MCP. If the particle enters one of the micro channels, it will eventually hit its inner surface. This is schematically shown in Fig. 4.3. The impact energy may create a free secondary electron which is accelerated by a large potential towards the backside of the MCP. Each secondary electron frees further electrons upon hitting the channel's inner surface. This leads to an avalanche of electrons which carry a macroscopic current. In order to further increase the current amplification, two MCPs are stacked in a so-called Chevron configuration where the channels of the first plate are tilted with respect to those of the second one (see Fig. 4.3).

Experimentally the electron avalanche (and therefore the primary particle) is detected by a small drop in the potential. This signal at time T_{MCP} is used to determine the ToF of the primary particle from

$$\mathrm{ToF} = T_{\mathrm{MCP}} - T_{\mathrm{pulser}} + T_0 \tag{4.6}$$

where T_{pulser} is a time reference obtained from a photo diode for each laser pulse. T_0 is a constant offset. A typical ion ToF spectrum is shown in Fig. 4.4(a).

In order to reconstruct the transversal momentum p_R, the hit position is measured. This is done with two perpendicular delay-line anodes (see Fig. 4.5). These are copper wires forming a grid of parallel, equidistant wires positively biased compared to the

[4] Increasing the spectrometer potential in order to guide the electrons to the detectors by means of the electric field alone is not an option, since the energy resolution for low energetic ions suffers from high spectrometer potentials.

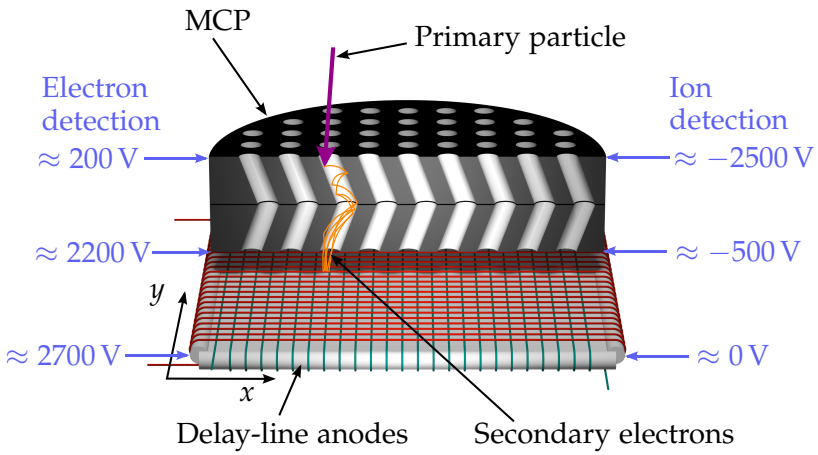

Fig. 4.3. Illustration of the MCP stack in Chevron configuration. Primary particles (purple) are accelerated towards the front side of the MCP. Secondary electrons (orange) are accelerated by a high voltages (blue) which leads to an electron multiplication within the micro channels. This results in a macroscopic current. After escaping the micro channel, the electron cloud impinges onto the delay-line anodes (see Fig. 4.5 for details).

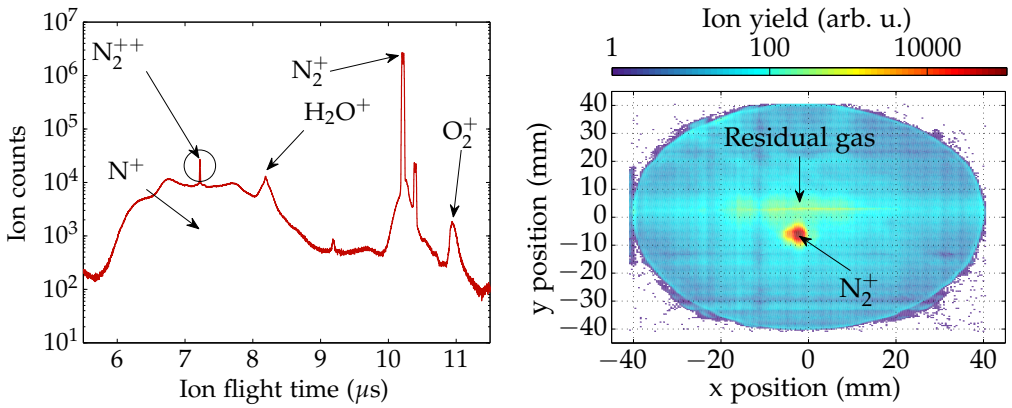

(a) (b)

Fig. 4.4. Typical raw spectra obtained with the REMI. **Panel (a):** ToF spectrum created in (dissociative) ionization of N_2. **Panel (b):** Corresponding hit position. Due to the velocity of the target jet in y-direction, the N_2^+ ions are displaced with respect to the events resulting from ionization of residual gas .

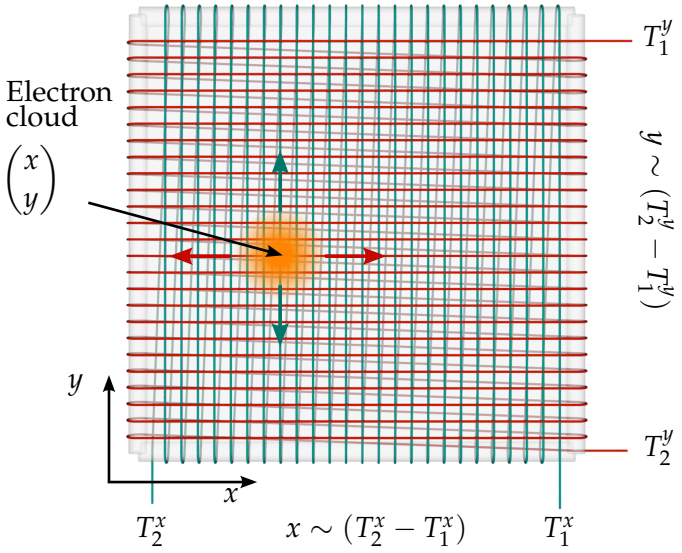

Fig. 4.5. The cloud of secondary electrons (orange) emerging from the MCP stack creates a signal on the delay-line anode which propagates through the wires. The impact position can be reconstructed from the times $T_{1/2}^{x/y}$ at which the signal reaches the ends of the wire. The x-position is obtained by the propagation time within the green wire. The red wire is used to determine the y-position.

backside of the MCP stack. The cloud of secondary electrons impinges onto these wires of which one is used to determine the x position and the other one measures the y position. The hit position (x, y) is reconstructed from

$$\begin{pmatrix} x \\ y \end{pmatrix} \propto \begin{pmatrix} T_2^x - T_1^x \\ T_2^y - T_1^y \end{pmatrix} \tag{4.7}$$

where T_2 and T_1 are the times at which the signals reach the two ends of the respective wire. Thus, the hit position is determined from the traveling time of the signals to the wire ends as indicated in Fig. 4.5. A typical ion detector image is shown in Fig. 4.4(b).

4.2. Momentum reconstruction

After having established fundamental knowledge on how the ToF and the hit position of a detected particle is determined experimentally, this section deals with the reconstruction of its momentum. The motion of particles with charge q and mass m within an electric field $\vec{E}$ and a magnetic field $\vec{B}$ is described by the Lorentz force

$$\vec{F}(\vec{r}) = q\left(\vec{E} + \dot{\vec{r}} \times \vec{B}\right) = m\ddot{\vec{r}}. \tag{4.8}$$

For the parallel magnetic and electric fields of a REMI, analytic solutions of this differential equation exist. This allows to derive formulas used for the reconstruction of

the initial 3-dimensional momenta of ions (see Sec. 4.2.1) and electrons (see Sec. 4.2.2). Limitations of our setup in terms of acceptance and momentum resolution are pointed out in Sec. 4.2.3.

4.2.1. Ions

Due to their large charge-to-mass ratio, effects of the magnetic field on the ion trajectories can be neglected as has been formally shown in Ref. [Sen09, p. 57-59]. By taking only the homogeneous electric field $\vec{E}(\vec{r}) = E_z$ into account, Eq. (4.8) simplifies to

$$\begin{pmatrix} F_x \\ F_y \\ F_z \end{pmatrix} = q_i \begin{pmatrix} 0 \\ 0 \\ E_z \end{pmatrix} = m_i \begin{pmatrix} \ddot{x} \\ \ddot{y} \\ \ddot{z} \end{pmatrix}. \tag{4.9}$$

Here q_i and m_i denote the ion's charge and mass respectively. Since the differential equations are not coupled, they can be treated component wise.

By integration of the z component and using that the detector is hit at $z = l$ and at $t = \mathrm{ToF}$,

$$l = \frac{1}{2}\frac{q_i}{m_i}\frac{U}{l}\mathrm{ToF}^2 + \frac{p_z}{m_i}\mathrm{ToF} + z_0 \tag{4.10}$$

is obtained. Here l denotes the spectrometer length and the electric field is expressed as[5] $E_z = U/l$. The (x, y) components can be written as

$$\begin{pmatrix} x \\ y \end{pmatrix} = \begin{pmatrix} p_x \\ p_y \end{pmatrix} \frac{\mathrm{ToF}}{m_i} + \begin{pmatrix} x_0 \\ y_0 \end{pmatrix}. \tag{4.11}$$

We assume in the following that the molecules are ionized in the center of the REMI and therefore $(x_0, y_0, z_0) = 0$.

Ion mass spectrometry

Identification of different particle species is important, when experiments involving the fragmentation of molecules are conducted. In a REMI, this is possible by measuring the ToF. Assuming[6] $p_z = 0$, Eq. (4.10) can be rearranged to

$$\mathrm{ToF} = \sqrt{2\frac{m_i}{q_i}\frac{l^2}{U}} \propto \sqrt{\frac{m_i}{q_i}}. \tag{4.12}$$

Thus the measured ToF depends on the charge-to-mass ratio. Particles with equal mass-to-charge ratios will exhibit similar ToFs. This is shown in Fig. 4.4(a) where the N_2^{++} and N^+ fragments have the same charge-to-mass ratio. Note, however, that the N^+ peak is much broader, since these fragments feature larger initial momenta.

[5] This is convenient since experimentally E_z is chosen by setting the potential U with a voltage supply.

[6] This approximation is justified since typically the center of a ToF peak is used to identify the particle species.

Ion momenta

After having established a method to identify particle species, we are interested in the longitudinal momentum of single particles. This is calculated by rearranging Eq. (4.10) to

$$p_z = l\frac{m_i}{\mathrm{ToF}} - \frac{1}{2}\frac{q_i U}{l}\mathrm{ToF}. \tag{4.13}$$

Obviously for fixed spectrometer parameters and a specific particle species, p_z only depends on the ToF.

Similarly, Eq. (4.11) is used to determine the (p_x, p_y) momentum components from the hit position (x, y) with

$$\begin{pmatrix} p_x \\ p_y \end{pmatrix} = \frac{m_i}{\mathrm{ToF}} \begin{pmatrix} x \\ y \end{pmatrix}. \tag{4.14}$$

4.2.2. Electrons

Electrons are affected by the magnetic field, due to their small mass. In this case, for parallel and homogeneous electric and magnetic fields, Eq. (4.8) is written as

$$\begin{pmatrix} F_x \\ F_y \\ F_z \end{pmatrix} = e\left[\begin{pmatrix} 0 \\ 0 \\ E_z \end{pmatrix} + \begin{pmatrix} \dot{y}B_z \\ -\dot{x}B_z \\ 0 \end{pmatrix}\right] = m_e \begin{pmatrix} \ddot{x} \\ \ddot{y} \\ \ddot{z} \end{pmatrix}. \tag{4.15}$$

Here, e and m_e denote the electrons charge and mass, respectively.

Longitudinal momentum

The z component of the above equation is similar to that of Eq. (4.9) since it is not affected by the magnetic field. Thus, the electrons' longitudinal momenta are calculated with

$$p_z = l\frac{m_e}{\mathrm{ToF}} - \frac{1}{2}\frac{eU}{l}\mathrm{ToF}. \tag{4.16}$$

Transversal momentum

The electrons' helical cyclotron trajectories within the magnetic field B_z complicate the reconstruction of the transversal momentum. A typical electron trajectory was shown in Fig. 4.1 (orange trajectory). The projection of such a trajectory onto the xy-plane is illustrated in Fig. 4.6.

The radius R_c of the cyclotron motion is calculated from the centrifugal force and the Lorentz force by

$$R_c = \frac{|\vec{p}_R|}{eB_z}, \tag{4.17}$$

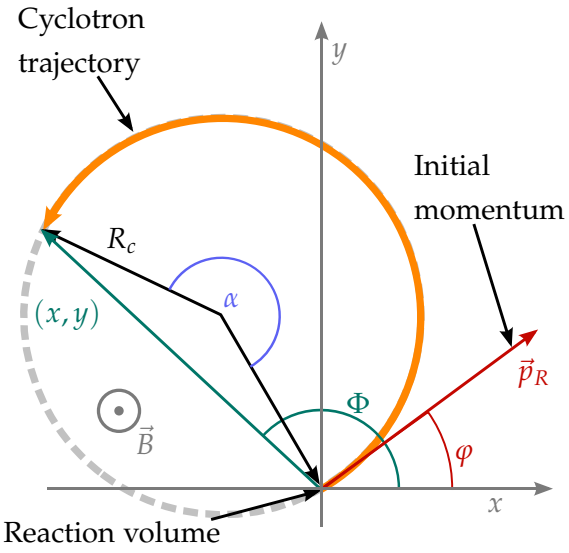

Fig. 4.6. Projection of the cyclotron trajectory of an electron onto the xy plane (detector plane). Knowing the ToF and the magnitude of the homogeneous magnetic field $\vec{B}$, it is possible to reconstruct the initial momentum $\vec{p_R}$ from the measured hit position (x,y). Figure adapted from Ref. [UMD+03].

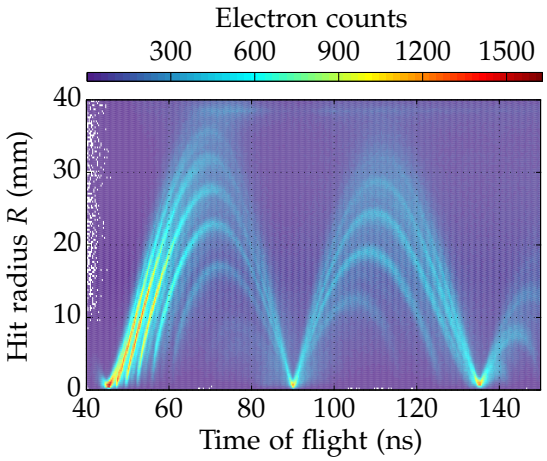

Fig. 4.7. Ionization of argon by XUV photons. Plotted is the number of detected electrons as a function of their hit distance from the MCP center $R = |(x,y)|$ (as defined in Fig. 4.6) and their ToF. Whenever the electrons have completed an integer number of cyclotron motions, they will hit the center of the detector.

where $|\vec{p}_R|$ denotes the magnitude of the initial transversal momentum. With this, the hit distance $|(x,y)|$ from the MCP center is given by

$$|(x,y)| = 2R_c|\sin(\alpha/2)|. \tag{4.18}$$

Using the cyclotron frequency $\omega_c = eB_z/m_e$, the angle $\alpha = \omega_c \cdot \mathrm{ToF}$ was defined. Rearranging the above equation and substituting $R_c = |\vec{p}_R|/(eB_z)$ yields

$$|\vec{p}_R| = |(x,y)|\frac{eB_z}{2|\sin(\alpha/2)|}. \tag{4.19}$$

This allows to calculate the magnitude of the initial transversal momentum from the ToF and the hit distance from the the reaction center. In order to determine the direction $\vec{p}_R$, the angles $\Phi := \arctan(x/y)$ and $\varphi := \arctan(p^x/p^y)$ must be considered. φ is then given by

$$\varphi = \Phi - \frac{\alpha(\mathrm{mod}\ 2\pi)}{2}. \tag{4.20}$$

The cyclotron motion of the electrons is visible in the experimental spectrum in Fig. 4.7. This also shows a downside of using an additional magnetic field for the projection of electrons onto the MCP detectors: For $\alpha = \omega_c \mathrm{ToF} = 2n\pi$ $(n \in \mathbb{N})$, the electrons will always hit the detector in the center. In this case an unambiguous reconstruction of the initial transversal momentum is not possible.

To overcome this problem, the magnetic field B_z and the acceleration potential U can be chosen such that this situation does not occur for electron ToFs which are of interest. This, however, is not always possible since for instance the full solid angle acceptance for highly-energetic ions and their momentum resolution pose conditions on suitable acceleration voltages as well. This is discussed in the next section.

4.2.3. 4π acceptance and momentum resolution

The confinement of charged particles in transversal directions works fundamentally different for ions and electrons. The ions are solemnly guided by the electric field towards the ion MCP while the confinement for the electrons is mainly due to the magnetic field. We will discuss the ions first:

Ion transversal acceptance

The transversal acceptance for ions can be calculated from Eq. (4.14). For this, we express the ToF in terms of the spectrometer potential U and the spectrometer length l (assuming zero longitudinal momentum). In addition the transversal momenta in Eq. (4.14) are expressed by the transversal kinetic energy $E^{\mathrm{trans}} = \left|(p_x, p_y)\right|^2/(2m_i)$. An ion will hit the detector, if $|(x,y)| < R_{\mathrm{MCP}}$. Therefore the transversal acceptance is given by

$$E^{\mathrm{trans}}_{\mathrm{ion}} < \left(\frac{R_{\mathrm{MCP}}\sqrt{Uq}}{2l}\right)^2 \approx 3\,\mathrm{eV}. \tag{4.21}$$

With the typical spectrometer parameters of $R_{\mathrm{MCP}} = 40\,\mathrm{mm}$, $U = 136\,\mathrm{V}$ and $l = 13.5\,\mathrm{cm}$, singly charged ions with kinetic energies above $E_{\mathrm{kin}} = 3\,\mathrm{eV}$ do not hit the detector for certain emission angles. In order to detect such ions, the acceleration voltage U must be increased. This, however, has negative impact on the ion momentum resolution.

Ion momentum resolution

The ion momentum uncertainty is governed by two terms: the momentum spread in the gas jet $\triangle p^{z,x,y}_{\mathrm{therm}}$ and the resolution of the spectrometer $\triangle p^{z,x,y}_{\mathrm{spec}}$. The jet momentum spread is anisotropic and was calculated to

$$\triangle p^{y}_{\mathrm{therm}} \approx 1.3\,\mathrm{a.u.} \quad \text{and} \quad \triangle p^{z,x}_{\mathrm{therm}} \approx 0.2\,\mathrm{a.u.}. \tag{4.22}$$

in Sec. 4.1.1 [Eqs. (4.3) and (4.5)] for the experiments presented in this work.

The resolution of the spectrometer in the p_z (ToF direction) momentum direction is limited by the error in the ToF measurement $\triangle T \approx 1\,\mathrm{ns}$ and the size of the laser focus which effectively adds an uncertainty to the spectrometer length $\triangle l \approx 50\,\mu\mathrm{m}$. In $p_{x,y}$ direction, the uncertainty in the determination of the hit position $\triangle x = \triangle y \approx 1\,\mathrm{mm}$ [Fis03, p. 55] limits the resolution. From Eqs. (4.10) and (4.11) the uncertainties are given by

$$\triangle p^{z}_{\mathrm{spec}} = \left[\left(5.68 \times 10^{-3}\,\mathrm{a.u.} \frac{qU}{\mathrm{eV}} \frac{\mathrm{cm}}{l} \frac{\triangle t}{\mathrm{ns}} \right)^2 \right. \quad \begin{cases} qU \text{ in eV} \\ l \text{ in cm} \\ \triangle t \text{ in ns} \end{cases} \tag{4.23}$$

$$\left. + \left(8.18 \times 10^{-4}\,\mathrm{a.u.} \sqrt{\frac{qU}{\mathrm{eV}}} \sqrt{\frac{m_i}{\mathrm{amu}}} \frac{\mathrm{cm}}{l} \frac{\triangle l}{\mu\mathrm{m}} \right)^2 \right]^{1/2} \quad \triangle l \text{ in } \mu\mathrm{m} \tag{4.24}$$

and

$$\triangle p^{x,y}_{\mathrm{spec}} = \left(5.78\,\mathrm{a.u.} \sqrt{\frac{qU}{\mathrm{eV}}} \sqrt{\frac{m_i}{\mathrm{amu}}} \frac{\triangle x}{l} \right) \quad \begin{cases} qU \text{ in eV} \\ m_i \text{ in amu} \\ l \text{ in cm} \\ \triangle x \text{ in cm} \end{cases} \tag{4.25}$$

Using a spectrometer length of $l \approx 14\,\mathrm{cm}$, an acceleration voltage of $U = 136\,\mathrm{V}$, and a mass of $m_i = 15\,\mathrm{amu}$ (N^+ fragment), numerical values for these uncertainties are given by

$$\triangle p^{z}_{\mathrm{spec}} \approx 0.13\,\mathrm{a.u.} \quad \text{and} \quad \triangle p^{x,y}_{\mathrm{spec}} \approx 1.26\,\mathrm{a.u.}. \tag{4.26}$$

The total momentum uncertainties are[7]

$$\triangle p_z = \sqrt{(\triangle p^z_{\text{spec}})^2 + (\triangle p^z_{\text{therm}}/2)^2} \approx 0.16\,\text{a.u.} \tag{4.27}$$

$$\triangle p_x = \sqrt{(\triangle p^x_{\text{spec}})^2 + (\triangle p^x_{\text{therm}}/2)^2} \approx 1.3\,\text{a.u.} \tag{4.28}$$

$$\triangle p_y = \sqrt{(\triangle p^y_{\text{spec}})^2 + (\triangle p^y_{\text{therm}}/2)^2} \approx 1.4\,\text{a.u.}. \tag{4.29}$$

In the worst case scenario (particle is emitted in y-direction), the kinetic energy resolution $\triangle E$ for an O^+ fragment is then given by

$$\triangle E = \sqrt{\frac{2E}{m_i}}\triangle p_y \approx \begin{cases} 2 \times 10^{-3}\,\text{eV for } E = 1\,\text{eV}. \\ 8 \times 10^{-4}\,\text{eV for } E = 0.1\,\text{eV}. \end{cases} \tag{4.30}$$

The momentum uncertainty can be estimated experimentally by evaluation of so-called momentum sum distributions. The measured uncertainties are

$$\triangle p_z^{\text{exp}} \approx 1.5\,\text{a.u.} \quad \text{and} \quad \triangle p_{x,y}^{\text{exp}} \approx 7\,\text{a.u.} \tag{4.31}$$

for spectrometer settings and particle species used in the calculations above. Thus, the calculations significantly underestimate the momentum uncertainty observed experimentally. This discrepancy was explained in Ref. [Sch14, p. 83] by additional uncertainties due to inhomogeneities of the electric field and tilts of the MCP detectors with respect to the spectrometer axis.

Electron transversal acceptance

The radius of the electron's cyclotron trajectory is given by R_c [Eq. (4.17)]. As a result, the distance between the electron and the detector center $|(x, y)|$ is always smaller than $2R_c$ (compare Fig. 4.6). Rearranging Eq. (4.17) and expressing the transversal momentum $|\vec{p}_R|$ by the transversal kinetic energy, we calculate a 4π acceptance of electrons with energies up to

$$E_{e^-}^{\text{trans}} = R_{\text{MCP}}^2 \frac{e^2 B_z^2}{8 m_e} \approx 22\,\text{eV}. \tag{4.32}$$

Here, the spectrometer parameters $R_{\text{MCP}} = 40\,\text{mm}$ and $B = 7.9\,\text{G}$ are used. Increasing the magnetic field B_z will increase the acceptance.

[7] If a fragment with mass m_i of the parent molecule with mass m_M is detected, the momentum uncertainty due to the jet temperature will be reduced by a factor of m_i/m_M. Since in this work, only momenta of fragments of homonuclear diatomic molecules are measured, the thermal momentum spread is reduced by a factor of 2 in the following equations.

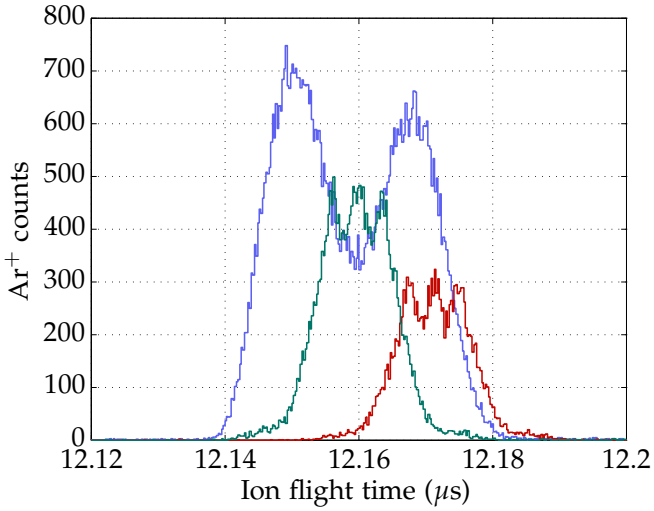

Fig. 4.8. Measured Ar^+ time of flight spectra. **Blue spectrum:** Ionization by XUV pulse. **Red spectrum:** Ionization by IR pulse after optimization of spatial overlap on CCD camera. **Green spectrum:** Ionization by IR pulse after optimization of spatial overlap with the flight-time method.

4.3. Experimental techniques

This technical section begins with the description of a method for finding the temporal and spatial overlap of the XUV and the IR pulse inside the REMI. The quality of this overlap is crucial for a successful pump-probe experiment. The method presented in Sec. 4.3.1 was used to tune the pulse overlap in all experiments presented in this work and has proven to be very reliable. Afterwards, in Sec. 4.3.2, the post analysis of the recorded data is described briefly with a focus on so-called particle coincidences which are routinely used in the data evaluation.

4.3.1. Optimizing the pulse overlap

For a coarse alignment of the XUV and IR beam, the aluminum filter pictured in Fig. 3.6 (b) can be removed from the beam path remotely. In this case, the fundamental light from both interferometer arms enters the REMI. The focal volume is imaged by a set of lenses onto a CCD camera. This allows to measure and to tune the spatial overlap. At the same time the collinearity of the beams is guaranteed if the IR probe beam is centered on the holey parabolic mirror in Fig. 3.6 (c)[8]. However, the spatial overlap achieved with this method alone is not very good. Therefore a different method is applied for the fine tuning, as explained in the following.

[8]Due to technical reasons, the beam is aligned to the center of the motorized iris instead of the parabolic mirror, whenever the HHG chamber is evacuated.

Different Ar^+ ToF spectra are shown in Fig. 4.8. The blue spectrum is obtained by ionization with the XUV pulse. The red spectrum is created by ionization with the IR pulse after alignment of the spatial overlap with the CCD camera image. Since the ToF depends on the effective spectrometer length, these spectra can be used to evaluate the spatial overlap in longitudinal direction (ToF direction). The discrepancy between the blue and red spectrum corresponds to a misalignment of about 200 µm which is much larger than the focal diameter of the pulses. By optimizing the alignment of the IR pulse, the ToF spectrum created by IR ionization can be shifted such, that it overlaps with the ToF spectrum obtained with the XUV pulse (see Fig. 4.8 blue and green spectra). This overlap can be set to an accuracy of about 2 ns corresponding to a spatial accuracy of about 10 µm. This is much less than the diameter of the XUV focus (which was estimated to 60 µm in Sec. 3.2.4).

This method works best, if the ToF uncertainty is small compared to the ToF. Therefore heavy targets like Ar and low acceleration voltages should be used according to Eq. (4.12). The spatial overlap in y-direction (see Fig. 4.1 for definition) is optimized by a similar technique. For this the Ar^+ hit position on the detector is compared for ionization with IR and XUV pulse[9].

If the beams are overlapping spatially, the coarse temporal overlap is found by changing the pump–probe delay with the motorized translation stage [Fig. 3.6 (d)] until an interference pattern is observed on the CCD camera. Afterwards, the pulse overlap is confirmed with a short reference measurement with an argon target. In this ionization by XUV and IR pulses, the kinetic energy spectrum of photoelectrons will feature sidebands if both pulses are overlapping temporally and spatially (as described in Sec. 3.2.5). The peak-to-peak ratio between the sideband and the main band is a good measure for the quality of the pulse overlap. If such a measurement is performed right before starting the intended experiment, the temporal position of these sidebands can be used to determine the temporal overlap between the pulses very precisely.

4.3.2. Post analysis and particle coincidences

During a single experiment, the ToFs and the hit positions of about 1000 to 2000 ionic fragments per second are detected over dozens of hours. This information is boiled down in the post analysis to be plotted in histograms.

First, digitalized timing signals from the MCPs and delay-line anodes (see Sec. 4.1.3) are converted into ToFs and hit positions on the detector. This is done on a shot-to-shot basis of the laser which is important to identify so-called particle coincidences as described below. In addition the momentary position of the pump–probe delay stage obtained from an ADC is stored with each valid event.

[9] Due to the lower momentum resolution in this direction, the achieved accuracies are lower than for the longitudinal directions. However, by fitting Gaussian functions to the spectra obtained by IR and XUV ionization, respectively, the centers of the distributions can be determined reliably.

By identifying ToF intervals with certain particle species, the 3-dimensional momenta are reconstructed from the ToF and hit position (see Sec. 4.2). All other kinematic properties like kinetic energy and emission angles are calculated from the momenta. The real power of the REMI is given by the possibility to analyze particle coincidences which can be used to obtain additional information about reaction pathways. This is explained with two examples:

- By correlating electron spectra with the ToF of coincident ions, electrons can be classified. This allows for example to compare the kinetic energies of electrons which were created in coincidence with N_2^{++} ions to the kinetic energy of those created in coincidence with N_2^+. That method is especially useful if one is interested in electrons created in processes with low rates (double ionization) compared to the main reaction channel (single ionization).

- The sum momentum of coincident particles can be used to identify reaction channels. For example if dissociative (double) ionization of N_2 is investigated, N^+ is a rather abundant reaction product. To distinguish the channels

$$\text{(a) } N_2 \xrightarrow{\text{single ionization}} N^+ + N \quad \text{and} \quad \text{(b) } N_2 \xrightarrow{\text{double ionization}} N^+ + N^+ \tag{4.33}$$

  it is useful to consider the sum momenta of the N^+ ions, whenever more than one is detected in a laser shot. Due to momentum conservation, particles originating from the same parent molecule will have a vanishing momentum sum. This allows to distinguish the N^+ ions created in process (b) (which typically has a low rate) from those created in process (a) (which typically has a high rate).

Both techniques described above are used in the data analysis in Chap. 6. Moreover, coincidences can be used to obtain additional kinematic information. This is used in so-called energy-correlation maps where the kinetic energy of particle A is plotted as a function of the kinetic energy of a coincident particle B. This method allows to obtain additional information about the involved reactions as shown for example in Refs. [FSC+13, FSC+14]. Another application is the correlation of emission angles of the two photoelectons created in double ionization of Ar, as done in Ref. [Cam13].

5. Probing O_2^+ potential-energy curves with an XUV–IR pump–probe experiment

Contents

5.1. Historical overview of wave-packet dynamics in diatomic molecules 80

5.2. Experimental spectra and vibrational wave-packet dynamics 82

5.3. Comparison between experimental data and simulated spectra . . . 99

5.4. Limitations of the quantum simulation 109

5.5. Summary of the O_2 experiments 113

The experimental data and parts of the results presented in this chapter have been published in the following article

Probing calculated O_2^+ potential-energy curves with an XUV-IR pump-probe experiment

P. Cörlin, A. Fischer, M. Schönwald, A. Sperl, T. Mizuno, U. Thumm, T. Pfeifer, R. Moshammer

PRA **91**, 043415– (2015)

cited as Ref. [CFS+15].

This chapter discusses a vibrational wave-packet oscillation within the Born-Oppenheimer potential-energy curve (PEC) belonging to the $O_2^+(a\,^4\Pi_u)$ electronic state. We begin with an overview of previous experiments on nuclear dynamics in diatomic molecules in Sec. 5.1. In Sec. 5.2 the experimental results are presented and discussed. Furthermore the pump–probe scheme is introduced and the involved electronic and vibrational states are identified. Afterwards, in Sec. 5.3 coupled-channel simulations are used to show that the wave-packet dynamics is sensitive to the shape of the binding PEC. In contrast, the kinetic energies of measured O^+ fragments strongly depend on the PEC associated with the final anti-bonding adiabatic $O_2^+(f\,^4\Pi_g)$ state of the molecular cation. This allows to test the predicted PECs. Minor discrepancies between the experimental data and our simulations are addressed in Sec. 5.4. The chapter is briefly summarized in Sec. 5.5.

5.1. Historical overview of wave-packet dynamics in diatomic molecules

During the 1980s and 1990s breakthroughs in laser science led to increasingly intense and short laser pulses. In the early 1990s, pulse durations down to 50 fs were reached [DJZ91, BGTG91]. Using such pulses in pump–probe experiments allowed the observation of ultra-fast molecular dynamics with a temporal resolution in the order of the pulse length [Zew00].

Around 1990 molecular vibrational wave packets were experimentally observed for the first time. Due to the – from our point of view – rather long pulse durations, the nuclear dynamics was measured in heavy molecules such as I_2 [DJZ91] or loosely bound systems like Na dimers (Na_2) [BGTG91]. Both properties result in a narrow spacing of the vibrational levels and thus in extremely large beating periods of hundreds of femtoseconds. The observation of increasingly fast processes was made possible in to following years by shorter and shorter pulse lengths [AGH+96, AHW+96, SBN04].

Sub 10 fs pulse durations achieved ten years later allowed to observe the wave-packet oscillation on the Born-Oppenheimer PEC belonging to the $H_2^+(X\,^2\Sigma_g^+)$ and $D_2^+(X\,^2\Sigma_g^+)$ electronic state[1]. Both molecules were studied extensively throughout the last decade with various pump–probe techniques [LLL+05, AUT+05, ERF+05, FER+07, NVC06, KLS+09, HT10, FGC+14]. They are especially attractive since they are well understood by theory and feature only a single cationic bound state.

This is in contrast to the large number of bound states found in the cations of more complex diatomic molecules such as O_2 , N_2 or CO. A selection of the corresponding PECs is shown in Fig. 5.1 for O_2^+. The number of states and the resulting competing reaction channels complicate the interpretation of experimental spectra. This could explain why the wave-packet evolution in the cations of medium sized diatomic molecules such as N_2 or O_2 [DBM+10, DMB+11, MAT12, BAT+11] has been in investigated less frequently than in H_2^+ and its isotopes [CFS+15].

In 2011, IR–IR experiments on molecular oxygen revealed the vibrational wave-packet dynamics in the $O_2^+(a\,^4\Pi_u)$ PEC [DMB+11] (blue PEC in Fig. 5.1). In that experiment, O_2 molecules were ionized by the strong field of the IR pump pulse. This launched a molecular wave packet due to the excitation of multiple vibrational states. The wave packet evolved in time for up to 1.2 ps before it was probed by a second IR pulse to the repulsive $O_2^+(f\,^4\Pi_g)$ state (green PEC in Fig. 5.1). In this case, the molecule dissociates and a pump–probe delay dependent yield of low energetic O^+ ions can be measured. The observed oscillation period was identified with the calculated vibrational level spacing of the binding $O_2^+(a\,^4\Pi_u)$ PEC. The exact numerical values, however, could not be explained [DMB+11]. Quantum simulations performed soon after that could resolve these issues in parts but discrepancies between the measured and simulated quantum-

[1] For convenience, PECs will be be identified by the electronic state they belong to, e.g. "[...] wave-packet oscillation on the $H_2^+(X\,^2\Sigma_g^+)$ PEC [...]", in the following.

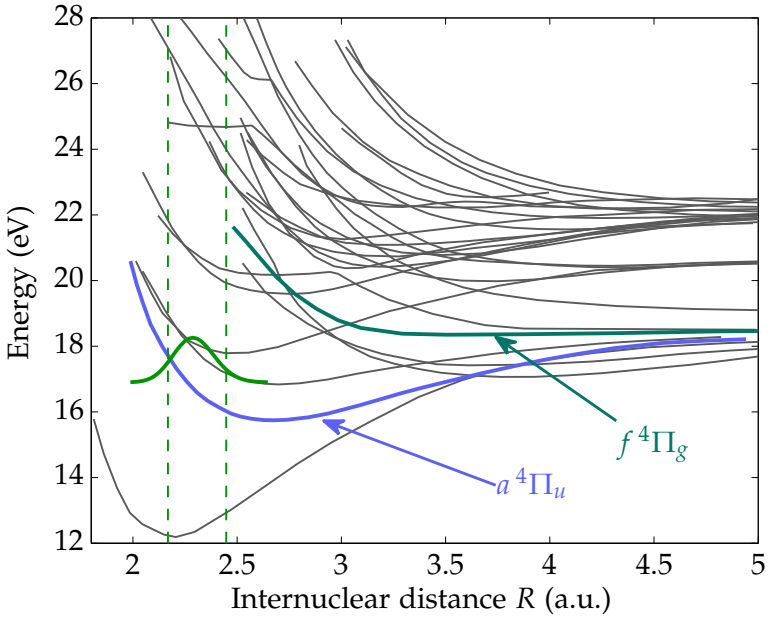

Fig. 5.1. Selection of O_2^+ PECs from Ref. [MMP+82]. Ionization to the $O_2^+(a\,^4\Pi_u)$ state creates a vibrational wave packet that oscillates within the corresponding PEC (blue curve) and can be probed to the $O_2^+(f\,^4\Pi_g)$ PEC (green curve). The vibrational ground-state wave function of the neutral O_2 ground state is given by the light green Gaussian curve. The Franck-Condon region is indicated by the dashed light green lines.

beat (QB) frequencies remain [MAT12]. In addition, the experimental kinetic-energy release (KER) spectra of O^+ showed distinct maxima in the O^+ yield which were not reproduced in simulated spectra.

In order to solve these issues, we repeated this experiment with an XUV–IR pump–probe setup. In this, the O_2 molecules are ionized by a single XUV photon. Thus the occupation of the vibrational states is described very well by the Franck-Condon principle whereas strong field ionization of molecules preferably populates low energetic vibrational states [UFSC+04]. In our experimental scheme the population is probed by a weak IR pulse to the repulsive $O_2^+(f\,^4\Pi_g)$ state. Because of its low peak intensity of about $3 \times 10^{12}\,\mathrm{W/cm^2}$ (compared to $3 \times 10^{14}\,\mathrm{W/cm^2}$ in the experiment described in Ref. [DMB+11]) the perturbation of the PECs is significantly reduced in our experiment. The very good agreement between our quantum simulations and the experimental data which will be shown in Sec. 5.3 is at least in parts due to the above mentioned advantages of an XUV–IR pump–probe technique.

5.2. Experimental spectra and vibrational wave-packet dynamics

The wave-packet oscillation discussed in the following sections as well as the kinematic properties of O^+ fragments and photoelectrons can be understood intuitively with the help of PECs. PECs of the O_2^+ molecular ion calculated in Ref. [MMP+82] are given in Fig. 5.1. The ground-state vibrational wave function of the neutral O_2 PEC (calculated in Ref. [BMR10]) is plotted as a light green curve and the FC region is indicated by light green vertical lines. In principle ionization by XUV photons with energies up to 40 eV can excite all ionic states plotted in Fig. 5.1. Thus bound O_2^+ and atomic O^+ fragments are created via a large number of competing reaction channels, although the ionization cross section to some of the states is rather low. The most important PECs for interpretation of the experimental results presented in this chapter is the binding $O_2^+(a\,^4\Pi_u)$ PEC (blue curve) within which the wave packet oscillates and the weakly repulsive $O_2^+(f\,^4\Pi_g)$ PEC (green curve) to which population is transferred in the probe step.

This section begins (Sec. 5.2.1) with a summary of the experimental parameters used during the measurement. Afterwards, in Sec. 5.2.2, pump–probe delay independent spectra are presented and reaction channels are identified. Pump–probe delay dependent spectra of the wave-packet motion are shown in Sec. 5.2.3 and a Morse potential is fitted to the experimental oscillation periods in Sec. 5.2.4. By Fourier transforming the experimental spectra, the vibrational states involved in the molecular dynamics are identified in Sec. 5.2.5. In Sec. 5.2.6 we will see that the influence of the strong IR field on the wave-packet oscillation period is negligible. Finally, in Sec. 5.2.7, the kinetic energy of photoelectrons detected in coincidence with low energetic O^+ ions

are presented. These spectra confirm the identification of the involved PECs.

5.2.1. Experimental parameters

The experimental data presented in this section has been recorded in a single experimental run beginning at 12:26pm on May 27th 2014 and ending 33 hours later at 09:34pm on May 28th 2014. The raw data was saved to the files:
`2014_05_27_03_XUV_IR_O2_2100fs_2200ct_G300V_[0001-1142].lmd`

The spectrometer was operated at an acceleration voltage of 300 V corresponding to an electric field of approximately 22.4 V cm^{-1}. At this field a 4π solid angle acceptance was guaranteed for O^+ with kinetic energies up to 4.6 eV [see Eq. (4.21)].

The IR average power was measured to be 125 mW behind the reaction microscope. At this power the IR intensity was just below the threshold for strong field ionization of O_2. Within the spatial overlap with the XUV beam, the effective IR intensity was estimated to be 3×10^{12} W/cm^2. The IR pulse length was estimated to be (12 ± 3) fs from an XUV-IR cross correlation (compare Sec. 3.2.5). The central wavelength of the IR pulse was 750 nm which corresponds to a photon energy of 1.65 eV. The total pump–probe delay range was 2120 fs.

5.2.2. Pump–probe delay independent spectra and identification of reaction channels

In the following, only pump–probe delay independent spectra are shown. These are used to identify the reaction channels involved in the ionization of O_2 by the broadband XUV pulse. Due to the large number of electronic states in molecular oxygen, this identification is not trivial.

The measured ion time-of-flight (ToF) spectrum integrated over the whole pump–probe delay range is shown in Fig. 5.2. The peaks in the ToF spectrum are assigned to particle species. Note that O_2^{++} and very low energetic O^+ feature similar ToFs due to their equal charge-to-mass ratio. The relevant reaction channels (for now ignoring the influence of the IR pulse) are given by

$$O_2 \xrightarrow{\text{XUV}} O_2^+ + e^- \tag{5.1}$$

$$O_2 \xrightarrow{\text{XUV}} O^+ + O + e^- \tag{5.2}$$

$$O_2 \xrightarrow{\text{XUV}} O_2^{++} + e^- + e^- \tag{5.3}$$

$$O_2 \xrightarrow{\text{XUV}} O^+ + O^+ + e^- + e^-. \tag{5.4}$$

Of those, the dominant channel is the ionization to stable O_2^+ [Eq. (5.1)]. Dissociative ionization of O_2 [Eq. (5.2)] has the second highest cross section and creates the majority of the counts in the O^+ ToF peak. The last two channels involve a double ionization process by a single XUV photon which has a reduced cross section compared to single

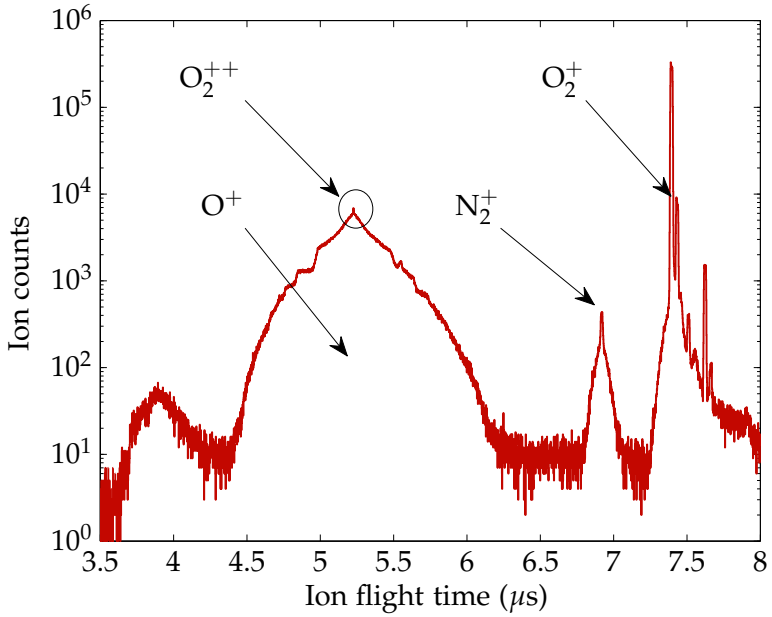

Fig. 5.2. Ion ToF spectrum obtained in the O_2 experiment. All relevant peaks are assigned to the corresponding particle species.

ionization. The double ionization is additionally suppressed by its high threshold of about 43 eV such that only the high energy tail of the harmonic spectrum can contribute to this process.

As introduced in Sec. 4.2, the initial 3-dimensional momenta of ions and electrons are reconstructed with the reaction microscope. From this the kinetic energy of the particles is calculated. In the dissociative ionization given by Eq. (5.2), the neutral O fragment cannot be detected. Its momentum can, however, be reconstructed from the O^+ momentum by exploiting momentum conservation. Since O^+ and O feature the same mass[2], they will have equal kinetic energies. This is used to determine the KER defined as

$$\mathrm{KER} = E^{\mathrm{kin}}_{\mathrm{O}^+} + E^{\mathrm{kin}}_{\mathrm{O}} = 2E^{\mathrm{kin}}_{\mathrm{O}^+}. \tag{5.5}$$

The KER spectrum associated with events within the O^+ and O_2^{++} ToF peak is plotted in Fig. 5.3(a). The KER of randomly aligned molecules is plotted as a red curve. The peaks at 1.6, 3.8, and 5.7 eV are known for many decades (compare Ref. [DSS68]). The one at 1.6 eV results from a predissociation out of the $B\,^2\Sigma_g^-$ PEC (see Fig. 5.4) to the $O^+(^4S) + O(^3P)$ continuum (see Fig. 5.4) [DSS68]. Predissiociation out of the $c^4\Sigma_u^-$ state (not plotted in Fig. 5.4) into the $O^+(^4S) + O(^3P)$ and $O^+(^4S) + O(^1D)$ dissociation continua (see Fig. 5.4) results in KERs of 3.8 and 5.7 eV respectively (compare Refs. [AMW+85, FRC85, CFR85, RVDL+85, LHC+98] and Refs. therein).

[2]The electron mass as well as the small recoil momentum induced by the electron can be neglected.

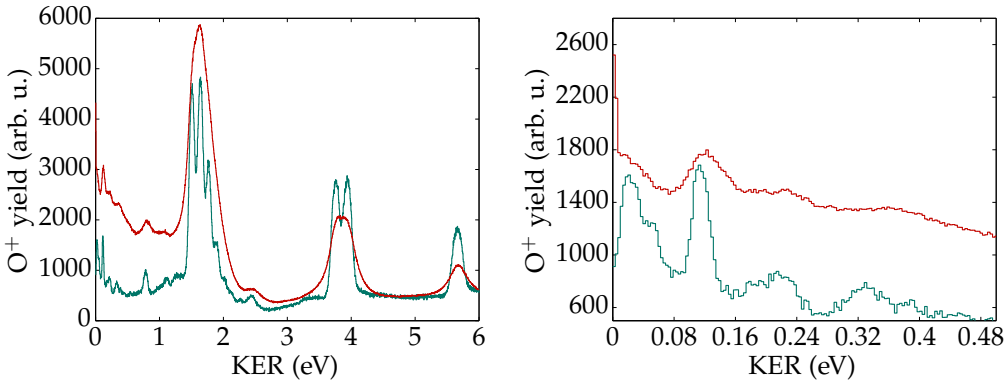

(a) O^+ KER whole range.

(b) O^+ KER low energy part.

Fig. 5.3. Experimental KER spectrum of O^+ ions. Red curve: The measured KER averaged over all molecular orientations. Green curve: The KER spectrum for molecules aligned parallel to the laser polarization. See text for identification of the peaks.

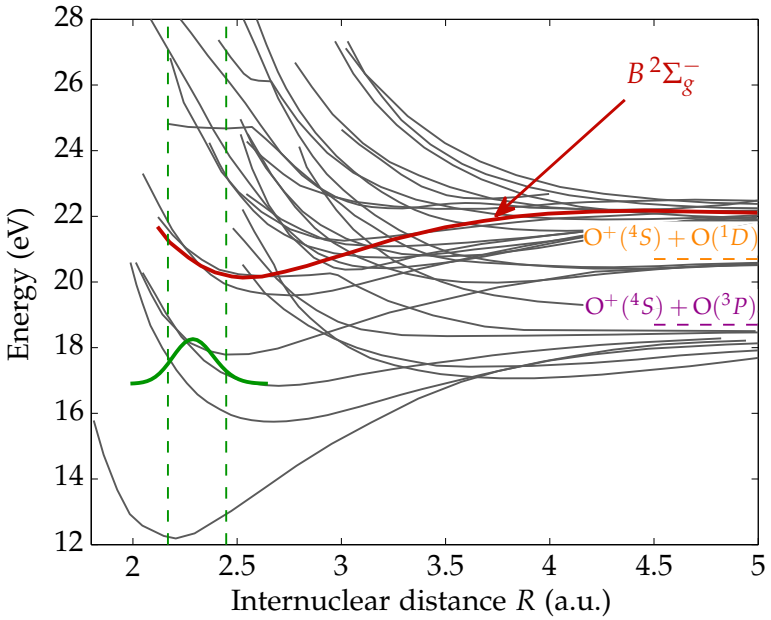

Fig. 5.4. O_2^+ PECs calculated in Ref. [MMP+82]. The $O_2^+(B\,^2\Sigma_g^-)$ PEC relevant for the experimentally observed predissociation is given as a red curve. Relevant dissociation continua are indicated by purple and orange colored dashed lines. The vibrational ground-state wave function of the neutral O_2 ground state is given by the light green Gaussian curve. The Franck-Condon region is indicated by the dashed light green lines.

The KER distribution of the O^+ fragments emitted under a small angle $\theta < 18°$ to the laser polarization is given by the green curve in Fig. 5.3. Since the momentum resolution is best in longitudinal direction (see Sec. 4.2.3), the vibrational levels of the $B\,^2\Sigma_g^-$ and the $c^4\Sigma_u^-$ states can be energetically resolved in the peaks at 1.6 and 3.8 eV respectively.

Figure 5.3(b) shows a magnified view of the low energy part of Fig. 5.3(a). The peak at very low KERs (smaller than 0.01 eV) is created by the detection of stable O_2^{++} dications. At KERs of 0.12, 0.22, and 0.33 eV another series of vibrational levels appears in the KER spectrum [best visible for the fragments emitted parallel to the laser polarization (green curve)]. This is due to the predissociation out of the $B\,^2\Sigma_g^-$ (red curve in Fig. 5.4) state into the $O^+(^4S) + O(^1D)$ continuum (see Fig. 5.4) which is possible for vibrational quantum numbers $v \geq 4$. The peak at 0.02 eV (only visible for KERs where molecular axis is aligned to the laser polarization) is created by the probing of the molecular wave packet as discussed in the following sections.

5.2.3. Wave-packet dynamics and pump–probe scheme

After having identified the dominant features in the pump–probe delay independent O^+ KER spectrum, the following sections focus on the O^+ yield as function of pump–probe delay and KER. The experimental data is shown in Fig. 5.5. In Fig. 5.5 (a), the experimentally observed O^+ ion counts (encoded in the color scale) are shown as a function of the KER and the pump–probe delay τ between the XUV and IR pulse. Experimental data for KER < 0.013 eV is not shown as the count rate of stable O_2^{++} (which has the same ToF as very low energetic O^+) dominates for these energies. For positive pump–probe delays, the XUV pulse precedes the IR pulse. The temporal overlap at $\tau = 0$ fs was determined from the sidebands measured in argon (compare Secs. 3.2.5 and 4.3.1). The variation of the O^+ yield is clearly visible for KER < 0.08 eV and is most pronounced around $\tau \approx 1270$ fs. The projection of the O^+ counts within the black frame onto the time delay axis is plotted in Fig. 5.5 (b).

The XUV–IR pump–probe scheme is given by the reaction (illustrated in Fig. 5.6)

$$O_2 \xrightarrow{\text{XUV}} O_2^+(a^4\Pi_u) + e^- \xrightarrow{\text{IR}} (O^+ + O)(f\,^4\Pi_g) + e^-. \tag{5.6}$$

Ionization by the XUV pulse prepares a vibrational wave packet in the $O_2^+(a^4\Pi_u)$ PEC. The experimentally observed oscillation in the O^+ yield with a period of $T_{\text{QB}} = 40$ fs is due to the oscillation of this wave packet which is probed resonantly by the IR pulse to the repulsive $O_2^+(f\,^4\Pi_g)$ PEC (as illustrated in Fig. 5.6). The pump–probe scheme and details of the spectra shown in Fig. 5.5 are discussed in more detail in the following.

According to the Franck-Condon principle, ionization to the the $O_2^+(a\,^4\Pi_u)$ electronic state by the XUV pulse excites multiple vibrational states in the corresponding PEC. These states feature different phase evolutions due to their different eigenenergies. As a result the superposition of these states leads to a time-dependent vibrational wave

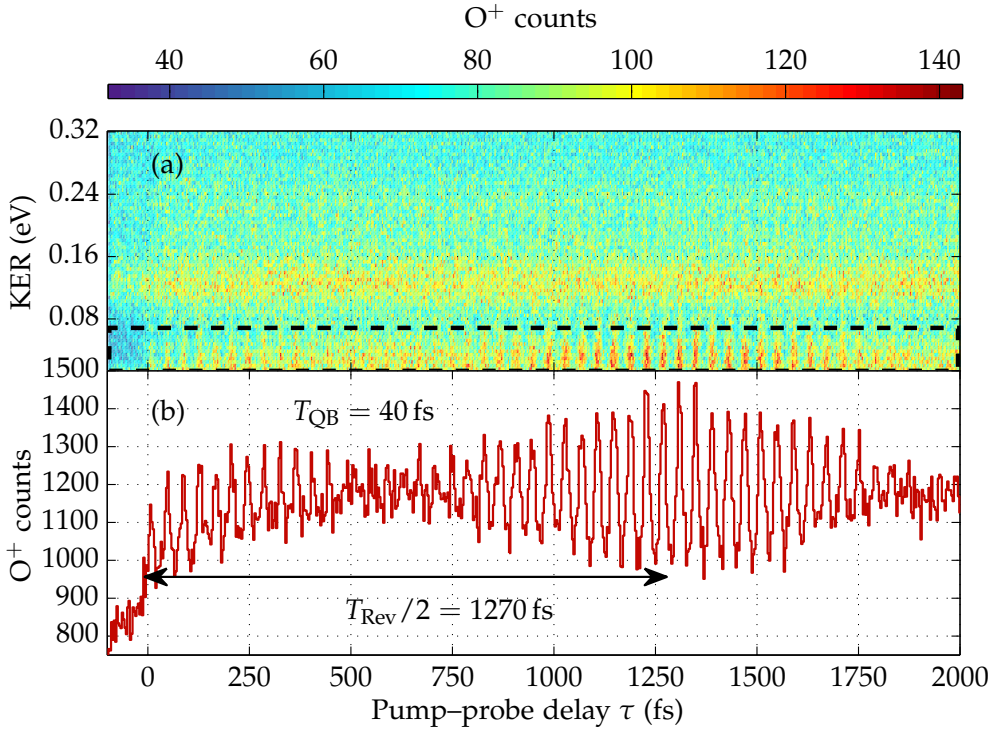

Fig. 5.5. Number of detected O^+ fragments as a function of the pump–probe delay τ and the KER. **Panel (b):** Projection of events within the dashed black box in panel (a) onto the time-delay axis. For positive delays, the XUV pulse precedes the IR pulse. The variation of the O^+ ion yield as function of τ with a period of $T_{QB} = 40\,\text{fs}$ is a signature of a nuclear wave-packet oscillation within the $O_2^+(a\,^4\Pi_u)$ PEC. Due to the anharmonicity of this potential, the oscillation amplitude decreases and reappears after $T_{Rev}/2 = 1270\,\text{fs}$.

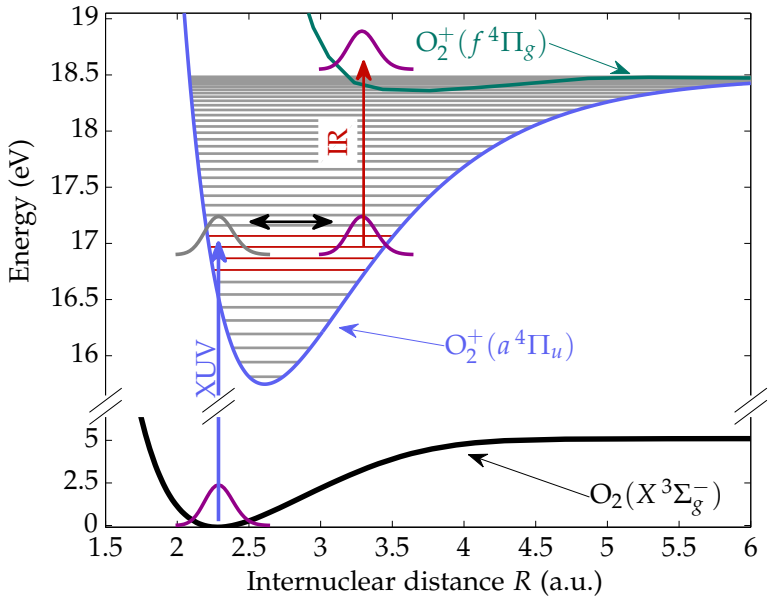

Fig. 5.6. XUV–IR pump–probe scheme. Population is transferred from the neutral electronic ground state ($X\,^3\Sigma_g^-$) (black curve) to the ionic $O_2^+(a\,^4\Pi_u)$ PEC (blue curve) by single photon ionization. For certain pump–probe delays, population is further elevated to the repulsive $O_2^+(f\,^4\Pi_g)$ PEC (green curve) by the IR probe pulse. In this case, the molecular ion will dissociate. Vibrational energies are plotted as gray horizontal lines. The nuclear wave packet observed in this work is created by excitation of the vibrational levels with quantum numbers $v = 8 \ldots 11$ (colored in red).

packet (see Sec. 2.4). This wave packet oscillates back and forth within the $O_2^+(a\,^4\Pi_u)$ PEC with a period T_{QB} that is inversely proportional to the level spacing of the excited vibrational states (see Sec. 2.4). After a variable pump–probe delay, the IR resonantly couples the $O_2^+(a\,^4\Pi_u)$ state to the repulsive $O_2^+(f\,^4\Pi_g)$ state. This coupling is most efficient at internuclear distances of $R_c \approx 3.2$ a.u. where the PECs are separated by approximately 1.65 eV, corresponding to the energy of a single IR photon. As a result only population of a small number of the excited vibrational states can actually be probed to the repulsive state. These vibrational levels are drawn as red horizontal lines in Fig. 5.6.

Since the IR pulse duration is shorter than the oscillation period, most population will be transfered to the repulsive state if the wave packet is localized at $R \approx R_c$. In this case, the molecule dissociates into a neutral O atom and an O^+ ion. The repulsive $O_2^+(f\,^4\Pi_g)$ PEC is almost flat for $R > R_c$ and thus the detected O^+ ions feature a low KER. If, on the other hand, the IR pulse interacts with the molecule at times when the wave packet is localized at $R \ll R_c$, no population is transfered to the repulsive state and the molecule does not break apart. These two cases illustrate the origin of the experimentally observed fast oscillation in the O^+ yield with a period of $T_{QB} = 40$ fs in Fig. 5.5.

The additional slow modulation of the oscillation amplitude is caused by the anharmonicity of the binding potential. The wave packet dephases due to the non-equidistant level spacing and is maximally delocalized at $\tau \approx 640$ fs. In this case the probe pulse can transfer population to the repulsive state independent of the pump–probe delay. After 640 fs the wave packet begins to rephase again and the pump–probe delay dependence increases again.

Surprisingly the oscillation amplitude within the half-revival at $T_{Rev}/2 = 1270$ fs is much larger than close to the temporal overlap of pump and probe pulse. This is in contrast to previous experiments on H_2 where the modulation within the revivals at increasingly larger time-delay was observed to be decreasing [FER+07]. A possible explanation for this interesting feature in our data might be an increased ionization cross section to the $O_2^+(a\,^4\Pi_u)$ state for perpendicular orientation between the molecular axis and the XUV polarization. For photon energies between 30 and 40 eV, where our XUV spectrum is most intense, this assumption is supported by quantum mechanical calculations in Ref. [LL02]. Due to dipole selection rules (see Sec. 2.2), the resonant probing process is only allowed for parallel transitions, where the molecule is oriented along the IR-pulse polarization direction. Thus, the molecular ion might require some time to align correctly to the probe field and the wave packet cannot be probed efficiently for very small pump–probe delays. This is further plausible since typical rotational periods of O_2 are (depending on the excited rotational states) of the order of hundreds of femtoseconds to a few picoseconds [CFS+15].

For negative pump–probe delays, the IR pulse precedes the XUV pulse. Due to its low intensity, the IR pulse has no measurable effect on the target as it cannot ionize the

oxygen molecule. Afterwards the trailing XUV pulse ionizes the target molecule. As a result no pump–probe delay dependence is expected for these time delays.

5.2.4. Adjusting a Morse potential to the experimental data

In the following, a Morse potential

$$V(R) = D_e \left(e^{-2a(R-R_0)} - 2e^{-a(R-R_0)} \right) \tag{5.7}$$

is adjusted to the experimentally observed oscillation period of $T_{\mathrm{QB}} = 40\,\mathrm{fs}$ and the half-revival time of $T_{\mathrm{Rev}}/2 = 1270\,\mathrm{fs}$. The parameter D_e tunes the depth of the potential, a determines its width and R_0 sets the equilibrium internuclear distance. The latter cannot be deduced from our data and is set to $R_0 = 2.61\,\mathrm{a.u.}$, as measured in a previous experiment [HH79]. The first two parameters are computed from T_{QB} and $T_{\mathrm{Rev}}/2$ using Eqs. (2.45) and (2.46) derived in Sec. 2.4.1:

$$\frac{2\pi}{T_{\mathrm{QB}}} = \left| a\sqrt{\frac{2D_e}{\mu}} - \frac{a^2}{\mu}\left(v_0 + \frac{1}{2}\right) \right| \tag{5.8}$$

$$\frac{2\pi}{T_{\mathrm{Rev}}} = \left| -\frac{a^2}{\mu} \right|. \tag{5.9}$$

Here, μ denotes the reduced mass of the oxygen ion and v_0 is the quantum number of the central vibrational level involved in the beating signature. The width of $a = 1.320\,\mathrm{a.u.}$ is directly determined from Eq. (5.9). However, v_0 is required for the calculation of the depth D_e from T_{QB} with Eq. (5.8). Without input from theory, it is impossible determine which vibrational levels contribute to the beating. Thus the adjusted Morse potential is plotted in Fig. 5.7 for different values of v_0 (red dashed PECs) and compared to theoretically predicted PECs from Refs. [MMP+82, MAT12]. For $v_0 = 9$ (red solid PEC), the depth is in best agreement with these PECs. In this case, D_e is calculated to $D_e = 0.1007\,\mathrm{a.u.}$ which is used in the following.

The Morse potential's shape (for $v_0 = 9$) is very similar to the two predicted PECs. Quantum simulations, however, will show that only the results obtained using the Morse potential reproduce all features of the experimental data (compare Sec. 5.3). This demonstrates the sensitivity of our experimental method onto the exact shape of the PEC.

5.2.5. Fourier transform and QB energies

In order to analyze the QB oscillation quantitatively it is convenient to change from the time-domain picture to the frequency domain by performing a Fourier transform. Since additionally the KER dependency of the oscillation shall be investigated, Fourier

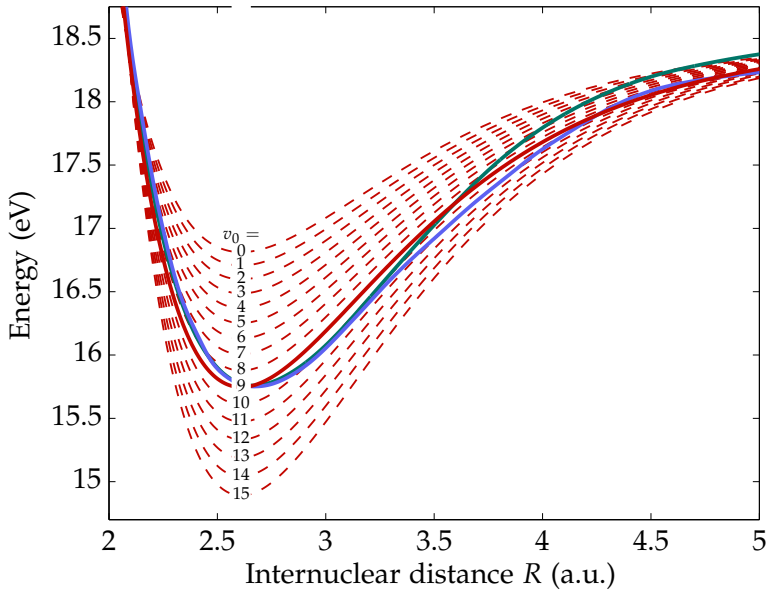

Fig. 5.7. Morse potentials adjusted to the experimentally observed QB period $T_{\mathrm{QB}} = 40\,\mathrm{fs}$ and half-revival time $T_{\mathrm{Rev}}/2 = 1270\,\mathrm{fs}$ for different parameters v_0 [see Eq. (5.8)] are plotted as dashed red curves. The potential minimum of $R_0 = 2.61\,\mathrm{a.u.}$ was determined in a previous experiment [HH79]. The depth of the Morse potential with $v_0 = 9$ (plotted as solid red curve) is in best agreement with the predicted $O_2^+(a\,^4\Pi_u)$ PECs from Refs. [MMP+82, MAT12] (plotted as blue and green curves, respectively).

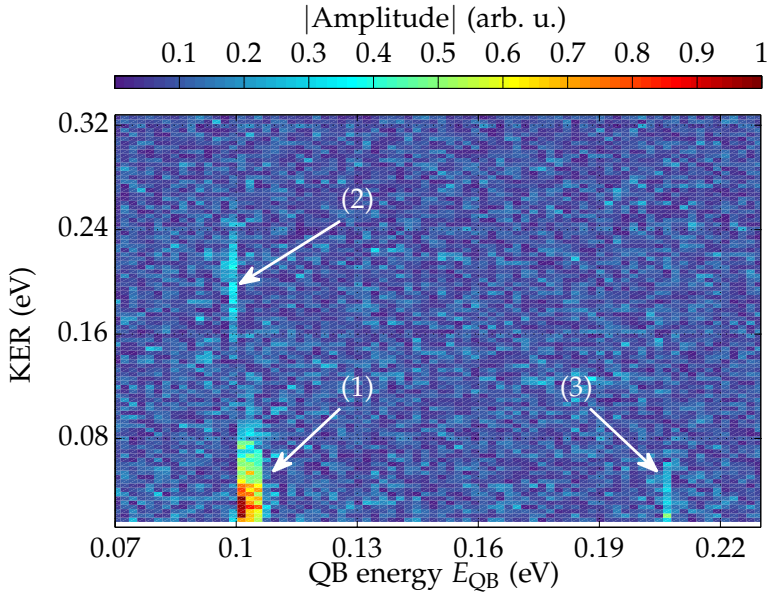

Fig. 5.8. QB spectrum of the data shown in Fig. 5.5 (a). The absolute value $|A(E_{QB}, KER)|$ of the Fourier amplitude (color scale) is plotted as function of KER and QB energy E_{QB}. The signals (1), (2), and (3) are discussed in the text.

transforms of the O^+ count rate $N_{O^+}(\tau, KER)$ are performed at fixed KER over the time interval $[0, 2\,ps]$. This results in a complex amplitude

$$A(E_{QB}, KER) = FT\{N_{O^+}(\tau, KER)\}. \tag{5.10}$$

Here the QB energy E_{QB} is related to the frequency ω_{QB} by $E_{QB} = \hbar\omega_{QB}$ and ω_{QB} is the Fourier complementary variable of the pump–probe delay τ.

$A(E_{QB}, KER)$ is a complex number and thus can be expressed as

$$A(E_{QB}, KER) = |A(E_{QB}, KER)|e^{i\phi_A(E_{QB}, KER)}. \tag{5.11}$$

$|A(E_{QB}, KER)|$ is a measurement for the intensity of a certain frequency component. Dynamical information about the dissociation process is encoded within the phase $\phi_A(E_{QB}, KER)$ [FGC+14], [Fis15, p. 114]. The energy resolution of this Fourier transform method is fundamentally limited by the sampling time $T_{sampl} = 2\,ps$ and is given by

$$\triangle E_{QB} = \hbar\frac{2\pi}{T_{sampl}} = 2 \times 10^{-3}\,eV. \tag{5.12}$$

$|A(E_{QB}, KER)|$ obtained from the experimental data is plotted in Fig. 5.8. In total three different signals are visible. Their origin is explained in the following:

- Signal (1): This signal corresponds to the visible oscillation in the time domain (compare Fig. 5.5) and is created by the beating between neighboring vibrational

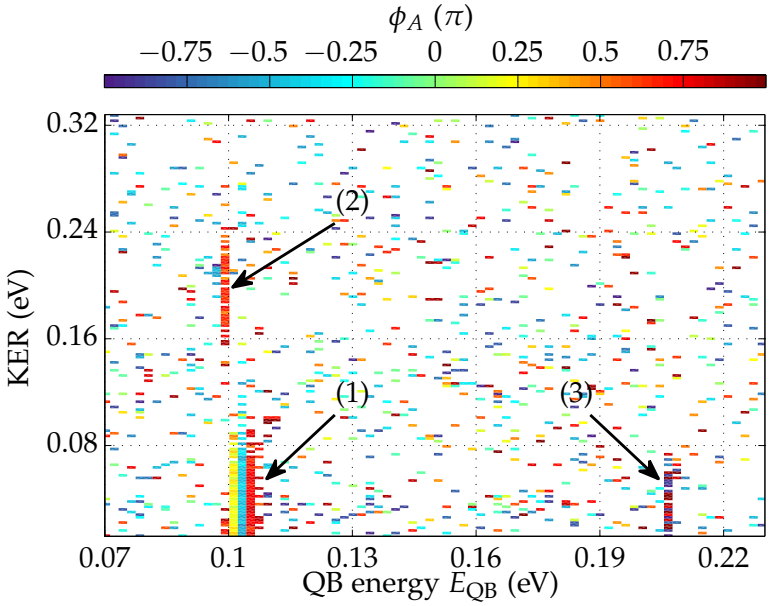

Fig. 5.9. The Fourier amplitude's phase value $\phi_A(E_{QB}, \mathrm{KER})$ (color scale) is plotted as function of KER and QB energy E_{QB}. In order to reduce the background, only parts of the signal where the absolute value $|A(E_{QB}, \mathrm{KER})|$ is larger than 20 % of the maximum value are plotted. The phase is independent of the KER for all signals.

states. The quantum-beat (QB) energy E_{QB} is in good agreement with the expected vibrational level spacings $E_{v=10} - E_{v=9} = 0.103\,\mathrm{eV}$ and $E_{v=9} - E_{v=8} = 0.106\,\mathrm{eV}$ of the $O_2^+(a\,^4\Pi_u)$ PEC calculated in Ref. [MAT12]. Experimentally these two energies are not resolved because the pump–probe delay range of 2 ps is to short to allow their separation in the energy domain. Quantum simulations show that a delay range of 4 ps would be sufficient to resolve these lines. The QB energies measured are significantly lower than those reported in an earlier IR–IR experiment [DMB+11] and in much better agreement with theory.

- Signal (2): This weak signal is created by the beating between the higher lying vibrational states (most likely with quantum numbers $v = 10$ and $v = 11$). It features a slightly lower QB energy compared to signal (1). This is due to a smaller vibrational spacing.

- Signal (3): Another weak signal at $E_{QB} \approx 0.207\,\mathrm{eV}$ is caused by the beating between vibrational states with $\triangle v = 2$ (most likely $v = 10$ and $v = 8$).

The Fourier phase $\phi_A(E_{QB}, \mathrm{KER})$ [introduced in Eq. (5.11)] is plotted in Fig. 5.9. A phase ϕ_A varying with the KER indicates that the fragment's kinetic energy depends on the relative phase between the intensity envelope of the laser pulse and the wave-packet oscillation. It has been shown previously, that in this case the time delay between XUV

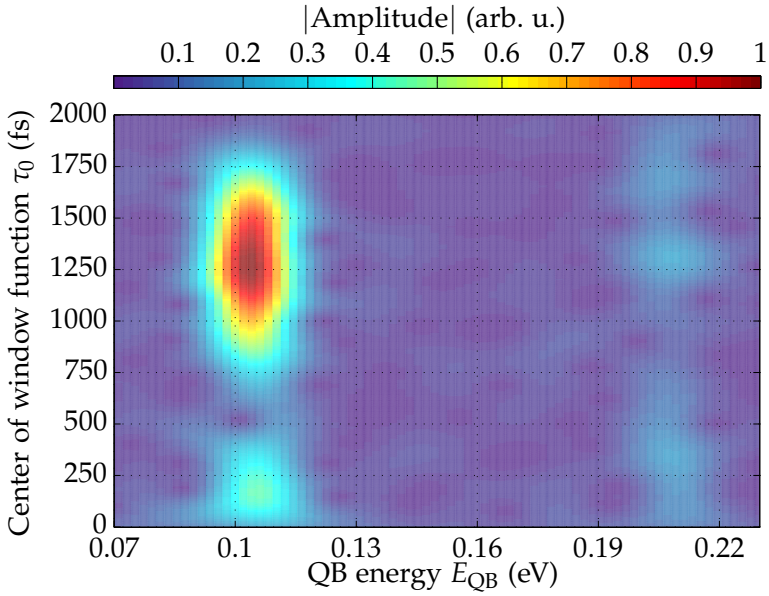

Fig. 5.10. Sliding window Fourier transform of the experimental signal from Fig. 5.5 (b). The width of the Gaussian window function is 200 fs (FWHM). The QB energy is independent of the window function's position.

and IR pulse can be used to control the KER of H^+ fragments by field-dressing the PEC during the dissociation process [FGC+14]. In the experiments presented here, the IR intensity is lower and the dressing of the PECs is negligible[3]. As a result, no KER dependence of the phase ϕ_A is observed within each of the lines shown in Fig. 5.9.

It is often discussed whether or not the IR probe-pulse influences the measured QB energy of the wave-packet dynamics. While there is no debate that the vibrational levels are shifted in the field-dressed PESs, it is often ignored that no field dressing is present until the IR pulse interacts with the molecule. In this work, this translates into a field-free evolution of the wave packet for up to 2 ps and an evolution in the dressed potential for about 10 fs. The ratio between the field free evolution and the evolution in the dressed potential is smaller for small pump–probe delays. In the limit of the temporal overlap, the molecular ion "lives" for most of the time within the IR field. As a result, the influence of the IR field on the measured QB energy can be tested by calculating E_{QB} for different pump–probe delays using a so-called *short-time Fourier transform*.

For this, the time-dependent O^+ yield plotted in Fig. 5.5 (b) is multiplied with a Gaussian window function with a width (FWHM) of 200 fs and center τ_0. The product is Fourier transformed and the absolute value of the amplitude is encoded in the color

[3]The smaller dipole coupling amplitude (see Fig. 5.15) between the relevant O_2^+ states compared to the H_2^+ states further reduces the field dressing.

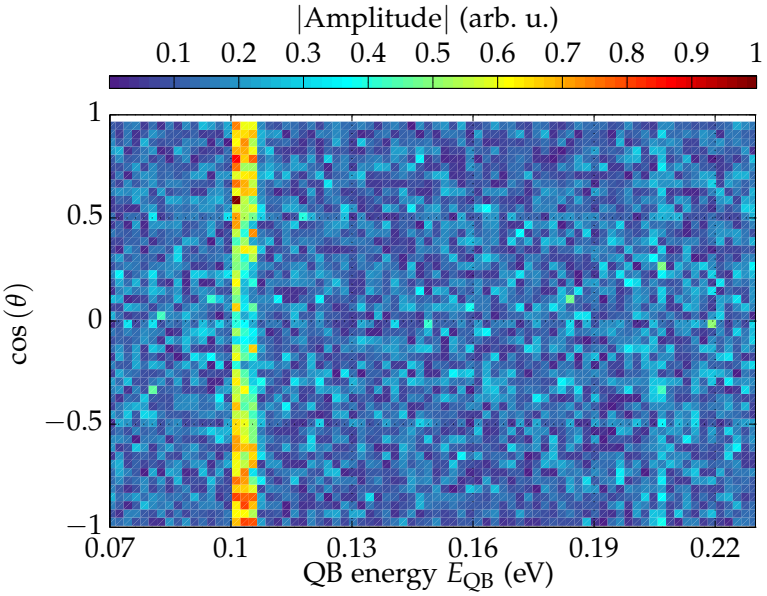

Fig. 5.11. QB spectrum of the delay-dependent yield of low energetic O^+ ions with KER smaller 0.08 eV as a function of $\cos(\theta)$. The angle θ designates the orientation of the molecular axis relative to the identical linear polarization directions of the XUV and IR pulses. The QB energy is independent of θ. The signal is strongest if molecular axis and laser polarization are aligned.

scale and plotted as a function of the QB energy (x-axis) and τ_0 (y-axis). This calculation is repeated while sliding the center t_0 of the Gaussian window along the pump–probe delay axis.

The result is shown in Fig. 5.10. Due to the Gaussian window function, the effective sampling time for the Fourier transform is smaller and thus the energy resolution is reduced to $\triangle E_{QB} = 2 \times 10^{-2}$ eV [see Eq. (5.12)]. Nevertheless, no dependence of the QB energy on the pump–probe delay is observed. The conclusion that for our pulse parameters field-dressing of the PEC does not influence the QB energy significantly will be further confirmed in the next section and by simulations in Sec. 5.4.2.

5.2.6. Angular dependence of the time-dependent O^+ yield

The $O_2^+(a\,^4\Pi_u)$ and $O_2^+(f\,^4\Pi_g)$ states can only be coupled by the field component parallel to the molecular axis due to dipole selection rules. Thus, if a molecule is not aligned parallel to the laser polarization, the effective field strength is reduced according to Eq. (2.28). As a result, the coupling between (and the perturbation of) the electronic states depends on the angle θ between IR laser polarization and the molecular axis. With the reaction microscope, the latter can be reconstructed for each fragmentation from the momentum vector of the O^+ ion.

A Fourier transform of the O^+ yield with KER $< 0.08\,\text{eV}$ as a function of the pump–probe delay and $\cos(\theta)$ is plotted in Fig. 5.11. The values $\cos(\theta) = \pm 1$ and $\cos(\theta) = 0$ correspond to molecules aligned along and perpendicular to the laser polarization, respectively [CFS+15][4]. The signal strength clearly depends on $\cos(\theta)$. This is expected since the probing is most efficient for parallel alignment of molecular axis and laser polarization. The QB energy on the other hand, does not depend on $\cos(\theta)$. This is a further indication for the independence of the measured QB energy on the IR intensity.

5.2.7. Photoelectron spectra

So far only ionic fragments have been discussed. Using the reaction microscope, we are able to detect photoelectrons as well. The QB spectrum of the photoelectrons detected in coincidence with O^+ ions with a KER between 0.013 and 0.08 eV – the KER region in which the oscillation is most pronounced – is plotted in Fig. 5.12 (a). This spectrum is used in the following to further confirm that the PECs involved in the nuclear motion have been identified correctly (compare for example Refs. [CLD+11, GRT+07] for a similar approach). As in the ion spectra, a clear signal is visible at $E_{\text{QB}} \approx 0.1\,\text{eV}$. The red bold curve in Fig. 5.12 (b) shows a projection of events belonging to this signal onto the E^e axis. This electron spectrum therefore corresponds to photoelectrons created by ionization to the $O_2^+(a\,^4\Pi_u)$ state.

In addition, the energy spectrum of electrons measured in coincidence with O^+ ions with KERs between 0.10 and 0.14 eV is given in Fig. 5.12 (b) (green bold curve). The O^+ yield in this KER interval is pump–probe delay independent and so is the corresponding photoelectron spectrum.

In the following paragraph the origin of this time-independent spectrum is discussed in more detail. Afterwards the envelope of the time-dependent spectrum [red thin curve in Fig. 5.12 (b)] is compared to the envelope of the background signal [green thin curve in Fig. 5.12 (b)].

Pump–probe delay independent photoelectron spectrum The channel discussed in the following is illustrated in Fig. 5.13 (green color). The peaks in the time-delay independent electron signal are separated by 3.2 eV which is the odd-harmonic spacing of the XUV spectrum ($\triangle E_{\text{HHG}} = 2\hbar\omega_{\text{IR}}$). The fact that the harmonic spectrum is clearly imprinted onto the electron energies is an indication that all PECs significantly contributing to this channel feature the same dissociation limit E_1^{diss}, since the electron energy E^e is given by

$$E_1^e = \hbar\omega_{\text{XUV}} - \text{KER} - E_1^{\text{diss}} \approx \hbar\omega_{\text{XUV}} - E_1^{\text{diss}}. \tag{5.13}$$

[4] Plotting as function of $\cos(\theta)$ instead of θ is convenient since this automatically features the solid angle correction of the experimental data.

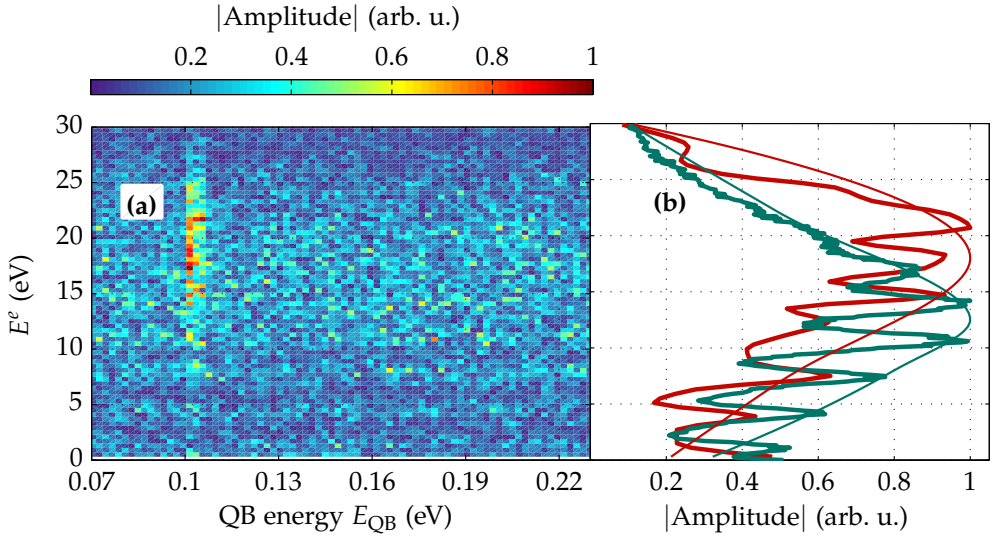

Fig. 5.12. Panel (a): QB spectrum of photoelectrons measured in coincidence with low energetic O^+ (KER interval between 0.013 and 0.08 eV). Plotted is the Fourier amplitude as a function of the QB energy and the photoelectron kinetic energy E_e. **Panel (b):** Red bold curve: Projection of the QB signal at $E_{QB} \approx 0.1$ eV shown in panel (a) onto the E_e axis. Green bold curve: Pump–probe delay independent background spectrum of electrons detected in coincidence with O^+ in a KER interval from 0.10 to 0.14 eV. For better comparison, the curves in panel (b) are smoothed and normalized. In addition schematic envelopes of the spectra are shown (thin red and green curve).

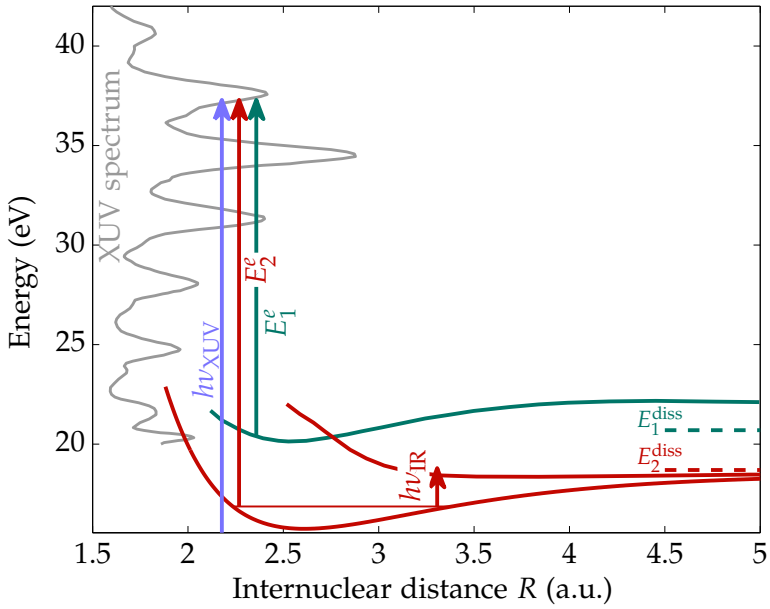

Fig. 5.13. Processes leading to the photoelectron spectra plotted in Fig. 5.12 (b). A spectrum of the XUV pulses generated in our experiment (data from Ref. [Sch15, p. 95]) is given as a gray inlay. Photoelectrons with kinetic energy E_2^e are created by ionization to the $a\,^4\Pi_u$ PEC (red PEC) and are associated with the observed wave-packet oscillation. Their energy distribution is given by the red spectrum in Fig. 5.12 (b). Photoelectrons with kinetic energy E_1^e created by ionization into the $B\,^2\Sigma_g^-$ state (green PEC) cause the time-independent signal in Fig. 5.12 (b) (green spectrum). Due to the lower ionization potential, photoelectrons associated with the wave-packet oscillation feature a higher kinetic energy than those created in ionization into the $B\,^2\Sigma_g^-$ state.

Since the KERs of the coincident O^+ ions (between 0.1 and 0.14 eV) are small compared to E^e, they can be neglected. As discussed in Sec. 5.2.2, the low-energetic, time-delay independent ion yield at KER $\approx$ 0.12 eV is caused by the predissociation of the $O_2^+(B\,^2\Sigma_g^-)$ state (green PEC in Fig. 5.13). It is therefore assumed that the time-delay independent spectrum [green bold curve Fig. 5.12 (b)] of electron measured in coincidence with ions of such a KER results from the ionization to this state. The $B\,^2\Sigma_g^-$ state predissociates into the $O^+(^4S^0) + O(^1D)$ continuum with dissociation energy $E_1^{\mathrm{diss}} = 20.7$ eV (compare Fig. 5.13).

Pump–probe delay dependent photoelectron spectrum The channel discussed in the following is illustrated in Fig. 5.13 (red color). The time-dependent electron spectrum [red bold curve in Fig. 5.12 (b)] results from the ionization to the $O_2^+(a\,^4\Pi_u)$ state and subsequent absorption of an additional IR photon. In this reaction, the molecule dissociates into the $O^+(^4S^0) + O(^3P)$ continuum with $E_2^{\mathrm{diss}} = 18.7$ eV (compare Fig. 5.13).

Thus the electron energy is given by

$$E_2^e = \hbar\omega_{\mathrm{XUV}} + \hbar\omega_{\mathrm{IR}} - \mathrm{KER} - E_2^{\mathrm{diss}} \approx \hbar\omega_{\mathrm{XUV}} + \hbar\omega_{\mathrm{IR}} - E_2^{\mathrm{diss}}. \tag{5.14}$$

As before, the KERs are negligible.

Comparing Eq. (5.13) and Eq. (5.14), a relative shift of the envelopes of the photo-electron spectra by

$$E_1^{\mathrm{diss}} - (E_2^{\mathrm{diss}} - \hbar\omega_{\mathrm{IR}}) \approx 3.7\,\mathrm{eV}. \tag{5.15}$$

is expected in Fig. 5.12 (b). The predicted shift is in qualitative agreement with the relative offset between the envelopes in Fig. 5.12 (b). This is a further indication that the PECs involved in the wave-packet dynamics have been identified correctly. The above argument is only valid because the photo-ionization cross sections to the $O_2^+(B\,^2\Sigma_g^-)$ and the $O_2^+(a\,^4\Pi_u)$ states are calculated to be almost constant for photon energies between 30 and 40 eV [LL02].

Additionally the electron spectrum can be used to exclude a second reaction pathway, namely

$$O_2 \xrightarrow{\mathrm{XUV}} O_2^* \xrightarrow{\mathrm{IR}} O^+ + O + e^-. \tag{5.16}$$

In this, the XUV pulse resonantly excites the molecule and the wave packet oscillates in the PEC corresponding to a neutral state. In this process strong-field ionization takes place in the probe step and a low energetic electron is emitted. ATI peaks created by multi-photon ionization are separated by 1.6 eV and their intensity typically decreases with increasing photon numbers (see Sec. 2.3.2). This process cannot be excluded experimentally if only ion spectra are considered.

The electron-energy spectrum plotted as a red curve in Fig. 5.12 (b) excludes this process for two reasons: first the electron yield increases with increasing E_e. Second the maxima in the electron yield are separated by ≈ 3.2 eV. Both features are signatures of ionization by a single, highly-energetic photon created in HHG [CFS+15].

5.3. Comparison between experimental data and simulated spectra

Having identified the electronic states involved in the wave-packet dynamics, we compare the experimental data with results of quantum simulations in this section. This enables us to test PECs predicted in Ref. [MMP+82] and in Ref. [MAT12]. These are shown in Fig. 5.14. In addition the Morse potential adjusted to the experimental data is plotted in the same figure.

In the following, the coupled-channel calculation introduced in Sec. 2.5.2 is used to simulate the wave-packet dynamics and the probing process (for the used method see

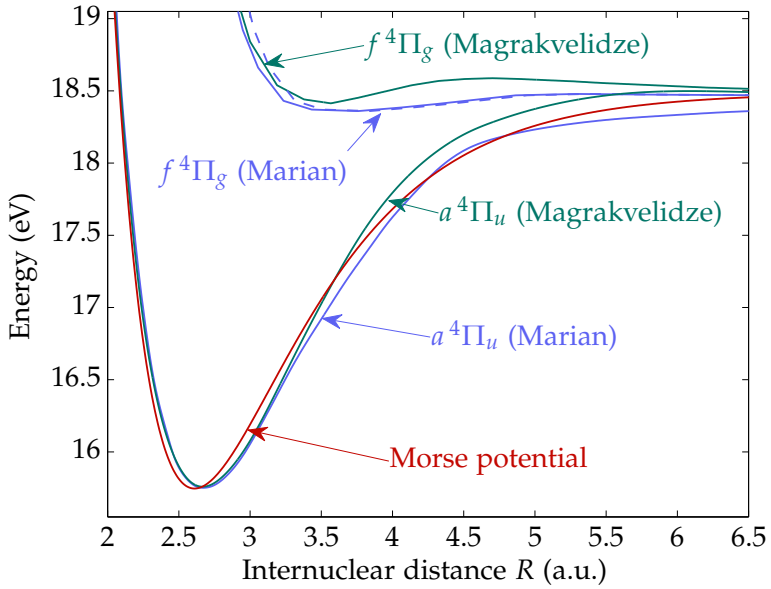

Fig. 5.14. Calculated binding $O_2^+(a\,^4\Pi_u)$ and repulsive $O_2^+(f\,^4\Pi_g)$ PECs calculated in Ref. [MAT12] (green curves) and in Ref. [MMP+82] (blue curves). The Morse potential adjusted to our experimental data is plotted in red.

for example Ref. [DMB+11, MAT12, MHJ+12, LNDD+13]). The code used in these calculations was developed by A. Fischer [Fis15]. The Schrödinger equation underlying the coupled-channel simulation is given by

$$i\frac{d}{dt}\begin{pmatrix}\psi_g(R,t)\\ \psi_u(R,t)\end{pmatrix} = \begin{pmatrix}-p^2/(2\mu)+V_g & -\langle\phi_g|\,z\,|\phi_u\rangle\,\mathcal{E}(t)\\ -\langle\phi_u|\,z\,|\phi_g\rangle\,\mathcal{E}(t) & -p^2/(2\mu)+V_u\end{pmatrix}\begin{pmatrix}\psi_g(R,t)\\ \psi_u(R,t)\end{pmatrix}. \tag{5.17}$$

In this, the indexes u, and g are identified with the eletronic states $O_2^+(a\,^4\Pi_u)$, and $O_2^+(f\,^4\Pi_g)$, respectively. The molecule is described in the Born-Oppenheimer approximation and the PECs are given by V. The electronic wave functions are denoted by ϕ, and the nuclear wave functions are labeled with ψ. The dipole matrix element $\langle O_2^+(f\,^4\Pi_g)|\,z\,|O_2^+(a\,^4\Pi_u)\rangle$ computed in Ref. [MAT12] (shown in Fig. 5.15) is used in our calculations.

The diagonal terms in the coupling matrix describe the propagation of the nuclear wave packet on the $O_2^+(a\,^4\Pi_u)$ and $O_2^+(f\,^4\Pi_g)$ PECs. In the absence of a laser field $\mathcal{E}(t)$ the propagation on the two PECs is decoupled. If, however, an electric field $\mathcal{E}(t)$ is present, the electronic states are coupled and population can be transferred from one PEC to the other.

In the following sections (Secs. 5.3.1 and 5.3.2) the results of our simulation for six different pairs of binding and repulsive PECs are presented and compared to the experiment. These combinations are illustrated in Fig. 5.16. The PECs calculated by Magrakvelidze et al. [MAT12] are plotted as green curves in Fig. 5.14 and those

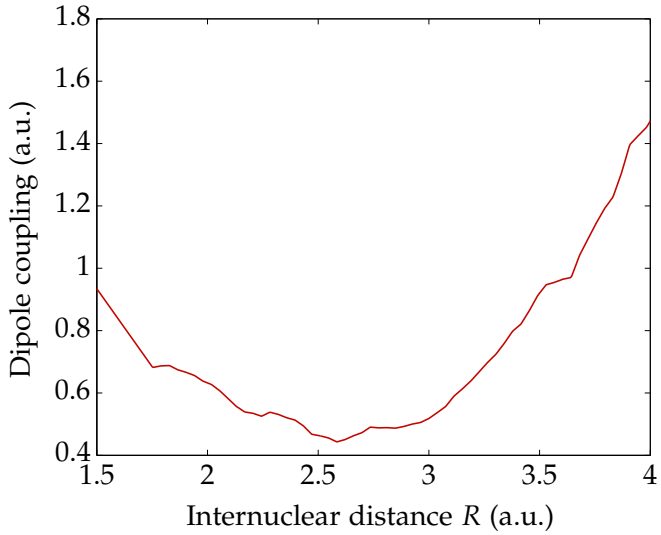

Fig. 5.15. Dipole coupling $\langle O_2^+(f\,^4\Pi_g)|\,z\,|O_2^+(a\,^4\Pi_u)\rangle$ used in the coupled-channel simulation. Data from Ref. [MAT12].

		Binding Potential		
		Marian [MMP+82]	Magrakvelidze [MAT12]	Morse
Repulsive potential	Marian [MMP+82]	Sec. 5.3.1	Sec. 5.3.1	Sec. 5.3.1
	Magrakvelidze [MAT12]	Sec. 5.3.2	Sec. 5.3.2	Sec. 5.3.2

Fig. 5.16. Combinations of PECs used in our simulations. The colors of the labels correspond to the colors of the PECs in Fig. 5.14.

Photon energy	Pulse length (intensity FWHM)	Peak intensity
1.65 eV	12 fs	3×10^{12} W/cm^2

Tab. 5.1. IR pulse parameters used for all simulations discussed in Sec. 5.3.

predicted by MARIAN ET AL. [MMP+82] are plotted as blue curves in Fig. 5.14. As the simulated results using these curves show some discrepancies to the experimental data, we additionally propagate the wave packet on the Morse potential (red curve in Fig. 5.14) adjusted to the experimental data (as described in in Sec. 5.2.4).

In all simulations presented throughout this section, the initial occupation of the vibrational states within the binding $O_2^+(a\,^4\Pi_u)$ PEC is determined from the Franck-Condon overlap with the vibrational ground-state wave function of the neutral O_2 molecule. For the calculation of this wave function, the PEC from Ref. [BMR10] is used (shown in Fig. 5.6).

The IR pulse parameters used for all simulations discussed throughout this section are summarized in Tab. 5.1 and match the parameters in our experiment.

5.3.1. Using the repulsive PEC from MARIAN ET AL. [MMP+82]

Panels	Binding PEC	Repulsive PEC	Shift (a.u.)
(a)	Exp. data	Exp. data	
(b)	Morse	[MMP+82]	0.08 (dashed curve)
(c)	[MMP+82]	[MMP+82]	0.00 (solid curve)
(d)	[MAT12]	[MMP+82]	0.08 (dashed curve)

Tab. 5.2. Input PECs for the coupled-channel simulations in Sec. 5.3.1. (a), (b), (c) and (d) refers to panels in Figs. 5.17 to 5.19. The last column denotes whether or not the a shifted version of the repulsive PEC has been used. All PECs are plotted in Fig. 5.14.

The simulated results presented in this section have been obtained by using the repulsive $O_2^+(f\,^4\Pi_g)$ PEC calculated by MARIAN ET AL. [MMP+82] (see Fig. 5.14). For certain binding PECs, the simulated spectra are in better agreement with experiment if this repulsive curve is shifted by 0.08 a.u. towards larger internuclear distances. This shifted PEC is displayed in Fig. 5.14 as a dashed blue curve. The used combinations of PECs are summarized in Tab. 5.2. The simulated spectra in the panels (b), (c) and (d) of Figs. 5.17 to 5.19 are discussed in the following.

Morse potential [panels (b)] If the coupled-channel simulation is performed using the Morse potential and the repulsive curve calculated in Ref. [MMP+82], the sim-

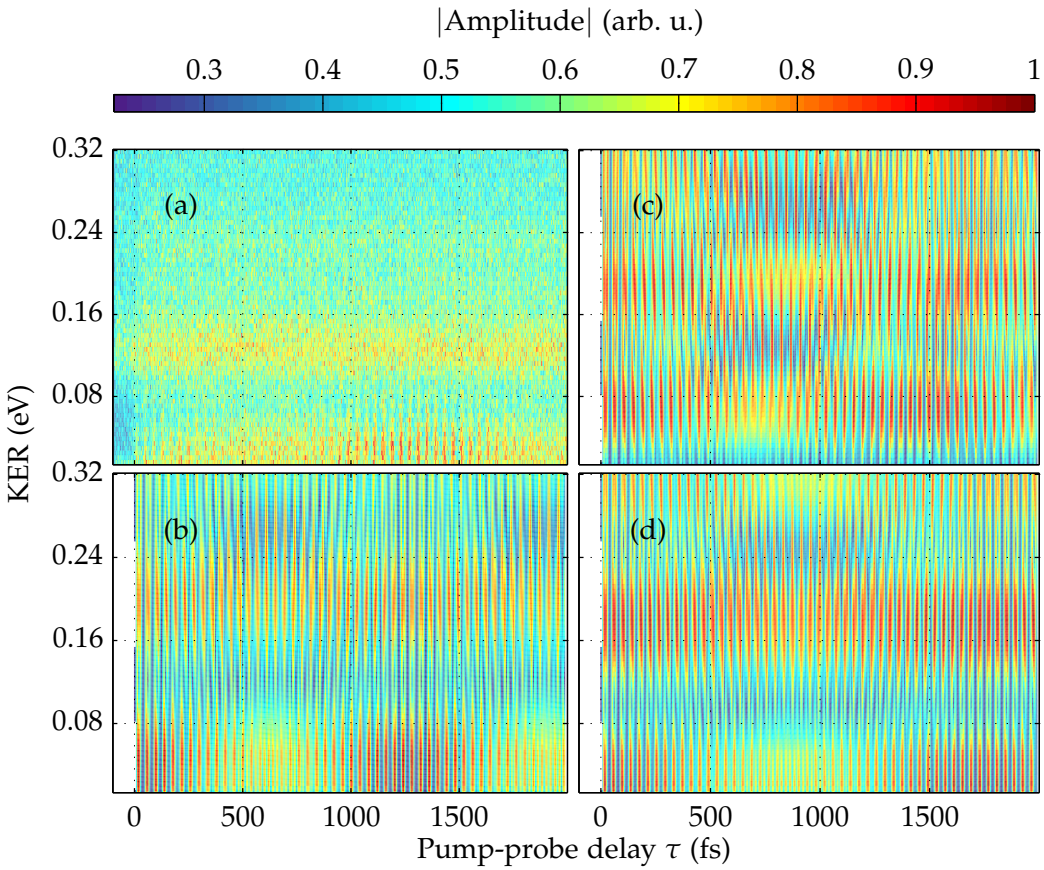

Fig. 5.17. Simulated and experimental yield of O^+ fragments as a function of the pump–probe delay and the KER. All calculations are performed with the pulse parameters listed in Tab. 5.1 and either the repulsive PEC from Ref. [MMP+82] or its shifted version (see Tab. 5.2). **Panel (a):** Experimental spectrum. **Panel (b):** Simulation using the Morse potential. **Panel (c):** Simulation using the binding PEC calculated by Marian et al. [MMP+82]. **Panel (d):** Simulation using the binding PEC calculated by Magrakvelidze et al. [MAT12].

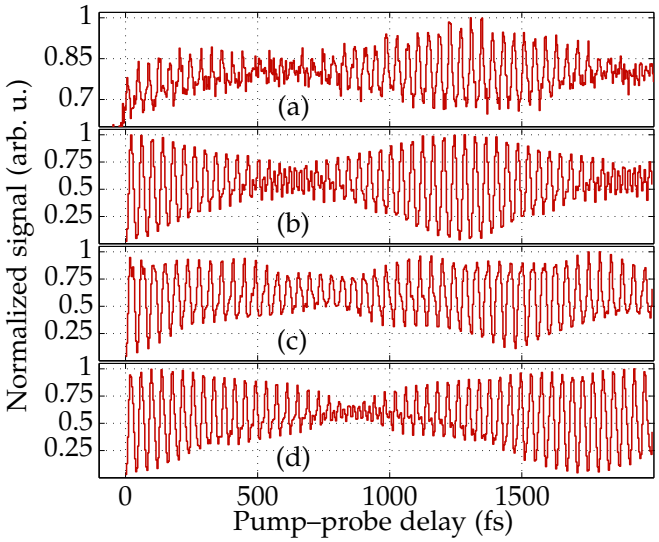

Fig. 5.18. Projections of the lower KER bands in Fig. 5.17. **Panel (a):** Experimental spectrum. **Panel (b):** Simulation using the Morse potential. **Panel (c):** Simulation using the binding PEC calculated by Marian et al. [MMP+82]. **Panel (d):** Simulation using the binding PEC calculated by Magrakvelidze et al. [MAT12].

ulated KER spectrum is shifted by about 50 meV towards lower KERs compared to the experimental data [CFS+15]. By treating the position of the repulsive PEC as a free parameter, it was found that the agreement with the experimental spectra is best, if the repulsive potential is shifted by 0.08 a.u. towards larger internuclear distances. This modified PEC is plotted as a dashed blue curve in Fig. 5.14 and was used for the simulation with the Morse potential. The results of the coupled-channel simulation are given in Fig. 5.17 (b). While in the experimental data, the O^+ yield-oscillation in the time domain is only visible for small KERs, an additional oscillation at KER $\approx$ 0.2 eV is present in the simulated spectrum.

A projection of the lower KER band (KER $<$ 0.08 eV) is plotted in Fig. 5.18 (b). The agreement between the experimental and simulated half-revival time is excellent. This is expected, since the Morse potential was adjusted to the experimentally observed half-revival time (as described in Sec. 5.2.4).

The simulated QB spectrum is shown in Fig. 5.19 (b). The position of the experimentally observed QB signals are indicated by white boxes. The agreement between theory and experiment is very good near the dominant QB energies ($E_{QB} \approx 0.1$ eV). For the large QB energies ($E_{QB} \approx 0.2$ eV), the experimental KER distribution is not reproduced. The relative intensities of the Fourier signals are not reproduced very well either. Possible reasons for this are discussed in Sec. 5.4.

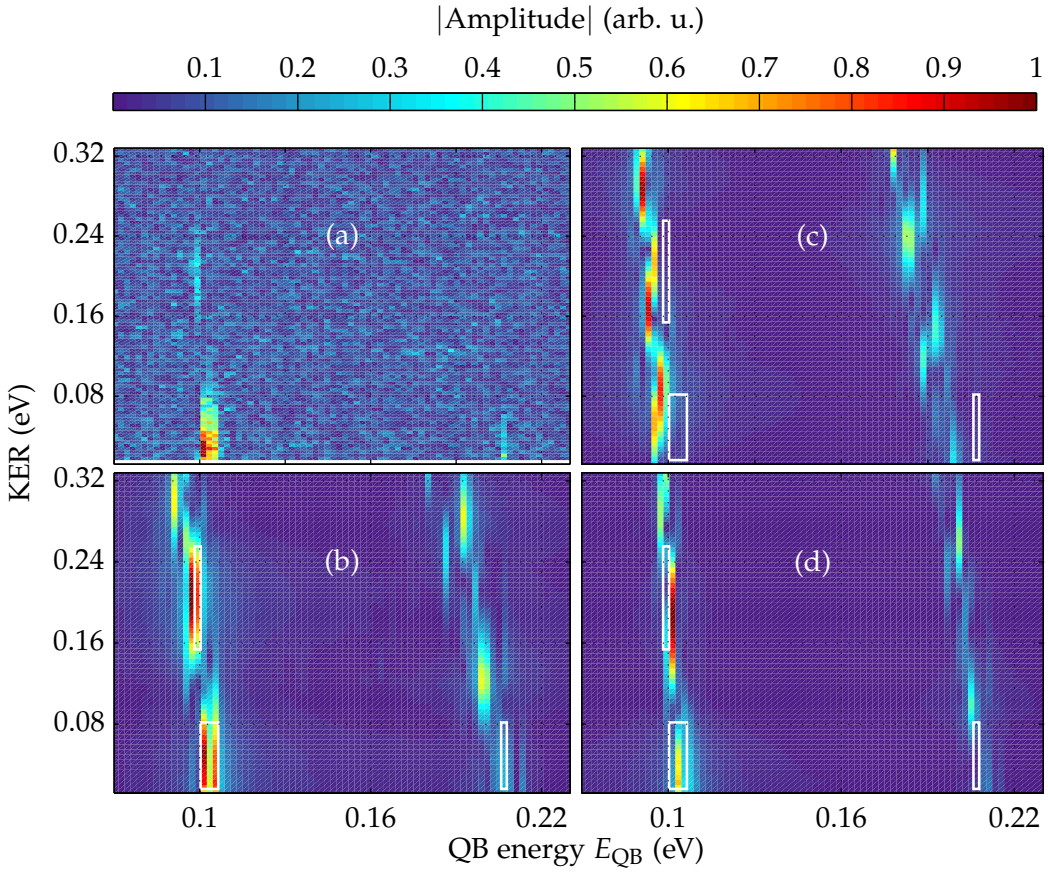

Fig. 5.19. Simulated and experimental QB spectra. See Tab. 5.2 and caption of Fig. 5.17 for details on the PECs used. **Panel (a):** Experimental spectrum. **Panel (b):** Simulation using the Morse potential. **Panel (c):** Simulation using the binding PEC calculated by Marian et al. [MMP+82]. **Panel (d):** Simulation using the binding PEC calculated by Magrakvelidze et al. [MAT12].

MARIAN ET AL. [MMP+82] potential [panels (c)] Here, the coupled-channel simulation is performed with the binding PEC calculated in Ref. [MMP+82]. As in the previous case, the simulated O^+ yield as a function of the pump–probe delay and the KER is shown in Fig. 5.17 (c). For this binding potential, the best agreement with the experimentally observed KER distribution is obtained if the original unshifted repulsive $f\,^4\Pi_g$ PEC is used.

The projection of the lower KER band is shown in Fig. 5.18 (c). The revival structure is close to 1500 fs and thus at larger times than in the experimental spectrum. The QB energies in Fig. 5.19 (c) are considerably smaller than the ones obtained in experiment. Also the KER distribution is shifted (especially in the time domain plot) compared to the experiment.

MAGRAKVELIDZE ET AL. [MAT12] potential [panels (d)] Finally, the results of the quantum calculations using the binding PEC calculated in Ref. [MAT12] are plotted in Fig. 5.17 (d). Similar to case (b), the shifted version of the repulsive PEC is used.

A projection of the lower KER band (KER < 0.08 eV) is plotted in Fig. 5.18 (d). The revival time at 1750 fs occurs 500 fs later than in our experiment. The QB spectrum corresponding to the simulated time-domain spectrum is shown in Fig. 5.19 (d). For low QB energies ($E_{\mathrm{QB}} \approx 0.1$ eV) the agreement between theory and experiment is very good. The experimental KER distribution is also well reproduced.

Summarizing, the main features of the experimental spectra are reproduced by the simulations for all binding PECs: The dominant QB energy is about 0.1 eV and the revival time is between 1 and 2 ps in all cases. On a quantitative level, however, the simulated revival times obtained using the theoretically predicted PECs overestimate the experimental revival time by several hundred of femtoseconds. In addition the simulated QB energies using the binding $a\,^4\Pi_u$ PEC from Ref. [MMP+82] are significantly lower than the experimental ones. The intensity distribution of the simulated Fourier amplitudes differs from the experimental distribution for all PECs used. Possible reasons for this will be discussed in Sec. 5.4.

5.3.2. Using the repulsive PEC from MAGRAKVELIDZE ET AL. [MAT12]

In the following, the results of the quantum simulations using the repulsive $O_2^+(f\,^4\Pi_g)$ PEC calculated by MAGRAKVELIDZE ET AL. [MAT12] (see Fig. 5.14) and different binding PECs are presented. The used combinations of PECs are summarized in Tab. 5.3. The time-domain specta are plotted in Fig. 5.20 and the QB spectra are plotted in Fig. 5.21.

Using this repulsive curve has no significant influence on the simulated revival times and QB energies. Therefore the discussion from the previous section applies here as

Panels	Binding PEC	Repulsive PEC	Shift (a.u.)
(a)	Exp. data	Exp. data	
(b)	Morse	[MAT12]	0.00 (solid curve)
(c)	[MMP+82]	[MAT12]	0.00 (solid curve)
(d)	[MAT12]	[MAT12]	0.00 (solid curve)

Tab. 5.3. Input PECs for the coupled-channel simulations in Sec. 5.3.2. (a), (b), (c) and (d) refers to panels in Figs. 5.20 and 5.21. The last column denotes whether or not a shifted version of the repulsive PEC has been used. All PECs are plotted in Fig. 5.14.

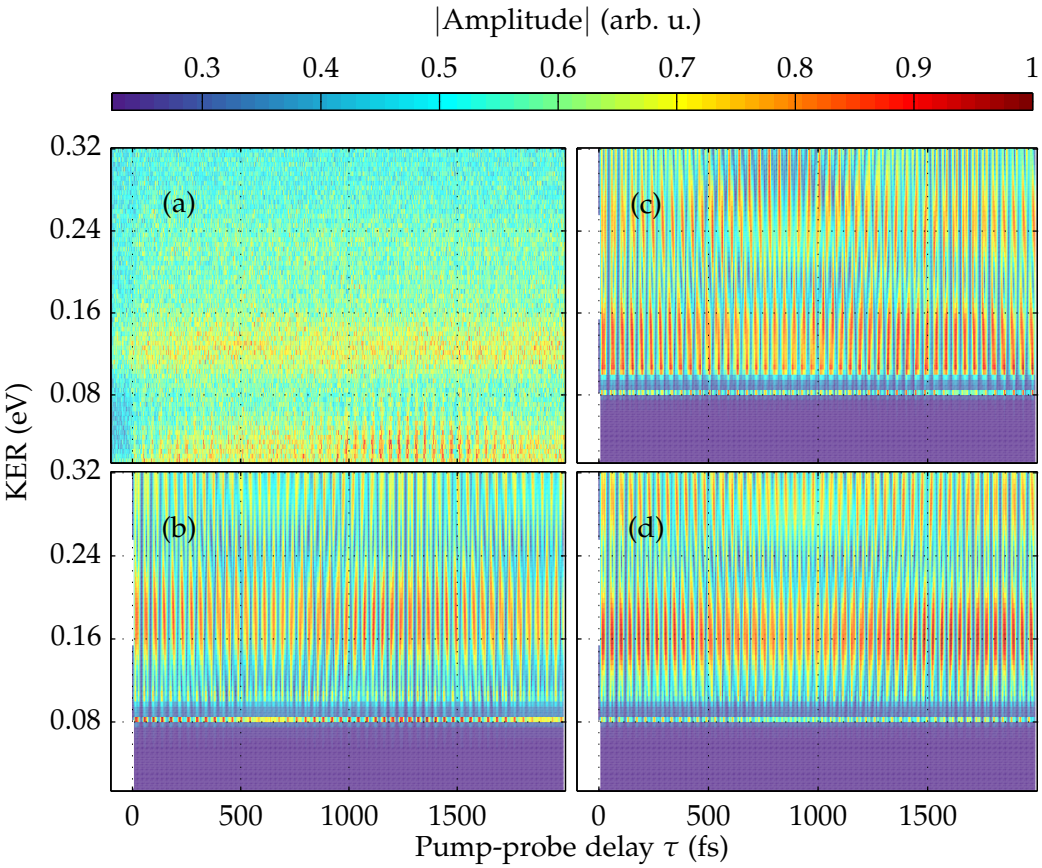

Fig. 5.20. Simulated and experimental yield of O^+ fragments as a function of the pump–probe delay and the KER. All calculations are performed with the pulse parameters listed in Tab. 5.1 and the repulsive PEC calculated in Ref. [MAT12] (see Tab. 5.3). **Panel (a):** Experimental spectrum. **Panel (b):** Simulation using the Morse potential. **Panel (c):** Simulation using the binding PEC calculated by Marian et al. [MMP+82]. **Panel (d):** Simulation using the binding PEC calculated by Magrakvelidze et al. [MAT12].

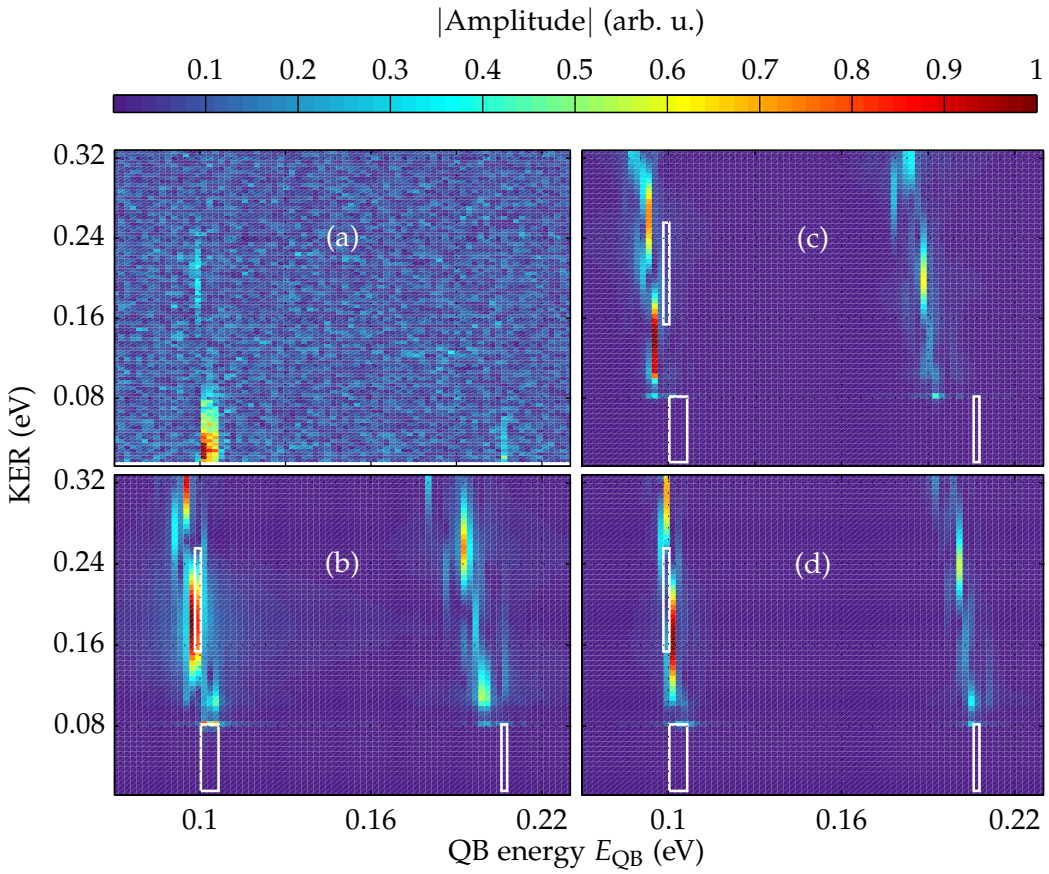

Fig. 5.21. Simulated and experimental QB spectra. See Tab. 5.3 and caption of Fig. 5.20 for details on the PECs. **Panel (a):** Experimental spectrum. **Panel (b):** Simulation using the Morse potential. **Panel (c):** Simulation using the binding PEC calculated by Marian et al. [MMP+82]. **Panel (d):** Simulation using the binding PEC calculated by Magrakvelidze et al. [MAT12].

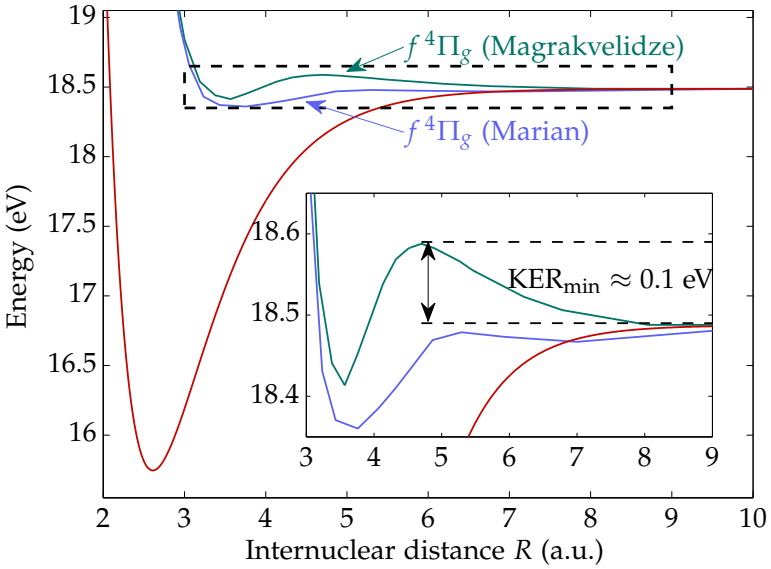

Fig. 5.22. Comparison between the $O_2^+(f\,^4\Pi_g)$ PEC calculated in Refs. [MMP+82] (blue PEC) and [MAT12] (green PEC). The energy region within the dashed box is magnified in the inset. The coupling to the binding PEC (red PEC) occurs at $R \approx 3.2$ a.u.. The potential barrier of the PEC from Ref. [MAT12] causes the missing amplitude at KERs below 0.1 eV in Figs. 5.20 and 5.21.

well. Instead the following discussion focuses on the missing amplitude at very low KER visible in Figs. 5.20 and 5.21 for all binding PECs used in the simulation.

As mentioned before, the coupling between the two electronic states is most efficient for $R \approx 3.2$ a.u.. The repulsive PEC predicted by Ref. [MAT12] features a local maximum in the potential at $R \approx 4.5$ a.u. (see Fig. 5.22). Therefore a part of the population probed to the repulsive state is trapped in a shallow potential well. Only the parts of the wave function which at the moment of being probed, have energy to overcome the barrier may contribute to a dissociation of the molecule. Since this barrier has a height of about 0.1 eV relative to the dissociation limit, no O^+ ions with KER $\lesssim 0.1$ eV are observed as illustrated in Fig. 5.22. Since the experimentally observed KERs reach down to almost zero, a potential barrier in the repulsive PEC is in contradiction to the results of our experiment.

5.4. Limitations of the quantum simulation

So far only the position of the signals (1) and (2) at $E_{QB} \approx 0.1$ eV in the QB spectrum (Fig. 5.19) has been discussed. This section explains the discrepancy between the experimentally measured and simulated Fourier amplitude as well as the shift of the simulated signal (3) at $E_{QB} \approx 0.2$ eV towards larger KERs compared to the experiment.

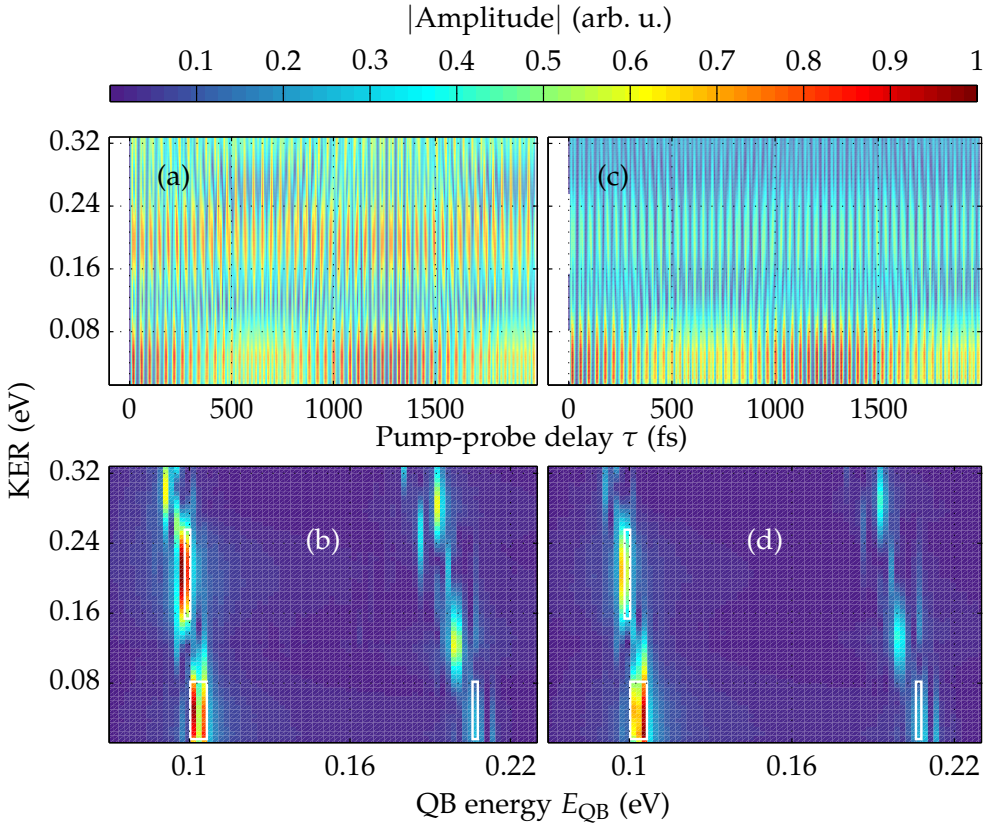

Fig. 5.23. All panels: Results of quantum simulation using the Morse potential and the (shifted) repulsive curve from Ref. [MMP+82]. All calculations are performed using the pulse parameters listed in Tab. 5.1. **Panels (a)** and **(b):** The original neutral PEC from Ref. [BMR10] is used. **Panels (c)** and **(d):** The neutral PEC calculated in Ref. [BMR10] is shifted by 0.1 a.u. towards larger internuclear distances R.

The measured (and simulated) Fourier amplitude is determined by two factors: The occupation of the vibrational levels during the pump step (discussed in Sec. 5.4.1) and the probing efficiency of the wave packet (discussed in Sec. 5.4.2).

5.4.1. Influence of pump step on the simulated spectra

The ionization during the pump step is not described by our quantum simulation. Instead the vibrational levels in the ionic PEC are occupied according to the Franck-Condon principle. Simulations show that the Franck-Condon overlap is very sensitive to the relative position of the neutral and ionic PECs. By shifting the neutral ground-state PEC from Ref. [BMR10] by only ± 0.1 a.u., changes the relative amplitudes of the Fourier signals significantly as shown in Fig. 5.23, due to the modified Franck-Condon factors. A small shift of the neutral ground state towards larger internuclear distances

reduces the population of higher lying vibrational states. In this case, the agreement with the experimental amplitudes is increased.

In addition the quantum simulation does not take a possible dependence of the ionization cross-section on the internuclear distance R into account. This could influence the occupation of the vibrational modes as well. The effect, however, is assumed to be small since the ground-state vibrational wave function is well localized and not distributed over a large range of R.

5.4.2. Influence of probe pulse parameters on the simulated spectra

No matter which vibrational states are occupied during the ionization, only those which can be coupled by the IR pulse to the dissociation continuum contribute to the beating signal observed in the experimental data. This coupling is sensitive to the IR probe pulse parameters. Besides the probe intensity and the photon energy, the exact IR pulse shape[5], prepulses or a chirp could further influence the probing efficiency. Last but not least, the probing efficiency depends on the dipole coupling (see Fig. 5.15) and the exact shape of the PECs in the coupling region.

The impact of moderate changes to the pulse length and to the intensity of pulse pedestals have been tested with the coupled-channel simulation. The obtained spectra are given in Appendix C. It turns out, that the QB energy and revival time are both insensitive to small variations of these parameters and so is the adjustment of the Morse potential. The KER distribution and the relative amplitudes between the QB signals, on the other hand, both are more sensitive to these parameters.

The influence of the IR pulse intensity on the simulated spectra is discussed in the following. It will turn out that for large intensities, the observed QB energies are shifted. This could explain why the QB energies observed in a previous IR–IR experiment [DMB+11] investigating the same wave-packet dynamics, are in contradiction to our experimental and simulated values.

In Figs. 5.24 and 5.25, the experimental data is compared with the results of quantum simulations using three different probe pulse peak intensities. For increasingly large intensities [Figs. 5.24 and 5.25, (c) and (d)], the KER distribution is shifted towards larger KERs and deeper bound vibrational states are probed. This leads to an effective shift of the QB energy observed low KERs. In the IR–IR pump–probe experiment presented in Ref. [DMB+11], very high IR probe intensities of up to $3 \times 10^{14}\,\mathrm{W/cm^2}$ were used. This might explain, why in that experiment the beating between neighboring vibrational states was observed at QB energies between 0.124 and 0.144 eV (these are significantly larger than the QB energies observed in our experiment).

The simulated KER spectrum is almost continuous at the highest intensity. This could be caused by the so-called elevator mechanism in which the final ionic KER is modified by the time-dependent electric field of the laser pulse [FGC+14]. Note, however, that

[5] A Gaussian temporal field envelope is assumed in the simulations.

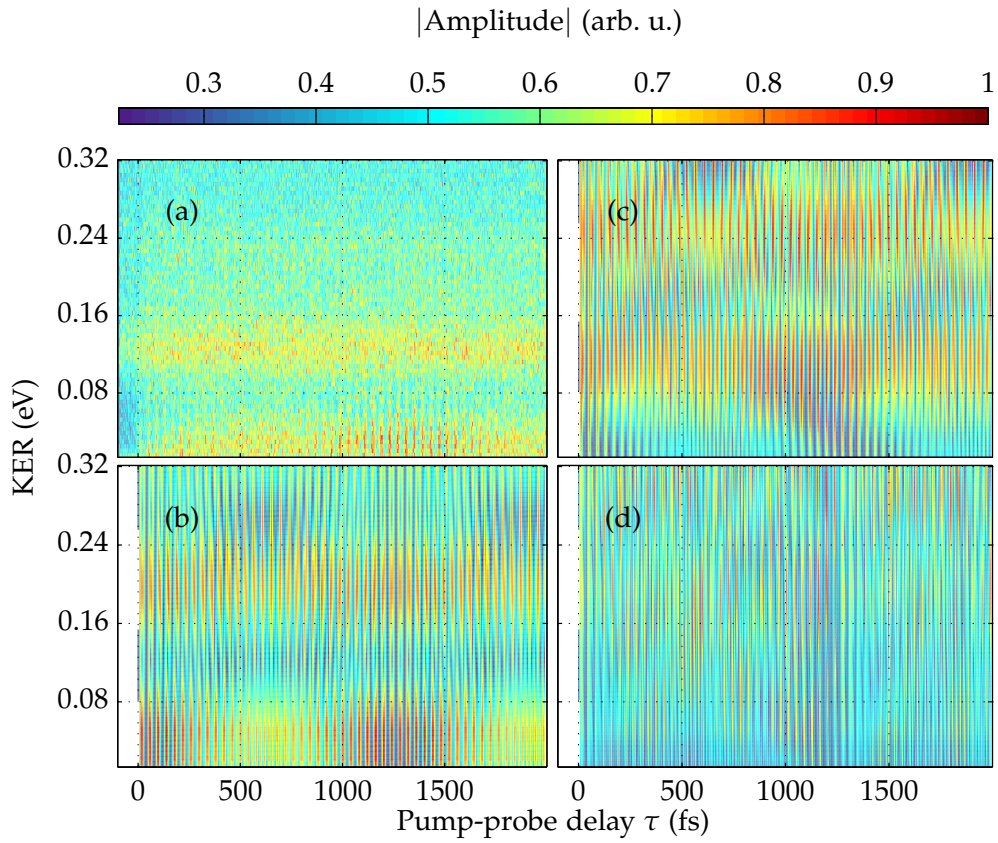

Fig. 5.24. Comparison of experimental results with the results of simulations using different IR pulse peak intensities. The other pulse parameters are as listed in Tab. 5.1. The Morse potential and the (shifted) repulsive curve from Ref. [MMP+82] are used in the simulation. **Panel (a):** Experimental data. Probe pulse intensities: **Panel (b):** $3 \times 10^{12}\,\mathrm{W/cm^2}$ peak intensity. **Panel (c):** $1 \times 10^{13}\,\mathrm{W/cm^2}$ peak intensity. **Panel (d):** $1 \times 10^{14}\,\mathrm{W/cm^2}$ peak intensity.

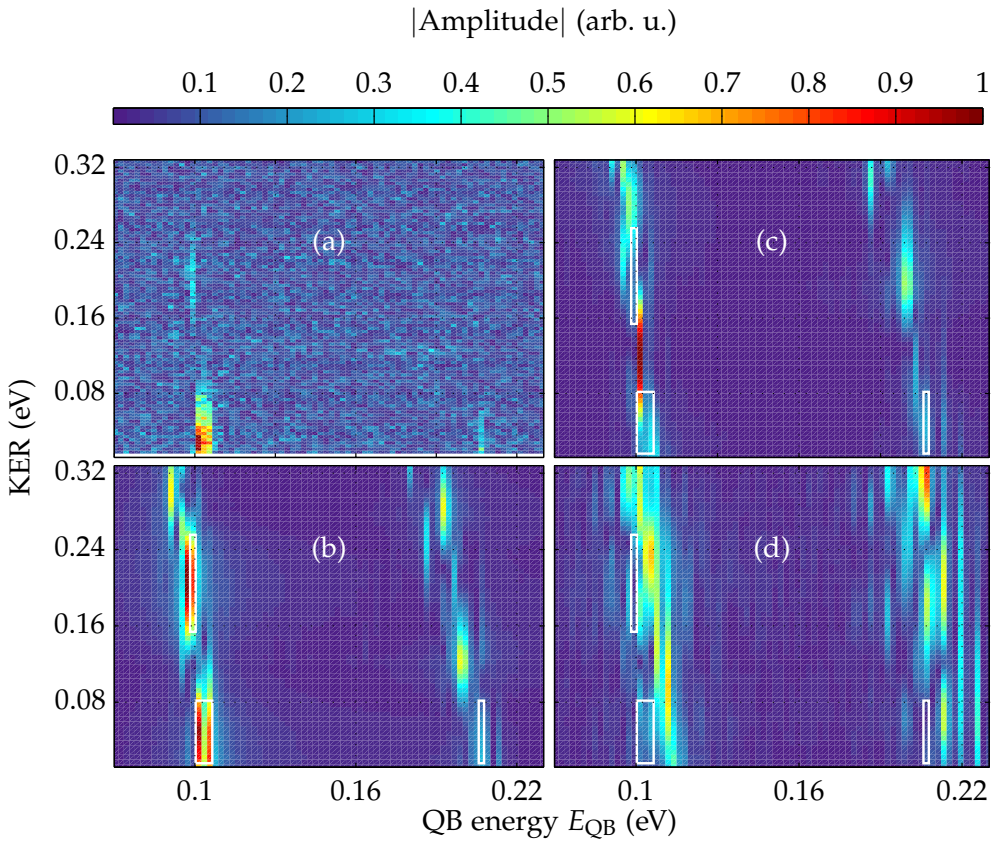

Fig. 5.25. QB spectrum of Fig. C.2. **Panel (a):** Experimental data. Probe pulse intensities: **Panel (b):** $3 \times 10^{12}\,\mathrm{W/cm^2}$ peak intensity. **Panel (c):** $1 \times 10^{13}\,\mathrm{W/cm^2}$ peak intensity. **Panel (d):** $1 \times 10^{14}\,\mathrm{W/cm^2}$ peak intensity. See caption of Fig. 5.24 for more details.

the simulated results obtained at the highest probe intensities must be treated with care because coupling to additional electronic states (which have not been taken into account) might occur in this case (see Sec. 2.5.2).

For probe intensities well below the $3 \times 10^{12}\,\mathrm{W/cm^2}$ used in our experiment, the simulated KER distribution and the QB energies do not change (compare Fig. C.1 in appendix). This leads to the conclusion that perturbation of the PECs during the probe process is negligible in our experiment.

5.5. Summary of the O_2 experiments

A nuclear wave packet within an O_2^+ PEC was observed for the first time in an XUV–IR pump–probe experiment (see Fig. 5.6 for the pump–probe scheme). Using a long pump–probe delay of 2 ps, the first half-revival is fully resolved in our data (see Fig. 5.5)

and a high energy resolution is obtained in the Fourier domain (see Fig. 5.8). The measured QB energies are in good agreement with the level spacing of the vibrational states embedded in the $O_2^+(a\,^4\Pi_u)$ PEC calculated in Ref. [MAT12].

Performing coupled-channel simulations with the PECs from Refs. [MMP+82] and [MAT12], however, results in simulated half-revival times which are larger than the one observed the experimental data. Using a Morse potential adjusted to the experimental data, on the other hand, reproduces the experimental revival time to a high accuracy (see Fig. 5.18). This allows to test the quality of calculated PECs and additionally proves the sensitivity of our method to small changes in the shape of the involved binding PEC.

The simulated KER spectra obtained with the repulsive $O_2^+(a\,^4\Pi_u)$ PEC calculated in [MAT12] does not show the very low KERs observed in the experimental data (see Fig. 5.21). This is due to the potential barrier of that PEC at $R \approx 4.5$ a.u. (shown in Fig. 5.22).

In simulations with IR intensities much larger than the $3 \times 10^{12}\,\mathrm{W/cm^2}$ used in our experiment, the simulated QB energies are shifted because population from deeper bound vibrational levels is promoted to the repulsive PEC (see Fig. 5.25). This effect might explain why larger QB energies where measured in a previous IR–IR experiment at intensities up to $3 \times 10^{14}\,\mathrm{W/cm^2}$. Coupled-channel calculations performed with very low probe intensities, on the other hand, do not show a shift of the QB energies towards smaller values (compare Fig. C.1 in the appendix).

6. Sequential XUV–IR double ionization of N_2 via an anti-bonding cationic state

Contents

6.1. Experimental parameters 116
6.2. Pump–probe delay independent spectra and identification of N_2^{++} events 117
6.3. Pump–probe delay dependent yield of N_2^{++} 118
6.4. Comparison between simulation and experiment 126
6.5. Pump–probe delay dependent yield of N^+ fragments 131
6.6. Summary of the N_2 experiments 133

In this chapter, the sequential double ionization of N_2 by the XUV and the IR pulse is discussed. The reaction is described by

$$N_2 \xrightarrow{\text{XUV}} (N_2^+)^* + e^- \xrightarrow{\text{IR}} N_2^{++} + e^- + e^-, \tag{6.1}$$

which is closely related to the reaction

$$N_2 \xrightarrow{\text{XUV}} (N_2^+)^* + e^- \xrightarrow{\text{IR}} N^+ + N^+ + e^- + e^- \tag{6.2}$$

measured and discussed in Ref. [GRT+07]. In that XUV–IR pump–probe experiment a delay dependent yield and KER of two coincident N^+ fragments was observed. It turned out that the two step ionization followed by a fragmentation [Eq. (6.2)] is possible even for very large pump–probe delays of several hundred femtosecond [GRT+07]. In the same experiment, an increased yield of stable N_2^{++} due to the reaction given in Eq. (6.1) was observed in the temporal overlap of the pulses. Due to a limited temporal resolution resulting from the usage of rather long IR laser pulses (28 fs), the nature of this increased yield could not be further analyzed (see [GRT+07, Supplementary Material]).

In this work, a similar experiment was repeated with (12 ± 3) fs IR pulses. This provides an increased temporal resolution which reveals an asymmetric increase in the N_2^{++} yield for small pump–probe delays shown in Fig. 6.1. In this chapter, the main features of this spectrum are explained by the sequential double ionization mechanism given in Eq. (6.1). By comparing the experimental results with simulations, it will

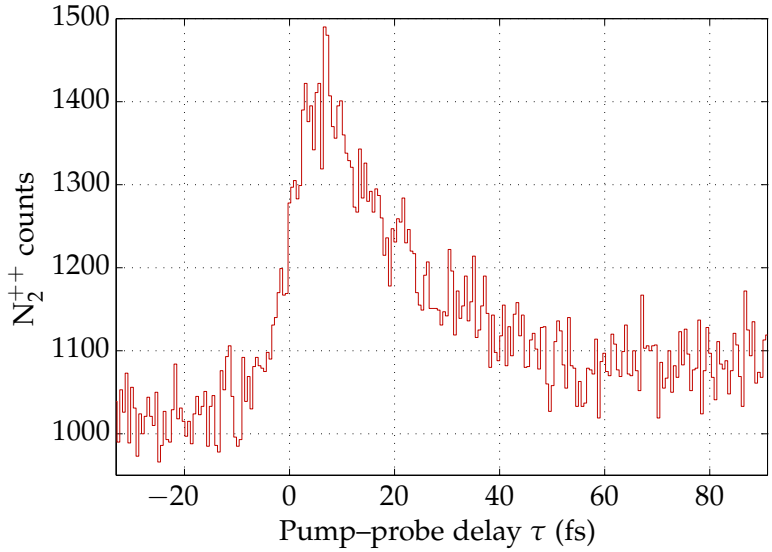

Fig. 6.1. Experimentally observed N_2^{++} yield as a function of the pump–probe delay. The XUV pulse precedes the IR pulse for positive delays. The increased yield for small (positive) pump–probe delays is due to a sequential double ionization by XUV and IR pulse.

turn out that the fragmentation dynamics of highly excited N_2^+ ions is encoded in the pump–probe dependent N_2^{++} yield.

This chapter begins in Sec. 6.1 with a summary of the experimental parameters used. Afterwards, in Sec. 6.2, pump–probe delay independent spectra obtained by ionization of N_2 are discussed. These spectra are used to identify the involved reaction channels, in particular the creation of N_2^{++} dications. The yield of these dications features a pronounced pump–probe time dependency as shown in Sec. 6.3. This observation is explained by a sequential double ionization via highly excited cationic satellite states. By comparing the experimental data to simulated spectra in Sec. 6.4, restrictions on the shape of involved PECs are made and a deeper understanding of the involved fragmentation dynamics is gained. In Sec. 6.5, the pump–probe dependent yield and KER of N^+ fragments is analyzed. The chapter ends with a brief summary (in Sec. 6.6).

6.1. Experimental parameters

All experimental data presented in this section was recorded in a 51 hours experimental run beginning at 17:12pm on April 15th 2014. The raw data is saved in the files: `2014_04_15_05_XUV_IR_N2_1000ct_120fs_G136V_[0001-1085].lmd`.

The acceleration voltage of the reaction microscope was set to 136 V which corresponds to an electric field of 10.2 V cm^{-1}. Thus N^+ ions with kinetic energies up to

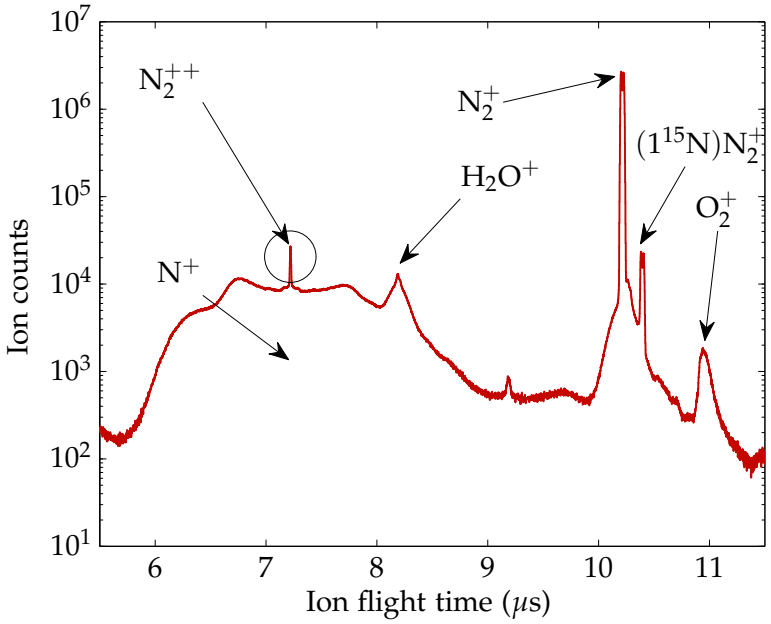

Fig. 6.2. Ion time-of-flight (ToF) spectrum obtained in the N_2 experiment. All relevant peaks are assigned to the corresponding particle species.

3 eV were detected over the full 4π solid angle [see Eq. (4.21)].

During the experiment, the average power of the IR probe beam was 125 mW. The effective IR intensity within the focus of the XUV beam was estimated to be $3 \times 10^{12}\,\mathrm{W/cm^2}$. The IR probe pulse duration was determined with an XUV–IR cross correlation (compare Sec. 3.2.5) to (12 ± 3) fs. The central wavelength of the IR pulse was 750 nm corresponding to a photon energy of 1.65 eV. The total pump–probe delay range was 126 fs.

6.2. Pump–probe delay independent spectra and identification of N_2^{++} events

As in Chap. 5, the time-of-flight (ToF) spectrum is used to identify ion species created in the experiment. The ToF spectrum integrated over the whole range of pump–probe delays is given in Fig. 6.2. Dominant peaks in this spectrum are created by N_2^+ (and its isotope) as well as N^+. Additional peaks are caused by the ionization of residual gas (H_2O^+ and O_2^+). The N_2^{++} dications discussed in the next section (Sec. 6.3) feature a charge-to-mass ratio equal to that of N^+. In contrast to the dissociation product N^+, the dications have very small kinetic energies as they only get a recoil momentum from the two photoelectrons. Thus the N_2^{++} ToF peak at 7.2 µs is sharp and it is located at the center of the N^+ peak.

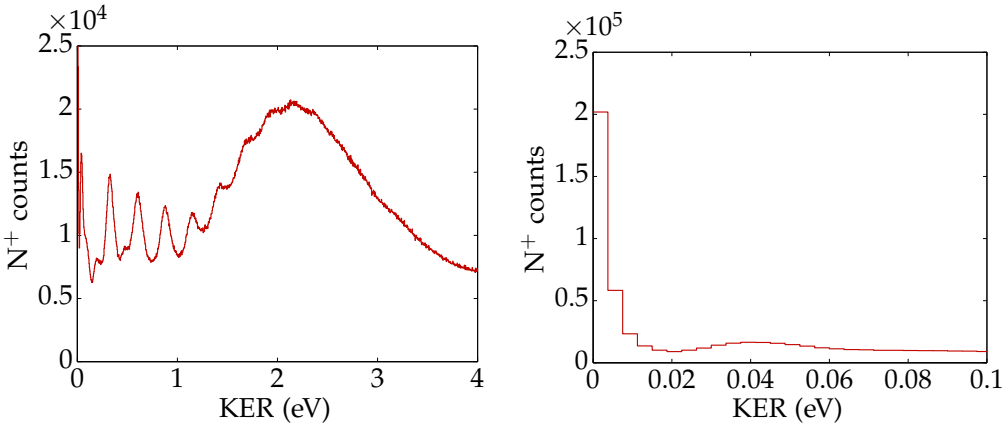

(a) N^+ KER whole range

(b) N^+ KER low energy part

Fig. 6.3. Experimentally obtained KER spectrum of N^+ ions. See text for identification of the peaks.

Having identified the particle species, the 3-dimensional momenta of all particles can be calculated. From these the kinetic-energy release (KER) defined as $\mathrm{KER} = E^{\mathrm{kin}}_{\mathrm{N}^+} + E^{\mathrm{kin}}_{\mathrm{N}} = 2E^{\mathrm{kin}}_{\mathrm{N}^+}$ can be calculated. The measured KER integrated over all pump–probe delays is shown in Fig. 6.3.

In the following, the peaks in the KER spectrum are briefly identified with the help of PECs and data from previous experiments. The main focus of this work, however, lies on the counts at very low KERs in Fig. 6.3(b) created by the detection of stable N_2^{++} ions which will be discussed in the next section (Sec. 6.3).

Potential-energy curves of N_2^+ calculated in Refs. [AIH+06, Gil65] are plotted in Fig. 6.4. In Fig. 6.3(a) several sharp peaks at KERs below 2 eV are clearly visible. These are created by the predissociation of the $N_2^+(C\,^2\Sigma_u^+)$ state (blue PEC in Fig. 6.4) into the $N(^4S) + N^+(^3P)$ continuum (see Refs. [LL74, RLB75, TA75, Erm76, EWK+06] and Refs. therein for further information). The broad peak centered at about 2 eV is created by the ionization to the repulsive $N_2^+(F\,^2\Sigma_g^+)$ state (red PEC in Fig. 6.4) followed by a fragmentation of the molecule [LKC+12].

6.3. Pump–probe delay dependent yield of N_2^{++}

In this section experimental data on the pump–probe delay dependent yield of N_2^{++} is presented and interpreted as a sequential double ionization described by

$$\mathrm{N_2}(X\,^1\Sigma_g^+) \xrightarrow{\mathrm{XUV}} (\mathrm{N_2^+})^* + \mathrm{e}^- \xrightarrow{\mathrm{IR}} \mathrm{N_2^{++}}(X\,^1\Sigma_g^+) + \mathrm{e}^- + \mathrm{e}^-. \tag{6.3}$$

We begin (in Sec. 6.3.1) with a discussion of the pump–probe scheme and an introduction of the PECs involved in the reaction given by Eq. (6.3). The N_2^{++} ion spectra are

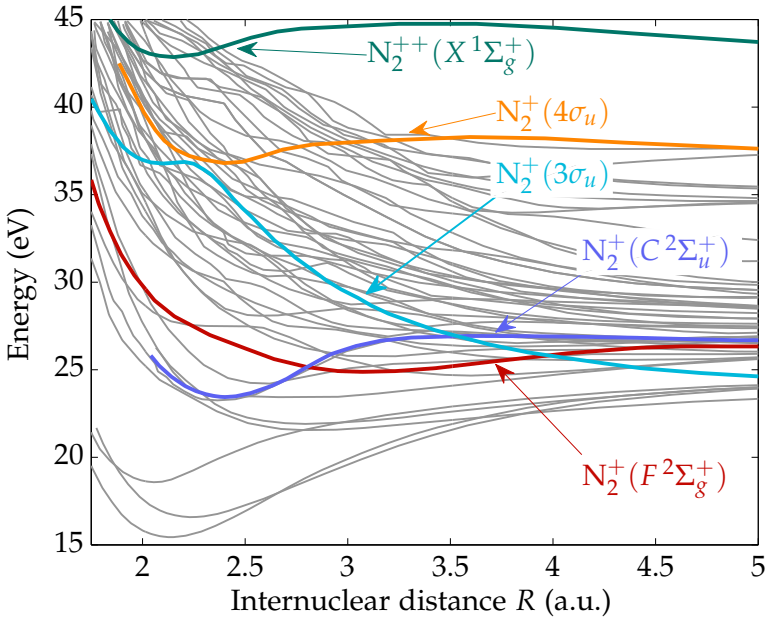

Fig. 6.4. N_2^+ PECs calculated in Refs. [AIH+06, Gil65]. Predissociation of the $N_2^+(C\,^2\Sigma_u^+)$ state (blue curve) and dissociating of the $N_2^+(F\,^2\Sigma_g^+)$ state (red curve) contribute to the pump–probe delay independent KER spectrum plotted in Fig. 6.3(a). PECs calculated in Ref. [GRT+07] are plotted as green, orange and turquoise curves. These PECs play a role in the pump–probe delay dependent N_2^{++} yield discussed in Sec. 6.3.

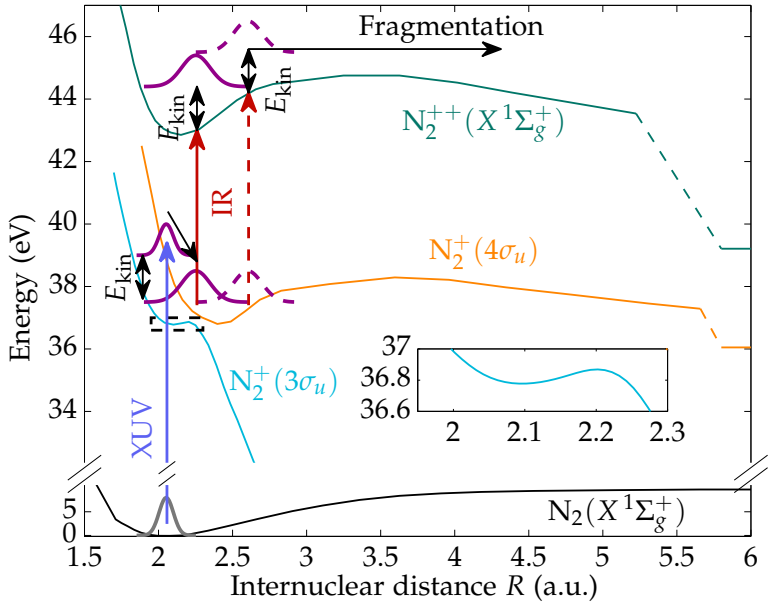

Fig. 6.5. Illustration of the pump–probe scheme resulting in a delay dependent yield of N_2^{++}. Ionization by the XUV pulse and by the IR pulse is illustrated by blue and red arrows, respectively. The dictionic ground state is given by the green curve. Two cationic satellite states are given in orange ($4\sigma_u$ state) and turquoise ($3\sigma_u$ state). All PECs are taken from Ref. [GRT+07]. Depending on the pump–probe delay between XUV and IR pulse, either a stable N_2^{++} dication is created or the molecule fragments into two N^+ ions. The first case is illustrated by the solid red arrow and the purple wave packet, the second case is indicated by the dashed red arrow and the dashed purple wave packet. The inset shows a magnified view of the $3\sigma_u$ PEC within the Franck-Condon region.

presented in Sec. 6.3.2. Afterwards, in Sec. 6.3.3, photoelectron spectra measured in coincidence with N_2^{++} are presented.

6.3.1. Pump–probe scheme

To explain the pump–probe delay dependent N_2^{++} yield plotted in Fig. 6.1, we consider the ionization of a $3\sigma_g$ valence electron by a highly-energetic XUV photon. In this process another $3\sigma_g$ electron is excited to a high lying Rydberg satellite state. These states can be considered as an independent electron orbiting an N_2^{++} dication. Of those satellite states, the final $4\sigma_u$ orbital has the largest overlap with the initial $3\sigma_g$ orbital and is therefore predominantly populated at photon energies of 43 eV according to Ref. [GRT+07]. The PEC of this $N_2^+(4\sigma_u)$ state is plotted as an orange curve in Fig. 6.5. It will turn out in Sec. 6.4 that for the interpretation of our experimental data the $N_2^+(3\sigma_u)$ satellite state must be considered as well. The corresponding PEC calculated in Ref. [GRT+07] is given by the turquiose curve in Fig. 6.5.

The ground-state vibrational wave function within the neutral $N_2(X\,^1\Sigma_g^+)$ PEC is plotted as a gray curve in Fig. 6.5. This wave function is promoted to the cationic satellite states by the ionization by the XUV pulse. The potential minimum of the $4\sigma_u$ PEC is shifted compared to the center of the Franck-Condon region. The $3\sigma_u$ PEC does not feature a (high) potential barrier at all. Thus excitation of either electronic state will cause the N_2^+ ion to dissociate immediately. Within the Franck-Condon interval, the $4\sigma_u$ PEC is much steeper than the almost flat $3\sigma_u$ PEC. Thus the dissociation will occur on very different timescales. In addition, small parts of the wave function will be trapped in the minimum of the $4\sigma_u$ PEC and form (meta-)stable N^+ ions.

The molecular dynamics can be understood with a simple quantum-mechanical model that will also be used for simulations in Sec. 6.4. In this model, after photoionization, the wave packet propagates on the PECs of the satellite states. The IR probe pulse can interrupt the dissociation of the molecular ion by further ionizing it to the $X\,^1\Sigma_g^+$ ground state of the dication. This is illustrated in Fig. 6.5 by the solid red arrow promoting the wave packet drawn as a solid purple curve. The strong-field ionization is well described by the multi-photon picture since the Keldysh parameter is given by[1] $\gamma \approx 4$ (see Sec. 2.3.2 and Fig. 2.7). The ionization is a non-resonant process (the photo-electron can carry away any excess energy) and it is in principle allowed for a large range of internuclear distances. Thus in the most simple model, the ionization cross-section is independent of R.

As the momentum of the wave packet is conserved during ionization, stable N_2^{++} is only formed for small pump–probe delays. For larger pump–probe delays – a situation illustrated by the dashed red arrow promoting the dashed purple wave packet – the kinetic energy gained on the cationic potential is large enough to overcome the potential barrier of the dicationic state. As a result the molecular dication will fragment in a Coulomb explosion and no stable N_2^{++} is detected. This explains the decrease of the N_2^{++} yield for increasing positive pump–probe delays in Fig. 6.1.

Parts of the wave packet will be trapped in the potential minimum of the $4\sigma_u$ satellite state. Even at large pump–probe delays, this population will form stable N_2^{++} when being probed by the IR pulse. This explains why the the N_2^{++} yield shown in Fig. 6.1 does not decrease to its original level even for large pump–probe delays. Quantum simulations in Sec. 6.4 will show that no population remains trapped within the shallow potential minimum of the $3\sigma_u$ state for times longer than a few tens of femtoseconds.

6.3.2. Ion spectra

The measured N_2^{++} yield as a function of the pump–probe delay is given in Fig. 6.6. Clearly visible is a rapid increase in the yield close to the temporal overlap of the XUV and IR pulse at $\tau = 0$. The temporal overlap between the pulses has been determined in an independent measurement using the method described in Secs. 3.2.5 and 4.3.1.

[1] Here an IR intensity of $3 \times 10^{12}\,\mathrm{W/cm^2}$ and an ionization potential of 6 eV was assumed.

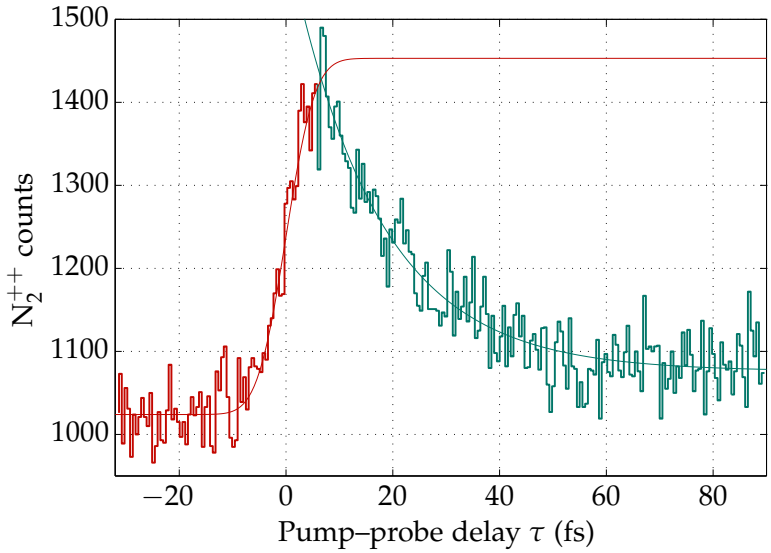

Fig. 6.6. Experimentally observed N_2^{++} yield as a function of the pump–probe delay. The temporal overlap between the pulses at $\tau = 0$ fs has been determined from the sidebands created in ionization of argon. The delay range is divided into two regions: (1) Negative delays where the IR precedes the XUV pulse including the temporal overlap, and (2) positive delays where the XUV pulse precedes the IR pulse. In those two regions, the N_2^{++} yield is given by the red, and the green histograms, respectively. In region (1) an Gauss error function (red curve) has been fitted to the data, whereas the yield in region (2) is well described by an exponential fit (green curve). See Tabs. 6.1 and 6.2 for functions and fitted parameters.

$a\left(\frac{1}{2}\,\mathrm{erf}\left[\frac{x}{\sqrt{2}b}\right]+1/2\right)+c$	a	b	FWHM	c
	429	4.24 fs	10 fs	1024

Tab. 6.1. Fitting parameters of the Gauss error function (plotted as a red curve in Fig. 6.6). The parameter b is related to the FWHM of a Gaussian function by FWHM $= 2.355b$.

For positive delays where the XUV pulse precedes the IR pulse, the yield decreases more slowly. In the following, first the rising edge and afterwards the falling edge is discussed.

Negative delays and rising edge The two step process illustrated in Fig. 6.5 is only possible, if the molecule interacts with the IR pulse *after* it has been ionized by the XUV pulse. Thus the N_2^{++} cations created for negative delays ($\tau < -15$ fs) originate from direct double ionization by an XUV photon.

In order to simplify the discussion of the increasing N_2^{++} yield close to the temporal overlap we (for now) consider an infinitely short XUV pulse and an IR pulse with a finite length. Let us further assume that the molecule does not dissociate after ionization and thus further ionization by the IR pulse can create stable N_2^{++} even for large positive delays. In this case, the probability for a multi-photon ionization by the IR pulse depends on the integrated IR intensity *trailing* the XUV pulse. Assuming a Gaussian intensity envelope, the rising edge of the distribution is therefore described by a Gauss error function[2].

It turns out that the above argument with the infinitely short XUV pulse is not necessary and a similar result is obtained for finite durations of the XUV pulse. In this case, the width of the Gauss error function depends on the cross correlation of XUV and IR pulse.

An error function fitted to the rising edge of the experimental data is plotted in Fig. 6.6 as a red curve. The fitting parameters are given in Tab. 6.1. The parameter $b = 4.24$ fs corresponds to a cross correlation with a FWHM of 10 fs. This is slightly smaller than the 14 fs cross correlation measured in the photoelectron spectrum of argon (compare Sec. 3.2.5). This discrepancy can be explained by the multi-photon ionization during the probe step. The probability for such a transition involving n photons is proportional to $I(t)^n$. For a Gaussian IR pulse intensity envelope $I(t)$ with a width of τ_{IR}, this leads to a reduced effective IR pulse duration

$$\tau_{\mathrm{IR}}^{\mathrm{eff}} = \frac{\tau_{\mathrm{IR}}}{\left(\sqrt{2}\right)^{n-1}} \approx \frac{12\,\mathrm{fs}}{\left(\sqrt{2}\right)^{n-1}}.$$

[2]The Gauss error function is defined by $\mathrm{erf}(x) := \frac{2}{\sqrt{\pi}} \int_0^x e^{-x'^2} \mathrm{d}x'$.

$a\,e^{-bx}+c$	a	b	$T_{1/2}=\ln(2)/b$	c
	524	$(0.060\pm0.008)\,\mathrm{fs}^{-1}$	$(11.6\pm1.5)\,\mathrm{fs}$	1076

Tab. 6.2. Fitting parameters of the exponential fit (plotted as a green curve in Fig. 6.6).

Thus the width of the effective cross correlation is reduced as well.

Falling edge The N_2^{++} yield decreases on a slower timescale for positive pump–probe delays. Also the functional dependence of the yield on the pump–probe delay clearly differs from the rising edge. This indicates that a dynamical progress occurring within the molecule is measured and not an increased double ionization cross-section due to the superposition of XUV and IR field.

The falling edge is well described by an exponential fit plotted as a green curve in Fig. 6.6. The fitting parameters are listed in Tab. 6.2. The "half-life" of this exponential is $T_{1/2}=(11.6\pm1.5)\,\mathrm{fs}$. Our simulations will show in Sec. 6.4 that such a timescale is consistent with the interpretation of a dissociating cationic state which can be probed to the potential minimum of the N_2^{++} PEC for small pump–probe delays.

The photoelectron spectra discussed in the following further confirm the above described sequential double ionization by XUV and IR pulse.

6.3.3. Photoelectron spectra

The number of photoelectrons detected in coincidence with N_2^{++} ions is shown in Fig. 6.7 as a function of the pump–probe delay τ and the electrons kinetic energy E_e. Due to the increased N_2^{++} yield at small pump–probe delays, the number of photoelectrons detected at such delays is increased as well. The kinetic-energy distribution peaks at small energies for all pump–probe delays. In Fig. 6.7 the pump–probe delays where the IR pulse precedes the XUV pulse are labeled *IR first*. For these delays, the sequential double ionization is not possible. Therefore, this distribution is considered as a background in the following. The delays where the IR pulse trails the XUV pulse (plus the temporal overlap) are labeled *XUV first*.

A background-free electron spectrum is shown in Fig. 6.8. This spectrum is obtained by bin-wise subtracting the average electron spectrum in the *IR first* region in Fig. 6.7 from the electron spectrum in Fig. 6.7. By integrating this background free electron spectrum in the pump–probe delay range from 5 to 20 fs, the kinetic energy spectrum given in Fig. 6.9 is obtained. The kinetic-energy distribution of electrons created during the sequential double ionization on N_2 is reflected in that spectrum.

The increased yield of low energetic photoelectrons in Fig. 6.9 can be explained by the multi-photon ionization of highly excited N_2^+ ions with the IR pulse. This further

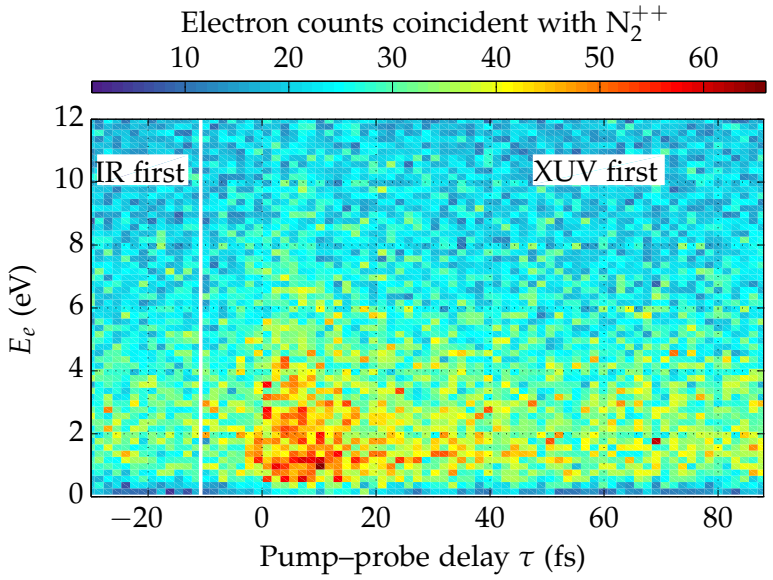

Fig. 6.7. The number of photoelectrons detected in coincidence with N_2^{++} ions is plotted as a function of the electron kinetic energy E_e and the pump–probe delay τ. Mostly low energetic electrons are detected.

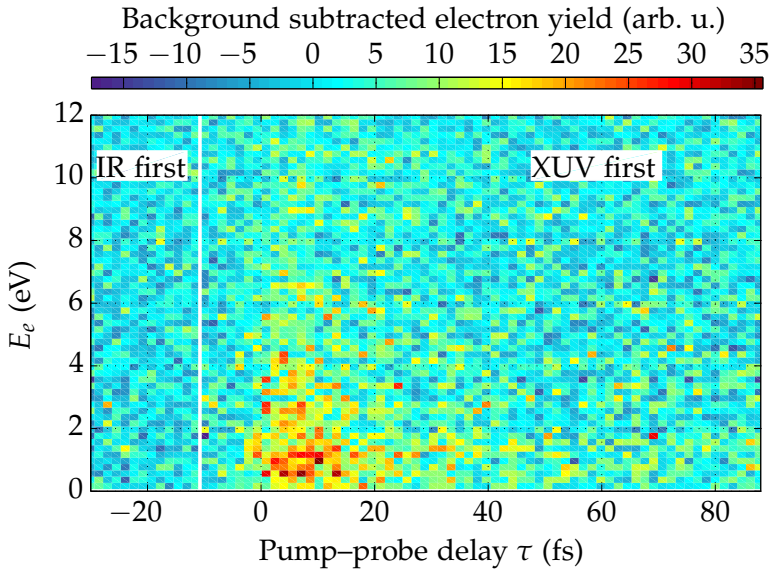

Fig. 6.8. Background free photoelectron yield measured in coincidence with N_2^{++} ions. This spectrum is obtained by bin-wise subtraction of the average electron spectrum in the *IR first* region of Fig. 6.7 from the total electron spectrum.

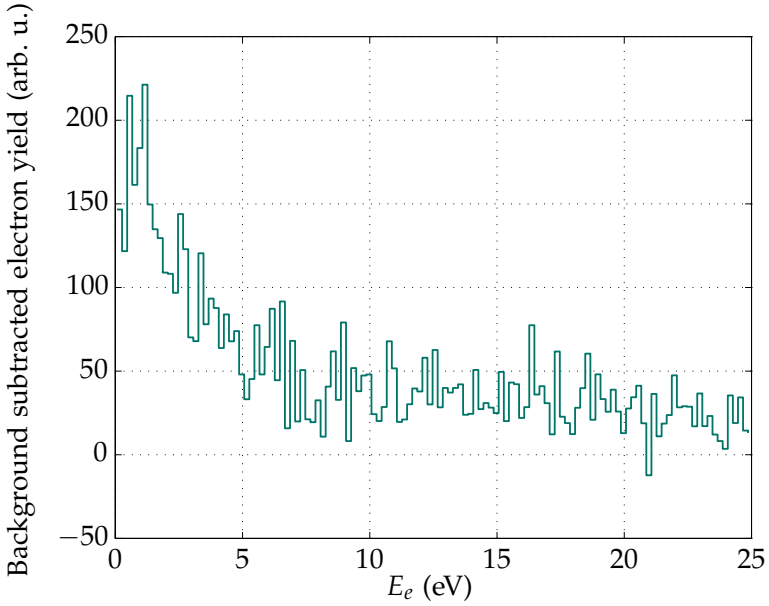

Fig. 6.9. Background corrected kinetic-energy distribution of electrons measured in coincidence with N_2^{++} for the delay interval from 5 and 20 fs obtained with a method described in the text.

confirms the hypothesis that pump–probe delay dependent yield of N_2^{++} is due to a sequential double ionization by XUV and IR pulse as described in Sec. 6.3.1. By comparing experimental and simulated spectra in the following section, predictions on the shape of the intermediate PEC can be made.

6.4. Comparison between simulation and experiment

The measured delay dependent N_2^{++} yield is compared to results of simulations in this section. The model used to describe the pump–probe scheme makes use of an assumed process consisting of four steps briefly explained in the following (details have been described in Sec. 2.5.1):

1. **XUV ionization:** The vibrational ground-state wave function ψ_0 of neutral N_2 is promoted to the cationic PEC according to the Franck-Condon principle.

2. **Propagation on the N_2^+ PECs:** The initial nuclear wave function $\psi(R, t = 0) = \psi_0$ is propagated on the PECs of the $4\sigma_u$ and $3\sigma_u$ satellite states up to the time $t = \tau$.

3. **Multi-photon ionization:** The wave packet $\psi(R, t = \tau)$ is promoted to the dicationic PEC at time τ instantaneously with unit probability. Details about the strong-field ionization by the IR pulse are not taken into account.

$a\,e^{-bx}+c$	a	b	$T_{1/2}=\ln(2)/b$	c
$4\,\sigma_u$ PEC	406	$(0.33\pm0.03)\,\mathrm{fs}^{-1}$	(2.1 ± 0.2) fs	1280
$3\,\sigma_u$ PEC	521	$(0.0566\pm0.0003)\,\mathrm{fs}^{-1}$	(12.2 ± 0.6) fs	1029

Tab. 6.3. Fitting parameters of the exponential fit to the simulated data sets. In two different simulations, the $4\,\sigma_u$ intermediate PEC and the $3\,\sigma_u$ PEC were used (both shown in Fig. 6.5). The fitted functions are plotted as a green curve in Figs. 6.10 and 6.11.

4. **Propagation on cationic PEC:** Finally, the wave function is propagated on the dicationic PEC until the bound parts (corresponding to the formation of stable N_2^{++}) are clearly separated from the dissociating parts of the wave packet. The absolute square of the bound amplitude as a function of τ gives the simulated N_2^{++} yield as a function of the pump–probe delay.

The results of the simulations using the PECs from Fig. 6.5 are shown in Figs. 6.10 and 6.11. The computed N_2^{++} yield is given by the blue curve in both figures. In the applied model, the action of both laser pulses occurs instantaneously. In order to take the finite experimental pulse duration (and thus the finite temporal resolution) into account, the simulated N_2^{++} yield is convoluted with a Gaussian function of 10 fs FWHM. This width corresponds to the experimental resolution estimated in Sec. 6.3.2 from the rising edge of the delay dependent N_2^{++} yield. In Figs. 6.10 and 6.11, the convoluted data is given by the red curve (rising edge) and green curve (falling edge). The simulations take neither the time-independent production of N_2^{++} nor the absolute amplitude of the delay dependent N_2^{++} yield into account. Thus the offset of the simulated yield at negative delays and the peak amplitude are adjusted to the experimental data. An exponential function is fitted to the falling edge (plotted as a dashed purple curve). The fit parameters are summarized in Tab. 6.3.

The simulated results using the $4\,\sigma_u$ satellite state are shown in Fig. 6.10. Two aspects of this spectrum contradict the experimental data. First, even for large positive pump–probe delays, the simulated N_2^{++} yield is high. This can be explained with the shape of the $4\,\sigma_u$ PEC. Due to its pronounced potential minimum, parts of the Franck-Condon wave packet remain trapped. This bound amplitude will lead to the formation of stable N_2^{++} even for large delays which (to this extend) is not observed in the experimental spectrum. Thus the experimental data contradicts a PEC with a potential minimum within the Franck-Condon region.

The second discrepancy is the extremely short "half-life"[3] $T_{1/2}=(2.1\pm0.2)$ fs fitted to the simulated data. This is explained by the steepness of the $4\,\sigma_u$ PEC and the resulting acceleration of the wave packet. Thus, within a few femtoseconds the unbound parts of the wave packet gain enough kinetic energy to overcome the potential barrier

[3] This also causes the rising edge of the convolution to be shifted compared to the experiment.

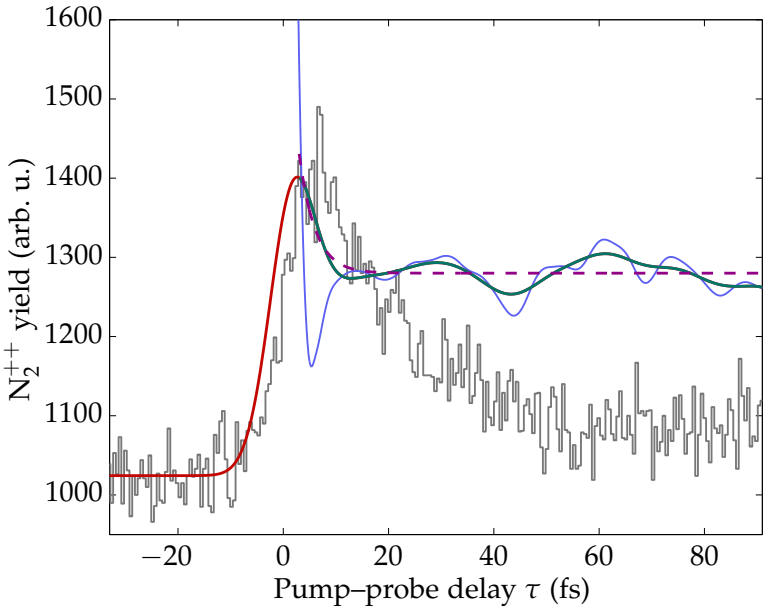

Fig. 6.10. Results of the simulation using the $4\sigma_u$ satellite PEC from Ref. [GRT+07] (see Fig. 6.5) compared to the experimental data (gray histogram). The blue curve gives the simulated N_2^{++} yield. The convolution with a 10 fs FWHM Gaussian function is plotted as a red and green curve. An exponential fit to the falling edge is plotted as a dashed purple curve. The fitted "half-life" is 2.1 fs. All fit parameters are summarized in Tab. 6.3.

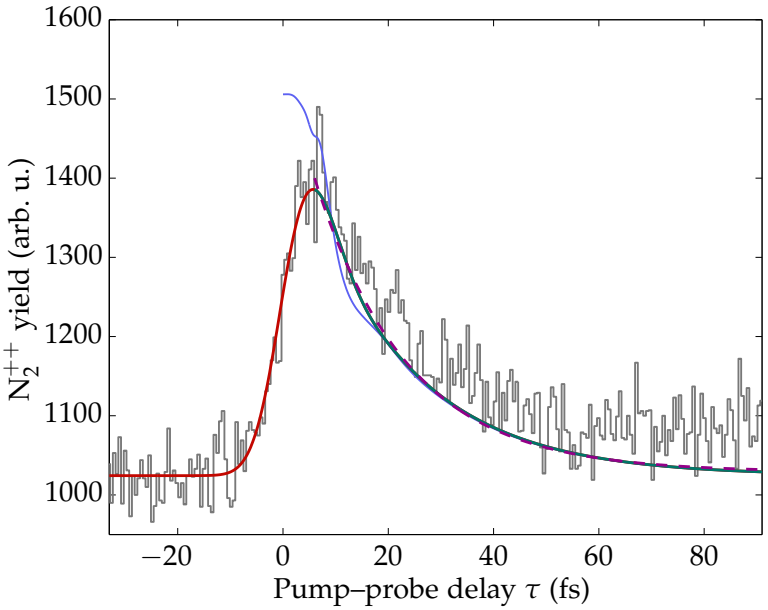

Fig. 6.11. Results of the simulation using the $3\,\sigma_u$ satellite PEC from Ref. [GRT+07] (see Fig. 6.5) compared to the experimental data (gray histogram). The blue curve gives the simulated N_2^{++} yield. The convolution with a 10 fs FWHM Gaussian function is plotted as a red and green curve. An exponential fit to the falling edge is plotted as a dashed purple curve. The fitted "half-life" is 12.2 fs. All fit parameters are summarized in Tab. 6.3.

of the dicationic PEC. Therefore, the large "half-life" in the experimental data can only be explained by an (almost) flat intermediate PEC.

These two constraints (flat PEC without potential minimum) are fulfilled by the $3\sigma_u$ satellite state calculated in Ref. [GRT+07] (see Fig. 6.5). The results of our simulation using this PEC are shown in Fig. 6.11. The (12.2 ± 0.6) fs "half-life" of the exponential fit is in excellent agreement with the experiment [$T_{1/2} = (11.6 \pm 1.5)$ fs]. In addition, the overall shape of the simulated N_2^{++} yield compares very well to the experiment.

Critical discussion of the simulation Despite the astonishing agreement between the experimental data and the simulated results using the $3\sigma_u$ PEC, the simulated data must be treated with care due to the following reasons.

- **Quality of the cationic PECs:** For all simulations presented, the PECs of N_2^+ satellite states calculated in Ref. [GRT+07] were used. These states were calculated using a mean-field method. In this, the energy of the excited electron is calculated in an effective potential created by the N_2^{++} ion. Electron correlations are thus not considered.

- **XUV ionization cross section and population of satellite states:** The XUV ionization cross section to different satellite states is not taken into account by our simulation. According to Ref. [GRT+07], the $N_2^+(4\sigma_u)$ satellite state is populated predominantly by ionization with a 40 eV photon. Simulations performed with this state, however, are in contradiction to the experimental data. Only by using the $N_2^+(3\sigma_u)$ satellite state, our calculations agree with the experiment. To which degree this specific state is populated by XUV ionization, is not discussed in Ref. [GRT+07].

- **N_2^+ PECs from other references:** N_2^+ PECs are predicted by various references [RLB75, BLK+92, HCR97, AIH+06]. Unfortunately none of the other highly excited PECs found in literature features a shape similar to that of the $N_2^+(3\sigma_u)$ satellite state calculated in Ref. [GRT+07]. Instead other predicted PECs are rather steep in the Franck-Condon region (see Fig. 6.4). All of these PECs will lead to a dissociation of the molecular ion within a few femtoseconds much faster than the timescales observed in the experiment. This has been verified for all PECs shown in Fig. 6.4 with quantum simulations.

- **Strong-field ionization:** The multi-photon ionization in the probe step is described in our simulation by a simplified model assuming a constant ionization cross section independent of the internuclear distance R. The simulated N_2^{++} yield might be modified if the ionization process is taken into account more accurately.

- **Coupling between N_2^+ PECs:** The density of states in highly excited N_2^+ is rather high (compare Fig. 6.4). Thus avoided crossings exist and Landau-Zener tunneling

processes [Zen32, Lan32] between different PECs might play a role. As a result, a single cationic PEC might not be enough to accurately describe the molecular dynamics.

- **N^+ KERs:** Ionization to the $N_2^+(3\sigma_u)$ satellite state followed by dissociation leads to very high KERs of about 13 eV. A pump–probe delay dependent yield of N^+ ions with this KER is expected because this dissociation is interrupted for small pump–probe delays by the probe pulse. In the experimental KER spectrum, however, such a delay dependence is not observed. This topic will be discussed in more detail in Sec. 6.5.

Taking these points into account, we conclude this section with the following remark: Only if a highly excited N_2^+ PEC which is flat in the Franck-Condon region is used in our calculations, the simulated results will be compatible with the experiment. To our knowledge, the only PEC predicted in literature fulfilling this condition is the $N_2^+(3\sigma_u)$ satellite state calculated in Ref. [GRT+07]. It will be shown in Sec. 6.5, however, that no delay dependence of the N^+ yield is observed for the KERs associated with the dissociation of the $3\sigma_u$ state. This indicates that the "real" PEC features a shape similar to the $3\sigma_u$ PEC predicted by Ref. [GRT+07], but with a different dissociation limit. Due to possible Landau-Zener transitions between different PECs, however, a combination of PECs featuring an effective shape similar to that of the $3\sigma_u$ satellite state must be as well considered as candidates for an intermediate state. A recently started collaboration with a theory group [GM15] will hopefully solve these issues and result in an unambiguous interpretation of the experimental data.

6.5. Pump–probe delay dependent yield of N^+ fragments

So far, only the delay dependence of the N_2^{++} yield has been discussed. According to the pump–probe scheme illustrated in Fig. 6.5, however, a delay dependence of the experimental N^+ yield is expected as well: The $N_2^+(4\sigma_u)$ satellite state is populated at an energy of about 39 eV and the dissociation limit is about 36 eV (see Fig. 6.5). As a result, if not further ionized by the IR pulse, N^+ ions with a KER of about 3 eV are created by the pump step (see also Ref. [GRT+07]). For positive pump–probe delays, however, the number of events with such a KER should be reduced due to the strong-field ionization by the IR pulse which either results in stable N_2^{++} or highly energetic N^+ ions due to the Coulomb explosion into $N^+ + N^+$.

The experimental N^+ counts as a function of the KER and the pump–probe delay are shown in Fig. 6.12. In this figure, the large number of N^+ ions resulting from the dissociation of the $N_2^+(F\,^2\Sigma_g^+)$ state (compare Sec. 6.2) masks the rather small delay dependent effects. For the pump–probe delays labeled *IR first*, the two step double ionization is not possible as discussed before. The average KER distribution for these pump–probe delays can therefore be considered as a background spectrum. By bin-wise

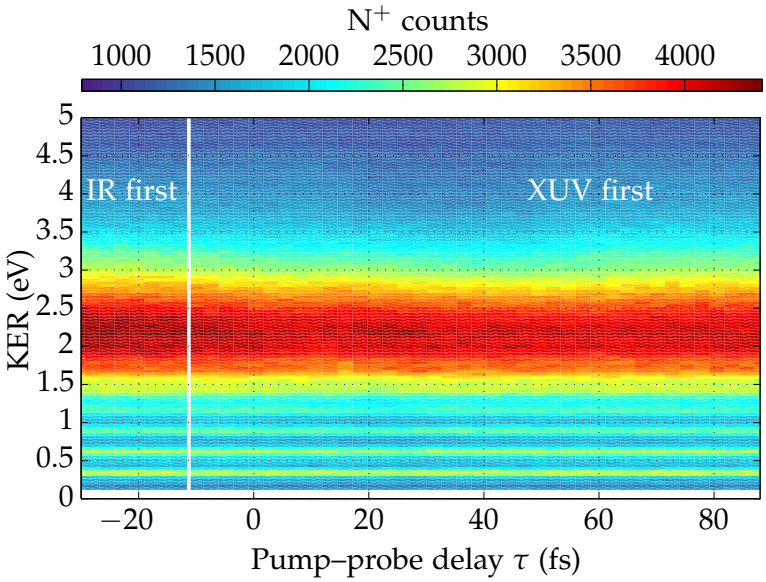

Fig. 6.12. Experimental N^+ yield as a function of the KER and the pump–probe delay.

subtracting this background from the KER distribution, the spectrum shown in Fig. 6.13 is obtained.

As expected, this spectrum shows a reduced number of N^+ ions with KERs between 2 and 3.5 eV for positive pump–probe delays. This is due to the multi-photon ionization by the IR pulse which results in stable N_2^{++} and in highly energetic fragments of the Coulomb explosion into $N^+ + N^+$. The reason for the slightly decreased N^+ yield at KERs between 3.5 and 4.5 eV at $\tau \approx 35$ fs as well as between 0.5 and 2 eV at $\tau \approx 20$ fs is unknown at this stage of the data evaluation.

As discussed in the previous section (Sec. 6.4), ionization to the $N_2^+(3\sigma_u)$ satellite state is favored by our simulations over the population of the $N_2^+(4\sigma_u)$ satellite state. The $3\sigma_u$ state is excited at about 37 eV and features a dissociation limit of only 24 eV. Thus population of this state would create a dissociation products with KERs of about 13 eV. For those KERs, however, no delay dependence is observed in our experimental data. The possibility that the $3\sigma_u$ PEC calculated in [GRT+07] does not resemble every detail of the "real" PEC involved in the sequential double ionization of N_2 must therefore be considered.

The number of two coincident N^+ fragments created with zero momentum sum (see Sec. 4.3.2) in the Coulomb explosion $N_2^{++} \rightarrow N^+ + N^+$ is plotted as a function of the KER and the pump–probe delay in Fig. 6.14. The yield is increased for positive pump–probe delays. In addition the KER decreases with increasing pump–probe delays. This was observed in Ref. [GRT+07] over a larger range of pump–probe delays up to 500 fs. The increased yield can be explained by a sequential double ionization via the $N_2^+(4\sigma_u)$

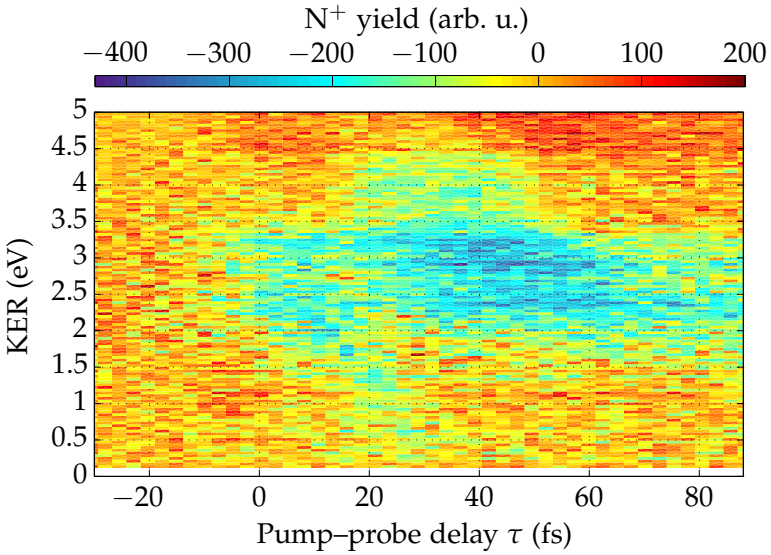

Fig. 6.13. Background subtracted experimental N^+ yield as a function of the KER and the pump–probe delay. The average KER spectrum for pump–probe delays labeled *IR fist* serves as a background spectrum. The N^+ yield at KERs between 2 and 3.5 eV is reduced for positive pump–probe delays.

satellite state. The KER decreases for increasing delay, because the separation between the $4\sigma_u$ PEC and the dicationic ground state decreases for increasing internuclear distance (compare Fig. 6.5).

6.6. Summary of the N_2 experiments

In the XUV–IR pump–probe experiment discussed in this chapter, a sequential double ionization of N_2 has been observed. The pump–probe scheme is illustrated in Fig. 6.5. For small time delays, the two-step process leads to the formation of stable N_2^{++} ions (see Fig. 6.1) and thus to an increased N_2^{++} yield. This yield decreases again with increasing pump–probe delay. The functional dependence on the time delay can be fitted by an exponential function with a "half-life" $T_{1/2} = (11.6 \pm 1.5)$ fs (see Fig. 6.6 and Tab. 6.2).

Results calculated with a simple quantum simulations were compared to the experimental data in Sec. 6.4. Using the $N_2^+(4\sigma_u)$ intermediate PEC in the simulation – which according to Ref. [GRT+07] is predominantly populated by the XUV ionization – yields results that are not compatible with our experiment (see Fig. 6.10). In contrast, the simulated results obtained with the $N_2^+(3\sigma_u)$ PEC are in excellent agreement with the experimental data as shown in Fig. 6.11.

The pump–probe delay dependent KER spectra of N^+ and coincident N^+ + N^+

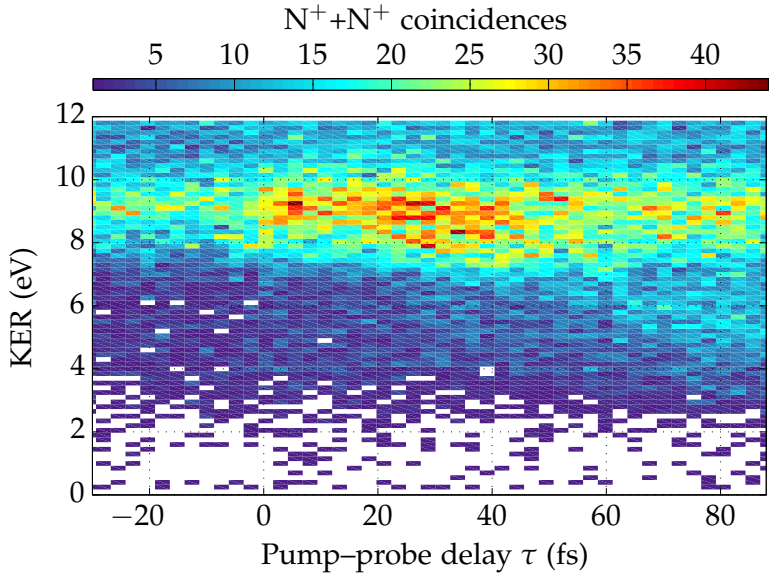

Fig. 6.14. Experimental yield of two coincident N^+ fragments as a function of the KER and the pump–probe delay. For positive pump–probe delays the yield is increased and the KER distribution is pump–probe delay dependent.

fragments (see Figs. 6.13 and 6.14) on the other hand are consistent with the $N_2^+(4\sigma_u)$ intermediate state. No pump–probe delay dependent N^+ yield caused by a dissociation of the $N_2^+(3\sigma_u)$ state could be identified.

In conclusion, the $N_2^+(3\sigma_u)$ satellite state cannot be unambiguously identified as the intermediate state in the sequential double ionization of N_2. Of all PECs known from literature, however, the $3\sigma_u$ is the only one being highly excited and nearly flat in the Franck-Condon region. Both properties are necessary to explain the experimental data. Thus the intermediate PEC either is the $3\sigma_u$ satellite state described in Ref. [GRT+07] or features many similarities to it in the Franck-Condon region.

7. Summary and outlook

In this thesis O_2 and N_2 was studied in XUV–IR pump–probe experiments. For this, the target molecules were ionized by a single photon from attosecond pulse train in the XUV energy region. The molecular dynamics triggered by the ionization was interpreted as a propagation of nuclear wave packets on Born-Oppenheimer potential energy curves (PEC). After a variable time delay, the wave packets are probed by an IR pulse, either by excitation (in the O_2 experiments) or by multi-photon ionization (in the N_2 experiments). Charged molecular fragments created in this process were detected using a reaction microscope.

These experiments are technically challenging since an XUV beam at constant intensity is needed for up to 72 hours acquisition time. Additionally, the interferometer used to mutually delay the pulses must be stable during this time. By a redesign of this interferometer as part of this thesis, the number of mirrors inside the interferometer arms was reduced by almost a factor of two. This and the accompanied reduction of the arm length resulted in an improved interferometric stability (see Sec. 3.2.4). Furthermore a good spatial overlap between XUV and IR pulse is required in order to obtain the highest possible contrast in pump–probe dependent reactions. By redesigning the XUV focusing system, the focal diameter of the pump–pulse was reduced significantly resulting in an improved pulse overlap (see Sec. 3.2.4). In addition, the XUV intensity within the reaction microscope was increased by the use of boron carbide coated (instead of gold coated) XUV focusing mirrors. Without those improvements on the experimental setup, the measurements summarized in the following could not have been performed successfully.

7.1. Summary of the O_2 experiments

The experiments on O_2 performed in the framework of this thesis were discussed in Chap. 5. In these measurements, the oscillating wave packet in the $O_2^+(a\,^4\Pi_u)$ PEC was examined for the first time with an XUV–IR pump–probe experiment. In the applied pump–probe scheme, the $a\,^4\Pi_u$ electronic state is coupled to the anti-bonding $O_2^+(f\,^4\Pi_g)$ state at internuclear distances of $R_c \approx 3.2$ a.u.. Thus population localized at R_c is probed to a weakly repulsive PEC leading to a dissociation of the molecular ion. Experimentally, the wave-packet oscillation manifests in a pump–probe delay dependent oscillatory yield of low energetic O^+ ions with a period of 40 fs (see Sec. 5.2.3). Using a large pump–probe delay range of 2 ps, we were able to fully trace

the first half-revival of the wave-packet oscillation at 1270 fs.

The QB energies, which can be identified with the vibrational level spacing in the binding potential, were obtained by a Fourier transform of the delay dependent O^+ yield (see Sec. 5.2.5). The QB energy $E_{QB} = 0.104\,eV$ of the strongest signal is in good agreement with the spacing between the vibrational levels with quantum numbers $v = 8, 9, 10$ in the $a\,^4\Pi_u$ PEC predicted in Ref. [MAT12]. There is a significant discrepancy between the QB energies observed in our experiment and those reported in a previous IR–IR pump–probe experiment (E_{QB} between 0.124 and 0.144 eV) [DMB+11]. The latter are not compatible with the theory either. This could be explained by the much higher probe intensity used in the IR–IR experiment.

Comparing the experimental results with coupled-channel simulations using different pairs of binding and repulsive PECs allows to test PECs calculated by Magrakvelidze et al. [MAT12] and Marian et al. [MMP+82] (see Sec. 5.3). Our simulations show that the repulsive $f\,^4\Pi_g$ PEC predicted by Ref. [MAT12] is not compatible with the experimental KER distribution. The experimental QB energies are very well reproduced if the binding $a\,^4\Pi_u$ PEC predicted by Ref. [MAT12] is used in our quantum calculations. Using the binding PEC from Ref. [MMP+82] results in smaller QB energies which contradict the experimental data. For both $a\,^4\Pi_u$ PECs predicted by theory, the simulated half-revival time is much larger than the experimental one.

Adjusting a Morse potential to the experimental data (see Sec. 5.2.4) allows to demonstrate the sensitivity of our method to small changes in the shape of the binding potential. Although the theoretically predicted PECs look very similar to the Morse potential, only simulations using the Morse potential can reproduce the experimentally observed half-revival time.

The energy resolution of the QB energies obtained from a Fourier transforming the experimental data, is only limited by the pump–probe delay. As shown in this work, an observed beating between only 3 vibrational states is sufficient to adjust a Morse potential which can be compared to predicted PECs. Thus XUV–IR pump–probe experiments could be used for high precision spectroscopy of vibrational states in molecular ions. A major drawback in our method is the necessity to resonantly couple two electronic states with the probe pulse. This limits the number of accessible vibrational states and the number of suitable PECs. If, however, the photon energy of the probe pulse could be tuned, XUV–IR pump–probe experiments could be used to obtain the shape of binding PECs in a large variety of diatomic molecules. Furthermore, tuning the probe wavelength would allow to access a larger number of vibrational states within a single PEC. With this, the shape of binding PECs could be "scanned" at varying internuclear distances [TNF08, MKBT14].

7.2. Summary of the N_2 experiments

In the N_2 experiments presented in Chap. 6, a dependence of the N_2^{++} yield on the XUV–IR pump–probe delay was observed. The increased N_2^{++} yield in the temporal overlap of the two pulses had been observed earlier but its underlaying mechanism could not be investigated due to a limited temporal resolution [GRT+07, Supplementary Material]. Employing shorter probe pulses, we observe a Gauss-error-function-like increase of the N_2^{++} yield in the temporal overlap. For small positive pump–probe delays (where the XUV pulse precedes the IR pulse), an exponential-like decrease of the N_2^{++} yield with a "half-life" of (11.6 ± 1.5) fs is observed.

Both features are explained in this work by a sequential double ionization involving an anti-bonding intermediate state (see Sec. 6.3.1). The cationic intermediate state is populated by ionization with the XUV pulse and its repulsive nature causes the molecular ion to dissociate. For small pump–probe delays, this dissociation can be interrupted by a multi-photon ionization with the IR pulse. This results in the formation of stable N_2^{++}.

Properties of the intermediate PEC were deduced by comparing the results of a simple quantum calculation with the experimental data. It turns out that the intermediate PEC is (almost) flat within the Franck-Condon region. Furthermore, the intermediate state must be highly excited to allow a few-photon ionization to the dicationic ground state. Of all PECs found in literature, these properties are only fulfilled by the $N_2^+(3\sigma_u)$ satellite state predicted in Ref. [GRT+07]. Simulations with this intermediate state are in excellent agreement with the experiment (see Sec. 6.4). Ref. [GRT+07], however, states that ionization with 40 eV XUV photons predominantly populates a different satellite state, namely the $N_2^+(4\sigma_u)$ state. Unfortunately, simulated results involving this intermediate state are in contradiction to the experimental data.

The situation is further complicated by the pump–probe delay dependent kinetic energy spectrum of N^+ fragments which shows signatures of a population of the $4\sigma_u$ state (see Sec. 6.4). A significant population of the $3\sigma_u$ state, on the other hand, is not supported by the N^+ spectrum.

In conclusion, an unambiguous identification of the intermediate state was not possible. The good agreement between our calculations and the experimental N_2^{++} yield indicates, however, that the involved intermediate state either is the $N_2^+(3\sigma_u)$ state predicted by Ref. [GRT+07] or resembles it within the Franck-Condon region. We are currently in contact with a theory group that might be able to calculate the PECs of the satellite states mentioned in Ref. [GRT+07] with a more sophisticated method. Due to their high excitation, this is a challenging task [GM15]. With the improved PECs, we might be able to resolve the remaining issues in the interpretation of our data.

7.3. Outlook

Ionization of molecules with broadband XUV radiation results in the excitation of a large number of electronic states. It has been shown in the analysis of the O_2 data that reactions in diatomic molecules can still be disentangled if PECs available. The N_2 experiments, on the other hand have shown that without reliable PECs predicted by theory, an unambiguous data interpretation is often very difficult and sometimes even impossible. This is even worse, if poly-atomic molecules are investigated, as the molecular dynamics occurs on multi-dimensional surfaces due to the additional degrees of freedom in the nuclear frame [Cör12, Sch15].

These issues are partially solved by reducing the bandwidth of the XUV pulse. If the energy $E_{\hbar\omega}$ of the absorbed photon is known precisely, the coincident measurement of the photoelectron energy E_e and the KER with the reaction microscope allows to pin down the electronic state populated during an ionization using the equation

$$E_{\hbar\omega} = \mathrm{KER} + E_e + E_{\mathrm{diss}}. \tag{7.1}$$

Here E_{diss} denotes the dissociation limit of the excited state. We are therefore working on methods to reduce the XUV bandwidth.

If the high-harmonic generation (HHG) occurs inside a glass capillary, the XUV spectrum can be tuned by varying the target gas pressure [DRB+99]. Such an HHG source is currently set up in our lab and characterized in the framework of a bachelor's project [Pal15]. In addition to that, normal incidence multi-layer optics instead of grazing incidence mirrors could serve as a wavelength filter in the XUV region as demonstrated in other experimental setups [GRT+07, SGS+08, ZRH+12].

The XUV pulses currently used in our experiment are created by HHG in an argon gas target. This results in photon energies up to 40 eV with the most intense harmonics being in the energy region between 30 and 38 eV (see Sec. 3.2.4). The double ionization threshold of most diatomic molecules and noble gases lies above[1] 38 eV. Thus the study of processes involving a double ionization in the pump step is difficult with the existing XUV source. By using a neon gas target, our beamline is capable of creating photon energies above 70 eV [Rie07, p. 57]. In this case, however, the conversion efficiency is drastically reduced. Thus, the XUV pulse intensities obtained by HHG in neon are currently to low for experiments with the reaction microscope.

The XUV photon flux could be increased by several methods in the near future. First, the already mentioned use of a glass capillary as a HHG target might lead to a better conversion efficiency compared to the aluminum tube. Replacing the 200 nm aluminum filter by a 100 nm filter can further increase the XUV flux inside the reaction microscope. Finally, replacing the two-mirror XUV focusing system described in Sec. 3.2.4 by a single toroidal mirror would decrease the losses. A possible side effect of the last

[1] Xenon is an exception with a double ionization potential of about 33 eV.

measure is a reduced focal spot size of the XUV beam which would improve the spatial overlap with the IR probe pulse.

Appendices

A. Atomic unit system and other non-SI units

In atomic and molecular physics, the atomic unit system is commonly used. In this system, electron mass m_e, elementary charge e, the classical Bohr radius a_0, the Planck's constant $\hbar$ and $1/(4\pi\epsilon_0)$ with the electric constant ϵ_0 are set to unity. "a.u." is the symbol used for any quantity given in atomic units. Table A.1 gives a selection of atomic units and their conversion factor to SI units.

Quantity	Expression	Value in SI units
mass	m_e	$9.109 \times 10^{-31}\,\mathrm{kg}$
charge	e	$1.602 \times 10^{-19}\,\mathrm{C}$
length	a_0	$5.292 \times 10^{-11}\,\mathrm{m}$
angular momentum	$\hbar = h/(2\pi)$	$1.055 \times 10^{-34}\,\mathrm{kg\,m^2\,s^{-1}}$
energy	$\hbar^2/(m_e a_0^2)$	$4.360 \times 10^{-18}\,\mathrm{J}$
time	$m_e a_0^2/\hbar$	$2.419 \times 10^{-17}\,\mathrm{m\,s^{-1}}$
velocity	$\hbar/(m_e a_0^2) = c\alpha$	$2.188 \times 10^{6}\,\mathrm{kg}$
momentum	$\hbar/a_0$	$1.993 \times 10^{-24}\,\mathrm{kg\,m\,s^{-1}}$

Tab. A.1. Atomic units. Table copied from [Sen09].

The unit gauss with the abbreviation G is used to quantify the magnetic field of the reaction microscope. The conversion to the SI unit Tesla is

$$1\,\mathrm{G} = 1 \times 10^{-4}\,\mathrm{T}.$$

B. Hamilton operator of diatomic molecule

The Hamilton operator of a diatomic molecule (see illustration in Fig. 2.1) is introduced in the following. In the center-of-mass coordinates, the kinetic energy operator of the nuclei $\hat{T}_n$ and that of the N electrons $\hat{T}_e$ (in atomic units) reads

$$\hat{T}_n = -\frac{1}{2\mu}\nabla_R^2 \quad \text{and} \quad \hat{T}_e = -\sum_{i=1}^{N}\nabla_{\boldsymbol{r}_i}^2, \tag{B.1}$$

respectively. Here we use the reduced mass $\mu = M_A M_B/(M_A + M_B)$.

The Hamilton operator describing a molecule with N electrons is then given by[1]

$$\hat{H} = \hat{T}_n + \hat{T}_e + V(\boldsymbol{r}, \boldsymbol{R}), \tag{B.2}$$

with the Coulomb potential $V(\boldsymbol{r}, \boldsymbol{R})$ for all particle pairs

$$V(\boldsymbol{r}, \boldsymbol{R}) = -\sum_{i=1}^{N}\frac{Z_A}{|\boldsymbol{r}_i - \boldsymbol{R}_A|} - \sum_{i=1}^{N}\frac{Z_B}{|\boldsymbol{r}_i - \boldsymbol{R}_B|} + \sum_{i<i'}\sum_{i=1}^{N}\frac{1}{|\boldsymbol{r}_i - \boldsymbol{r}_i'|} + \frac{Z_A Z_B}{R}, \tag{B.3}$$

introducing the internuclear distance $R = |\boldsymbol{R}_B - \boldsymbol{R}_A|$ and the electron coordinates $\boldsymbol{r}_i$.

[1] Here and in the following, vectors are represented by bold variables.

C. Results of coupled-channel simulations for varying IR pulse parameters

The coupled-channel simulation is used in the following to test the influence of various IR pulse parameters, such as a pulse pedestal, the IR intensity and the IR pulse length. The Morse potential (red curve in Fig. 5.14) and the repulsive $O_2^+(f\,^4\Pi_g)$ PEC calculated in Ref. [MMP+82] (blue curve in Fig. 5.14) were used in all simulations presented here.

Low IR intensities The quantum-beat energies do not shift, if the simulation is performed with lower probe intensities than the $3 \times 10^{12}\,\mathrm{W/cm^2}$ used in our experiment. This is shown in Fig. C.1.

IR pulse pedestal Due to their spiky frequency spectrum, femtosecond laser pulses spectrally broadened with a hollow-core fiber are known to have so-called pulse pedestals reaching up to a few percent of the pulse peak intensity. The influence of a pedestal with several hundred femtosecond duration on the observed wave-packet dynamics is simulated in this section. The results are plotted in Figs. C.2 and C.3. In these the experimental data is plotted in panels (a). In panel (b), the simulation is performed with a Gaussian probe pulse with 12 fs (intensity) FWHM envelope without a pedestal. In panels (c) and (d) an additional Gaussian pedestal of 120 fs (intensity) FWHM intensity is taken into account. The peak intensity of this pedestal is 0.25 % and 1 % of the pulse peak intensity in the panels (c) and (d) respectively.

Figures C.2 and C.3 show, that the pulse pedestal has very little effect on the QB spectrum and the revival time. The simulated KER distribution in the time domain (Fig. C.2) is strongly modified. Due to the pedestal, the KER distribution gets more confined to two bands at KER ≈ 0.22 eV and KER ≈ 0.02 eV. This has been simulated for example in Refs. [TNF08,MAT12] resulting in comparable effects. The interpretation is that the temporal resolution is decreased due to the longer effective pulse duration. Thus according to Heisenberg's uncertainty principle the (kinetic) energy resolution increases [MAT12].

IR pulse length It was discussed before that the laser pulse length in a pump–probe experiment must be shorter than typical timescales of motion in order to temporally resolve the dynamics. In this section, the experimental results are compared to the quantum simulations using different probe pulse lengths. In the pump–probe delay

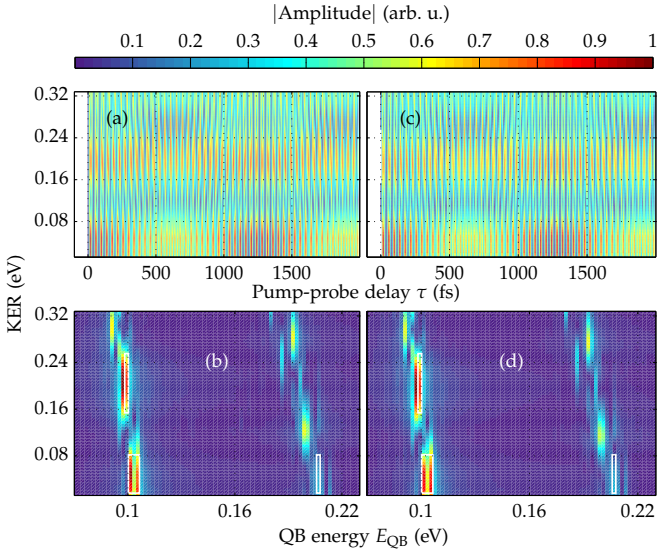

Fig. C.1. Simulated spectra. **Panel (a) and (b):** Simulated data for a probe pulse intensities of $3 \times 10^{12}\,\mathrm{W/cm^2}$ peak intensity corresponding to the experimental pulse parameters. **Panel (c) and (d):** Simulated data for a probe pulse intensities of $3 \times 10^{11}\,\mathrm{W/cm^2}$ peak intensity much lower than the experimental parameter.

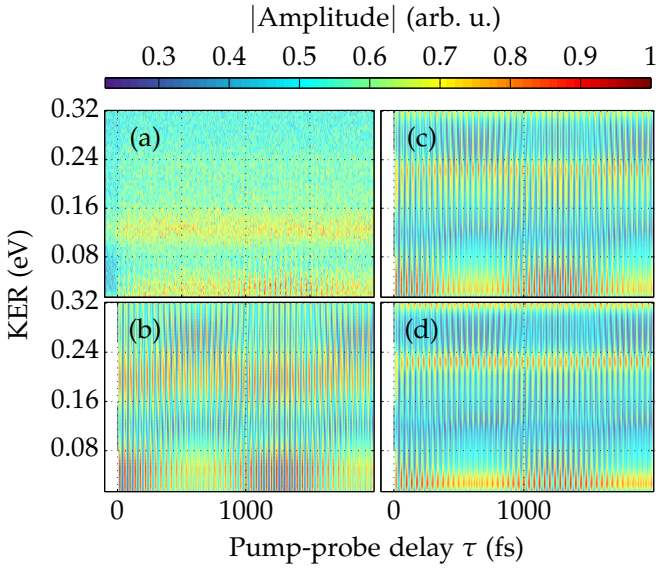

Fig. C.2. Comparison of experimental results with the results of simulations using different Gaussian IR pulse pedestals with 120 fs intensity FWHM. The other pulse parameters are as listed in Tab. 5.1. The Morse potential and the (shifted) repulsive curve from Ref. [MMP+82] are used in the simulation. **Panel (a):** Experimental data. Simulations: **Panel (b):** No pulse pedestal. **Panel (c):** Pedestal peak intensity is 0.25 % of the pulse peak intensity. **Panel (d):** Pedestal peak intensity is 1 % of the pulse peak intensity.

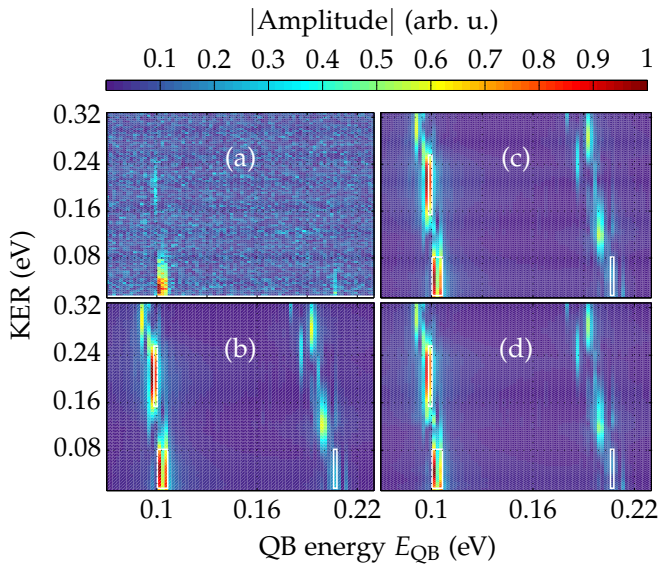

Fig. C.3. QB spectrum of Fig. C.2. **Panel (a):** Experimental data. Simulations using different pedestal peak intensities: **Panel (b):** No pulse pedestal. **Panel (c):** Pedestal peak intensity is 0.25 % of the pulse peak intensity. **Panel (d):** Pedestal peak intensity is 1 % of the pulse peak intensity. See caption of Fig. C.2 for more details.

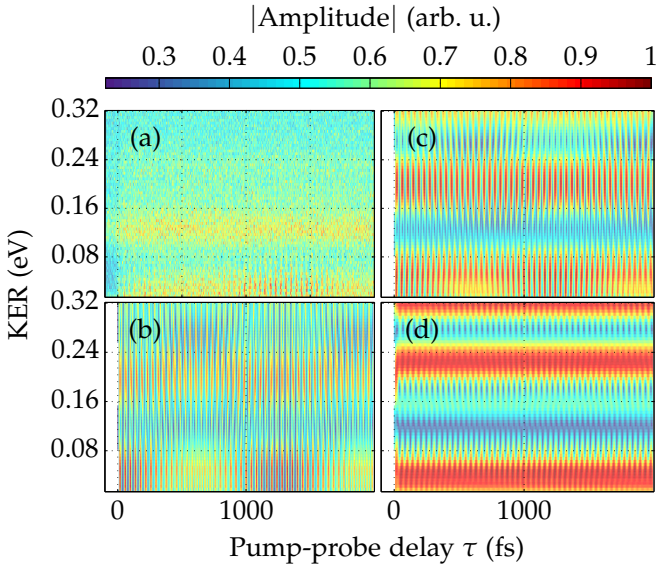

Fig. C.4. Comparison of experimental results with the results of simulations using different IR pulse lengths. The other pulse parameters are as listed in Tab. 5.1. The Morse potential and the (shifted) repulsive curve from Ref. [MMP+82] are used in the simulation. **Panel (a):** Experimental data. Probe pulse length (intensity FWHM): **Panel (b):** 12 fs. **Panel (c):** 20 fs. **Panel (d):** 40 fs.

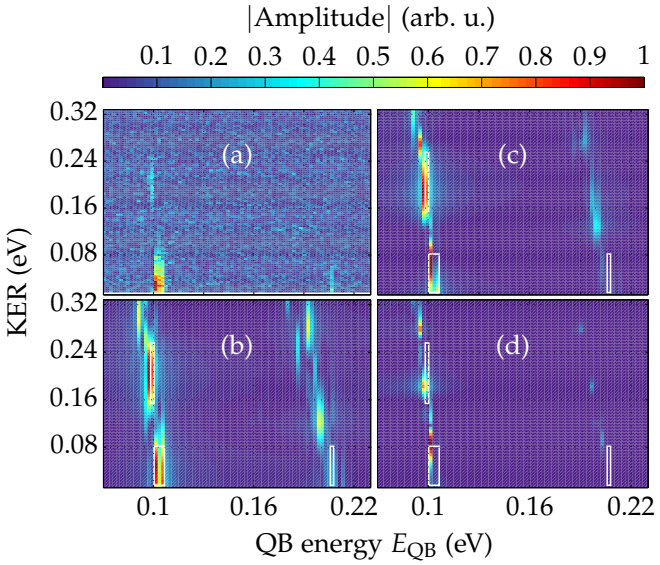

Fig. C.5. QB spectrum of Fig. C.4. **Panel (a):** Experimental data. Probe pulse length (intensity FWHM): **Panel (b):** 12 fs. **Panel (c):** 20 fs. **Panel (d):** 40 fs. See caption of Fig. C.4 for more details.

dependent plots (Fig. C.4), the modulation depth of pump–probe dependent count rate is clearly reduced for larger pulse lengths. In the QB spectra (Fig. C.5), however, the QB energy of the signals does not change drastically. Note that for increasing pulse length (Fig. C.5 (c) and (d)) the line at $E_{QB} \approx 0.1$ eV splits into two signals separated in the KER. This is why this line might seem to have shifted in Fig. C.5 (d) on the first glance. The splitting in KER can be explained by resolving the vibrational states in the KER spectrum (this is related to the simulations with a pulse pedestal and their discussion). This has been observed in simulations of an XUV–IR pump–probe experiment in H_2 previously and was interpreted in terms of Floquet states [KLS+09].

Bibliography

[AD04] Pierre Agostini and Louis F. DiMauro. The physics of attosecond light pulses. *Reports on Progress in Physics*, 67(6):813–, 2004. [cited on p. 31]

[ADK86] M. V. Ammosov, N. B. Delone, and V. P. Krainov. Tunnel ionization of complex atoms and of atomic ions in an alternating electromagnetic field. *Soviet Physics - JETP*, 64(6):1191–1194, 1986. [cited on p. 25]

[AFM+79] P. Agostini, F. Fabre, G. Mainfray, G. Petite, and N. K. Rahman. Free-Free Transitions Following Six-Photon Ionization of Xenon Atoms. *Phys. Rev. Lett.*, 42(17):1127–1130, April 1979. [cited on p. 25]

[AGH+96] A. Assion, M. Geisler, J. Helbing, V. Seyfried, and T. Baumert. Femtosecond pump-probe photoelectron spectroscopy: Mapping of vibrational wave-packet motion. *Phys. Rev. A*, 54(6):R4605–R4608, December 1996. [cited on p. 80]

[AHW+96] S. H. Ashworth, T. Hasche, M. Woerner, E. Riedle, and T. Elsaesser. Vibronic excitations of large molecules in solution studied by two-color pump-probe experiments on the 20 fs time scale. *The Journal of Chemical Physics*, 104(15):5761–5769, 1996. [cited on p. 80]

[AIH+06] Tomohiro Aoto, Kenji Ito, Yasumasa Hikosaka, Akihiro Shibasaki, Ryo Hirayama, Norifumi Yamamono, and Eisaku Miyoshi. Inner-valence states of N_2^+ and the dissociation dynamics studied by threshold photoelectron spectroscopy and configuration interaction calculation. *The Journal of Chemical Physics*, 124(23):–, 2006. [cited on p. 118, 119, 130]

[AKS+14] A.S. Alnaser, M. Kübel, R. Siemering, B. Bergues, Nora G Kling, K.J. Betsch, Y. Deng, J. Schmidt, Z.A. Alahmed, A.M. Azzeer, J. Ullrich, I. Ben-Itzhak, R. Moshammer, U. Kleineberg, F. Krausz, R. de Vivie-Riedle, and M.F. Kling. Subfemtosecond steering of hydrocarbon deprotonation through superposition of vibrational modes. *Nat Commun*, 5:–, May 2014. [cited on p. 5]

[ALO+06] A. S. Alnaser, I. Litvinyuk, T. Osipov, B. Ulrich, A. Landers, E. Wells, C. M. Maharjan, P. Ranitovic, I. Bochareva, D. Ray, and C. L. Cocke. Momentum-imaging investigations of the dissociation of D_2^+ and the isomerization of

acetylene to vinylidene by intense short laser pulses. *Journal of Physics B: Atomic, Molecular and Optical Physics*, 39(13):S485–, 2006. [cited on p. 4]

[AMW+85] T. Akahori, Y. Morioka, M. Watanabe, T. Hayaishi, K. Ito, and M. Nakamura. Dissociation processes of O_2 in the VUV region 500-700 Å. *Journal of Physics B: Atomic and Molecular Physics*, 18(11):2219–, 1985. [cited on p. 84]

[AUT+05] A. Alnaser, B. Ulrich, X. Tong, I. Litvinyuk, C. Maharjan, P. Ranitovic, T. Osipov, R. Ali, S. Ghimire, Z. Chang, C. Lin, and C. Cocke. Simultaneous real-time tracking of wave packets evolving on two different potential curves in $H_2{}^+$ and $D_2{}^+$. *Phys. Rev. A*, 72:030702, Sep 2005. [cited on p. 4, 80]

[Bal85] J. J. Balmer. Notiz über die Spectrallinien des Wasserstoffs. *Ann. Phys.*, 261(5):80–87, 1885. [cited on p. 9]

[BAT+11] I. Bocharova, A. Alnaser, U. Thumm, T. Niederhausen, D. Ray, C. Cocke, and I. Litvinyuk. Time-resolved Coulomb-explosion imaging of nuclear wave-packet dynamics induced in diatomic molecules by intense few-cycle laser pulses. *Phys. Rev. A*, 83:013417, Jan 2011. [cited on p. 80]

[BDMK98] Sterling Backus, Charles G. Durfee, Margaret M. Murnane, and Henry C. Kapteyn. High power ultrafast lasers. *Review of Scientific Instruments*, 69(3):1207–1223, 1998. [cited on p. 51, 52]

[BE03] Stephen J. Blanksby and G. Barney Ellison. Bond dissociation energies of organic molecules. *Accounts of Chemical Research*, 36(4):255–263, 2003. PMID: 12693923. [cited on p. 3]

[BGTG91] T. Baumert, M. Grosser, R. Thalweiser, and G. Gerber. Femtosecond time-resolved molecular multiphoton ionization: The Na_2 system. *Phys. Rev. Lett.*, 67(27):3753–3756, December 1991. [cited on p. 80]

[BK00] Thomas Brabec and Ferenc Krausz. Intense few-cycle laser fields: Frontiers of nonlinear optics. *Rev. Mod. Phys.*, 72(2):545–591, April 2000. [cited on p. 5, 25, 29]

[BLHE12] Wilhelm Becker, XiaoJun Liu, Phay Jo Ho, and Joseph H. Eberly. Theories of photoelectron correlation in laser-driven multiple atomic ionization. *Rev. Mod. Phys.*, 84:1011–1043, Jul 2012. [cited on p. 31]

[BLK+92] P. Baltzer, M. Larsson, L. Karlsson, B. Wannberg, and M. Carlsson Göthe. Inner-valence states of N_2^+ studied by uv photoelectron spectroscopy and configuration-interaction calculations. *Phys. Rev. A*, 46(9):5545–5553, November 1992. [cited on p. 130]

[BMR10] Laimutis Bytautas, Nikita Matsunaga, and Klaus Ruedenberg. Accurate ab initio potential energy curve of O_2. II. core-valence correlations, relativistic contributions, and vibration-rotation spectrum. *The Journal of Chemical Physics*, 132(7):074307, 2010. [cited on p. 82, 102, 110]

[BO27] M. Born and R. Oppenheimer. Zur Quantentheorie der Molekeln. *Ann. Phys.*, 389(20):457–484, 1927. [cited on p. 10]

[Boy08] Robert Boyd. *Nonlinear Optics*. Academic Press, third edition edition, 2008. [cited on p. 47]

[Cam84] R. Campargue. Progress in overexpanded supersonic jets and skimmed molecular beams in free-jet zones of silence. *J. Phys. Chem.*, 88(20):4466–4474, September 1984. [cited on p. 64]

[Cam13] Nicolas Camus. *Non-sequential double ionization of atoms with phase-controlled ultra-short laser pulses*. PhD thesis, Ruperto-Carola University of Heidelberg, Germany, 2013. [cited on p. 77]

[CAT+14] F. Calegari, D. Ayuso, A. Trabattoni, L. Belshaw, S. De Camillis, S. Anumula, F. Frassetto, L. Poletto, A. Palacios, P. Decleva, J. B. Greenwood, F. Martín, and M. Nisoli. Ultrafast electron dynamics in phenylalanine initiated by attosecond pulses. *Science*, 346(6207):336–339, 2014. [cited on p. 6]

[CDS+10] W. Cao, S. De, K. P. Singh, S. Chen, M. S. Schöffler, A. S. Alnaser, I. A. Bocharova, G. Laurent, D. Ray, S. Zherebtsov, M. F. Kling, I. Ben-Itzhak, I. V. Litvinyuk, A. Belkacem, T. Osipov, T. Rescigno, and C. L. Cocke. Dynamic modification of the fragmentation of CO^{q+} excited states generated with high-order harmonics. *Phys. Rev. A*, 82(4):043410–, October 2010. [cited on p. 6]

[CFR85] K. Codling, L. J. Frasinski, and K. J. Randall. Competition between autoionisation and predissociation in the Rydberg series approaching the $c\,^4\Sigma_u^-$ state of O_2^+. *Journal of Physics B: Atomic and Molecular Physics*, 18(9):L251–, 1985. [cited on p. 84]

[CFS+15] Philipp Cörlin, Andreas Fischer, Michael Schönwald, Alexander Sperl, Tomoya Mizuno, Uwe Thumm, Thomas Pfeifer, and Robert Moshammer. Probing calculated O_2^+ potential-energy curves with an XUV-IR pump-probe experiment. *Phys. Rev. A*, 91(4):043415–, April 2015. [cited on p. 79, 80, 89, 96, 99, 104]

[Cha11] Zenghu Chang. *Fundamentals of attosecond optics*. CRC Press, 2011. [cited on p. 29, 30, 31]

[CLD+11] W. Cao, G. Laurent, S. De, M. Schöffler, T. Jahnke, A. S. Alnaser, I. A. Bocharova, C. Stuck, D. Ray, M. F. Kling, I. Ben-Itzhak, Th. Weber, A. L. Landers, A. Belkacem, R. Dörner, A. E. Orel, T. N. Rescigno, and C. L. Cocke. Dynamic modification of the fragmentation of autoionizing states of O_2^+. *Phys. Rev. A*, 84:053406, Nov 2011. [cited on p. 96]

[Cor93] P. B. Corkum. Plasma perspective on strong field multiphoton ionization. *Phys. Rev. Lett.*, 71(13):1994–1997, September 1993. [cited on p. 29, 30]

[Cör12] Philipp Cörlin. *Laser induced Coulomb-explosion of allene molecules: Experiment and simulation*. Diploma thesis, Ruprecht-Karls-Universität, Heidelberg, 2012. [cited on p. 138]

[CZC14] Michael Chini, Kun Zhao, and Zenghu Chang. The generation, characterization and applications of broadband isolated attosecond pulses. *Nat Photon*, 8(3):178–186, March 2014. [cited on p. 31]

[DBM+10] S. De, I. Bocharova, M. Magrakvelidze, D. Ray, W. Cao, B. Bergues, U. Thumm, M. Kling, I. Litvinyuk, and C. Cocke. Tracking nuclear wave-packet dynamics in molecular oxygen ions with few-cycle infrared laser pulses. *Phys. Rev. A*, 82:013408, Jul 2010. [cited on p. 4, 80]

[Dem10] Wolfgang Demtröder. *Atoms, Molecules and Photons - An Introduction to Atomic-, Molecular- and Quantum Physics*. Springer-Verlag Berlin Heidelberg, 2 edition, 2010. [cited on p. 10, 12, 13, 15]

[Dem14] Wolfgang Demtröder. *Laser Spectroscopy 1 - Basic Principles*. Springer-Verlag Berlin Heidelberg, 5 edition, 2014. [cited on p. 44]

[Dem15] Wolfgang Demtröder. *Laser Spectroscopy 2 - Experimental Techniques*. Springer-Verlag Berlin Heidelberg, 5 edition, 2015. [cited on p. 51]

[DJZ91] M. Dantus, M. H. M. Janssen, and A. H. Zewail. Femtosecond probing of molecular dynamics by mass-spectrometry in a molecular beam. *Chemical Physics Letters*, 181(4):281–287, June 1991. [cited on p. 80]

[DK00] Nikolai B. Delone and V. P. Krainov. *Multiphoton Processes in Atoms*. Springer Berlin Heidelberg, 2000. [cited on p. 25]

[DMB+11] S. De, M. Magrakvelidze, I. A. Bocharova, D. Ray, W. Cao, I. Znakovskaya, H. Li, Z. Wang, G. Laurent, U. Thumm, M. F. Kling, I. V. Litvinyuk, I. Ben-Itzhak, and C. L. Cocke. Following dynamic nuclear wave packets in N_2, O_2, and CO with few-cycle infrared pulses. *Phys. Rev. A*, 84(4):043410–, October 2011. [cited on p. 4, 80, 82, 93, 100, 111, 136]

[DR06] Jean-Claude Diels and Wolfgang Rudolph. *Ultrashort Laser Pulse Phenomena: Fundamentals, Techniques, and Applications on a Femtosecond Time Scale*. Academic Press, 2006. [cited on p. 46, 47]

[DRB+99] Charles G. Durfee, Andy R. Rundquist, Sterling Backus, Catherine Herne, Margaret M. Murnane, and Henry C. Kapteyn. Phase Matching of High-Order Harmonics in Hollow Waveguides. *Phys. Rev. Lett.*, 83:2187–2190, Sep 1999. [cited on p. 138]

[DSS68] P. H. Doolittle, R. I. Schoen, and K. E. Schubert. Dissociative Photoionization of O_2. *The Journal of Chemical Physics*, 49(11):5108–5115, 1968. [cited on p. 84]

[Dun62] Gordon H. Dunn. Anisotropies in Angular Distributions of Molecular Dissociation Products. *Phys. Rev. Lett.*, 8(2):62–64, January 1962. [cited on p. 20]

[Ede04] J.G. Eden. High-order harmonic generation and other intense optical field-matter interactions: review of recent experimental and theoretical advances. *Progress in Quantum Electronics*, 28(3-4):197–246, 2004. [cited on p. 31]

[EPC+08] P. Eckle, A. N. Pfeiffer, C. Cirelli, A. Staudte, R. Dörner, H. G. Muller, M. Büttiker, and U. Keller. Attosecond Ionization and Tunneling Delay Time Measurements in Helium. *Science*, 322(5907):1525–1529, 2008. [cited on p. 21]

[ERF+05] Th. Ergler, A. Rudenko, B. Feuerstein, K. Zrost, C. D. Schröter, R. Moshammer, and J. Ullrich. Time-Resolved Imaging and Manipulation of H_2 Fragmentation in Intense Laser Fields. *Phys. Rev. Lett.*, 95(9):093001–, August 2005. [cited on p. 4, 80]

[ERF+06] Th. Ergler, A. Rudenko, B. Feuerstein, K. Zrost, C. D. Schröter, R. Moshammer, and J. Ullrich. Spatiotemporal Imaging of Ultrafast Molecular Motion: Collapse and Revival of the $D_2{}^+$ Nuclear Wave Packet. *Phys. Rev. Lett.*, 97:193001, Nov 2006. [cited on p. 4]

[Erg06] Thorsten Ergler. *Zeitaufgelöste Untersuchungen zur Fragmentationsdynamik von H_2 (D_2) in ultra-kurzen Laserpulsen*. PhD thesis, Ruperto-Carola University of Heidelberg, Germany, 2006. [cited on p. 21]

[Erm76] Peter Erman. Direct Measurement of the N_2^+ *C* State Predissociation Probability. *Physica Scripta*, 14(1-2):51–, 1976. [cited on p. 118]

[EWK+06] A. Ehresmann, L. Werner, S. Klumpp, Ph. V. Demekhin, M. P. Lemeshko, V. L. Sukhorukov, K-H. Schartner, and H. Schmoranzer. Predissociation of the N $_2^+(C\,^2\Sigma_u^+)$ state observed via $C\,^2\Sigma_u^+ \rightarrow X\,^2\Sigma_g^+$ fluorescence after resonant $1s^{-1}\pi^*$ excitation of N_2 molecule. *Journal of Physics B: Atomic, Molecular and Optical Physics*, 39(6):L119–, 2006. [cited on p. 118]

[Fec14] Lutz Fechner. *High resolution experiments on strong-field ionization of atoms and molecules: test of tunneling theory, the role of doubly excited states, and channel-selective electron spectra*. PhD thesis, Ruperto-Carola University of Heidelberg, Germany, 2014. [cited on p. 23]

[FER+07] B. Feuerstein, Th. Ergler, A. Rudenko, K. Zrost, C. D. Schröter, R. Moshammer, J. Ullrich, T. Niederhausen, and U. Thumm. Complete Characterization of Molecular Dynamics in Ultrashort Laser Fields. *Phys. Rev. Lett.*, 99:153002, Oct 2007. [cited on p. 80, 89]

[FGC+14] A. Fischer, M. Gärttner, P. Cörlin, A. Sperl, M. Schönwald, T. Mizuno, G. Sansone, A. Senftleben, J. Ullrich, B. Feuerstein, T. Pfeifer, and R. Moshammer. Molecular wave-packet dynamics on laser-controlled transition states. *ArXiv e-prints*, October 2014. [cited on p. 80, 92, 94, 111]

[FGG+12] D. Fischer, D. Globig, J. Goullon, M. Grieser, R. Hubele, V. L. B. de Jesus, A. Kelkar, A. LaForge, H. Lindenblatt, D. Misra, B. Najjari, K. Schneider, M. Schulz, M. Sell, and X. Wang. Ion-Lithium Collision Dynamics Studied with a Laser-Cooled In-Ring Target. *Phys. Rev. Lett.*, 109:113202, Sep 2012. [cited on p. 63]

[Fis03] Daniel Fischer. *Mehr-Teilchen-Dynamik in der Einfach- und Doppelionisation von Helium durch geladene Projektile*. PhD thesis, Ruprecht-Karls-Universität, Heidelberg, 2003. [cited on p. 65, 73]

[Fis15] Andreas Fischer. *Dissociative Photoionization of Molecular Hydrogen – A Joint Experimental and Theoretical Study of the Electron-Electron Correlations induced by XUV Photoionization and Nuclear Dynamics on IR-Laser Dressed Transition States*. PhD thesis, Ruperto-Carola University of Heidelberg, Germany, 2015. [cited on p. 26, 27, 38, 39, 92, 100]

[FKD+14] Avner Fleischer, Ofer Kfir, Tzvi Diskin, Pavel Sidorenko, and Oren Cohen. Spin angular momentum and tunable polarization in high-harmonic generation. *Nat Photon*, 8(7):543–549, July 2014. [cited on p. 31]

[FKZ+04] M. Fischer, N. Kolachevsky, M. Zimmermann, R. Holzwarth, Th. Udem, T. W. Hänsch, M. Abgrall, J. Grünert, I. Maksimovic, S. Bize, H. Marion, F. Pereira Dos Santos, P. Lemonde, G. Santarelli, P. Laurent, A. Clairon,

C. Salomon, M. Haas, U. D. Jentschura, and C. H. Keitel. New Limits on the Drift of Fundamental Constants from Laboratory Measurements. *Phys. Rev. Lett.*, 92(23):230802–, June 2004. [cited on p. 43]

[FLL+88] M. Ferray, A. L'Huillier, X. F. Li, L. A. Lompre, G. Mainfray, and C. Manus. Multiple-harmonic conversion of 1064 nm radiation in rare gases. *Journal of Physics B: Atomic, Molecular and Optical Physics*, 21(3):L31–, 1988. [cited on p. 5, 28]

[FRC85] L. J. Frasinski, K. J. Randall, and K. Codling. Predissociation of the $c\,^4\Sigma_u^-$ state of O_2^+. *Journal of Physics B: Atomic and Molecular Physics*, 18(5):L129–, 1985. [cited on p. 84]

[FSC+13] Andreas Fischer, Alexander Sperl, Philipp Cörlin, Michael Schönwald, Helga Rietz, Alicia Palacios, Alberto González-Castrillo, Fernando Martín, Thomas Pfeifer, Joachim Ullrich, Arne Senftleben, and Robert Moshammer. Electron Localization Involving Doubly Excited States in Broadband Extreme Ultraviolet Ionization of H_2. *Phys. Rev. Lett.*, 110:213002, May 2013. [cited on p. 77]

[FSC+14] Andreas Fischer, Alexander Sperl, Philipp Cörlin, Michael Schönwald, Sebastian Meuren, Joachim Ullrich, Thomas Pfeifer, Robert Moshammer, and Arne Senftleben. Measurement of the autoionization lifetime of the energetically lowest doubly excited $Q_1\,^1\Sigma_u^+$ state in H_2 using electron ejection asymmetry. *Journal of Physics B: Atomic, Molecular and Optical Physics*, 47(2):021001, 2014. [cited on p. 77]

[fXRO] Center for X-Ray Optics. Filter Transmission. `http://henke.lbl.gov/optical_constants/filter2.html`. Online; accessed 08.07.2015. [cited on p. 58]

[Gil65] F. Gilmore. Potential energy curves for N_2, NO, O_2 and corresponding ions. *Journal of Quantitative Spectroscopy and Radiative Transfer*, 5:369–389, April 1965. [cited on p. 118, 119]

[GM31] Maria Göppert-Mayer. Über Elementarakte mit zwei Quantensprüngen. *Ann. Phys.*, 401(3):273–294, 1931. [cited on p. 25]

[GM15] Kirill Gokhberg and Tsveta Miteva. Private communication. 2015. [cited on p. 131, 137]

[Gop10] Ram Gopal. *Electron Wave Packet Interferences in Ionization with Few-Cycle Laser Pulses and the Dissociative Photoionization of D_2 with Ultrashort Extreme Ultraviolet Pulses*. PhD thesis, Ruperto-Carola University of Heidelberg, Germany, 2010. [cited on p. 20, 61, 63, 64, 66]

[GRT+07] Etienne Gagnon, Predrag Ranitovic, Xiao-Min Tong, C. L. Cocke, Margaret M. Murnane, Henry C. Kapteyn, and Arvinder S. Sandhu. Soft X-ray-Driven Femtosecond Molecular Dynamics. *Science*, 317(5843):1374–1378, September 2007. [cited on p. 6, 7, 96, 115, 119, 120, 128, 129, 130, 131, 132, 133, 134, 137, 138]

[GSCS96] T. E. Glover, R. W. Schoenlein, A. H. Chin, and C. V. Shank. Observation of Laser Assisted Photoelectric Effect and Femtosecond High Order Harmonic Radiation. *Phys. Rev. Lett.*, 76:2468–2471, Apr 1996. [cited on p. 60]

[GSH+08] E. Goulielmakis, M. Schultze, M. Hofstetter, V. S. Yakovlev, J. Gagnon, M. Uiberacker, A. L. Aquila, E. M. Gullikson, D. T. Attwood, R. Kienberger, F. Krausz, and U. Kleineberg. Single-Cycle Nonlinear Optics. *Science*, 320(5883):1614–1617, 2008. [cited on p. 5, 31]

[GST+00] R. E. Grisenti, W. Schöllkopf, J. P. Toennies, G. C. Hegerfeldt, T. Köhler, and M. Stoll. Determination of the Bond Length and Binding Energy of the Helium Dimer by Diffraction from a Transmission Grating. *Phys. Rev. Lett.*, 85(11):2284–2287, September 2000. [cited on p. 17]

[GUH+05] Christoph Gohle, Thomas Udem, Maximilian Herrmann, Jens Rauschenberger, Ronald Holzwarth, Hans A. Schuessler, Ferenc Krausz, and Theodor W. Hansch. A frequency comb in the extreme ultraviolet. *Nature*, 436(7048):234–237, July 2005. [cited on p. 51]

[HCR97] M. Hochlaf, G. Chambaud, and P. Rosmus. Quartet states in the N_2^+ radical cation. *Journal of Physics B: Atomic, Molecular and Optical Physics*, 30(20):4509–, 1997. [cited on p. 130]

[Her87] H. Hertz. Ueber einen Einfluss des ultravioletten Lichtes auf die electrische Entladung. *Ann. Phys.*, 267(8):983–1000, 1887. [cited on p. 9]

[HH79] K. P. Huber and G. Herzberg. *Molecular Spectra and Molecular Structure, Vol. 4*. Van Nostrand Reinold Company, 1979. [cited on p. 90, 91]

[HL27] W. Heitler and F. London. Wechselwirkung neutraler Atome und homöopolare Bindung nach der Quantenmechanik. *Zeitschrift für Physik*, 44:455–472, 1927. [cited on p. 11]

[HL07] William M. Haynes and David R. Lide. *CRC Handbook of Chemistry and Physics*. CRC Press, Taylor & Francis Group, 2007. [cited on p. 3]

[HMFT07] Akiyoshi Hishikawa, Akitaka Matsuda, Mizuho Fushitani, and Eiji J. Takahashi. Visualizing Recurrently Migrating Hydrogen in Acetylene Dication by Intense Ultrashort Laser Pulses. *Phys. Rev. Lett.*, 99(25):258302–, December 2007. [cited on p. 4]

[HS15] Ingolf V. Hertel and Claus-Peter Schulz. *Atoms, Molecules and Optical Physics 2. Molecules and Photons - Spectroscopy and Collisions*. Springer Berlin Heidelberg, 2015. [cited on p. 11, 14, 15, 16, 17, 19, 21, 28]

[HT10] Feng He and Uwe Thumm. Dissociative ionization of H_2 in an attosecond pulse train and delayed laser pulse. *Phys. Rev. A*, 81:053413, May 2010. [cited on p. 80]

[HWC+02] Jennifer L. Herek, Wendel Wohlleben, Richard J. Cogdell, Dirk Zeidler, and Marcus Motzkus. Quantum control of energy flow in light harvesting. *Nature*, 417(6888):533–535, May 2002. [cited on p. 5]

[ISS05] Misha Yu Ivanov, Michael Spanner, and Olga Smirnova. Anatomy of strong field ionization. *Journal of Modern Optics*, 52(2-3):165–184, January 2005. [cited on p. 25]

[JMTY05] R. Jason Jones, Kevin D. Moll, Michael J. Thorpe, and Jun Ye. Phase-Coherent Frequency Combs in the Vacuum Ultraviolet via High-Harmonic Generation inside a Femtosecond Enhancement Cavity. *Phys. Rev. Lett.*, 94:193201, May 2005. [cited on p. 51]

[JRH+10] Y. H. Jiang, A. Rudenko, O. Herrwerth, L. Foucar, M. Kurka, K. U. Kühnel, M. Lezius, M. F. Kling, J. van Tilborg, A. Belkacem, K. Ueda, S. Düsterer, R. Treusch, C. D. Schröter, R. Moshammer, and J. Ullrich. Ultrafast Extreme Ultraviolet Induced Isomerization of Acetylene Cations. *Phys. Rev. Lett.*, 105(26):263002–, December 2010. [cited on p. 4]

[Kel65] L. V. Keldysh. Ionization in the field of a strong electromagnetic wave. *Soviet Physics JETP*, 20:1307–1314, May 1965. [cited on p. 23]

[Kel10] U. Keller. Ultrafast solid-state laser oscillators: a success story for the last 20 years with no end in sight. *Applied Physics B*, 100(1):15–28, 2010. [cited on p. 46, 51]

[KFF+09] Manuel Kremer, Bettina Fischer, Bernold Feuerstein, Vitor L. B. de Jesus, Vandana Sharma, Christian Hofrichter, Artem Rudenko, Uwe Thumm, Claus Dieter Schröter, Robert Moshammer, and Joachim Ullrich. Electron Localization in Molecular Fragmentation of H_2 by Carrier-Envelope Phase Stabilized Laser Pulses. *Phys. Rev. Lett.*, 103:213003, Nov 2009. [cited on p. 5]

[KGT+15] Ofer Kfir, Patrik Grychtol, Emrah Turgut, Ronny Knut, Dmitriy Zusin, Dimitar Popmintchev, Tenio Popmintchev, Hans Nembach, Justin M. Shaw, Avner Fleischer, Henry Kapteyn, Margaret Murnane, and Oren Cohen.

Generation of bright phase-matched circularly-polarized extreme ultraviolet high harmonics. *Nat Photon*, 9(2):99–105, February 2015. [cited on p. 31]

[KGU+04] R. Kienberger, E. Goulielmakis, M. Uiberacker, A. Baltuska, V. Yakovlev, F. Bammer, A. Scrinzi, Th. Westerwalbesloh, U. Kleineberg, U. Heinzmann, M. Drescher, and F. Krausz. Atomic transient recorder. *Nature*, 427(6977):817–821, February 2004. [cited on p. 5]

[KHG+12] T. Kessler, C. Hagemann, C. Grebing, T. Legero, U. Sterr, F. Riehle, M. J. Martin, L. Chen, and J. Ye. A sub-40-mHz-linewidth laser based on a silicon single-crystal optical cavity. *Nat Photon*, 6(10):687–692, October 2012. [cited on p. 43]

[Kir60] G. Kirchhoff. Ueber das Verhältniss zwischen dem Emissionsvermögen und dem Absorptionsvermögen der Körper für Wärme und Licht. *Ann. Phys.*, 185(2):275–301, 1860. [cited on p. 9]

[KLS+09] F. Kelkensberg, C. Lefebvre, W. Siu, O. Ghafur, T. T. Nguyen-Dang, O. Atabek, A. Keller, V. Serov, P. Johnsson, M. Swoboda, T. Remetter, A. L'Huillier, S. Zherebtsov, G. Sansone, E. Benedetti, F. Ferrari, M. Nisoli, F. Lépine, M. F. Kling, and M. J. J. Vrakking. Molecular Dissociative Ionization and Wave-Packet Dynamics Studied Using Two-Color XUV and IR Pump-Probe Spectroscopy. *Phys. Rev. Lett.*, 103:123005, Sep 2009. [cited on p. 4, 80, 147]

[KOB+14] Andreas Kaldun, Christian Ott, Alexander Blättermann, Martin Laux, Kristina Meyer, Thomas Ding, Andreas Fischer, and Thomas Pfeifer. Extracting Phase and Amplitude Modifications of Laser-Coupled Fano Resonances. *Phys. Rev. Lett.*, 112:103001, Mar 2014. [cited on p. 5]

[KR60] W. Kolos and C. C. J. Roothaan. Accurate Electronic Wave Functions for the H_2 Molecule. *Rev. Mod. Phys.*, 32:219–232, Apr 1960. [cited on p. 12, 13]

[Kre09] Manuel Kremer. *Einfluß der Träger-Einhüllenden-Phase auf die Wechselwirkung ultrakurzer Laserpulse mit Molekülen*. PhD thesis, Ruprecht-Karls-Universität Heidelberg, 2009. [cited on p. 21]

[KS89] K. C. Kulander and B. W. Shore. Calculations of Multiple-Harmonic Conversion of 1064-nm Radiation in Xe. *Phys. Rev. Lett.*, 62(5):524–526, January 1989. [cited on p. 28]

[KSK92] Jeffrey L. Krause, Kenneth J. Schafer, and Kenneth C. Kulander. High-order harmonic generation from atoms and ions in the high intensity regime. *Phys. Rev. Lett.*, 68(24):3535–3538, June 1992. [cited on p. 28]

[Lan32] L. Landau. Zur Theorie der Energieubertragung. II. *Physikalische Zeitschrift der Sowjetunion*, 2:46–51, 1932. [cited on p. 131]

[LBI+94] M. Lewenstein, Ph. Balcou, M. Yu. Ivanov, Anne L'Huillier, and P. B. Corkum. Theory of high-harmonic generation by low-frequency laser fields. *Phys. Rev. A*, 49(3):2117–2132, March 1994. [cited on p. 31]

[LHC+98] Y. Lu, Z. X. He, J. N. Cutler, S. H. Southworth, W. C. Stolte, and J. A. R. Samson. Dissociative photoionization study of O_2. *Journal of Electron Spectroscopy and Related Phenomena*, 94:135–147, June 1998. [cited on p. 84]

[LIV14] Franck Lepine, Misha Y. Ivanov, and Marc J. J. Vrakking. Attosecond molecular dynamics: fact or fiction? *Nat Photon*, 8(3):195–204, March 2014. [cited on p. 5]

[LKC+12] M. Lucchini, K. Kim, F. Calegari, F. Kelkensberg, W. Siu, G. Sansone, M. J. J. Vrakking, M. Hochlaf, and M. Nisoli. Autoionization and ultrafast relaxation dynamics of highly excited states in N_2. *Phys. Rev. A*, 86(4):043404–, October 2012. [cited on p. 118]

[LL74] A.J. Lorquet and J.C. Lorquet. Isotopic effects in accidental predissociation. The case of the $C\,^2\Sigma_u^+$ state of N_2^+. *Chemical Physics Letters*, 26(1):138–143, May 1974. [cited on p. 118]

[LL02] Ping Lin and Robert R. Lucchese. Theoretical studies of cross sections and photoelectron angular distributions in the valence photoionization of molecular oxygen. *The Journal of Chemical Physics*, 116(20):8863–8875, 2002. [cited on p. 89, 99]

[LLL+05] F. Légaré, Kevin Lee, I. Litvinyuk, P. Dooley, A. Bandrauk, D. Villeneuve, and P. Corkum. Imaging the time-dependent structure of a molecule as it undergoes dynamics. *Phys. Rev. A*, 72:052717, Nov 2005. [cited on p. 80]

[LMMJ+04] R. López-Martens, J. Mauritsson, P. Johnsson, K. Varjú, A. L'Huillier, W. Kornelis, J. Biegert, U. Keller, M. Gaarde, and K. Schafer. Characterization of high-order harmonic radiation on femtosecond and attosecond time scales. *Applied Physics B*, 78(7-8):835–840, 2004. [cited on p. 60]

[LMR01] Robert J. Levis, Getahun M. Menkir, and Herschel Rabitz. Selective Bond Dissociation and Rearrangement with Optimally Tailored, Strong-Field Laser Pulses. *Science*, 292(5517):709–713, 2001. [cited on p. 5]

[LNDD+13] C. Lefebvre, T. T. Nguyen-Dang, F. Dion, M. J. J. Vrakking, V. N. Serov, and O. Atabek. Attosecond pump-probe transition-state spectroscopy of laser-induced molecular dissociative ionization: Adiabatic versus nonadiabatic

dressed-state dynamics. *Phys. Rev. A*, 88:053416, Nov 2013. [cited on p. 100]

[LR47] Jr. Lamb, Willis E. and Robert C. Retherford. Fine Structure of the Hydrogen Atom by a Microwave Method. *Phys. Rev.*, 72(3):241–243, August 1947. [cited on p. 9]

[LSK91] A. L'Huillier, K. J. Schafer, and K. C. Kulander. Higher-order harmonic generation in xenon at 1064 nm: The role of phase matching. *Phys. Rev. Lett.*, 66(17):2200–2203, April 1991. [cited on p. 28]

[MA13] Ashley J. Maker and Andrea M. Armani. Nanowatt threshold, alumina sensitized neodymium laser integrated on silicon. *Opt. Express*, 21(22):27238–27245, Nov 2013. [cited on p. 43]

[Mai60] T. H. Maiman. Stimulated Optical Radiation in Ruby. *Nature*, 187(4736):493–494, August 1960. [cited on p. 43]

[MAT12] M. Magrakvelidze, C. M. Aikens, and U. Thumm. Dissociation dynamics of diatomic molecules in intense laser fields: A scheme for the selection of relevant adiabatic potential curves. *Phys. Rev. A*, 86(2):023402–, August 2012. [cited on p. x, 6, 39, 80, 82, 90, 91, 93, 99, 100, 101, 102, 103, 104, 105, 106, 107, 108, 109, 114, 136, 144]

[MFTH11] Akitaka Matsuda, Mizuho Fushitani, Eiji J. Takahashi, and Akiyoshi Hishikawa. Visualizing hydrogen atoms migrating in acetylene dication by time-resolved three-body and four-body Coulomb explosion imaging. *Phys. Chem. Chem. Phys.*, 13(19):8697–8704, 2011. [cited on p. 4]

[MGA+14] Erik P. Mansson, Diego Guenot, Cord L. Arnold, David Kroon, Susan Kasper, J. Marcus Dahlstrom, Eva Lindroth, Anatoli S. Kheifets, Anne L'Huillier, Stacey L. Sorensen, and Mathieu Gisselbrecht. Double ionization probed on the attosecond timescale. *Nat Phys*, 10(3):207–211, March 2014. [cited on p. 5]

[MGJ+87] A. McPherson, G. Gibson, H. Jara, U. Johann, T. S. Luk, I. A. McIntyre, K. Boyer, and C. K. Rhodes. Studies of multiphoton production of vacuum-ultraviolet radiation in the rare gases. *J. Opt. Soc. Am. B*, 4(4):595–601, 1987. [cited on p. 5, 28]

[MHJ+12] M. Magrakvelidze, O. Herrwerth, Y. H. Jiang, A. Rudenko, M. Kurka, L. Foucar, K. U. Kühnel, M. Kübel, Nora G. Johnson, C. D. Schröter, S. Düsterer, R. Treusch, M. Lezius, I. Ben-Itzhak, R. Moshammer, J. Ullrich, M. F. Kling, and U. Thumm. Tracing nuclear-wave-packet dynamics in singly and doubly charged states of N_2 and O_2 with XUV-pump–XUV-probe experiments. *Phys. Rev. A*, 86:013415, Jul 2012. [cited on p. 100]

[Mil88] D. R. Miller. Free jet sources. In *Atomic and Molecular Beam Methods Volume 1*. Oxford University Press, 1988. [cited on p. 64, 65]

[MKBT14] M Magrakvelidze, A Kramer, K Bartschat, and U Thumm. Complementary imaging of the nuclear dynamics in laser-excited diatomic molecular ions in the time and frequency domains. *Journal of Physics B: Atomic, Molecular and Optical Physics*, 47(12):124003–, 2014. [cited on p. 136]

[MMP+82] Christel M. Marian, Ralf Marian, Sigrid D. Peyerimhoff, Bernd A. Hess, Robert J. Buenker, and Georg Seger. Ab initio CI calculation of O_2^+ predissociation phenomena induced by a spin-orbit coupling mechanism. *Molecular Physics*, 46(4):779–810, July 1982. [cited on p. x, 6, 81, 82, 85, 90, 91, 99, 100, 101, 102, 103, 104, 105, 106, 107, 108, 109, 110, 112, 114, 136, 144, 145, 146]

[Mor29] Philip M. Morse. Diatomic molecules according to the wave mechanics. II. vibrational levels. *Phys. Rev.*, 34:57–64, Jul 1929. [cited on p. 34]

[MUU+94] R. Moshammer, J. Ullrich, M. Unverzagt, W. Schmidt, P. Jardin, R. E. Olson, R. Mann, R. Dörner, V. Mergel, U. Buck, and H. Schmidt-Böcking. Low-Energy Electrons and Their Dynamical Correlation with Recoil Ions for Single Ionization of Helium by Fast, Heavy-Ion Impact. *Phys. Rev. Lett.*, 73(25):3371–3374, December 1994. [cited on p. 3, 61]

[Nie07] Thomas Niederhausen. *Quantum Dynamics in Laser-Assisted Collision, Laser-Molecule Interactions, and Particle-Surface Scattering*. PhD thesis, Kansas State University, 2007. [cited on p. 39]

[NVC06] Hiromichi Niikura, D. Villeneuve, and P. Corkum. Controlling vibrational wave packets with intense, few-cycle laser pulses. *Phys. Rev. A*, 73:021402, Feb 2006. [cited on p. 4, 80]

[OKA+14] Christian Ott, Andreas Kaldun, Luca Argenti, Philipp Raith, Kristina Meyer, Martin Laux, Yizhu Zhang, Alexander Blattermann, Steffen Hagstotz, Thomas Ding, Robert Heck, Javier Madronero, Fernando Martin, and Thomas Pfeifer. Reconstruction and control of a time-dependent two-electron wave packet. *Nature*, 516(7531):374–378, December 2014. [cited on p. 5]

[OKR+13] Christian Ott, Andreas Kaldun, Philipp Raith, Kristina Meyer, Martin Laux, Jörg Evers, Christoph H. Keitel, Chris H. Greene, and Thomas Pfeifer. Lorentz Meets Fano in Spectral Line Shapes: A Universal Phase and Its Laser Control. *Science*, 340(6133):716–720, 2013. [cited on p. 5]

[Ott12] Christian Ott. *Attosecond multidimensional interferometry of single and two correlated electrons in atoms*. Diploma thesis, Ruprecht-Karls-Universität Heidelberg, 2012. [cited on p. 54]

[Pal15] Lukas Palm. Bachelor thesis – Work in progress. 2015. [cited on p. 138]

[PAT+09] V. Pervak, I. Ahmad, M. K. Trubetskov, A. V. Tikhonravov, and F. Krausz. Double-angle multilayer mirrors with smooth dispersion characteristics. *Opt. Express*, 17(10):7943–7951, May 2009. [cited on p. 53]

[PCA+10] Tenio Popmintchev, Ming-Chang Chen, Paul Arpin, Margaret M. Murnane, and Henry C. Kapteyn. The attosecond nonlinear optics of bright coherent X-ray generation. *Nat Photon*, 4(12):822–832, December 2010. [cited on p. 28]

[PCP+12] Tenio Popmintchev, Ming-Chang Chen, Dimitar Popmintchev, Paul Arpin, Susannah Brown, Skirmantas Ališauskas, Giedrius Andriukaitis, Tadas Balčiunas, Oliver D. Mücke, Audrius Pugzlys, Andrius Baltuška, Bonggu Shim, Samuel E. Schrauth, Alexander Gaeta, Carlos Hernández-García, Luis Plaja, Andreas Becker, Agnieszka Jaron-Becker, Margaret M. Murnane, and Henry C. Kapteyn. Bright Coherent Ultrahigh Harmonics in the keV X-ray Regime from Mid-Infrared Femtosecond Lasers. *Science*, 336(6086):1287–1291, 2012. [cited on p. 28]

[PCS+11] Adrian N. Pfeiffer, Claudio Cirelli, Mathias Smolarski, Reinhard Dörner, and Ursula Keller. Timing the release in sequential double ionization. *Nat Phys*, 7(5):428–433, May 2011. [cited on p. 21]

[PMM87] M. Pessot, P. Maine, and G. Mourou. 1000 times expansion/compression of optical pulses for chirped pulse amplification. *Optics Communications*, 62(6):419 – 421, 1987. [cited on p. 51]

[PTB+01] P. M. Paul, E. S. Toma, P. Breger, G. Mullot, F. Augé, Ph. Balcou, H. G. Muller, and P. Agostini. Observation of a Train of Attosecond Pulses from High Harmonic Generation. *Science*, 292(5522):1689–1692, 2001. [cited on p. 31]

[PTS+08] V. Pervak, C. Teisset, A. Sugita, S. Naumov, F. Krausz, and A. Apolonski. High-dispersive mirrors for femtosecond lasers. *Opt. Express*, 16(14):10220–10233, Jul 2008. [cited on p. 53]

[REF+06] A. Rudenko, Th. Ergler, B. Feuerstein, K. Zrost, C.D. Schröter, R. Moshammer, and J. Ullrich. Real-time observation of vibrational revival in the fastest molecular system. *Chemical Physics*, 329:193–202, October 2006. [cited on p. 4]

[Rei08] H. R. Reiss. Limits on tunneling theories of strong-field ionization. *Phys. Rev. Lett.*, 101:043002, Jul 2008. [cited on p. 25]

[Rie07] Helga Rietz. *Aufbau und Inbetriebnahme einer Apparatur zur Erzeugung hoher harmonischer Strahlung und deren Charakterisierung*. Diploma thesis, Ruprecht-Karls-Universität Heidelberg, 2007. [cited on p. 54, 138]

[Rie12] Helga Rietz. *Attosekundenphysik mit dem Reaktionsmikroskop: Eine Konzeptstudie, erste Experimente und mögliche Anwendungen*. PhD thesis, Ruperto-Carola University of Heidelberg, Germany, 2012. [cited on p. 54, 57, 59, 60]

[RLB75] A.L. Roche and H. Lefebvre-Brion. Some ab initio calculations related to the predissociation of the $C\,^2\Sigma_u^+$ state of N_2^+. *Chemical Physics Letters*, 32(1):155–158, April 1975. [cited on p. 118, 130]

[Rob04] R.W. Robinett. Quantum wave packet revivals. *Physics Reports*, 392(1–2):1–119, March 2004. [cited on p. 32, 33, 34]

[RVDL+85] M. Richard-Viard, O. Dutuit, M. Lavollee, T. Govers, P. M. Guyon, and J. Durup. O_2^+ ions dissociation studied by threshold photoelectron-photoion coincidence method. *The Journal of Chemical Physics*, 82(9):4054–4063, 1985. [cited on p. 84]

[Sak09] J. J. Sakurai. *Modern quantum mechanics*. Pearson Education, 4 edition, 2009. [cited on p. 39]

[SBC+06] G. Sansone, E. Benedetti, F. Calegari, C. Vozzi, L. Avaldi, R. Flammini, L. Poletto, P. Villoresi, C. Altucci, R. Velotta, S. Stagira, S. De Silvestri, and M. Nisoli. Isolated Single-Cycle Attosecond Pulses. *Science*, 314(5798):443–446, 2006. [cited on p. 31]

[SBGG+13] Michael Schuricke, Klaus Bartschat, Alexei N. Grum-Grzhimailo, Ganjun Zhu, Jochen Steinmann, Robert Moshammer, Joachim Ullrich, and Alexander Dorn. Coherence in multistate resonance-enhanced four-photon ionization of lithium atoms. *Phys. Rev. A*, 88:023427, Aug 2013. [cited on p. 63]

[SBN04] Albert Stolow, Arthur E. Bragg, and Daniel M. Neumark. Femtosecond Time-Resolved Photoelectron Spectroscopy. *Chem. Rev.*, 104:1719–1757, 2004. [cited on p. 80]

[SCBK94] Christian Spielmann, P.F. Curley, T. Brabec, and Ferenc Krausz. Ultrabroadband femtosecond lasers. *Quantum Electronics, IEEE Journal of*, 30(4):1100–1114, 1994. [cited on p. 43, 46, 50]

[Sch14] Kirsten Schnorr. *XUV Pump–Probe Experiments on Electron Rearrangement and Interatomic Coulombic Decay in Diatomic Molecules*. PhD thesis, Ruperto-Carola University of Heidelberg, Germany, 2014. [cited on p. 64, 65, 74]

[Sch15] Michael Schönwald. *On the Contribution of autoionizing states to XUV radiation-induced double ionization of nitrous oxide (N_2O)*. PhD thesis, Johann Wolfgang Goethe-Universität in Frankfurt am Main, Deutschland, 2015. [cited on p. 56, 98, 138]

[Sen09] Arne Senftleben. *Kinematically complete study on electron impact ionisation of aligned hydrogen molecules*. PhD thesis, Ruperto-Carola University of Heidelberg, Germany, 2009. [cited on p. 69, 142]

[SFK+10] M. Schultze, M. Fieß, N. Karpowicz, J. Gagnon, M. Korbman, M. Hofstetter, S. Neppl, A. L. Cavalieri, Y. Komninos, Th. Mercouris, C. A. Nicolaides, R. Pazourek, S. Nagele, J. Feist, J. Burgdörfer, A. M. Azzeer, R. Ernstorfer, R. Kienberger, U. Kleineberg, E. Goulielmakis, F. Krausz, and V. S. Yakovlev. Delay in Photoemission. *Science*, 328(5986):1658–1662, 2010. [cited on p. 5]

[SGS+08] Arvinder S. Sandhu, Etienne Gagnon, Robin Santra, Vandana Sharma, Wen Li, Phay Ho, Predrag Ranitovic, C. Lewis Cocke, Margaret M. Murnane, and Henry C. Kapteyn. Observing the Creation of Electronic Feshbach Resonances in Soft X-ray-Induced O_2 Dissociation. *Science*, 322(5904):1081–1085, 2008. [cited on p. 138]

[SIKS79] Haruhisa Soda, Ken-ichi Iga, Chiyuki Kitahara, and Yasuharu Suematsu. GaInAsP/InP Surface Emitting Injection Lasers. *Japanese Journal of Applied Physics*, 18(12):2329, 1979. [cited on p. 43]

[SM85] Donna Strickland and Gerard Mourou. Compression of amplified chirped optical pulses. *Optics Communications*, 56(3):219 – 221, 1985. [cited on p. 51]

[Smi87] Ian W. M. Smith. Direct probing of reactions. *Nature*, 328(6133):760–761, August 1987. [cited on p. 3]

[SPDC90] Robin Shakeshaft, R. M. Potvliege, Martin Dörr, and W. E. Cooke. Multiphoton processes in an intense laser field. IV. the static-field limit. *Phys. Rev. A*, 42(3):1656–1668, August 1990. [cited on p. 25]

[Spe13] Alexander Sperl. *XUV–IR pump–probe experiments: Exploring nuclear and electronic correlated quantum dynamics in the hydrogen molecule*. PhD thesis, Ruperto-Carola University of Heidelberg, Germany, 2013. [cited on p. 49, 52, 64]

[SSKF94] Robert Szipöcs, Christian Spielmann, Ferenc Krausz, and Kárpát Ferencz. Chirped multilayer coatings for broadband dispersion control in femtosecond lasers. *Opt. Lett.*, 19(3):201–203, Feb 1994. [cited on p. 53]

[SSL+14] J. Seres, E. Seres, B. Landgraf, B. Ecker, B. Aurand, T. Kuehl, and C. Spielmann. High-harmonic generation and parametric amplification in the soft X-rays from extended electron trajectories. *Sci. Rep.*, 4:–, February 2014. [cited on p. 28]

[SSV+05] J. Seres, E. Seres, A. J. Verhoef, G. Tempea, C. Streli, P. Wobrauschek, V. Yakovlev, A. Scrinzi, C. Spielmann, and F. Krausz. Laser technology: Source of coherent kiloelectronvolt X-rays. *Nature*, 433(7026):596–596, February 2005. [cited on p. 28]

[Sve10] Orazio Svelto. *Principles of Lasers*. Springer US, 5 edition, 2010. [cited on p. 45, 46, 50, 51]

[SYDK93] K. J. Schafer, Baorui Yang, L. F. DiMauro, and K. C. Kulander. Above threshold ionization beyond the high harmonic cutoff. *Phys. Rev. Lett.*, 70(11):1599–1602, March 1993. [cited on p. 25]

[SZS+11] Michael Schuricke, Ganjun Zhu, Jochen Steinmann, Konstantinos Simeonidis, Igor Ivanov, Anatoli Kheifets, Alexei N. Grum-Grzhimailo, Klaus Bartschat, Alexander Dorn, and Joachim Ullrich. Strong-field ionization of lithium. *Phys. Rev. A*, 83:023413, Feb 2011. [cited on p. 63]

[TA75] Joel Tellinghuisen and D.L. Albritton. Predissociation of the $C\,^2\Sigma_u^+$ state of N_2^+. *Chemical Physics Letters*, 31(1):91–96, February 1975. [cited on p. 118]

[TNF08] Uwe Thumm, Thomas Niederhausen, and Bernold Feuerstein. Time-series analysis of vibrational nuclear wave-packet dynamics in $D_2{}^+$. *Phys. Rev. A*, 77:063401, Jun 2008. [cited on p. 136, 144]

[TSN+11] P. Tzallas, E. Skantzakis, L. A. A. Nikolopoulos, G. D. Tsakiris, and D. Charalambidis. Extreme-ultraviolet pump-probe studies of one-femtosecond-scale electron dynamics. *Nat Phys*, 7(10):781–784, October 2011. [cited on p. 5]

[TTY95] K. T. Tang, J. P. Toennies, and C. L. Yiu. Accurate Analytical He-He van der Waals Potential Based on Perturbation Theory. *Phys. Rev. Lett.*, 74(9):1546–1549, February 1995. [cited on p. 17]

[TZL02] X. M. Tong, Z. X. Zhao, and C. D. Lin. Theory of molecular tunneling ionization. *Phys. Rev. A*, 66(3):033402–, September 2002. [cited on p. 28]

[UFSC+04] X. Urbain, B. Fabre, E. M. Staicu-Casagrande, N. de Ruette, V. M. Andrianarijaona, J. Jureta, J. H. Posthumus, A. Saenz, E. Baldit, and C. Cornaggia. Intense-Laser-Field Ionization of Molecular Hydrogen in the Tunneling Regime and Its Effect on the Vibrational Excitation of H_2^+. *Phys. Rev. Lett.*, 92(16):163004–, April 2004. [cited on p. 82]

[UMD+03] J. Ullrich, R. Moshammer, A. Dorn, R. Dörner, L. Ph. H. Schmidt, and H. Schmidt-Böcking. Recoil-ion and electron momentum spectroscopy: reaction-microscopes. *Reports on Progress in Physics*, 66(9):1463–, 2003. [cited on p. 71]

[USB87] J. Ullrich and H. Schmidt-Böcking. Time-of-flight spectrometer for the determination of microradian projectile scattering angles in atomic collisions. *Physics Letters A*, 125(4):193 – 196, 1987. [cited on p. 3]

[USBK88] J. Ullrich, H. Schmidt-Böcking, and C. Kelbch. Determination of very small projectile scattering angles by measuring recoil-ion transverse velocities . *Nuclear Instruments and Methods in Physics Research Section A: Accelerators, Spectrometers, Detectors and Associated Equipment*, 268(1):216 – 224, 1988. [cited on p. 3]

[YCK+08] V. Yanovsky, V. Chvykov, G. Kalinchenko, P. Rousseau, T. Planchon, T. Matsuoka, A. Maksimchuk, J. Nees, G. Cheriaux, G. Mourou, and K. Krushelnick. Ultra-high intensity- 300-TW laser at 0.1 Hz repetition rate. *Opt. Express*, 16(3):2109–2114, Feb 2008. [cited on p. 43]

[Zen32] Clarence Zener. Non-adiabatic crossing of energy levels. *Proc. R. Soc. Lond. A*, 137(6):696–702, 1932. [cited on p. 131]

[Zew88] Ahmed H. Zewail. Laser Femtochemistry. *Science*, 242(4886):1645–1653, December 1988. [cited on p. 3]

[Zew00] Ahmed H. Zewail. Femtochemistry: Atomic-Scale Dynamics of the Chemical Bond. *J. Phys. Chem. A*, 104(24):5660–5694, June 2000. [cited on p. 3, 80]

[ZGH+04] Marcus Zimmermann, Christoph Gohle, Ronald Holzwarth, Thomas Udem, and Theodor W. Hänsch. Optical clockwork with an offset-free difference-frequency comb: accuracy of sum- and difference-frequency generation. *Opt. Lett.*, 29(3):310–312, Feb 2004. [cited on p. 43]

[ZRH+12] X. Zhou, P. Ranitovic, C. W. Hogle, J. H. D. Eland, H. C. Kapteyn, and M. M. Murnane. Probing and controlling non-Born-Oppenheimer dynamics in highly excited molecular ions. *Nat Phys*, 8(3):232–237, March 2012. [cited on p. 138]

[Zro05] Karl Zrost. *Wechselwirkung von Atomen und kleinen Molekülen mit intensiven Laserpulsen*. PhD thesis, Ruperto-Carola University of Heidelberg, Germany, 2005. [cited on p. 21]

[ZZC+12] Kun Zhao, Qi Zhang, Michael Chini, Yi Wu, Xiaowei Wang, and Zenghu Chang. Tailoring a 67 attosecond pulse through advantageous phase-mismatch. *Opt. Lett.*, 37(18):3891–3893, Sep 2012. [cited on p. 5, 31]

Danksagung

An diesem Punkt möchte ich mich herzlich bei allen bedanken, die zum erfolgreichen Abschluss dieser Arbeit beigetragen haben.

Mein Dank gilt zu allererst meinem Betreuer Robert Moshammer, der mir nicht nur bei der Durchführung und Auswertung meiner Experimente mit Rat und Tat zur Seite stand, sondern immer auch den Austausch mit anderen Wissenschaftlern unterstützt und gefördert hat – sei es durch die Teilnahme an Konferenzen, die Herstellung persönlicher Kontakte zu anderen Forschungsgruppen oder aber durch die Hilfe bei der Publikation meiner Ergebnisse. Durch ihn habe ich wertvolle Einblicke in die Welt der Wissenschaft erhalten.

Sehr geholfen haben mir auch Thomas Pfeifer, Uwe Thumm und Joachim Ullrich durch wertvolle Diskussionen, motivierende Gespräche und konstruktive Anregungen für die Planung der Experimente und die Datenauswertung.

Andreas Wolf danke ich für seine Bereitschaft, meine Doktorarbeit als Zweitkorrektor zu begutachten.

Bei meinen Laborkollegen Andreas Fischer, Alexander Sperl, Michael Schönwald, Tomoya Mizuno, Lukas Palm und Madlen Steudtner bedanke ich mich für die gute Arbeitsatmosphäre, die fachliche Unterstützung und für den – im wahrsten Sinne des Wortes – unermüdlichen Einsatz bei nächtlichen Messungen am Institut.

Insbesondere Alexander hat mir mit Engelsgeduld all die Tricks und Kniffe beim Betrieb eines Femtosekundenlasers beigebracht. Ohne seine Unterstützung bei scheinbar endlosen Suchen des zeitlichen Pulsüberlappes, beim Neudesign des Pump–Probe Interferometers und bei der wochenlangen Justage der XUV-Fokussiereinheit hätten die hier präsentierten Messungen niemals durchgeführt werden können. Außerdem hat mich Alex nicht nur durch seine fachlichen, sondern auch durch seine sportlichen Leistungen inspiriert und motiviert.

Andreas Fischer hat mich seit den Anfängen meines Physikstudiums begleitet und mir mit seinem unerschöpflichen Fachwissen zuerst als Wohnheimsnachbar bei Mathezetteln, später bei Diplomprüfungen und schließlich als Büronachbar bei meiner Doktorarbeit zur Seite gestanden. Die von ihm geschriebenen Coupled-Channel Simulation hat den wissenschaftlichen Wert der experimentellen Daten immens gesteigert. Auch seine Aufbewahrung eines Ersatzschlüssels zu meiner Wohnung war gelegentlich Gold wert.

Tomoya Mizuno stand mir bei der Durchführung der entscheidenden Messungen im Frühjahr 2014 zur Seite. Ich bin ihm sehr Dankbar, dass er mir viel Arbeit im Labor

abgenommen hat, als ich mit der Datenauswertung begonnen habe.

Ebenso gilt mein Dank für die schöne und lehrreiche Zeit am Institut Michael Schuricke, Lutz Fechner, Andreas Kaldun, Martin Gärttner, Sebastian Meuren, Nicolas Camus, Helga Rietz, Kirsten Schnorr, Georg Schmid, Sven Augustin und all den anderen aktiven und ehemaligen Mitgliedern der Abteilung Pfeifer/Ullrich.

Für die hilfreichen Korrekturen und Anmerkungen zu dieser Arbeit danke ich Andreas Fischer, Lutz Fechner, Kirsten Schnorr, Alexander Sperl und Michael Schuricke. Bei Bernd Knape und Claus-Dieter Schröter bedanke ich mich für die wertvolle technische Unterstützung im Labor.

Auch meiner Familie und Großeltern, möchte ich an dieser Stelle ganz herzlich danken für die Unterstützung und das Interesse, das ihr meiner wissenschaftlichen Arbeit entgegengebracht habt und auch für die gelegentliche Ablenkung. Und natürlich danke ich Verena für die vielen wunderschönen Ablenkungen von dieser Arbeit, z.B. durch eine Gebirgsüberquerung, das Durchschwimmen von Flüssen und das Erklimmen von Vulkanen. Und für alles andere.

Erklärung:

Ich versichere, dass ich diese Arbeit selbstständig verfasst habe und keine anderen als die angegebenen Quellen und Hilfsmittel benutzt habe.

Heidelberg, den 03. August 2015,

.....

Philipp Cörlin